UNIVERSITY OF CALIFORNIA SAN DIEGO

Ultrasound and photoacoustic imaging in chronic wound care

A Dissertation submitted in partial satisfaction of the requirements
for the degree Doctor of Philosophy

in

Bioengineering

by

Yash Mantri

Committee in charge:

Professor Jesse V. Jokerst, Chair
Professor Adam J. Engler, Co-Chair
Professor Ratneshwar Lal
Professor Andrea R. Tao
Professor Yingxiao Wang

2022

The Dissertation of Yash Mantri is approved, and it is acceptable in quality and form for publication on microfilm and electronically.

University of California San Diego

2022

TABLE OF CONTENTS

LIST OF FIGURES

LIST OF TABLES

ACKNOWLEDGEMENTS

First, I would like to thank Prof. Jesse Jokerst for giving me the opportunity to pursue a PhD in his lab. He supported my transition from the master's to PhD program and provided me an environment that I could thrive in. During my time at the lab, I have learned to collaborate, come up with new ideas, test them, fail, and persevere. I had a unique PhD experience as I developed wet lab skills on my bench, culture cells, develop animal models, and lead multiple clinical research projects. This would not be possible without the opportunities his lab presented.

I would also like to thank all my lab mates both past and present whose constant support, critique, and collaborative efforts significantly improved the quality of my work. I would specially like to thank Dr. Ali Hariri, Dr. Colman Moore, Raina Borum, Dr. Jorge Palma-Chavez, Dr. Maurice Retout, Jason Tsujimoto, Sarah Loshinsky, and Barak Davidi for all their help throughout the years.

Throughout my PhD I had the privilege to collaborate with exceptional clinicians, nurses, and scientists. A big thank you to Dr. Caesar Anderson, Dr. Pranav Garimella, and Dr. William Penny, who guided me through all my clinical research endeavors. I would also like to acknowledge the entire nursing team at the UC San Diego Health Hyperbaric Medicine and Wound Care. They were exceptionally welcoming and patient with me.

Finally, I would like to thank my family and friends as without their constant support I would not be the person or scientist I am today. My parents Poonam and Ramesh Mantri who embody the spirit of hard work and perseverance over all else. My sisters Sumegha Mantri and Vishaka Mantri Roininen for being the perfect support system a brother could ever ask for. My brother-in-law's Sunil Vallu and Mikko Mantri Roininen for all the gentleman drinks. My friends, Veer Doshi, Laksheeta Johari, Nikhil Patel, Ria Khetan, Shikhar Agrawal, Izaac Sit, and Megan

Liang for all the adventures and tolerating me over the last few years. Special thank you to Pancha, for the unconditional love and a tail wag happy enough to light up your mood after a day of failed experiments.

I also acknowledge all other collaborators:

Chapter 1, in full, is a reprint of the material as it appears in Engineering plasmonic nanoparticles for enhanced photoacoustic imaging. Mantri, Yash; Jokerst, Jesse V., ACS Nano, 2020.The dissertation author was the primary investigator and author of this paper.

Chapter 2, in full, is a reprint of the material as it appears in Iodide-doped precious metal nanoparticles: measuring oxidative stress in vivo via photoacoustic imaging. Mantri, Yash; Davidi, Barak; Lemaster, Jeanne E.; Hariri Ali; Jokerst, Jesse V., Nanoscale, 2019. The dissertation author was the primary investigator and author of this paper.

Chapter 3, in part, has been submitted for publication of the material as it may appear in Photoacoustic enhancement of ferricyanide treated silver chalcogenide coated gold nanorods, 2022, Mantri, Yash; Sit, Izaac; Zhou, Jiajing; Grassian, Vicki H.; Jokerst, Jesse V. The dissertation author was the primary researcher and author of this paper.

Chapter 4, in full, is a reprint of the material as it appears in Point of Care ultrasound as a tool to assess wound size and tissue regeneration after skin grafting. Mantri, Yash; Tsujimoto, Jason; Penny, William F.; Garimella, Pranav S.; Anderson, Caesar A; Jokerst, Jesse V., Ultrasound in Medicine and Biology, 2021. The dissertation author was the primary investigator and author of this paper.

Chapter 5, in full, is a reprint of the material as it appears in Photoacoustic monitoring of angiogenesis predicts response to therapy in healing wounds. Mantri, Yash; Tsujimoto, Jason; Donovan, Brian; Fernandes, Christopher C.; Garimella, Pranav S.; Penny, William F.; Anderson,

Caesar A; Jokerst, Jesse V., Wound Repair and Regeneration, 2021. The dissertation author was the primary investigator and author of this paper.

Chapter 6, in full, is a reprint of the material as it appears in Monitoring peripheral hemodynamic response to changes in blood pressure via photoacoustic imaging. Mantri, Yash; Dorobek, Tyler R.; Tsujimoto, Jason; Penny, William F; Garimella, Pranav S.; Jokerst, Jesse V., Photoacoustics, 2022. The dissertation author was the primary investigator and author of this paper.

Chapter 7, in full, is a reprint of the material as it appears in The impact of skin tone on photoacoustic oximetry and tools to minimize bias. Mantri, Yash; Jokerst, Jesse V., Biomedical Optics Express, 2022. The dissertation author was the primary investigator and author of this paper.

VITA

2017 Bachelor of Technology in Biomedical Engineering, D.Y. Patil University

2021 Master of Science in Bioengineering, University of California San Diego

2022 Doctor of Philosophy in Degree major, University of California San Diego

PUBLICATIONS

Mantri, Y.; Jokerst, J. V., Engineering plasmonic nanoparticles for enhanced photoacoustic imaging. *ACS nano* **2020,** *14* (8), 9408-9422.

Mantri, Y.; Davidi, B.; Lemaster, J. E.; Hariri, A.; Jokerst, J. V., Iodide-doped precious metal nanoparticles: measuring oxidative stress in vivo via photoacoustic imaging. *Nanoscale* **2020,** *12* (19), 10511-10520.

Mantri, Y.; Tsujimoto, J.; Penny, W. F.; Garimella, P. S.; Anderson, C. A.; Jokerst, J. V., Point-of-Care Ultrasound as a Tool to Assess Wound Size and Tissue Regeneration after Skin Grafting. *Ultrasound in Medicine & Biology* **2021,** *47* (9), 2550-2559.

Mantri, Y.; Tsujimoto, J.; Donovan, B.; Fernandes, C. C.; Garimella, P. S.; Penny, W. F.; Anderson, C. A.; Jokerst, J. V., Photoacoustic monitoring of angiogenesis predicts response to therapy in healing wounds. *Wound Repair and Regeneration* **2021**.

Mantri, Y.; Jokerst, J. V., Impact of skin tone on photoacoustic oximetry and tools to minimize bias. *Biomedical Optics Express* **2022,** *13* (2), 875-887.

Mantri, Y.; Dorobek, T. R.; Tsujimoto, J.; Penny, W. F.; Garimella, P. S.; Jokerst, J. V., Monitoring peripheral hemodynamic response to changes in blood pressure via photoacoustic imaging. *Photoacoustics* **2022**, 100345.

Mantri, Y.*; Jin, Z.*; Retout, M.; Cheng, Y.; Zhou, J.; Jorns, A.; Fajtova, P.; Yim, W.; Moore, C.; Xu, M.; Creyer, M.; Borum, R. M.; Zhou, J.; Wu, Z.; He, T.; Penny, W. F.; O'Donoghue, A. J.; Jokerst, J., A Charge-Switchable Zwitterionic Peptide for Rapid Detection of SARS-CoV-2 Main Protease. *Angewandte Chemie International Edition* **2021**.

Hariri, A.; Alipour, K.; **Mantri, Y**.; Schulze, J. P.; Jokerst, J. V., Deep learning improves contrast in low-fluence photoacoustic imaging. *Biomedical optics express* **2020,** *11* (6), 3360-3373.

Moore, C.; Borum, R. M.; **Mantri, Y**.; Xu, M.; Fajtová, P.; O'Donoghue, A. J.; Jokerst, J. V., Activatable carbocyanine dimers for photoacoustic and fluorescent detection of protease activity. *ACS sensors* **2021,** *6* (6), 2356-2365.

Yim, W.; Zhou, J.; **Mantri, Y**.; Creyer, M. N.; Moore, C. A.; Jokerst, J. V., Gold nanorod–melanin hybrids for enhanced and prolonged photoacoustic imaging in the near-infrared-II window. *ACS Applied Materials & Interfaces* **2021,** *13* (13), 14974-14984.

Chavez, J. P.; Wear, K. A.; **Mantri, Y**.; Jokerst, J. V.; Vogt, W. C., Photoacoustic imaging phantoms for assessment of object detectability and boundary buildup artifacts. *Photoacoustics* **2022**, 100348.

Schlereth, M.; Stromer, D.; **Mantri, Y**.; Tsujimoto, J.; Breininger, K.; Maier, A.; Anderson, C.; Garimella, P. S.; Jokerst, J. V., Initial Investigations Towards Non-invasive Monitoring of Chronic Wound Healing Using Deep Learning and Ultrasound Imaging. *arXiv preprint arXiv:2201.10511* **2022**.

Hariri, A.; Moore, C.; **Mantri, Y**.; Jokerst, J. V., Photoacoustic imaging as a tool for assessing hair follicular organization. *Sensors* **2020,** *20* (20), 5848.

Mozaffarzadeh, M.; Moore, C.; Golmoghani, E. B.; **Mantri, Y**.; Hariri, A.; Jorns, A.; Fu, L.; Verweij, M. D.; Orooji, M.; de Jong, N., Motion-compensated noninvasive periodontal health monitoring using handheld and motor-based photoacoustic-ultrasound imaging systems. *Biomedical Optics Express* **2021,** *12* (3), 1543-1558.

Yim, W.; Borum, R. M.; Zhou, J.; **Mantri, Y**.; Wu, Z.; Zhou, J.; Jin, Z.; Creyer, M.; Jokerst, J. V., Ultrasmall gold nanorod-polydopamine hybrids for enhanced photoacoustic imaging and photothermal therapy in second near-infrared window. *Nanotheranostics* **2022,** *6* (1), 79.

He, T.; Bradley, D. G.; Zhou, J.; Jorns, A.; **Mantri, Y**.; Hanna, J. V.; Jokerst, J. V., Hydro-Expandable Calcium Phosphate Micro/Nano-Particles with Controllable Size and Morphology for Mechanical Ablation. *ACS Applied Nano Materials* **2021,** *4* (4), 3877-3886.

Jin, Z.; Jorns, A.; Yim, W.; Wing, R.; **Mantri, Y**.; Zhou, J.; Zhou, J.; Wu, Z.; Moore, C.; Penny, W. F., Mapping Aerosolized Saliva on Face Coverings for Biosensing Applications. *Analytical Chemistry* **2021,** *93* (31), 11025-11032.

Zhou, J.; Yim, W.; Zhou, J.; Jin, Z.; Xu, M.; **Mantri, Y**.; He, T.; Cheng, Y.; Fu, L.; Wu, Z., A fiber optic photoacoustic sensor for real-time heparin monitoring. *Biosensors and Bioelectronics* **2022,** *196*, 113692.

Jin, Z.; Yeung, J.; Zhou, J.; Cheng, Y.; Li, Y.; **Mantri, Y**.; He, T.; Yim, W.; Xu, M.; Wu, Z.; Fajtová, P.; Creyer, M.; Moore, C.; Fu, L.; Penny, W. F.; O'Donoghue, A. J.; Jokerst, J., Peptidic Sulfhydryl for Interfacing Nanocrystals and Subsequent Sensing of SARS-CoV-2 Protease. *Chemistry of Materials* **2022**.

Zhou, J.; Xu, M.; Jin, Z.; Borum, R. M.; Avakyan, N.; Cheng, Y.; Yim, W.; He, T.; Zhou, J.; Wu, Z.; **Mantri, Y**.; Jokerst, J., Versatile Polymer Nanocapsules via Redox Competition. *Angewandte Chemie International Edition* **2021,** *60* (50), 26357-26362.

ABSTRACT OF THE DISSERTATION

Ultrasound and photoacoustic imaging in chronic wound care

by

Yash Mantri

Doctor of Philosophy in Bioengineering

University of California San Diego, 2022

Professor Jesse V. Jokerst, Chair
Professor Adam J. Engler, Co-Chair

Photoacoustic imaging is an emerging imaging modality whereby pulsed laser illumination generates pressure transients that are detectable using conventional ultrasound. Plasmonic nanoparticles such as gold nanorods and spheres are commonly employed exogenous contrast agents for both sensing and therapeutic applications. This dissertation first presents a detailed review of engineering plasmonic nanoparticles for enhanced photoacoustic imaging followed by the design of iodide and chalcogenide doped silver-coated gold nanorods for oxidative stress sensing and enhanced photoacoustics. Clinically, photoacoustics leverages hemoglobin and melanin as endogenous contrast agents for breast, vascular, and wound imaging. The rest of this dissertation focuses on the use of ultrasound and photoacoustic imaging to monitor and predict chronic wound healing in human subjects. Chronic wounds are a major health problem that cause the medical infrastructure billions of dollars every year. Chronic wounds are often difficult to heal

and cause significant discomfort. Although wound specialists have numerous therapeutic modalities at their disposal, tools that could 3D-map wound bed physiology and guide therapy do not exist. Visual cues are the current standard but are limited to surface assessment; clinicians rely on experience to predict response to therapy. Photoacoustic imaging can solve these major limitations. Chronic wound patients often receive skin grafts to promote tissue regeneration, but grafting makes it impossible to monitor the underlying wound bed. Ultrasound imaging can be used to size wounds in three dimensions, monitor, and predict tissue loss or regeneration under a skin graft. The addition of photoacoustic imaging allows functional imaging of angiogenesis and perfusion into the wound bed, both essential for wound healing. An increase in photoacoustic signal corresponds to higher perfusion and the rate of photoacoustic signal increase can predict if a wound is likely to heal or not. Clinical photoacoustic imaging can be limited by melanin, a major optical absorber giving skin its characteristic color. Subjects with darker skin tones and hence high melanin content absorb more photons leaving less light to probe deeper tissues of interest. The bias against darker skin tones subjects can be easily minimized by designing tools that account for variable melanin concentrations.

Chapter 1: Engineering plasmonic nanoparticles for enhanced photoacoustic imaging

1.1 Abstract

Photoacoustic (PA) imaging is an emerging imaging modality whereby pulsed laser illumination generates pressure transients that are detectable using conventional ultrasound. Plasmonic nanoparticles such as gold nanorods and nanostars are often used as PA contrast agents. The thermoelastic expansion model best describes the PA response from plasmonic nanoparticles: Light absorption causes a small increase in temperature leading to thermoelastic expansion. The conversion of optical energy into pressure waves ($\mathbf{p_o}$) is dependent on several features: i) absorption coefficient ($\boldsymbol{\mu_a}$), ii) thermal expansion coefficient ($\boldsymbol{\beta}$), iii) specific heat capacity ($\mathbf{C_p}$) of the absorbing material, iv) speed of sound in the medium (**c**), and v) the illumination fluence (**F**). Controlling the geometry, composition, coatings and solvents around plasmonic nanostructures can help tune these variables to generate the optimum PA signal. The thermoelastic expansion model is not limited to plasmonic structures and holds true for all absorbing molecules. Here, we focus on ways to engineer these variables to enhance the PA response from plasmonic nanoparticles.

1.2 Introduction

Conventional optical imaging uses a light in-light out approach, which limits depth penetration due to scattering in tissue. Ultrasound imaging uses a sound in-sound out approach, which reduces scattering but lacks the spectral capabilities and high contrast of optical imaging. Photoacoustic (PA) imaging solves these limitations and provides spectral ultrasound imaging based on varying optical absorption. PA uses a light in-sound out approach where pulsed light is absorbed to generate pressure transients that are detectable by ultrasound.[1, 2]

PA imaging benefits from contrast agents that produce signal with different characteristics compared to background. The most commonly used endogenous contrast agents are oxygenated and deoxygenated hemoglobin and melanin.[2, 3] Oxy- and deoxy-hemoglobin have distinct absorption spectra. Thus, PA signals obtained at different wavelengths can be unmixed to quantify blood oxygen saturation—a key parameter for diagnostics.[4] Exogenous contrast agents with different optical properties can increase contrast and can be engineered as activatable sensing and therapeutic platforms. These exogenous contrast agents range from dyes [5-7] and small molecules [8-10] to nano [11-13] and micro particles.[14-17] Engineering highly efficient contrast agents can increase sensitivity, image quality, and early-stage diagnostics; it can improve therapeutic efficiency.

To design efficient contrast agents, it is important to understand the method of signal generation of which there are four primary mechanisms: thermal or thermoelastic expansion, vaporization,[15, 18, 19] optical breakdown, and photochemical processes.[20] For biomedical applications and contrast agent development, we are usually interested in the thermoelastic expansion route because it does not change or break the properties of the biological sample under observation.[1] Herein, light absorption causes a small increase in temperature (in the millikelvin range) leading to the brief expansion of the contrast agent.[1, 21, 22] This creates a pressure transient

that can be detected acoustically. There is no bulk heating of the medium because the expansion is spatially and thermally confined using light pulses shorter than the thermal relaxation time of the absorber.[23] The resulting PA signal is a function of the optical, thermal, and elastic properties of the sample.

The pressure difference generated due to thermal expansion (ρ_o) is given below in **Equation 1.1**.[1] Here, β is the thermal expansion coefficient of the absorbing material in K^{-1}; **c** is the speed of sound in ms^{-1} in the medium; C_p is the specific heat capacity of the absorber in J/(K kg); μ_a is the absorption coefficient in cm^{-1}; and **F** is the irradiation fluence in J/cm^2. Γ is the Grüneisen parameter (**Equation 1.2)** characterizing the thermo-acoustic conversion efficiency, and **A** is the local energy deposition density in J/cm^3 (**Equation 1.3**).

$$\rho_o = \left(\frac{\beta c^2}{C_p}\right)\mu_a F = \Gamma A \qquad \text{Equation (1.1)}$$

$$\Gamma = \left(\frac{\beta c^2}{C_p}\right) \qquad \text{Equation (1.2)}$$

$$A = \mu_a F \qquad \text{Equation (1.3)}$$

Plasmonic nanoparticles make good photoacoustic contrast agents because of their high absorption cross section, relative inertness, high stability, and a tunable localized surface plasmon resonance (LSPR).[24, 25] Gold (spheres, rods, plates, shells, stars) and other metal nanostructures are particularly common as PA contrast agents. They are easily functionalized and can respond to specific chemical cues.[26, 27]

To enhance PA signal generation from plasmonic nanoparticles, researchers have turned a few "knobs" as described in **Equation 1.1**. The illumination fluence (**F**) is not a nanoparticle

property and can be tuned separately, e.g., by laser power. The speed of sound (**c**) is a function of the tissue type and can be difficult to manipulate externally. However, the absorption coefficient (μ_a), thermal expansion coefficient (β), and specific heat capacity of the absorber (C_p) can be tuned by modifying the nanoparticle shape, material, solvent, etc. **Equation 1.1** can be applied to all absorbing molecules such as endogenous hemoglobin and melanin and is not just limited to plasmonic nanostructures.[1] Here, we review how the nanoparticle properties can be engineered to enhance PA signal (ρ_o). We focus on the thermoelastic expansion model of PA generation and review ways to engineer the variables presented in **Equation 1.1**.

1.3 Absorption coefficient (μ_a)

The absorption coefficient describes how well a material absorbs incident photons at a defined wavelength—it is directly proportional to photoacoustic signal. As light traverses through a sample it is either scattered or absorbed. Scattering and absorption is strong in tissues hence optical imaging techniques have limited depth penetration (approx. 100 μm). The reduced scattering coefficients for soft tissue and water from 600-900 nm ranges from 10-20 cm^{-1} and less than 0.003 cm^{-1} respectively. The absorption coefficient ranges from 0.1-0.5 cm^{-1} and 0.0015-0.067 cm^{-1} respectively.[28, 29] For PA signal generation, the excitation light must be absorbed to induce thermoelastic expansion (**Equation 1.1**). A high μ_a produces high PA signal (**Equation 1.1**), and there are various ways to increase the absorption coefficient of nanoparticles: increasing absorbance at a wavelength of interest, plasmon coupling leading to local field enhancement and spectral shifts, and shape control of nanoparticles.

1.3.1 Increasing absorbance

Absorbance measures light attenuation through a sample. It combines the effects of photon absorption and scattering. Increased absorption and reduced scattering increase the absorption cross section of a particle. The absorption cross-section is the probability that a photon of a particular wavelength is absorbed by a particle. Typical values for nanoparticles range from 2.9-33.5 x 10^{11} cm^2.[30] Nanoparticles are employed as PA contrast agents because of their high absorption cross-section compared to other small molecules.[31] Generally increasing the absorbance leads to an increase in photoacoustic signal.[32-35] Coatings like polydopamine,[36, 37] melanin, [38] titanium dioxide,[39] graphene oxide, [40] and reduced-graphene oxide [41, 42] on gold nanoparticles increase the absorbance and subsequent PA amplitude. Although uncoated nanoparticles and coatings alone showed no enhancement in all these reports, they do not show if a mixture of the core and shell materials lead to PA enhancement. A unique example was reported by Leng *et al.* in 2018; they engineered gold nanorod-copper sulfide heterostructures with enhanced photothermal conversion efficiency and photostability.[43] They showed that depositing Cu_7S_4 on gold nanorod tips instead of a uniform shell around a nanorod core reduced scattering and increased absorption. The increased absorption lead to a 62% increase in photothermal efficiency. Its effect on PA signal generation remains to be seen.

Adding dyes like rhodamine B,[44] indocyanine green,[45-47] cyanine 5.5, methylene blue, and quenchers like QSY_{21} to nanoparticles like gold or single walled carbon nanotubes increase absorption and enhance PA signals up to 100-fold.[48, 49] Upon irradiation, electrons excited to a higher energy state can relax back to their ground state by i) non-radiative pathway or vibrational relaxation ii) radiative pathway or fluorescence or iii) inter-system crossing or phosphorescence.

Maximizing non-radiative relaxation increases PA amplitude as more energy is converted to heat and thermoelastic expansion.[50]

1.3.2 Plasmon coupling leading to local field enhancement and spectral shifts that changes μ_a

Individual plasmonic oscillations on noble metal nanostructures can be coupled when nanoparticles are in close proximity to each other.[51] Plasmonic coupling can cause the electric field in the interparticle gap to be boosted by several orders of magnitude, which far exceeds the field enhancement for a single plasmonic nanoparticle.[52-56] The plasmon modes of close particles can either be in phase or out of phase with each other. This causes attraction or repulsion leading to a decrease (redshift) or an increase (blueshift) in the hybridized plasmon resonance.[57] Usually, a decrease in nanoparticle size causes a blue shift whereas an increase in size due to nucleation or aggregation causes a red shift. [58] A red shifted LSPR increases μ_a in the near infrared (NIR) range which is favorable for PA imaging. The magnitude of the plasmon shift depends on the particle geometry, plasmon resonance of individual particles, and the interparticle spacing.[53, 59]

PA enhancement due to plasmonic coupling has been extensively reported over the years. Gold nanoparticle strings,[60] biodegradable gold nanovesicles,[61] self-assembled semiconducting-gold nanoparticles,[62] aggregated gold-silica Janus nanoparticles [63] and many more examples show that plasmonic coupling between two or more nanoparticles shifts the LSPR into the biological optical window (650-900 nm). Increasing absorbance in the NIR range results in PA enhancement compared to un-coupled controls. Lu *et al.* (2020) reported a clever method for plasmon coupling-related PA enhancement:[64] They manipulated the LSPR band of AuNPs by enzymatic hydrolysis and induced self-assembly of nanoparticles. Nanoparticle assemblies responded to specific enzymatic cues (collagenase IV) and self-assembled via hydrogen bonding, Π - Π stacking, and

hydrophobic interactions. Self-assembly of AuNPs resulted in a red-shifted absorption spectrum due to plasmon coupling. The increase in absorbance in the NIR range (680-800 nm) along with thermal overlap of assembled particles resulted in 2-fold enhancement in PA intensity.

Recently our group reported iodide-doped silver-coated gold nanorods as an activatable PA contrast agent to measure oxidative stress.[13] We showed that absorption spectra of gold nanorods (AuNRs) can be blue shifted when coated with increasing amounts of silver. Blue shifting of the absorbance reduces μ_a in the NIR range and the PA response at 680 nm. Selective etching of the silver iodide shell using reactive oxygen and nitrogen species can recover the absorption spectra and μ_a of the bare AuNRs. The increase in μ_a at 680 nm resulted in a 70% increase in PA intensity in a mouse model of zymosan induced oxidative stress.

1.4 Shape and size control

Optimizing the geometry of plasmonic nanoparticles can significantly affect their optical and photoacoustic properties.[65] Gold nanoparticles are the most commonly used plasmonic PA contrast agents.[66] They can be synthesized as spheres,[67] cubes,[68] plates,[69] rods,[12, 13, 70-72] cages,[73-75] shells,[76] bipyramids[77], and stars.[78, 79] The tips and edges lead to enhancement of the electromagnetic field as electron density increases at the tips. Simulations have shown that sharper tips have a higher μ_a compared to rounded tips.[80] The emergence of hotspots where plasmons relax thermally via electron-phonon coupling can help generate the PA signal. Electron-phonon coupling describes the movement of atoms in a crystal lattice due to electron oscillations.[81-83] Various shapes exhibit different ratios of absorption and scattering so some shapes are better suited for PA than others. Gold nanospheres are easy to synthesize but their LSPR ($\approx$ 530 nm) lies outside the biological optical window.

Gold nanorods are the most widely used PA contrast agents because of their easily tunable absorption spectrum; unfortunately, they are fairly unstable under high fluence laser illumination.[84] Gold nanocages and nanoshells are also applied as biomedical PA contrast agents. Chigrin and co-workers modelled and showed that the most promising geometries are high aspect ratio gold nanorods and gold nanostars with high absorption and low scattering coefficients.[85] Knights *et al.* (2019) showed that 40-50 nm AuNRs produced the highest PA signal but were also cytotoxic; 10 nm AuNRs were efficient photoacoustic converters at equivalent total mass showing 2.5-fold PA enhancement.[86] There is a considerable amount of data on how PA is affected by shape and size of gold nanoparticles but a comprehensive model that can predict PA response from other plasmonic geometries is still missing.

1.5 Moving plasmonics into the second near infrared window (1000-1700 nm)

Until recently, the field has devoted most of its efforts into engineering plasmonic nanostructures that operate within the first biological optical window (600-900 nm). There exists a second NIR window (1000-1700 nm) where biological tissues have low background. Designing contrast agents that operate within this range can help image deeper by reducing scattering from tissue. Illumination fluence (F) can be increased when using longer (less energetic) wavelengths which is governed by the maximum permissible exposure limit. Although water absorbs strongly at 1450 nm, researchers have shown promising results by moving plasmonics into the NIR-II window. Most of the work in this area is around semiconductor-based polymeric nanoparticle assemblies with broadband absorption.[87-89] Recently, Chen et al . (2019) reported a miniaturized gold nanorod for photoacoustic imaging in the NIR-II window. [90] The LSPR peak of gold nanorods is controlled by the nanoparticle's aspect ratio. Increasing aspect ratio, red shifts the LSPR of nanorods. Aspect ratios of 6 or higher can push the LSPR into the NIR-II range. The common

seed-mediated synthesis of high aspect ratio gold nanorods results in particles that absorb in the NIR-II range but have large dimensions (120 x 18 nm).[72, 90] But for *in vivo* applications nanoparticles must be less than 100 nm in size to favor extravasation and accumulation in tumors. Chen and coworkers (2019) synthesized high aspect ratio gold nanorods (49 x 8 nm) using a seedless synthesis process.[90] The resulting nanoparticles showed peak absorbance at 1064 nm and 3.5-fold photoacoustic enhancement. PA signal from miniaturized nanorods was higher due to a higher surface area to volume ratio compared to their larger counterparts.

The absorption coefficient of plasmonic nanostructures can be easily tuned via the material properties or shape of the nanostructure.[91] For enhanced PA, the ideal nanoparticle should have high light absorbance and low scattering properties. Nanoparticle geometry and size have a significant impact on its optical properties. Geometries with sharp tips such as nanostars exhibit localized plasmon hotspots that result in a higher μ_a. Moving plasmonics into the NIR-II window can help image deeper within tissues. The use of longer and lower energy wavelengths will aid in the clinical translation of PA by keeping exposure levels under the maximum permissible exposure limit while still providing sufficient imaging signal.

Another unique example was demonstrated by Wang *et al.* in 2014.[92] Using FDTD simulations they modelled "rod in shell" nanoparticles with absorption in both the NIR-I and II windows. Their model nanoparticle had a gold core (60 nm x 20 nm), a composite Ag:Au (1:1) outer shell (4 nm), and a hollow gap in between (5 nm). Under longitudinal excitation mode, their nanoparticle showed two distinct absorption peaks at 681 and 1158 nm respectively. This was attributed to near-field enhancement and plasmon hybridization between the core and shell layers. With a higher absorption cross-section compared to uncoated gold nanorods, these rod in shell particles could show high efficiency in both PA and photothermal therapy (PTT) applications.

Broadening the absorbance of gold nanoparticles into the NIR-II range via shape control; gold nanoechinus[93] or with coatings; polydopamine blackbody[37] have been reported. As described earlier, plasmonic coupling of nanoparticles due to self-assembly or aggregation can also red shift its absorbance spectra. The red shift can be engineered into the NIR-II range. Overall, the high absorption cross-section, tunability and sensitivity of plasmonic nanoprobes along with the ability to image deeper and with higher fluence make their move into the second biological optical window highly desirable.[50, 94] Since most of the work done in this field is based on semiconducting and organic probes, plasmonics remains a relatively new but extremely promising area of study.

1.6 Thermal expansion coefficient (β)

The thermal expansion coefficient describes how the size of an object changes as a function of temperature. The thermal expansion coefficient is a material property and hence very difficult to change in a nanoparticle. To the best of our knowledge there have been no reports of engineering the thermal expansion coefficient of a nanoparticle. However, many groups have modelled and partially shown that the PA signal is a summed contribution of the thermal expansion of the nanoparticle and its solvent. During a laser pulse, heat cannot be completely confined within the nanoparticle—some of it is diffuses into the solvent leading to a shell-like layer of the solvent around the nanoparticle with elevated temperature. The resulting temperature increase induces thermal expansion in both the nanoparticle and the solvent (**Figure 1.1**). The amount of heat transferred into the solvent depends on the length of the laser pulse, interfacial thermal resistance (kapitza resistance) at the nanoparticle-solvent interface, and the thermoelastic properties of the solvent itself.[95] Hence, tuning the solvent properties can enhance the PA signal.

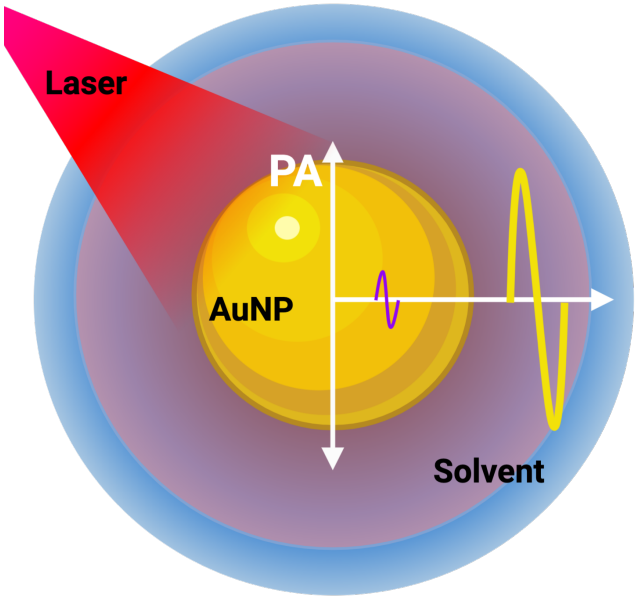

Figure 1. 1 Solvent generated PA signal.
During a laser pulse, heat is transferred into the solvent, which undergoes thermoelastic expansion and produces up to 93% of the PA response (yellow curve) compared to the absorbing nanoparticle (purple curve). PA amplitude is directly proportional to the rate of heat flux from the nanoparticle to the solvent and depends on the laser pulse width, kapitza resistance (thermal resistance at the nanoparticle-solvent interface), and the thermoelastic properties of the solvent itself. The red region around the nanoparticle depicts the heated region of the solvent.

The PA varying response of silica-coated gold nanospheres in water, silicone oil, and toluene was reported in 2012 by Chen *et al.* [95] They showed that the PA signal is proportional to the temperature-dependent Grüneisen parameter (**Equation 1.2)** of the respective solvent. Ethanol has a much higher β and a much lower specific heat capacity (C_p) compared to water at room temperature.[96] Hence, the Grüneisen parameter (**Equation 1.2)** for ethanol is 11.7-fold greater than that of water at room temperature.[96] Shi *et al.* (2016) modelled and experimentally showed that changing the solvent from water to ethanol for gold nanospheres resulted in a 4.5-fold higher PA signal.[96] Furthermore, coating gold nanospheres with a shell having a higher thermo-acoustic conversion efficiency than water could enhance PA signal. The β for PDMS is 4.5-fold higher than that of water. By confining the heat distribution within the PDMS shell a 3.5-fold PA enhancement was observed by Shi *et al.* (2016) [96]

Emelianov and others have modelled shown that over 90% of the PA signal is generated within the solvent compared to the absorbing nanoparticle.[95-97] The optical energy absorbed by the nanoparticle diffuses into the solvent as heat because of the small size of nanoparticles (high surface area-to-volume ratio). The intensity of the PA signal is proportional to the outgoing heat flux.[95] Water is a unique solvent to study the PA response of a nanoparticle. The thermal expansion of water disappears at 3.98°C as water is densest at that temperature hence any PA signal generated from the heating solvent vanishes, but the PA generated from the nanoparticle can still be transmitted.[95]

Coatings such as silica,[98-100] reduced graphene oxide[41], and zinc tera(4-pyridyl)porphyrin[101] can change the kapitza resistance or thermal conductance at the nanoparticle-solvent interface leading to PA enhancement. In the thermoelastic expansion model of PA each nanoparticle has its own thermal profile; the particle itself and the heated solvent around it (**Figure 5**). When aggregated, the thermal profiles of individual nanoparticles can overlap and collectively add to increase the rate of heat flux into the solvent.[102] This was demonstrated by Bayer et. al in 2013. [103] PA signal from aggregated silica-coated gold nanoparticles was up to 7-fold higher compared to dispersed silica-coated gold nanoparticles. A 25 nm thick silica shell around gold nanorods measuring 65 x 12 nm in size ensured that there was no plasmonic coupling between aggregated nanoparticles. *In vitro* tests showed that PA signal linearly increased as a function of particle concentration.

Another distinctive example was demonstrated by Chen *et al.* in 2017; here, they synthesized temperature sensitive poly(N-isopropylacrylamide) (PNIPAM) nanoparticles loaded with gold nanorods or copper sulfide nanospheres.[104] PNIPAM shrinks above its lower critical solution temperature (LCST) at 32°C. The gold nanorods or copper sulfide nanospheres were

drawn closer together as the temperature increased above 32ºC—this increased the thermal flux from the cluster into the surrounding medium. Using this dynamic nanogel they were able to enhance PA signal from gold nanorods and copper sulfide nanospheres up to 22 and 30-fold respectively (OD = 3.33 for 1 cm optical path length). Even below the LCST, PNIPAM-AuNR showed a 3.5-fold PA enhancement versus pure AuNR solution, which was attributed to random thermal overlap of nanoparticles within the gel matrix. PNIPAM-CuS showed no change in optical absorption due to aggregation but showed a 5.5-fold PA enhancement above the LCST. This confirmed that enhancement was due to thermo-dynamic and not plasmonic coupling effects.

The PA signal generated from core-shell nanoparticles specifically gold-silica core-shell nanostructures has been studied and modelled extensively. There are conflicting reports that show both PA enhancement (up to 3-fold for AuNRs)[95, 98, 99, 105, 106] and a PA decrease[107] upon silica coating. The most comprehensive model in this field was recently reported by Shahbazi *et al.* in 2019.[97] This group modelled the heat transfer and PA signal generation from a core-shell gold nanosphere using a nanosecond pulsed laser illumination. They considered the interfacial thermal resistance at the core-shell and shell-solvent interface and the temporal waveform of the laser pulse and showed that both parameters had a dramatic impact on PA amplitude. They also showed that only 7% of the PA signal is generated within the nanoparticle and that the fluid-generating region is a spherical shell almost twice as thick as the radius of the nanoparticle.

Other groups have looked at the ideal core-shell sizes and reported various values. Chen *et al.* (2012) observed the highest PA response from 13 nm gold cores coated with 18 nm silica shells.[95] Kumar *et al.* (2018) reported 6-fold enhancement using 35 nm gold cores coated with 20 nm silica shells.[106] Both groups reported that increasing the shell thickness above a certain value results in loss of PA signal as the thermal energy is confined within the shell and does not diffuse

into the solvent. Using thin shells with short duration laser pulses result in the highest amplification.

On the contrary, Pang *et al.* (2019) reported that the kapitza resistance has negligible effect on PA signal generation and silica coating causes a reduction in PA amplitude.[107] For uncoated gold nanospheres under 5 ns pulsed illumination, the kapitza resistance had a negligible effect on PA amplitude. To see the effects of kapitza resistance they dropped the pulse duration to 0.1 ns. They assume that the kapitza resistance at the shell-water interface is within the same order of magnitude as the uncoated control. The thermal conductivity of gold (314 W/m.K) is much higher than silica (0.2 W/m.K). Others have shown that the rate of heat dissipation is approximately 1.6-fold faster for silica-coated gold nanoparticles compared to uncoated controls and hence the kapitza resistance should be different for the two as well.[108]

Engineering the thermal expansion coefficient of a nanoparticle has yet to be reported. Most (>90%) of the PA response is generated by the solvent around the nanoparticle, and thus choosing a solvent with a high β can significantly enhance the PA response; however, this is not always possible in biological applications. The kapitza resistance can be tuned to maximize the thermal energy transfer from the nanoparticle to its solvent. Thin silica coatings that reduce the kapitza resistance have shown promise in this direction.

1.7 Specific heat capacity (C_p)

The specific heat capacity is the amount of thermal energy required to raise the temperature of a substance per unit of mass. Photoacoustic calorimetry is often used to measure the thermal properties of materials.[109] To the best of our knowledge there is no reported example of engineering the specific heat capacity of a nanoparticle to tune PA response. Alloying metals can result in a new specific heat capacity compared to individual metals. Although there is no reported example

of engineering the specific heat capacity of a nanoparticle, there is an example of alloyed Au-Ag nanoparticles that lead to PA enhancement. Hatef *et al.* (2015) reported that PA signals from Au-Ag alloyed nanoparticles was up to 2.5 and 10-fold higher compared to only gold or silver nanoparticles respectively.[110] They attributed this enhancement to an increased absorption cross section and did not investigate the effects of alloying on the specific heat capacity of the particle. It would be interesting to study the effect of alloying and changing the specific heat capacity of nanoparticles to engineer a desired PA response.

1.8 Laser fluence (F)

Fluence is defined as the laser pulse energy (J) incident on the effective focal spot (cm^2). Laser pulse energy is a function of optical power and the pulse width (usually nanosecond scale). Although laser fluence is an externally controlled variable as described in **Equation 1.1**. Various groups have reported optimal laser configurations to obtain the maximum PA generation. The non-linear increase in PA intensity as a function of laser fluence is widely reported for gold nanoparticles. The non-linearity is usually attributed to changes in thermophysical parameters due to a localized increase in temperature at higher laser fluences.[111] Increasing the pulse width also increases the laser fluence causing the PA signal to increase as long as thermal confinement is met. PA intensity usually plateaus at longer pulse widths.[96]

More recently groups have reported femtosecond pulsed irradiation for PA imaging. Although laser fluence under fs pulses is lower, groups have found ingenious ways to enhance PA and thermal stability.[112] Femtosecond pulses can allow for two-photon photoacoustics using longer wavelengths and increasing depth penetration.[113] Masim *et al.* (2017) reported PA enhancement from gold nanoparticles using a pair of time-delayed femtosecond pulses (pulse width = 40 fs and E_p = 0.1 mJ).[114] They studied photoacoustic intensity as a function of time delay between two

pulses from 0-15 ns and showed that PA increased from 0-15 ns. They also showed that enhancement was maximum when the first pulse was 20-30% of the total energy delivered. The first pulse primed the solution for bubble generation (cavitation) while the second pulse was used to acquire the PA response (2-fold higher). Laser pulses with sharper temporal waveforms produce PA signals that are more sensitive to environmental changes (such as thermal resistance) and thus increase the probability of signal amplification.[97] Contrast agents that excite at the same wavelength but emit PA signal at various ultrasound frequencies could also help in multiplexing and sensing applications.

The laser fluence is a key parameter to obtain relevant PA signal. It is important to keep the laser fluence under the maximum permissible exposure limit (typically under 20 mJ/cm^2). The use of femtosecond pulses can generate stronger PA signal via other mechanisms such as cavitation. Although increasing laser fluence can lead to PA enhancement, high fluence illumination can also lead to nanoparticle degradation especially in non-spherical structures.[100]

1.9 Future outlooks

The thermal expansion model of nanoparticle-based photoacoustic signal generation still remains the primary mode to create contrast in biomedical applications. The absorption coefficient (μ_a) is the easiest knob to tune to enhance PA contrast. Increasing the absorbance and reducing scattering using plasmonically coupled heterostructures or by incorporating NIR absorbing dyes can help design more efficient PA contrast agents. Shape control can engineer the local electromagnetic field enhancement around a nanoparticle, but the field lacks a more comprehensive comparison between different shapes. Nanoparticles that absorb in the second optical window (1000-1700 nm) can help image deeper and reduce scattering.[90] Challenges like the absorption of water (1450 nm) still need to be overcome, but there are significant advances in

this area already.[115] Engineering dispersion and shapes of chiral nanoparticles can lead to remarkable sensitivity in the optical properties (refractive index) of the nanoparticle. Polarization-dependent excitation could offer strong contrast even in highly absorbing media and biological tissues. [116-118] Nanoprobes that change their optical properties in different suspension environments can be excellent sensing platforms. Recently, CuS nanoplates that responded to refractive index changes (160−600 nm RIU^{-1}) in their suspension media with changes in particle diameter and operation wavelength (1100-1250 nm) were reported.[119]

Tuning the thermal expansion coefficient (β) of a nanoparticle is challenging. While phase changing hybrid plasmonic nanoparticles could be promising,[120] there is no such report for PA applications. Most of the PA signal is generated within the solvent and tuning the rate of heat flux into the solvent is a key parameter to optimize the PA response. Silica-coated gold nanoparticles are the most studied nanosystem in the field, and it may be useful to study other plasmonic-semiconducting nanosystems.

The specific heat capacity (C_p) of a nanoparticle is difficult to engineer but alloyed nanoparticles with tunable thermophysical properties can further enhance the PA contrast. The laser fluence (**F**) is a key parameter for good contrast. Anisotropic nanoparticles tend to be unstable under high fluence illumination because they deform into a more thermodynamically favorable shape. Using femtosecond pulses that enhances contrast via other methods of PA generation is encouraging.

Other ways to enhance PA such as cavitation are promising.[121] Nanoparticle-coated microbubbles have shown up to a 10-fold increase in PA amplitude due to cavitation even at low laser fluences.[15]

Deep-learning tools are usually used to increase PA contrast during image processing.[122] Tools that can model and predict the photoacoustic behavior of various old and novel nanoparticles may benefit the field in the future.

Gold is the most commonly used contrast agent due to its highly tunable optical properties, high photoacoustic conversion efficiency, and relative biological inertness. Of course, other materials can also generate PA signal: polypyrrole coated iron-platinum [123] and platinum-chelated bilirubin have also been reported [124] with excellent biocompatibility and a strong PA response under 808 nm illumination. Homan *et al*. (2011) and others have shown that functionalized silver nanoparticles can be used as a PA sensing platform for a host of biomedical imaging applications. [125, 126] Ku *et al.* (2012) reported copper sulfide nanoparticles operating in the NIR-II window (1064 nm) as a PA contrast agent. Operating in the NIR-II window, they were able to image ~ 5 cm deep in chicken breast.[127] Although PA contrast agents other than gold have been reported an empirical study to compare different nanoplatforms is still missing.

It is important to note that the thermoelastic expansion model of PA generation in **Equation 1.1** holds true for all absorbing molecules such as melanin, hemoglobin, small molecules and not just for plasmonic nanoparticles.[1] A substantial amount of work has been done with non-plasmonic PA contrast agents [128-130], but more work is required with other plasmonic nanoplatforms.

1.10 Plasmonic stability

Although gold nanorods are widely used as photoacoustic contrast agents, they are plagued with low photothermal stability. The rod structure is thermodynamically unfavorable leading to nanoparticle reshaping under high fluence illumination. Reducing illumination fluence by using light emitting diodes (LEDs) instead of lasers can offer a cheap and easy solution. LEDs operate

well below the MPE which is the currently holding back the clinical translation of Laser-based PA systems. But **Equation 1.1** clearly shows that reducing F will also reduce p_o. This may be acceptable if μ_a, β or C_p are tuned to make a highly efficient contrast agent. Furthermore, two-photon excitation using less energetic and longer wavelengths can improve photostability and depth penetration. Some work on organic polymer-plasmonic and dye-plasmonic hybrid nanostructures has been reported in this space. [44, 131, 132]

In the advent that low-fluence illumination is not feasible nanoprobes can also be shielded using coatings to improve their photothermal stability. For gold nanorods, coatings like silica,[100] reduced graphene oxide[41] and polydopamine[36] have increased photothermal stability. Increasing the surface area to volume ratio of nanoparticles allows faster dissipation of heat into the solvent which increases PA amplitude and photothermal stability. Miniaturized gold nanorods (48 x 8 nm) show 3-fold higher photothermal stability compared to larger rods with the same aspect ratio (120 x 18 nm).[90] Other materials and morphologies such as palladium nanosheets have also shown enhanced stability but the tests in this study were carried out at a relatively low fluence of 4 mJ/cm^2.[133] Improving photothermal stability will always be highly sought after as it allows contrast agents to be imaged for longer time periods. Higher stability can also increase sensitivity and allow longer illumination times which can improve the efficacy for PTT applications.

1.11 Safety and clinical translation

Reducing the cytotoxicity of contrast agents is paramount for successful clinical translation. Gold is a commonly used contrast agent for PA because of its relative biological inertness. However, the both the surface chemistry and the underlying substrate are important. Indeed, gold nanorods are plagued with cytotoxicity issues because of the cetyltrimethylammonium bromide (CTAB) surfactant used during gold nanorod synthesis. CTAB

forms a bilayer around the gold nanorod giving it a high positive charge keeping it colloidally stable. CTAB can cause defects in the cell membrane leading to cell death.[134, 135] High doses of CTAB are often used as a positive control for cell death in cytotoxicity assays.[13] A substantial body of work has been done to reduce the cytotoxic effects of gold nanoparticles through surface modifications using polyethylene glycol,[136] phosphatidylcholine,[137] bovine serum albumin,[138] polyacrylic acid and poly(allylamine) hydrochloride.[135] A comparative study on shape dependent cytotoxic effects of gold nanoparticles (spheres, rods and stars) revealed that cytotoxicity was highest in rods followed by stars and nanospheres respectively.[139] Gold nanoparticles were also found to be more biocompatible (72%) than silver nanoparticles (58%) at 100 μM using HepG2 cells.

The cytotoxicity of plasmonic contrast agents is the biggest hurdle for their clinical translation. Although designing multifunction probes is beneficial for complex sensing and therapeutic applications, it is often accompanied with complex synthesis processes and cytotoxic nanoparticles. Designing simpler yet safer nanoparticles would aid in the quick translation of PA contrast agents into clinics. While others like Halas and West have used plasmonics for photothermal therapy,[140] we are unaware of research groups using plasmonics and PA in humans but the use of endogenous contrast agents such as melanin[141] and hemoglobin[142] have been reported. Unlike plasmonics, the endogenous nature of these contrast agents means that they cannot be tuned to maximize their PA response. The ability to carefully engineer plasmonic probes to specifically optimize the PA response for various biomedical applications makes them highly desirable.[143, 144]

1.12 Conclusion

Overall, plasmonic nanoparticles can be engineered for photoacoustic imaging by tuning one of the many "knobs" presented in **Equation 1.1**. The acquired PA signal is a complex response from the nanoparticle, its shell, and the solvent around it. Although other methods of PA enhancement like cavitation are not properly understood they are still promising. The field will continue to strive towards increasing the biocompatibility and photothermal stability of plasmonic nanostructures. This will facilitate more sensitive contrast agents for clinical translation. Multimodal and multifunctional nanoprobes are an important future research focus for photoacoustics.

1.13 Acknowledgements

Chapter 1, in full, is a reprint of the material as it appears in Engineering plasmonic nanoparticles for enhanced photoacoustic imaging. Mantri, Yash; Jokerst, Jesse V., ACS Nano, 2020.The dissertation author was the primary investigator and author of this paper.

Chapter 2: Iodide-doped precious metal nanoparticles: Measuring oxidative stress *in vivo* via photoacoustic imaging

2.1 Abstract

Accumulation of reactive oxygen and nitrogen species (RONS) can induce cell damage and even cell death. RONS are short-lived species, which makes direct, precise, and real-time measurement difficult. Biologically relevant RONS levels are in the nM-μM scale; hence, there is a need for highly sensitive RONS probes. We previously used hybrid gold-core silver-shell nanoparticles with mM sensitivity to H_2O_2. These particles reported the presence of RONS via spectral shifts which could easily be quantified via photoacoustic imaging. Here, we used halide doping to tune the electrochemical properties of these materials to better match the oxidation potential of RONS. This work describes the synthesis, characterization, and application of these AgI-coated gold nanorods (AgI/AuNR). The I:Ag molar ratio, pH, and initial Ag shell thickness were optimized for good RONS detection limits. Halide doping lowers the reduction potential of Ag from E^0_{Ag} = 0.80 V to E^0_{AgI} = - 0.15 V resulting in a 1000-fold increase in H_2O_2 and 100,000-fold increase in $ONOO^-$ sensitivity. The AgI/AuNR system also etches 45-times faster than undoped Ag/AuNR. The AgI/AuNR easily reported the endogenously produced RONS in established cells lines as well as murine models.

2.2 Introduction

Reactive oxygen and nitrogen species (RONS) are naturally produced byproducts of aerobic metabolism.[145, 146] Low levels of RONS play a regulatory role via autophagy and are also involved in cell signaling.[147, 148] Under oxidative stress conditions, RONS production increases dramatically leading to degradation of proteins, lipids, DNA, cell cycle arrest and even cell death.[148-150] Dysregulated RONS can lead to diseases such as cancer,[151-153] Alzheimer's disease,[154] and heart disease.[155] RONS are short-lived species, which makes direct, precise, and real-time measurements difficult. Quantitative analysis of these redox radicals is generally difficult due to high concentrations of glutathione, varying concentrations of metals, and other redox-sensitive agents, which can catalyze or inhibit radical reactions.[156, 157] Physiologically, RONS are found as a milieu of oxidative species which include radicals such as hydrogen peroxide, peroxynitrate, superoxide, hydroxyl, hypochlorite, nitroxyl, singlet oxygen, nitric oxide and many more.[158, 159] A mixture of these species causes more damage in comparison to one oxidant at high concentration.[158]

There are several existing approaches to measuring RONS. Fluorescent molecules such as 2',7' – dichlorofluorescin diacetate (DCFDA) offer *in vitro* assessments.[157, 160-162] Fluorescent probes provide high sensitivity and real time imaging but have limited utility *in vivo*. Electrochemical biosensors made from single walled carbon nanotubes have also shown nanomolar sensitivity to H_2O_2 in macrophage cells:[163] These are useful tools to study metabolic pathways in single cells but are difficult to implement in tissue systems. *In vivo* imaging of H_2O_2 in real time using a chemoselective bioluminescent reporter (peroxy-caged luciferin-1) has also been reported.[164] Unfortunately, this technique requires genetically modified cells that produce

luciferase and therefore not viable for clinical applications. Furthermore, these purely optical methods are limited by poor penetration through tissue.

In contrast to optical methods, photoacoustic (PA) imaging is an excellent non-invasive tool that combines the depth penetration and high resolution of ultrasound with the high contrast and spectral capabilities of optical imaging.[1, 165, 166] Photoacoustic signal is generated when an absorbing particle undergoes thermoelastic expansion under pulsed illumination. Expansion results in the formation of acoustic pressure waves that is detectable by ultrasound. Nanoparticles are often used as activatable, exogenous contrast agents in PA due to highly tunable shape, size and functionalization.[167-171] PA has been used to image RONS species previously using semiconductor polymer nanoparticles,[172, 173] but RONS imaging has not yet leveraged the incredibly high molar extinction coefficients of plasmonic particles[24, 174] for ultralow detection limits. Indeed, gold nanorods (AuNR) are often employed as PA contrast agents because of their high photothermal conversion efficiency and relative chemical inertness.[12, 71, 175] Tuning the aspect ratio of AuNR allows one to engineer particles that have a maximum absorbance within the biological optical window,[176-179] and AuNRs have been used with PA to sense chemical species, track cells, image tumors, and as theranostic tools.[71, 98, 180, 181]

Many PA probes take an "always on" approach via enhanced accumulation, permeability, and retention effect to generate PA contrast in images. Other probes respond to biochemical cues via an activatable signal for both *in vitro* and *in vivo* applications.[9, 170, 182-191] Previously, we and others have reported silver/gold theranostic nanoparticles for RONS sensing and antibacterial treatment.[71, 192] This was silver shell/gold core nanorods (Ag/AuNR) that selectively etched silver ions in the presence of RONS (H_2O_2 and $ONOO^-$) with reporting via PA imaging via spectral shifts. The bare AuNR have a near infrared (NIR) resonance that is blue shifted after the shell is

added. When the shell is oxidized by the RONS, the NIR resonance is restored, and the resulting PA signal directly reports the quantity of RONS (**Figure 1A**). Thus, this PA signal reports the amount of Ag^+ released and the quantity of RONS. However, this system required mM concentrations of RONS to etch the silver coating and activate the system—this was a fundamental limitation of this work because biologically relevant concentrations are on the nM to μM scale.[8, 193-196]

In this work, we used electrochemical principles and nanoengineering to make the nanoparticle sensitive to lower RONS concentrations. More specifically, we doped the silver shell with iodide because this doping would reduce the standard reduction potential of the silver to match the oxidation potential of the RONS species more closely. After careful characterization of the product, we validated this system in both *in vitro* and *in vivo* models of human disease. The iodide-doped system offers detection limits that are three to five log orders lower than un-doped systems and underscores the utility of this material for imaging RONS.

2.3 Rationale for iodide doping and synthetic control

One possible way to increase sensitivity to RONS is to reduce the reduction potential of the Ag shell (E^0_{Ag} = 0.80 V) to better complement the reduction potentials of the RONS. Doping Ag with halides would lower the reduction potential (E^0_{AgF} = 0.78 V, E^0_{AgCl} = 0.22 V, E^0_{AgBr} = 0.07 V, and E^0_{AgI} = - 0.15 V). However, it is necessary to stabilize the shell because silver and silver halides are photosensitive making them unfavorable candidates for PA imaging.[197] Fortunately, the gold core offers abundant electrons to stabilize the Ag shell for halide doping.[198-200] We selected AgI because it is the least photosensitive and has the lowest standard reduction potential of the four halides. It resists reduction by metals but is etched under acidic conditions.[201] Doping halides into bulk Ag is diffusion limited.[200, 202-204] The X^- is chemically adsorbed on the surface

forming a porous film through which more X^- can diffuse through the bulk metal. Iodide is more aggressive in doping into Ag due to its higher polarizability, increased stability, lower reduction potential, and low activation energy versus other halides.[203] I^- also forms a more porous film than Cl^- and Br^- leading to higher dopant concentrations.[203-206]

2.4 Materials and methods

2.4.1 Materials

Hexadecyltrimethylammonium bromide (CTAB, Cat. #1102974), gold (III) chloride trihydrate (Cat. #520918), L-ascorbic acid (Cat. #A7506), silver nitrate (Cat. #209139), sodium borohydride (Cat. #2133462), potassium iodide (Cat. #746428), sodium hydroxide (Cat. #S5881), hydrochloric acid (Cat. #339253), hydrogen peroxide (Cat. #216763), potassium superoxide (Cat. #278904), sodium hypochlorite (Cat. #239305), tert-butyl hydroperoxide (Cat. #416665), tert-butyl peroxide (Cat. #168521), sodium nitrite (Cat. #237213), Angeli's salt (Cat. #176695), iron (II) perchlorate hydrate (Cat. #33408), 2',7'-dichlorofluorescin diacetate (DCFDA Cat. #D6883), N-acetylcysteine (NAC) from Escherichia coli (Cat. #A9165), and zymosan A from Saccharomyces cerevisiae (Cat. #Z4250) were purchased from Sigma-Aldrich (Atlanta, GA, USA). Peroxynitrite was purchased from EMD Millipore Co. (Cat. #516620, MA, USA). McCoy's 5A medium with L-glutamine, sodium bicarbonate; without phenol red was purchased from GE Healthcare Bio-Sciences Corp. (Cat. #SH30270.01, MA, USA). Vybrant MTT cell proliferation assay kit was purchased from Life Technologies Corp. (Cat. #V13154, NY, USA). All reagents were used without further purification. Aqueous solutions were made by diluting in distilled water unless otherwise mentioned.

2.4.2 Gold nanorod (AuNR) synthesis

AuNRs were synthesized using the seed-mediated growth method used in a previous report with some modifications.[71] Gold seeds were prepared by adding 5 ml of CTAB (0.2 M) to 2.5 ml of $HAuCl_4.3H_2O$ (0.001 M) and further reduced with 0.6 ml of ice-cold $NaBH_4$ (0.01 M) under vigorous stirring for 2 min. The growth solution was prepared by adding 500 ml of $HAuCl_4 \bullet 3H_2O$ (0.001 M) to 500 ml of CTAB (0.2 M). To this, 36 ml of $AgNO_3$ (0.004 M) and 7 ml of L-ascorbic acid (0.089 M) was added. Next, 1.2 ml of freshly prepared gold seed solution was added, and the reaction mixture was left undisturbed for 30 – 60 mins until the solution turned purple/dark brown. After 12 hrs of additional reaction the mixture was washed three times via centrifugation at 12500 rpm for 15 min with distilled water to remove excess CTAB and unreacted gold. Synthesized AuNR were suspended in distilled water and stored at 4 ^{o}C.

2.4.3 Preparation of the silver-coated AuNR (Ag/AuNR) and iodide-doped AuNR (AgI/AuNRs)

Ag-coated AuNRs were synthesized using previous reports with a few modifications.[71, 207] Ag/AuNRs with increasing Ag-shell thickness were made by increasing the Ag:Au molar ratio: 80 µL of AuNR stock (AuNR concentration 10.95 nM) was suspended in a mixture containing 1.5 ml distilled water and 1 ml CTAB (0.1 M). Next, various amounts of $AgNO_3$ (0.01 M) 25, 45, 65, 85, 110, 145, and 175µL were added to separate vials and stirred at 600 rpm. Then, 110 µL of L-ascorbic acid (0.1 M) and 300 µL of NaOH (0.1 M) was added under vigorous stirring for 30 min. The synthesized Ag/AuNR shell/core particles were washed twice via centrifugation at 12500 rpm for 15 min to remove excess Ag and CTAB. Iodide doping of Ag to form AgI can be done under acidic conditions as proposed by Mulvaney and later demonstrated by Vasan.[204, 208] We studied the effect of Ag:I molar ratio, pH, and initial Ag shell thickness on iodide doping. Finally,

Ag/AuNR with a Ag:Au molar ratio of 3.32 were doped with iodide by first adjusting pH to 5 using HCl (0.1 M) and adding KI in a 1:1 molar ratio of Ag:I. The reaction was stirred at 600 rpm for 2 hours to ensure complete doping. The doped particles were washed twice with centrifugation at 12500 rpm for 15 min to remove unreacted iodide. The particles were stored at 4°C wrapped in aluminum foil to prevent any photoetching.

2.4.4 Transmission electron microscopy (TEM)

TEM samples were examined using a JEOL JEM-1400Plus transmission electron microscope operating at 80 kV. Images were recorded using a Gatan OneView 4K digital camera and processed using ImageJ 1.51s. Samples were prepared by drop casting 20 µL of nanoparticle suspension onto 300 mesh carbon-coated copper grids.

2.4.5 Absorption spectra

All absorption spectra were measured using a Molecular Devices Spectramax M5 microplate reader using 150 µL of solution in 96-well plates. Unless otherwise mentioned, absorbance was read from 350 – 900 nm with a step size of 10 nm and plotted using GraphPad Prism Software.

2.4.6 Energy dispersive X-Ray spectroscopy (EDX)

EDX samples were analyzed using FEI Apreo FESEM, operating at 20 kV with a spot size of 5 and emission current -90 µA; 20 µL of sample were drop-cast onto 300-mesh carbon-coated copper grids.

2.4.7 Powder X-Ray diffraction (pXRD)

Samples were characterized by pXRD with the Bruker D8 Advance used in Bragg-Brentanno geometry. Cu radiation: 1.54 Angstroms, equipped with a Ni K-beta filter. The 2θ scan

range was 10-80° in increments of 0.02 and exposure of 0.25 seconds per scan. Samples were prepared by spinning down 1000 µL of nanoparticle suspension and resuspending them in 20 µL of water via sonication.

2.4.8 Dynamic light scattering (DLS) and zeta potential

Hydrodynamic diameter and zeta potential were measured using a Malvern Instruments Zetasizer ZS 90; 200 µL of nanoparticle suspension was diluted in 800 mL of distilled water.

2.4.9 Inductively coupled plasma - mass spectrometry (ICP-MS)

The ICP-MS analysis was done on a Thermo Scientific iCAP RQ ICP-MS in the Environmental and Complex Analysis Laboratory at UC San Diego. Samples were washed twice to remove unreacted reagents and then digested overnight in *aqua regia* before analysis.

2.4.10 RONS selectivity and sensitivity studies

To compare the dose dependent response of the particles, 200 µL of AuNR, Ag/AuNR and AgI/AuNR were treated with 10^{-3}, 5^{-3}, 10^{-2}, 5^{-2}, 10^{-1}, 5^{-1}, 1, 5, 10, and 50 mM of H_2O_2 for 18 hours at room temperature. Separately, particles were also treated with 10^{-6}, 10^{-5}, 10^{-4}, 10^{-3}, 10^{-2}, 10^{-1}, 1, and 10 mM of $ONOO^-$ for 18 hours at room temperature. Absorption spectra after treatment with H_2O_2 and $ONOO^-$ was taken and plotted ratiometrically as Absorbance at 780 nm:Absorbance at 578 nm. The rationale behind the choice of wavelength; 780 nm is the peak absorbance of the etched-AgI/AuNR treated with 50 mM H_2O_2 and 578 nm is the peak absorbance of unetched AgI/AuNR.

To test RONS selectivity, nanoparticles were treated with 1 mM of hydrogen peroxide (H_2O_2), peroxynitrite ($ONOO^-$), nitroxyl (HNO), nitrite (NO_2^-), tert-butoxy radical ($C_4H_9O^\bullet$), tert-butyl hydrogen peroxide (tBuOOH), hypochlorite (OCl^-), superoxide (O_2^-), and hydroxyl radical

(•OH). Hydroxyl radicals were generated via the Fenton Reaction between H_2O_2 and iron (II) perchlorate hydrate ($Fe(ClO_4)_2 \bullet xH_2O$).[8]

2.4.11 Etching kinetics

The kinetics of Ag and AgI etching were studied using change in absorbance at 680 nm when treated with 0.5 and 50 mM H_2O_2 over 18 hours at room temperature with a step size of 10 min.

2.4.12 Cell culture

To test whether endogenously produced RONS can oxidize the Ag and AgI shell, we treated AuNR, Ag/AuNR, and AgI/AuNR with cell media from ovarian cancer cell cultures (SKOV3). The 2'-7' dichlorofluorescin diacetate (DCFDA) assay was used to confirm that SKOV3 cells naturally produce RONS. Briefly, cells were cultured using phenol free McCoy's 5A medium; 10,000 cells were plated onto 12-well tissue culture plates and incubated till 80% confluent. Cells were incubated with DCFDA (20 μM in PBS) for 45 minutes in the dark and imaged using a Life Technologies EVOS FL microscope with FITC filter sets at 10X magnification. As a negative control, cells were treated with N-acetyl cysteine (NAC; final concentration 10 mM in PBS) for 1 hour to scavenge RONS. Finally, 200 μL of nanoparticle suspension was treated with 200 μL of SKOV3 cell media and incubated for 30 min. Photoacoustic response was studied at 680 nm. Nanoparticle cytotoxicity was assessed using the MTT cell proliferation assay kit.

2.4.13 Photoacoustic imaging

All photoacoustic images were acquired using the Visualsonics Vevo 2100 LAZR imaging system at 680 nm. All photoacoustic spectra were acquired from 680 – 970 nm with a step size of

5 nm. All *in vitro* samples were imaged using the LZ250 transducer (21 MHz center frequency) and all *in vivo* studies were imaged using the LZ550 transducer (40 MHz center frequency).

2.4.14 *In Vivo* RONS sensing

All animal experiments were performed in accordance with NIH guidelines approved by the Institutional Animal Care and Use Committee (IACUC) under protocol S15050 at the University of California, San Diego. Zymosan was used to stimulate endogenous production of RONS in a murine model. [8, 173, 209] 100 µL of zymosan (20 mg/ml in PBS) was injected intramuscularly into the femoris muscle of the upper hind limb and incubated for 20 min (*n = 3*). After incubation 100 µL of AuNR, Ag/AuNR and AgI/AuNR (0.3 nM particle concentration) was injected and their photoacoustic response was monitored at 0, 5, 10, 15, 20, 30, 45, 60 and 90 minutes. We used zymosan only and PBS injections as negative controls. All images were processed using the Vevo LAB 3.1.0 software. We studied the increase in photoacoustic response as a ratio of photoacoustic intensity at t = x minutes : photoacoustic intensity at t = 0 min.

2.5 Results and discussion

2.5.1 Synthesis of Ag/AuNR.

Figure 2.1B-E shows TEM images and **Figure 2.1G** shows the absorption spectra of AuNRs and Ag/AuNRs with varying shell thickness. The AuNR had an aspect ratio of 3.1 ± 0.44 (n > 150 particles) with a peak absorbance at 735 nm. The color of the colloidal suspension changed from brown to green to purple to red and finally orange with increasing shell thickness (**Figure 2.1F**). The Ag:Au molar ratio increased linearly ($R^2 = 0.93$) with increasing amounts of added Ag (**Figure 2.6**). Increasing shell thickness results in a blue shift of the absorption spectrum due to reduction of the aspect ratio from 3.1 to 1.25 for 15 nm shells (Ag:Au = 3.71; **Figure 2.1G**).

Increasing the amount of Ag results the emergence of a new 400 nm peak which can be attributed to the unsymmetrical growth of the silver shell.[71, 207, 210] This was further confirmed with dynamic light scattering (DLS) (**Figure 2.7**). DLS studies then hydrodynamic diameter of a particle, which is assumed to be spherical. This is a major limitation of this technique to characterize rod like structures. Here, two peaks are seen for all samples. The smaller peak (5-7 nm) is attributed to the rotational diffusion coefficient of non-spherical AuNRs.[211] After silver coating and subsequent iodide doping, the hydrodynamic diameter increases by 2.5 nm along with the rotational diffusion coefficient as particles increase in size. [207, 210]

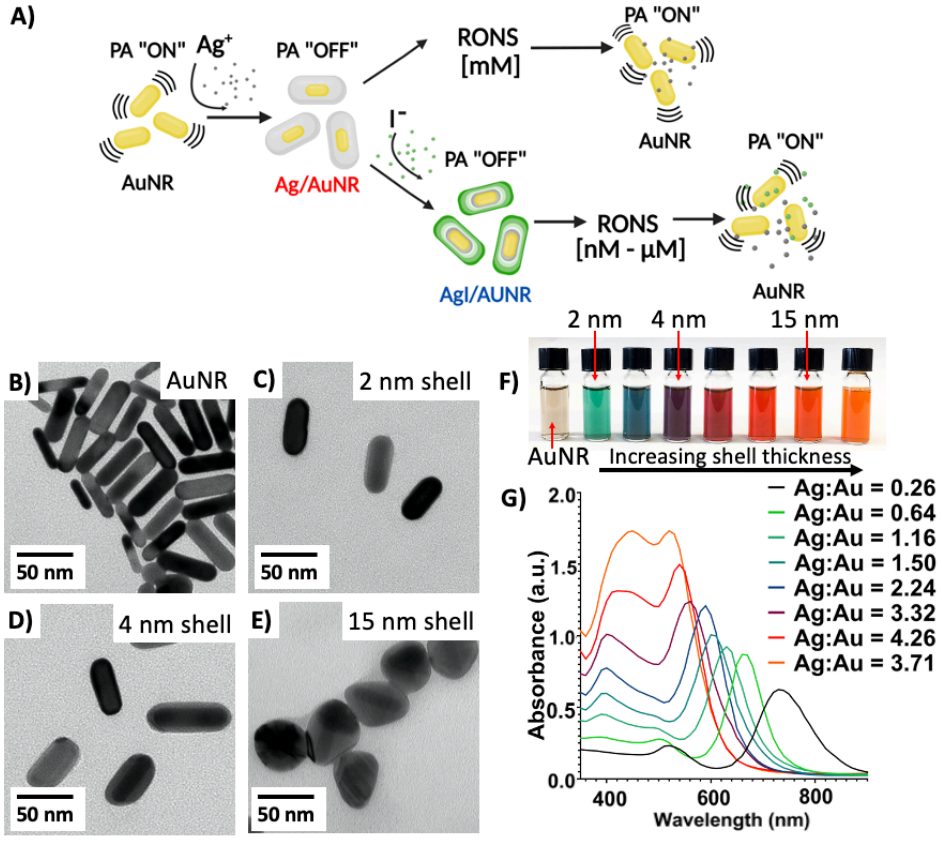

Figure 2. 1 Schematic of shell optimization.
Schematic representation of the current work. Iodide doping results in biologically relevant [nM - µM] sensitivity to RONS (**A**). TEM images of synthesized AuNR (**B**), Ag-coated AuNR with shell thickness 2 nm (**C**), 4 nm (**D**), 15 nm (**E**). Photograph of AuNR and Ag/AuNR with increasing shell thickness (**F**). The color changes from brown-green-purple-red-orange. Absorption spectra of AuNR and Ag/AuNR with increasing shell thickness (**G**). Increasing shell thickness results in a blue shift of the longitudinal plasmon peak as the aspect ratio reduces. Inset, final molar ratio of immobilized Ag:Au after coating through ICP-MS.

There are three synthetic "knobs" to optimize the doping of the Ag shell: molar ratio of I:Ag, pH, and the initial Ag shell thickness (see **Figure 2.8**). The molar ratio of I:Ag had relatively minor effects. Excess iodide results in the leaching of Ag from the gold surface and the formation of Ag nanoparticles—this further increases the absorbance at 390 nm (**Figure 2.8A**). The peak broadening and baseline increase in absorbance at high I:Ag ratio suggests particle destabilization and aggregation. A 1:1 molar ratio of I:Ag showed no peak shift but produced the predicted dampening in absorbance indicating successful doping.[200, 212]

The pH is the most important variable in determining doping because iodide is best doped into Ag under acidic conditions.[204, 208] However, in excessively acidic media, Ag can be oxidized and etched off the gold core (**Figure 2.8B**). The red-shift, lower absorbance, and peak broadening seen at pH 2, 3, and 4 suggest Ag shell etching and Au core degradation. In more basic conditions, the forward reaction is unfavorable as shown in Equation 2.1. Hence, pH 5 was selected as the most favorable condition.

$$Ag_n + mH^+ + mI^- \rightarrow Ag_{n-m}(AgI)_m + (m/2)H_2 \qquad \textbf{(Equation 2.1)}$$

The initial Ag shell thickness could also affect the final product because a thinner shell is more susceptible to changes in pH (**Figure 2.8C**). Aqueous suspensions of Ag/AuNRs with varying shell thicknesses were adjusted to pH 5 and doped with a 1:1 ratio of I:Ag. The nanoparticles with thinner shells showed more peak broadening compared to their undoped controls. Iodide impurities in CTAB is known to disrupt AuNRs which reaffirms the importance of a thicker (> 4 nm) Ag protective shell.[213-215] Particles with a Ag:Au molar ratio of 3.32 or more

(through ICP-MS) showed no change in their spectra and were further characterized and used for all other tests.

2.5.2 Characterization of iodide doping

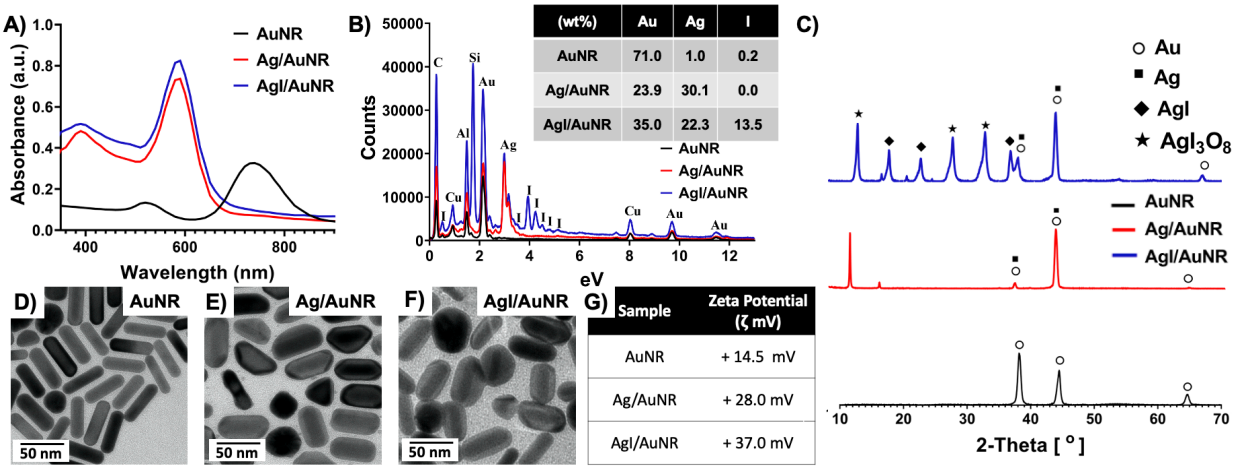

Figure 2. 2 Characterization of iodide-doped Au/Ag hybrid nanoparticles.
(**A**) Absorption spectra of bare AuNR, Ag/AuNR, and iodide-doped Ag/AuNR (all samples were from the same batch of synthesis and doping). There is no change in the absorption spectra of doped and undoped Ag/AuNRs. EDX spectra (**B**) and *p*XRD analysis (**C**) of iodide-doped Ag/AuNRs show characteristic I^-, AgI, and AgI_3O_8 peaks. TEM images of AuNR (**D**), Ag/AuNR (**E**), and AgI/AuNR (**F**) show retention of the core-shell structure after iodide doping. There was no significant change in shell thickness on iodide doping. Doping iodine displaces the counter NO_3^- from the particle surface resulting in an increase in positive zeta potential (**G**).

The electrons supplied by the gold core stabilizes and maintains the silver shell on the Au for successful I^- doping.[200] In this design, these electrons are from the Au core.[199] The initial I^- adsorption results in dampening of the 390 nm peak (**Figure 2.2A and Figure 2.8A**). The slight red shift of the transverse peak to 395 nm accompanied by peak broadening indicates the formation of bulk AgI.[204] However, there are many sources of spectral error, and thus we used complementary techniques to confirm these observations.

EDX spectroscopy was used to further characterize the particles (**Figure 2.2B**). Bare AuNR showed slight amounts of Ag because Ag is used to control the anisotropic growth of AuNRs during synthesis .[216, 217] I (0.2 wt%) was detected in bare AuNR possibly due to contamination in the CTAB used during synthesis.[215] However, the iodide contamination had no

effect on rod formation with rod yield greater than 90%. The Ag/AuNRs showed clear peaks of Au and Ag with a Ag:Au molar ratio of 2.3 that was further confirmed by ICP – MS (Ag:Au = 3.32) (**Figure 2.6**). Iodide-doped Ag/AuNRs showed characteristic peaks for iodide with a I:Ag molar ratio of 0.5 (starting concentration was 1:1). While EDX is obviously a surface weighted technique, this EDX data suggests that not all of the I^- formed AgI, which is expected because doping initially starts with surface adsorption and complex formation followed by diffusion-mediated doping.[206]

The *p*XRD analysis of all samples showed characteristic peaks for Au and Ag (JCPDS 04-0784 and 04-0783) (**Figure 2.2C**). The crystal structure for Au and Ag are very similar, and it is difficult to separate one from the other. The formation of AgI is obvious on the *p*XRD analysis for AgI/AuNR (**Figure 2.2C**). The presence of characteristic α-AgI_3O_8 peaks representing the 111, 004, and 114 crystallographic planes (JCPDS 66-0314) further suggest that the adsorbed AgI is complexed with oxygen. Furthermore, the 100, 101, and 110 peaks for β-AgI (JCPDS 09-0374) show that bulk AgI also exists in the sample. The presence of crystalline β-AgI could also be attributed to AgI nanoparticle formation due to Ag leaching from the gold surface. TEM images of AgI/AuNRs showed the preservation of the shell-core structure and no signs of Ag nanoparticle formation (**Figure 2.2E and F**). There was no significant change in coated particle size. This suggests that the doping must have occurred on and in the shell with bulk AgI in the shell and AgI_3O_8 at the surface.

We also studied the surface chemistry using zeta potential (**Figure 2.2G**). The zeta potential of Ag/AuNRs becomes more positive with iodide doping. This is because the KI removes the NO_3^- counter ion from the Ag surface as KNO_3.[204] Preoxidation of the surface Ag atom by a

nucleophile imparts a small positive charge at the surface and a corresponding negative charge within the particle.[204, 218] This high charge facilitates the high colloidal stability of AgI/AuNRs.

Finally, we studied the photostability of AgI/AuNRs over 5 minutes of 680 nm pulsed laser illumination (**Figure 2.9**). the PA intensity reduced only 17% over 5 minutes indicating that synthesized AgI/AuNR are stable under pulsed laser illumination.

2.5.3 *In vitro* RONS sensing

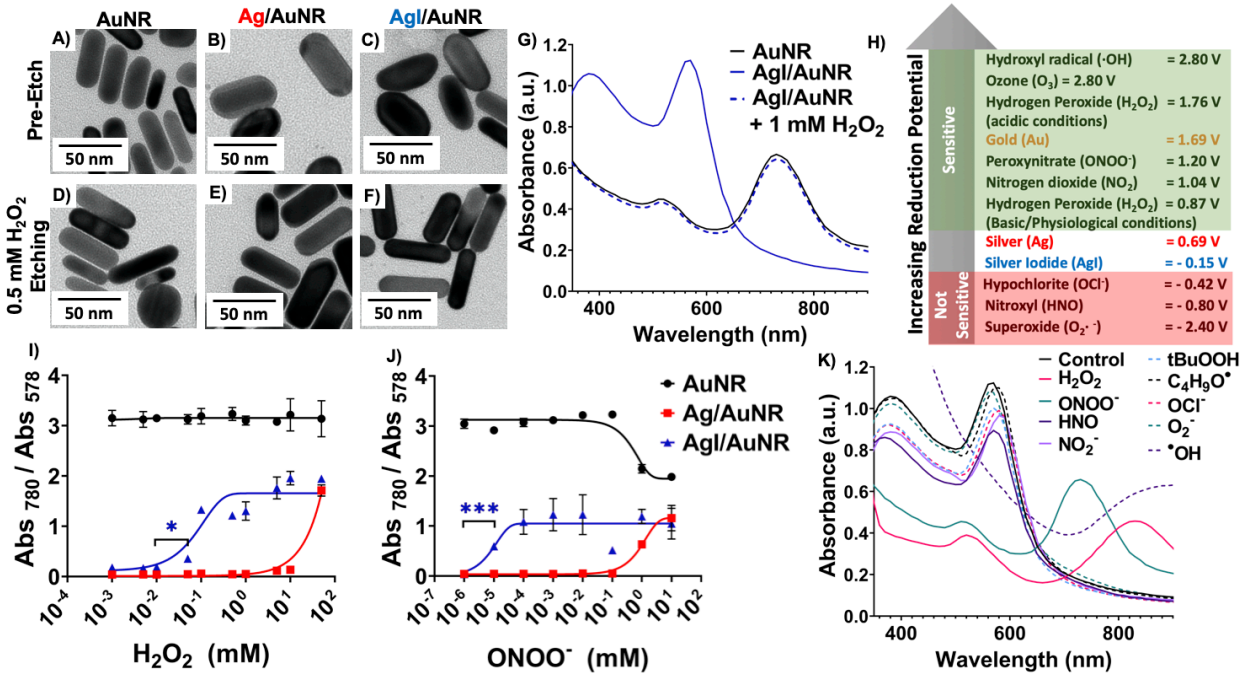

Figure 2. 3 RONS sensitivity and selectivity.
TEM Images of AuNR, Ag/AuNR, and AgI/AuNR pre-and-post etching with 0.5 mM H_2O_2 (**A-F**). AgI/AuNR shows complete etching of AgI shell (**C, F**), AuNR and Ag/AuNR remain unaffected by H_2O_2. Bare AuNR has peak absorbance at 735 nm which blue-shifts on AgI coating. Subsequent etching with 1 mM H_2O_2 recovers the AuNR absorption spectrum (**G**). A slight negative reduction potential of AgI makes it a better electron donor and get oxidized by redox species with reduction potential higher than E^0_{AgI} = - 0.15 V. Redox species with lower reduction potential cannot etch off the AgI shell (**H**). AgI/AuNR is 1000-fold more sensitive to H_2O_2 and 100,000-fold more sensitive to $ONOO^-$ compared to un-doped Ag/AuNR (**I-J**) (*n = 3*). RONS with positive reduction potential like H_2O_2 (E^0_{H2O2} = 0.87 V in alkaline/physiological conditions), $ONOO^-$ (E^0_{ONOO-} = 1.2 V), and $^{\bullet}OH$ ($E^0_{\bullet OH}$ = 2.8 V) cause AgI shell etching whereas O_2^- (E^0_{O2-} = - 2.4 V) had the least effect on the nanoparticles (**K**). Error bars represent the standard deviation of three replicate samples. *: p<0.05; **: p<0.01.

Figure 2.3 shows the iodide-doped particles' response to RONS. TEM images (**Figure 2.3A-F**) pre-and-post etching with 0.5 mM H_2O_2 showed that H_2O_2 had no effect on AuNR, slight

etching on Ag/AuNRs, and complete shell removal for AgI/AuNRs. The H_2O_2 treatment causes selective AgI shell etching and the recovery of core AuNR's original spectrum (**Figure 2.3G**). The detection limit for H_2O_2 and $ONOO^-$ with the iodide-doped particles are 50 μM and 100 nM respectively, which is 1000-fold and 100,000-fold more sensitive than undoped Ag/AuNR controls (**Figure 2.3 I-J**) ($p < 0.05$, n=3). Increased sensitivity to H_2O_2 (E^0_{H2O2} = 0.87 V in alkaline conditions) and $ONOO^-$ (E^0_{ONOO-} = 1.2 V) due to iodide-doping can be credited to the lower standard reduction potential of AgI (E^0_{AgI} = - 0.15 V) and (E^0_{AgIO3} = 0.35 V) compared to Ag (E^0_{Ag} = 0.80 V). The higher sensitivity to $ONOO^-$ is likely due to its higher reduction potential. The undoped Ag/AuNR are responsive to 50 mM H_2O_2 and 1 mM $ONOO^-$. It is also possible that AgI_3O_8/AgI layers in the iodide-doped samples become oxidized and then etch off more readily compared to the undoped controls. Our previous work showed that Ag/AuNR were responsive to 5 mM H_2O_2 and 0.25 mM $ONOO^-$, which is lower than this study. The difference in RONS response can be attributed to batch-to-batch variability of particles and to different shell thicknesses. Our previous work used thicker shelled particles.

We also tested the response of AgI/AuNR to 1 mM of other redox species (**Figure 2.3K**). Etching selectivity is a function of the reduction potential of the oxidative species (**Figure 2.3H**). Reduction potential is the tendency of a chemical species to gain or lose electrons. A more positive redox potential implies a greater tendency to gain electrons and become reduced. As a result, $^{\bullet}OH$ ($E^0_{\bullet OH}$ = 2.8 V) had the most effect, and O_2^- (E^0_{O2-} = - 2.4 V) had the least effect on the particles. The variation in etching is understandable as high positive reduction potential of $^{\bullet}OH$ makes it a good electron acceptor whereas a negative reduction potential for O_2^- makes it a great electron donor. The slight negative reduction potential of AgI makes it a good electron donor to $^{\bullet}OH$ and in turn get oxidized off the Au core. The high oxidizing power of $^{\bullet}OH$ etches off the AgI shell and

further degrades the Au core (E^0_{Au} = 1.69 V) as observed in the absorption spectrum (**Figure 2.3K**).

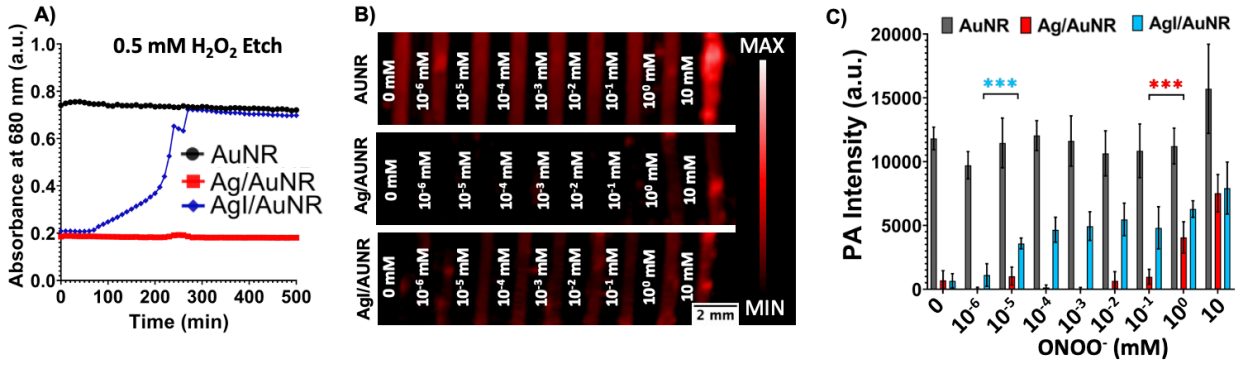

Figure 2. 4 Etching kinetics and photoacoustic response.
With 0.5 mM H_2O_2, AgI/AuNR takes ~5 hours to completely etch whereas AuNR and Ag/AuNR show no change in absorbance for over 9 hours. **(A)** Photoacoustic images at 680 nm of AuNR, Ag/AuNR and AgI/AuNR treated with varying concentration of $ONOO^-$ (**B**). Plot comparing photoacoustic intensity of nanoparticles after treatment with varying concentrations of $ONOO^-$ from B (**C**). The detection limit for AgI/AuNR was 10^{-5} mM and for Ag/AuNR was 1 mM ($p < 0.001$). Error bars represent the standard deviation of six regions-of-interest.

Kinetically, AgI/AuNR etches ~45 times faster than Ag/AuNR when treated with 50 mM H_2O_2 (**Figure 2.12B**). The detection limit of $ONOO^-$ and H_2O_2 with photoacoustic imaging followed the same trend as the absorbance (**Figure 2.4 B-C and Figure 2.11**). A significant increase ($p < 0.001$) in photoacoustic signal is observed versus baseline with 10^{-5} mM of $ONOO^-$ and 10^{-2} mM of H_2O_2. AuNR treated with 10 mM H_2O_2 showed an uncharacteristic PA enhancement. H_2O_2 is known to decompose under high fluence illumination into water and oxygen. At high enough concentrations of 10 mM there could be oxygen nanobubble formation and PA enhancement due to cavitation. In addition, plasmonic materials are known to aggregate at higher ionic strength.

While these initial experiments tested individual RONS species, the *in vivo* situation is a complex milieu of RONS. Thus, we used SKOV3 cells to model this milieu because they are known to produce high levels of free radicals.[71, 219-221] The DCFDA assay (**Figure 2.13**) confirmed that SKOV3 cells endogenously produce RONS, and that these RONS are scavenged with NAC.

The nanoparticles were treated with cell-free media, SKOV3 media, and SKOV3 media treated with NAC (**Figure 2.14**). Photoacoustic signal from both Ag/AuNR and AgI/AuNR turned "ON" when treated with RONS-enriched media.

The MTT assay for cell cytotoxicity (**Figure 2.15**) showed that nanoparticles at 0.01- 0.1 nM had no toxicity versus the PBS negative control. At high concentrations of 1 nM, particles exhibited higher toxicity which can be attributed to the higher amounts of residual CTAB in those samples. Hence, all *in vivo* experiments were carried out at 0.3 nM particle concentrations to keep toxicity as low as possible and generate sufficient signal from the nanoparticles.

2.5.4 *In vivo* RONS sensing

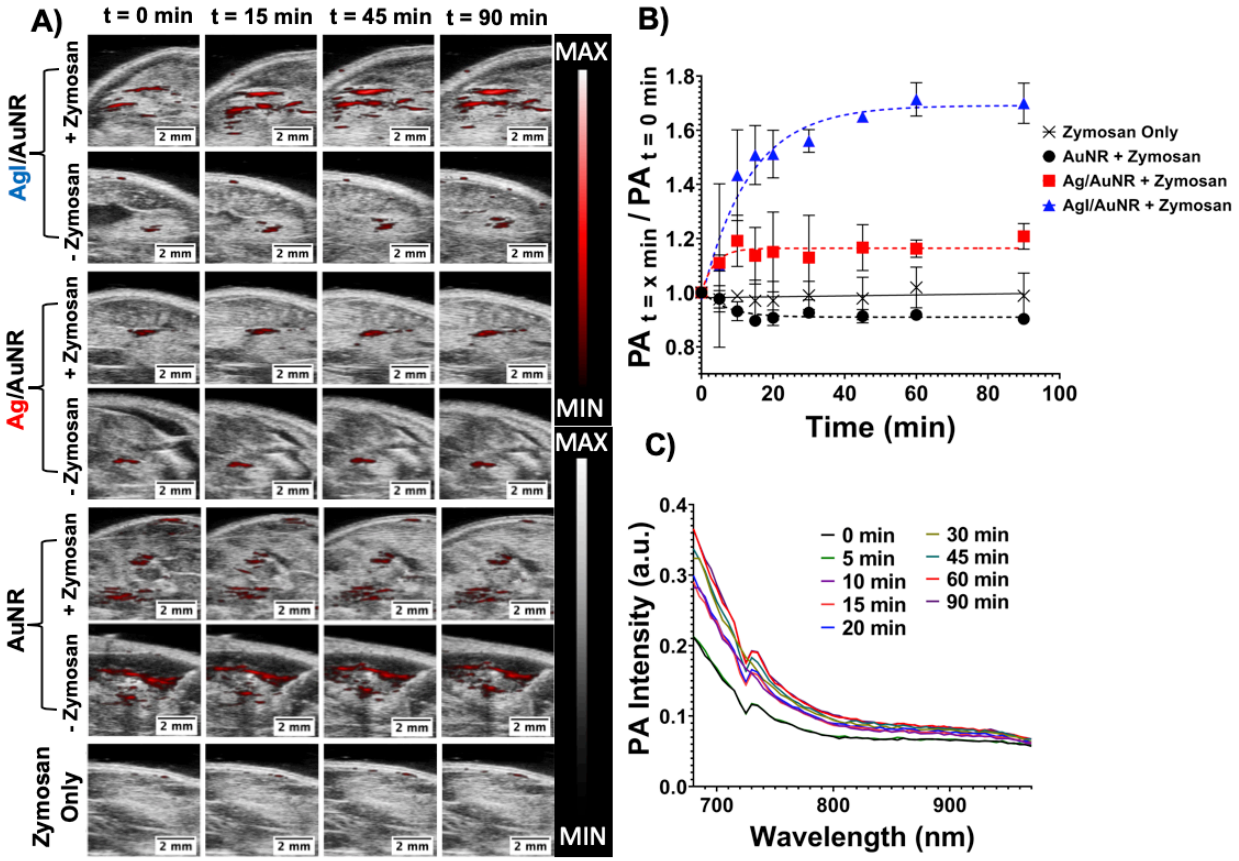

Figure 2. 5 *In vivo* photoacoustic oxidative stress sensing.
Zymosan was used to generate oxidative stress intramuscularly in a murine model (*n = 3*). Photoacoustic images acquired at 680 nm. Signal was monitored at t = 0, 5, 10, 15, 20, 30, 45, 50, and 90 minutes. Representative photoacoustic-ultrasound images of AgI/AuNR, Ag/AuNR, and AuNR with and without zymosan treatment (**A**). Photoacoustic intensity at t = x min / photoacoustic intensity at t = 0 min for zymosan only and nanoparticles treated with zymosan (**B**). There is a 70% increase in photoacoustic signal for AgI/AuNR, 20% increase for Ag/AuNR, and 10% decrease for AuNR over 90 minutes. The zymosan-only control remains unchanged. Photoacoustic spectra of AgI/AuNR (+ zymosan) shows increasing photoacoustic response at 680 nm over 90 minutes (**C**). Error bars represent standard deviation of three replicate animals.

Finally, we used zymosan to stimulate intramuscular RONS generation in a murine model (n=3). **Figure 2.5** shows the response of AuNR, Ag/AuNR, and AgI/AuNR to endogenously generated RONS. Over 90 minutes, the photoacoustic signal from AgI/AuNR in the presence of RONS increased by 70% compared to 20% for Ag/AuNR. The AuNR signal reduced by 10% which can be attributed to laser-induced nanorod deformation.[100, 222] Photoacoustic spectral data

showed a clear increase in photoacoustic intensity at 680 nm for AgI/AuNR and no change for Ag/AuNR and AuNR. AgI/AuNR turned on only in the presence of RONS as zymosan-free controls showed < 5% change in signal over 90 minutes (**Figure 2.16**).

2.6 Conclusion

This work presents the synthesis, characterization, and application of a hybrid iodide-doped Au/Ag nanoparticle. In summary, iodide can be doped into Ag/AuNR under acidic conditions. The I:Ag molar ratio and initial thickness of Ag shell play an important role in successful iodide doping, which lowers the reduction potential of the Ag shell making the nanoparticles 1,000 times more sensitive to H_2O_2 and 100,000 times more sensitive to $ONOO^-$ compared to undoped Ag/AuNR. Photoacoustic imaging can be used to sense RONS levels *in vivo*. Importantly, the Ag^+ and I^- released here can also serve as antibacterial agents, and future work will test the antibacterial efficacy of these materials including in smart wound dressings.

2.7 Acknowledgements

Chapter 2, in full, is a reprint of the material as it appears in Iodide-doped precious metal nanoparticles: measuring oxidative stress in vivo via photoacoustic imaging. Mantri, Yash; Davidi, Barak; Lemaster, Jeanne E.; Hariri Ali; Jokerst, Jesse V., Nanoscale, 2019. The dissertation author was the primary investigator and author of this paper.

2.8 Supplementary information

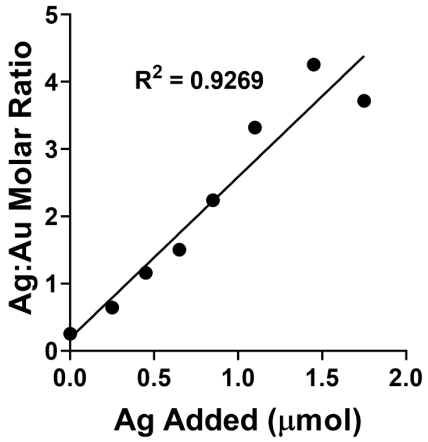

Figure 2. 6 Final immobilized Ag:Au molar ratio measured by ICP-MS.
Ag shell thickness can be controlled by adding increasing amounts of $AgNO_3$ during the Ag coating step.

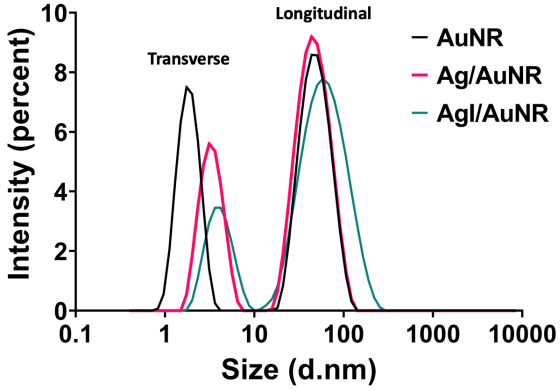

Figure 2. 7 Nanoparticles characterized using dynamic light scattering (DLS).
Two peaks can be observed for the transverse and longitudinal sections of the rod structure. Silver deposition is more favorable on the 110 facet of the gold which is along the longitudinal edge. As a result, the rod becomes thicker, but the length remains relatively the same. Doping with Iodide results in a 1 nm increase in shell thickness which can be attributed to AgI_3O_8 complex formation. The poly dispersity index (PDI) for AuNR: 0.55, Ag/AuNR: 0.59 and AgI/AuNR: 0.67. The PDI is unusually high because DLS assumes the particles are spherical and is not optimized to characterize rod like structures.

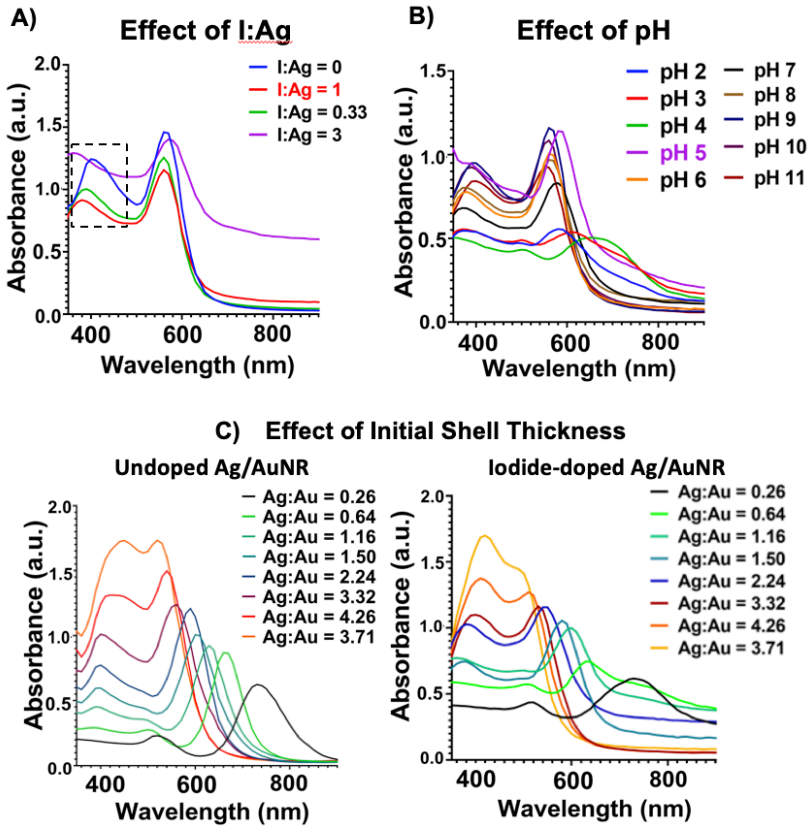

Figure 2. 8 Optimizing reaction conditions for iodide doping.
Effect of I:Ag molar ratio (**A**). An I:Ag greater than 1 results in particle destabilization whereas <1 does not maximize doping. A 1:1 ratio is optimal. Effect of pH on doping (**B**). Iodide can be doped into Ag under acidic conditions, but highly acidic conditions result in Ag shell etching; pH 5 was optimal. Effect of initial Ag shell thickness on doping efficiency (**C**). A thin shell is more susceptible to damage under acidic conditions than a thick shell (Ag:Au molar ratio > 3.32). Hence, A Ag:Au molar ratio > 3.32 is found to be optimal for shell doping.

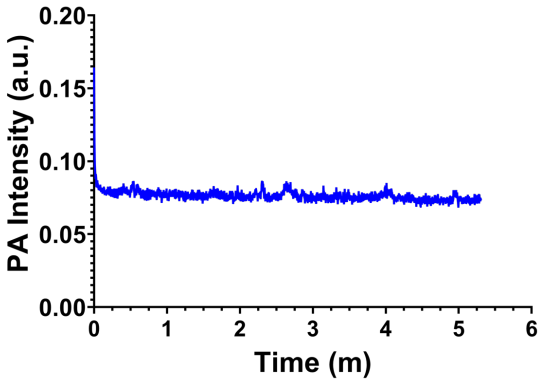

Figure 2. 9 Photostability.
Synthesized AgI/AuNRs show a 17% decrease in PA amplitude over 5 minutes of 680 nm illumination. PA intensity is low here because AgI/AuNRs have peak absorbance at 578 nm.

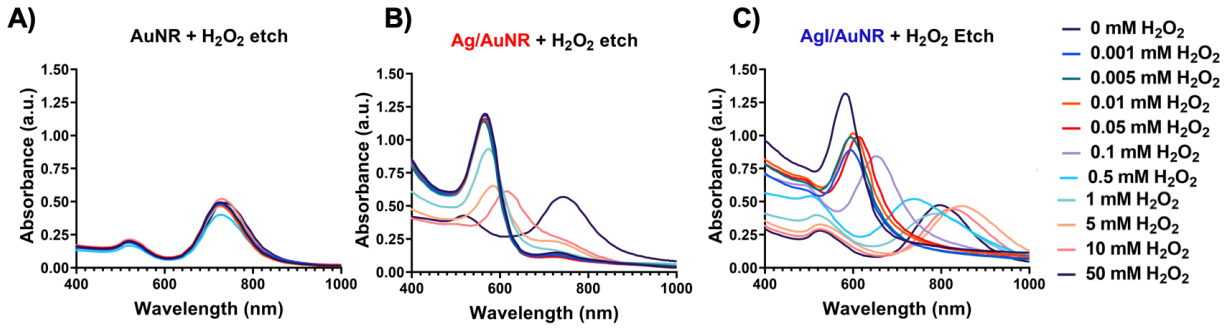

Figure 2. 10 H_2O_2 etching.
AuNR is unaffected when treated with varying concentrations of H_2O_2 (**A**). Ag/AuNR starts to etch at 10 mM (**B**) and AgI/AuNR starts to etch at 0.05 mM H_2O_2 (**C**).

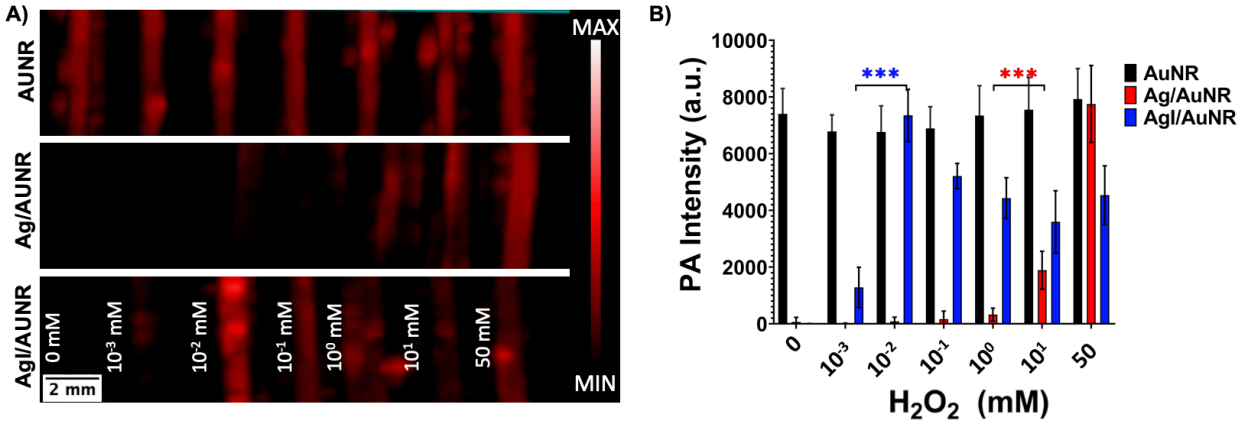

Figure 2. 11 Photoacoustic imaging of H_2O_2 etching.
Photoacoustic images of AuNR, Ag/AuNR, and AgI/AuNR treated with varying concentrations of H_2O_2 (**A**). Plot comparing photoacoustic intensity after treatment with varying concentrations of H_2O_2 (**B**). There is a significant ($p < 0.001$) increase in photoacoustic intensity at 10^{-2} mM H_2O_2 for AgI/AuNR and at 10 mM for Ag/AuNR. AgI/AuNR is 1000-fold more sensitive to H_2O_2 than undoped Ag/AuNR. The error bars represent the standard deviation of six regions-of-interest.

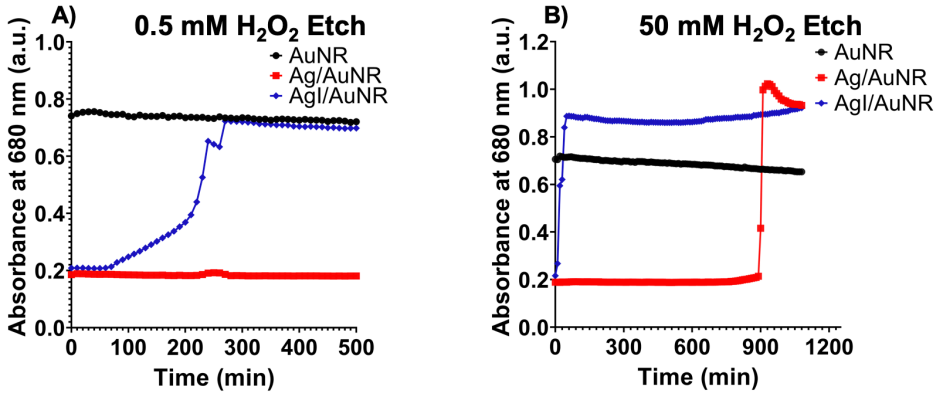

Figure 2. 12 H_2O_2 etching kinetics.
At 0.5 mM H_2O_2 AgI/AuNR takes ~5 hours to completely etch whereas AuNR and Ag/AuNR show no change in absorbance at 680 nm (**A**). At 50 mM AgI/AuNR etches 45 times faster than undoped particles which take over 15 hours to etch (**B**).

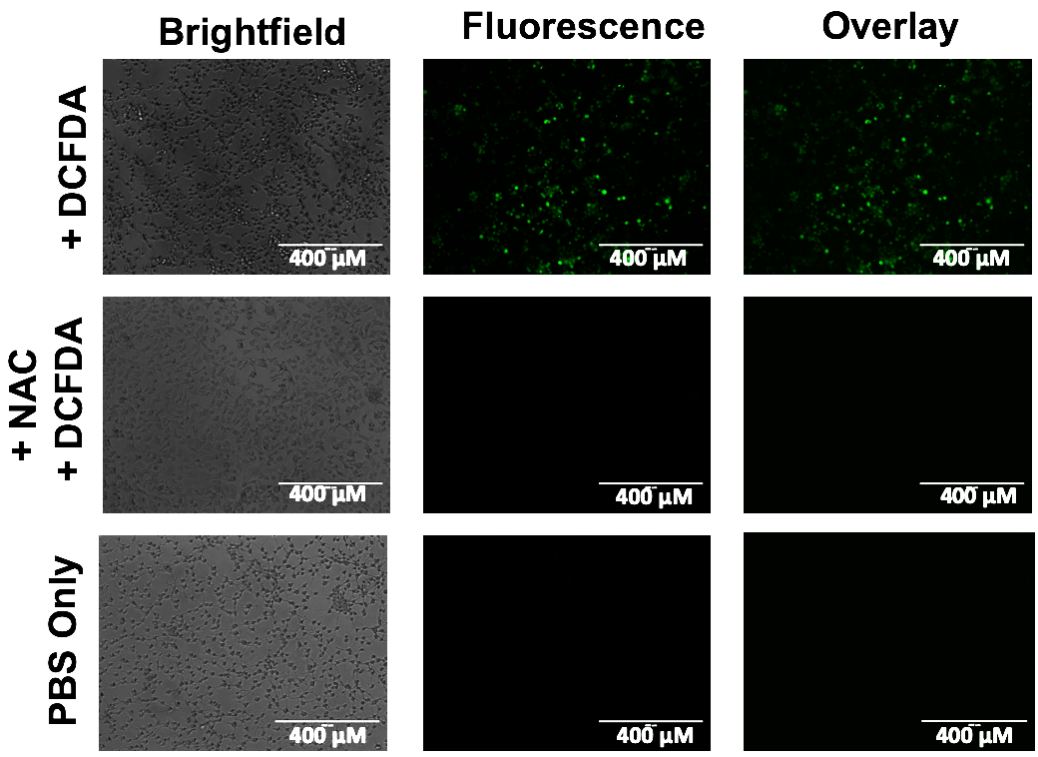

Figure 2. 13 SKOV3 DCFDA assay.
Ovarian cancer (SKOV3) cells naturally produce RONS that can be scavenged with NAC. DCFDA is a ROS-sensitive fluorophore that is emissive only in the presence of ROS. Cells treated with DCFDA showed green fluorescence whereas cells treated with DCFDA + NAC showed no fluorescence.

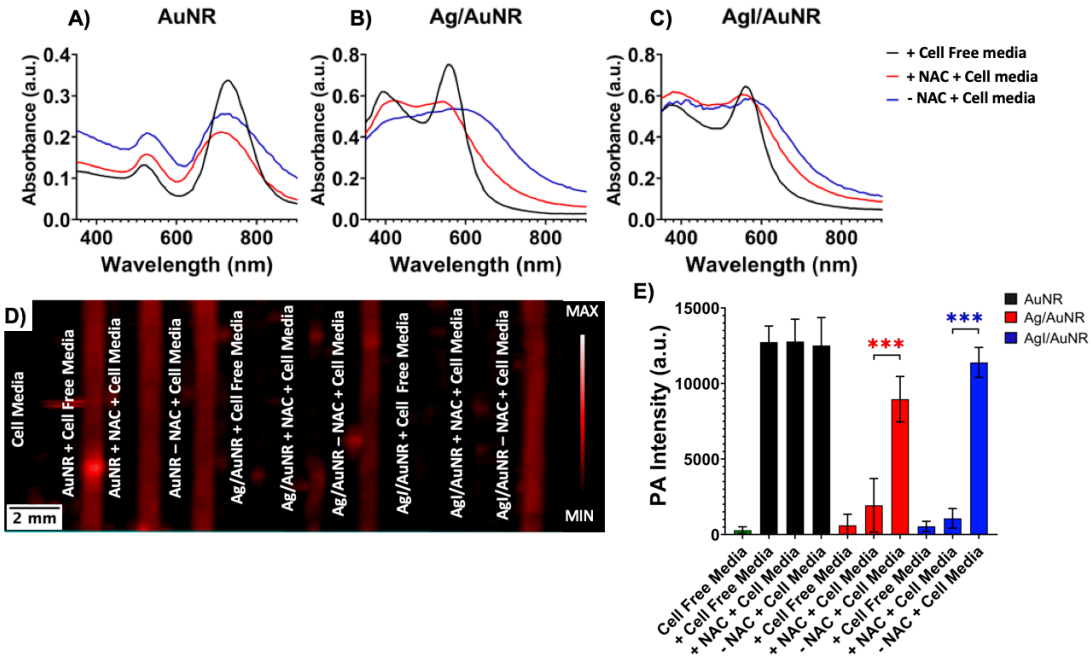

Figure 2. 14 SKOV3-generated RONS photoacoustic response.
Absorbance spectra of AuNR, Ag/AuNR and AgI/AuNR when treated with cell free media, + NAC + cell media and – NAC + cell media. NAC is a RONS scavenger. Absorbance at 680 nm increases more when treated with – NAC + cell media (**A-C**). Photoacoustic image at 680 nm of samples from A-C (**D**). Cell-free media has negligible photoacoustic signal. AuNR shows no change in signal with or without RONS scavenging. Ag/AuNR and AgI/AuNR both show etching when treated with – NAC + cell media (RONS enriched) that leads to increased PA signal (**E**). ($p < 0.001$) Error bars represent standard deviation of six regions-of-interest.

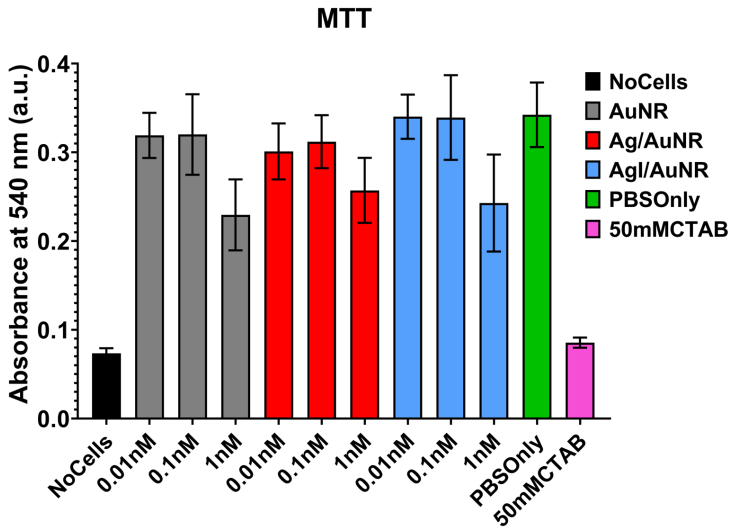

Figure 2. 15 Cell cytotoxicity assay.
At lower concentrations of 0.01 nM and 0.1nM, synthesized particles are not significantly more toxic than PBS only negative control. At higher concentrations of 1 nM, particles exhibit higher toxicity due to higher amounts of residual CTAB. All *in vivo* experiments were performed at 0.3 nM particle concentration.

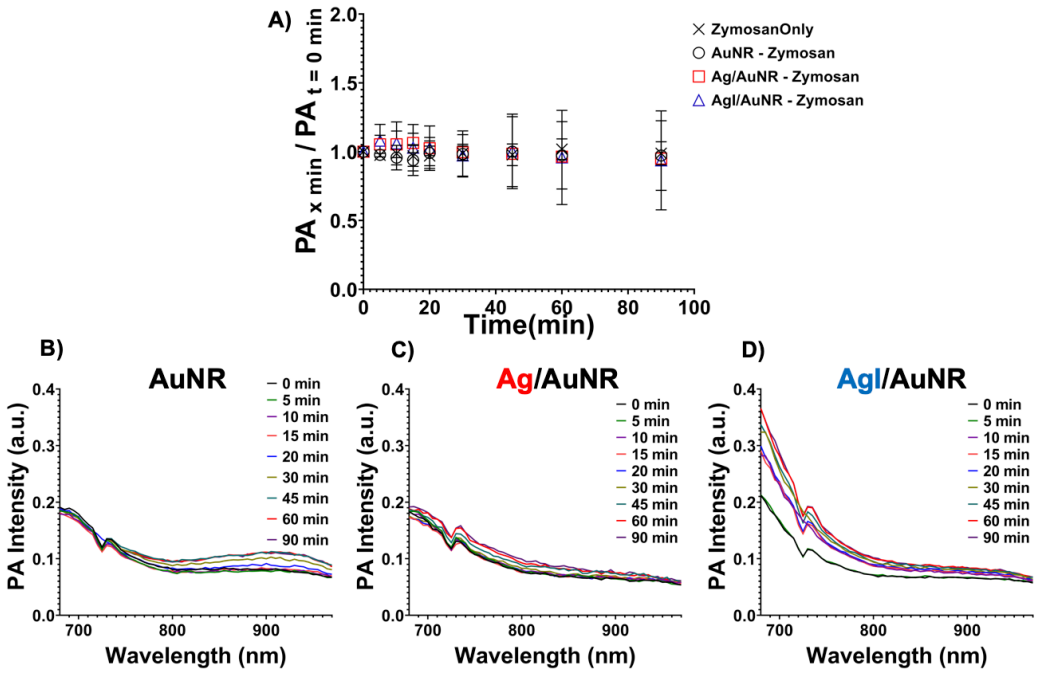

Figure 2. 16 *In vivo* RONS sensing.
Photoacoustic intensity at t = x min / photoacoustic intensity at t = 0 min for zymosan only and nanoparticles in the absence of zymosan (**A**). There is no RONS generation without Zymosan as a result the particles show no change in photoacoustic intensity compared to their baseline at t= 0 min. Photoacoustic spectra of AuNR, Ag/AuNR, and AgI/AuNR over 90 minutes in the presence of zymosan (**B-D**). AuNR and Ag/AuNR show no change in spectra over 90 min whereas AgI/AuNR shows a clear increase in signal at 680 nm.

Chapter 3: Photoacoustic enhancement of ferricyanide treated silver chalcogenide coated gold nanorods.

3.1 Abstract

Plasmonic gold nanorods (AuNRs) are often employed as photoacoustic (PA) contrast agents due to their ease of synthesis, functionalization, and biocompatibility. These materials can produce activatable signal in response to a change in optical absorbance intensity or absorbance wavelength. Here we report a surprising finding: Ag_2S/Se-coated AuNRs have a ~40-fold PA enhancement upon addition of an oxidant but with no change in absorption spectra. We then study the mechanism underlying this enhancement. Electron micrographs and absorption spectra show good colloidal stability and retention of the core-shell structure after potassium hexacyanoferrate (III) (HCF) addition ruling out aggregation and morphology-induced PA enhancement. X-ray diffraction data showed no changes ruling out crystallographic phase changes upon HCF addition thus leading to induced PA enhancement. Attenuated total reflectance Fourier transform infrared (ATR-FTIR) spectroscopy and zeta potential analysis suggests that PA enhancement is driven by the irreversible displacement of CTAB with HCF. This is further confirmed using elemental mapping with energy dispersive X-ray analysis. PA characterization after HCF addition showed a four-fold increase in the Grüneisen parameter (Γ) thus resulting in PA enhancement. The PA enhancement is not seen in uncoated AuNRs or spherical particles. Two possible mechanisms for PA enhancement are proposed: First, the photo-induced redox heating at the Ag_2S/Se shell-HCF interface resulting in an increase in temperature dependent Γ. Second, an enhanced electrostriction response due to HCF adsorption on a layered plasmonic nanoparticle surface resulting in a high thermal expansion coefficient (β) that is directly proportional to Γ.

3.2 Introduction

Plasmonic gold nanostructures such as spheres and rods are the most widely used nanoparticle-based photoacoustic (PA) contrast agents.[223, 224] Gold nanorods (AuNRs) are particularly useful due to their easily tunable size, high photothermal conversion efficiency, ease of synthesis, functionalization, and a tunable localized surface plasmon resonance (LSPR) [86, 225, 226] We and others have previously reported the use of AuNRs for PA-based cell tracking,[227] cancer imaging,[12, 228, 229] oxidative stress sensing,[230] and theranostics.[71, 231]

PA imaging uses nanosecond pulsed illumination to generate pressure waves detectable by conventional ultrasound transducers. The absorption of light results in thermally-confined heating of the nanoparticle (millikelvin range).[1] The increase in temperature causes thermoelastic expansion of the nanoparticle, thus creating pressure transients that propagate through the sample medium.[1, 223] The intensity of the resulting PA signal is a function of the optical and thermo-elastic properties of the nanoparticle and its surroundings (**Equation 3.1**).[95, 223]

$$\rho_o = \left(\frac{\beta c^2}{C_p}\right) \mu_a F = \Gamma A \qquad \text{Equation 3.1}$$

Here, $\boldsymbol{\rho_o}$ describes PA intensity.[1] β is the thermal expansion coefficient in K^{-1}; $\mathbf{C_p}$ is the specific heat capacity in $JK^{-1}kg^{-1}$; and $\boldsymbol{\mu_a}$ is the absorption coefficient in cm^{-1} of the absorbing material. Term **c** is the speed of sound in the imaging medium in ms^{-1}; and **F** is the irradiation fluence in Jcm^{-2}. $\boldsymbol{\Gamma}$ is the Grüneisen parameter ($\beta c^2 C_p^{-1}$) and characterizes the thermo-acoustic conversion efficiency, and **A** ($\mu_a F$) is the local energy deposition density in Jcm^{-3}. [223, 232] An ideal PA contrast agent has a high optical absorption, low scattering properties, and a high phothermal conversion efficiency.[14, 233-235]

There are various ways to enhance PA signal generated by AuNRs. PA intensity is directly proportional to laser fluence. Increasing laser fluence and shortening pulse width can lead to PA enhancement.[96, 223, 236] Increasing the nanoparticle concentration results in a higher μ_a and hence higher PA.[237-240] AuNR coatings such as silica,[98, 99, 103] polydopamine,[241, 242] titanium dioxide,[39] and reduced graphene oxide[41] have shown significant PA enhancement by reducing the Kapitza resistance (thermal resistance at the particle solvent interface). This in turn improves thermal confinement to enhance AuNR PA signal.[96, 223, 243] On the contrary, others have shown a reduction of PA signal on silica coating.[244] Studies have also shown that up to 93% of the PA signal is generated by the thermal expansion of the solvent. Hence, using solvents with a high β and low C_p can also enhance PA intensity.[95, 101, 245] The Γ of conventional solvents such as water is directly proportional to temperature. Hence, an increase in solvent temperature can also result in PA enhancement.[95, 246] In summary, engineering AuNRs with LSPRs and μ_a responsive to chemical cues is the most common technique for PA signal modulation.[223, 247]

Previously, we investigated the use of silver and iodide-doped silver coated AuNRs for oxidative stress sensing.[71, 230] These were shell-core (Ag/AgI-AuNR) that showed selective etching of the shell in the presence of reactive oxygen and nitrogen species (RONS). The bare AuNRs had a near infrared (NIR) LSPR that blue shifted on shell coating, resulting in low PA signal in the NIR range. Selective etching of the shell layer resulted in full recovery of the AuNR LSPR and its PA signal. In both works, we used potassium hexacyanoferrate (III) (HCF) as a positive control that selective oxidized the Ag/AgI shell (Ag^+/Ag^0 E^0 = 0.79 V). The reduction potential of the Au^+/Au^0 (E^0 = 1.69 V) core was much higher than that of HCF Fe^{3+}/Fe^{2+}(E^0 = 0.77 V) and hence the AuNR core was recovered. As a part of this study, we also synthesized Ag_2S and Ag_2Se coated AuNRs as negative controls (E^0 of $Ag_2S_{(s)} + 2e^- \rightarrow 2Ag_{(s)} + S^{2-}_{(aq)}$ = -0.69 V) that show no etching

in the presence of HCF or RONS.[77] The negative reduction potential of silver chalcogenides means that they do not readily donate electrons and get oxidized. Indeed, we observed no etching of the silver chalcogenide shell and no change in LSPR on HCF treatment but observed a ~40-fold PA enhancement. The PA enhancement is interesting because traditionally an increase in absorption (μ_a) at the imaging wavelength results in PA enhancement.[223] Surprisingly, these silver chalcogenide-coated AuNRs showed no change in absorbance after HCF treatment but much higher PA signal. Thus, the goal of this work was to study the interaction between HCF and the nanoparticle surface to elucidate the mechanism underlying this surprising PA enhancement.

3.3 Materials and methods

3.3.1 Materials

Hexadecyltrimethylammonium bromide (CTAB, Cat. #1102974), L-ascorbic acid (Cat. #255564), silver nitrate (Cat. #209139), potassium hexacyanoferrate (III) (HCF, Cat. #244023), gold (III) chloride trihydrate (Cat. #520918), selenourea (Cat. #230499), and titanium (IV) oxide (Cat. #718467) were purchased from Sigma Aldrich (Atlanta, GA, USA). Sodium borohydride (Cat. #S678-25) and sodium hydroxide (Cat. #1310-73-2) were purchased from Fisher Scientific (Pittsburgh, PA, USA). Sodium sulfide (Cat. #65122-06) was purchased from Alfa Aesar (Tewksbury, MA, USA). All chemicals were used as received without further purification.

3.3.2 Nanoparticle synthesis

CTAB-stabilized AuNRs were synthesized using a seed-mediated growth method reported previously.[230] Gold seeds were synthesized by adding 5 ml of CTAB (0.2 M) to 2.5 ml of $HAuCl_4.3H_2O$ (0.001 M); 0.6 ml of ice-cold $NaBH_4$ (0.01 M) was used as a reducing agent under vigorous stirring for 2 min. The growth solution was a mixture of 500 ml $HAuCl_4 \bullet 3H_2O$ (0.001

M) and 500 ml CTAB (0.2 M). Next, 7 ml of L-ascorbic acid (0.089 M) and 36 ml of $AgNO_3$ (0.004 M) was added to the growth solution. The color of the solution turned from dark orange to colorless. Finally, 1.2 ml of the seed solution was added, and the reaction mixture was hand swirled for 5 s. The reaction vessel was left undisturbed for 12 h as the solution turned purple/dark brown. The AuNRs were washed thrice via centrifugation at 12500 rpm for 15 min each and stored at 4 ^oC; the stock concentration was 9.35 nM. All experiments were carried out using the same batch of AuNRs.

The silver chalcogenide coating of AuNRs was done in a two-step process (**Figure 3.1A**).[77] AuNRs were first coated with a silver shell.[230] Next, 0.48 ml of AuNRs (9.35 nM) was diluted in a mixture of 12 ml water and 2 ml CTAB (0.1 M). To this, we added 0.36 ml of $AgNO_3$ (0.010 M), 0.34 ml L-ascorbic acid (0.1 M), and 0.84 ml NaOH (0.1 M). The reaction was vigorously stirred for 30 min as the color changed from pink to dark green. The resulting silver coated AuNRs (Ag/AuNRs) were doped with 0.36 ml of Na_2S (0.010 M) or $SeC(NH_2)_2$ (0.010 M) under vigorous stirring for 2 h while open to air. The Na_2S and $SeC(NH_2)_2$ doping results in the formation of Ag_2S/AuNR and Ag_2Se/AuNR respectively. Nanoparticles were further purified *via* centrifugation at 12500 rpm for 15 min and dispersed in water.

3.3.3 Absorption spectroscopy (UV-Vis-NIR)

All optical absorption spectra were acquired using the BioTek Synergy H1 microplate reader from Agilent (Santa Clara, CA, USA). We used 150 µl of solution in a 96-well plate. Unless otherwise mentioned, absorption spectra were acquired between 280 – 995 nm with a step size of 5 nm.

3.3.4 Dynamic light scattering (DLS) and zeta potential

DLS and zeta potential were measured using a Malvern Instruments Zetasizer ZS 90; 0.2 ml of particles were diluted in 0.8 ml of water.

3.3.5 Transmission electron microscopy (TEM) and energy dispersive X-ray spectroscopy (EDX)

All high-resolution electron micrographs (HR-TEM; mag: 650000X) and EDX maps were acquired using a ThermoFisher Talos 200X system at an operating voltage of 200 kV. Low magnification (mag: 150,000X) TEM images were acquired on a JEOL JEM-1400Plus system operating at 80 kV. Images were recorded using a Gatan OneView 4K digital camera.

3.3.6 Powder X-ray diffraction (pXRD)

pXRD was acquired using a Bruker D8 Advance operating in Bragg-Brentano geometry. Cu-radiation: 1.54 Å, equipped with a Ni K-beta filter. The 2θ scan range was 10-80^{o} with a step size of 0.02^{o} and exposure of 0.25 s. Samples were prepared by concentrating 1 ml of synthesized nanoparticles to 0.02 ml via centrifugation and then redispersing in distilled water.

3.3.7 Attenuated total reflectance-Fourier transform infrared spectroscopy (ATR-FTIR)

A more detailed description of the attenuated total reflectance-Fourier transform infrared (ATR-FTIR) spectroscopy setup can be found elsewhere.[248, 249] Infrared spectra were collected using a Nicolet iS10 FTIR spectrophotometer with a mercury cadmium telluride detector. Spectra were averaged over 100 scans with a 4 cm^{-1} resolution over the spectral range from 750 to 4000 cm^{-1}; OMNIC 9 software was used to collect data. The software was also used for background subtractions and baseline corrections. For solution-phase spectra, samples were pipetted onto the AMTIR crystal and covered. The chamber was purged with dry air to remove atmospheric gases

for approximately 30 min before each spectrum was collected. All *in-situ* spectroscopic measurements involved collecting spectra every 2.5 min during an aqueous over the sample as described below.

For dynamic, *in-situ* measurements, a dry nanoparticle thin film was first created by drop casting 1 mL of a ~27 nM nanoparticle concentration onto the crystal and dried overnight with a continuous dry air purge. For displacement reactions on silver chalcogenide coated-AuNRs, water was flowed at ~1 mL/min for 60 min to remove loose particles followed by a background scan. Next, 50 μM HCF was flowed over for the film for 90 min and another scan was taken. Then, 50 μM CTAB was flowed over the thin film for 90 min and another scan was taken. Finally for desorption, water was flowed over the film for 60 min.

For displacement reactions on AuNR, a dried particle film was created by drop casting 1 mL of ~27 nM particles onto the AMTIR crystal and dried overnight. Water background, HCF adsorption, CTAB displacement and water desorption were similarly done as previously mentioned but at ~0.2 mL/min. The flow rate was reduced to minimize film dewetting on the AMTIR crystal because the AuNR thin film was less stable on the AMTIR crystal compared to the silver chalcogenide coated AuNRs.

3.3.8 Photoacoustic (PA) imaging

All PA images were acquired using the Visualsonics Vevo 2100 LAZR from Fujifilm Visualsonics Inc. (Toronto, Canada). Images were acquired at 710 nm, pulse width 4-6 nm, using the LZ250 transducer, F_c = 21 MHz. PA spectrum was acquired between 680 – 970 nm with a step size of 2 nm.

PA enhancement was initiated using potassium hexacyanoferrate (III) (HCF). Silver chalcogenide-coated AuNRs were washed twice via centrifugation at 12500 rpm for 5 min and

redispersed in distilled water to remove excess CTAB. Next 50 μM HCF was added to initiate PA enhancement. All HCF treated characterization was done using the same batch of particles treated with 50 μM HCF.

The Grüneisen parameter was measured by controlling sample temperature between 6 – 45 ^{o}C. The slope of PA intensity *vs.* sample temperature reports the Grüneisen parameter.[250-252] Particle photostability was measured by monitoring the PA intensity under 7 min of laser illumination. The effect of laser fluence on PA signal generation was studied using agarose-TiO_2 nanoparticle filters as described previously.[253] Nine agarose-TiO_2 optical filters ranging from 0 – 8 mg/ml TiO_2 were used to modulate laser fluence on the sample. The laser fluence was measured using a laser pyroelectric energy sensor (PE50BF-C, Ophir LLC, USA).

3.3.9 Data processing

PA, EDX, and TEM images were processed using ImageJ version 2.1.0/1.53c using region of interest analysis (ROI). All data was plotted using GraphPad Prism 9.3.1 (350).

3.4 Results and discussion

The figures in this section focus on Ag_2S/AuNR. Characterization and PA data on Ag_2Se/AuNR can be found in the supplementary information (**Section 3.6**).

3.4.1 Nanoparticle synthesis and characterization

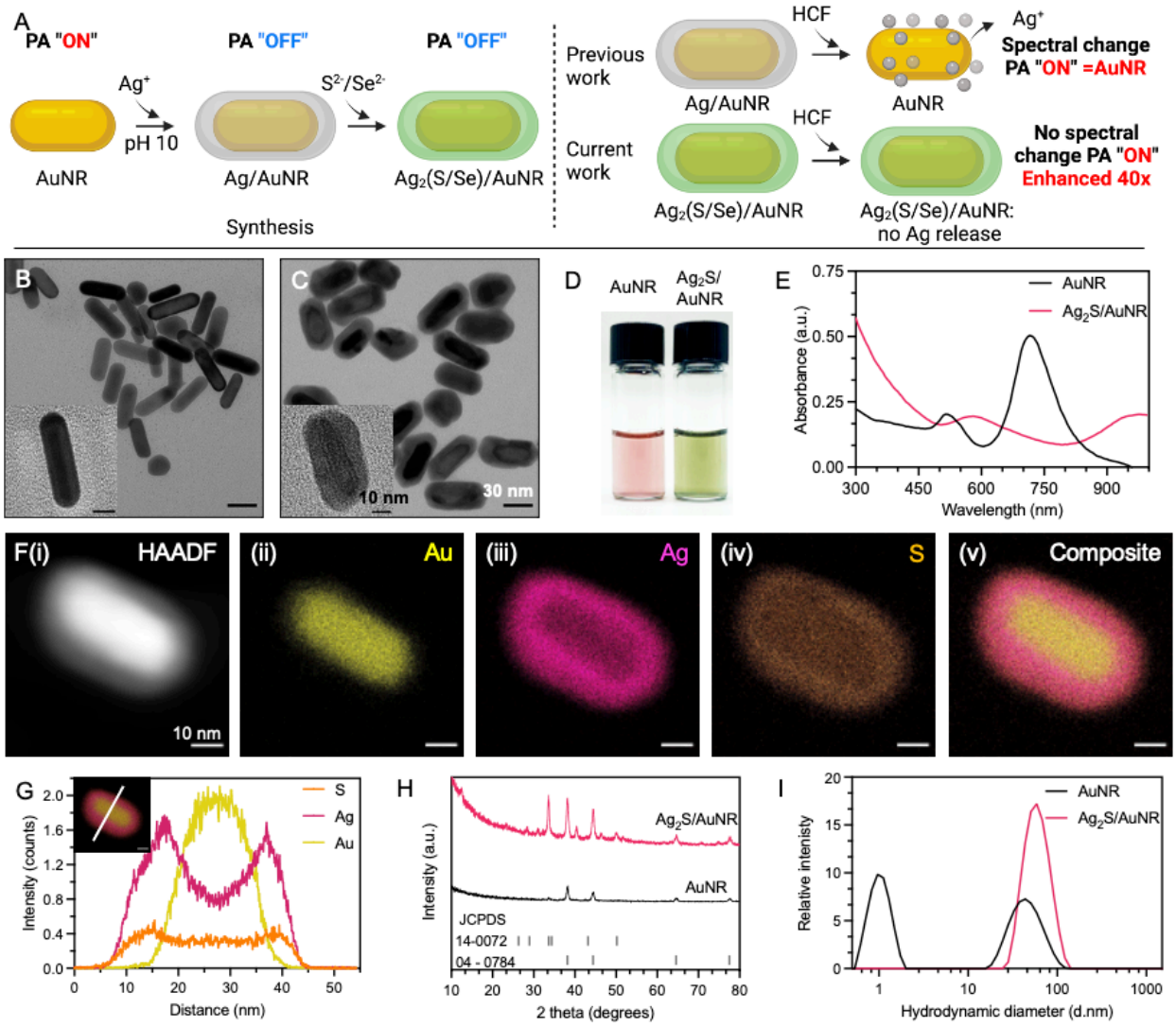

Figure 3. 1 Ag_2S/AuNR synthesis and characterization.
A. Schematic representation of silver chalcogenide coated AuNRs synthesis and HCF treatment. **B-C.** TEM images of synthesized AuNRs and Ag_2S/AuNR shows a core-shell particle. (Inset: HRTEM). The AuNR aspect ratios were 3.08 ± 0.35, and the Ag_2S shell thickness was 7.3 ± 1.4 nm. Scale bars on low- and high-resolution images are 30 and 10 nm, respectively. **D.** The addition of a Ag_2S shell changes the AuNR suspension color from pale pink to green. **E.** Synthesized AuNRs had a characteristic absorption spectrum peak absorbance at 710 nm. Ag_2S shell coatings lead to a red-shift and attenuation of the spectrum into the infrared region. **F-G.** EDX mapping of Ag_2S/AuNR confirms a gold nanorod core and Ag_2S shell formation. Scale bars represent 10 nm. **H.** pXRD analysis of Ag_2S/AuNR shows characteristic crystal facets for both Ag_2S and Au. **I.** DLS shows an 8.1 nm increase in particle hydrodynamic diameter after Ag_2S coating.

The AuNRs were synthesized using a seed-mediated method.[230] AuNR aspect ratio was 3.08 ± 0.35 (n > 100 particles) with a peak absorbance of 710 nm (**Figure 3.1B, E**). HRTEM and pXRD confirmed characteristic 111, 200, 220, and 311 Au crystal facets (JCPDS 04-0784, **Figure**

3.1H).[210, 254] DLS showed two peaks at 1.2 and 50.7 nm. DLS inherently assumes that all particles are spherical and hence not ideal to size rod-like particles. The 1.2 nm peak can be attributed to rotational diffusion coefficient of AuNRs.[230]

Coating with chalcogenides results in a core-shell nanostructure (**Figure 3.1C and 3.6A**) with a visible color change from pale pink AuNRs to green Ag_2S/Se coated AuNRs (**Figure 3.1D, 3.6C**). The Ag_2S/AuNR and Ag_2Se/AuNR had a shell thickness of 7.3 ± 1.4 nm and 6.6 ± 1.5 nm, respectively. DLS showed an increase in 8.1 nm and 7.6 nm the particle's hydrodynamic diameter for Ag_2S/AuNR and Ag_2Se/AuNR respectively (**Figure 3.1I and 3.6E**). The absorption spectra were attenuated and red shifted after coating (**Figure 3.1E, 3.6C**). The degree of red shifting and the degree of attenuation depends on the shell thickness and the high refractive index of silver chalcogenide shell, respectively.[77] EDX mapping of Ag_2S/AuNR shows a gold nanorod core surrounded by a silver sulfide shell (**Figure 3.1 F-G**). pXRD analysis after shell coating showed characteristic crystal facets for Au, Ag_2S, and Ag_2Se (JCPDS 04-0784, 14-0072, and 24-1041 respectively).

3.4.2 HCF-mediated PA enhancement

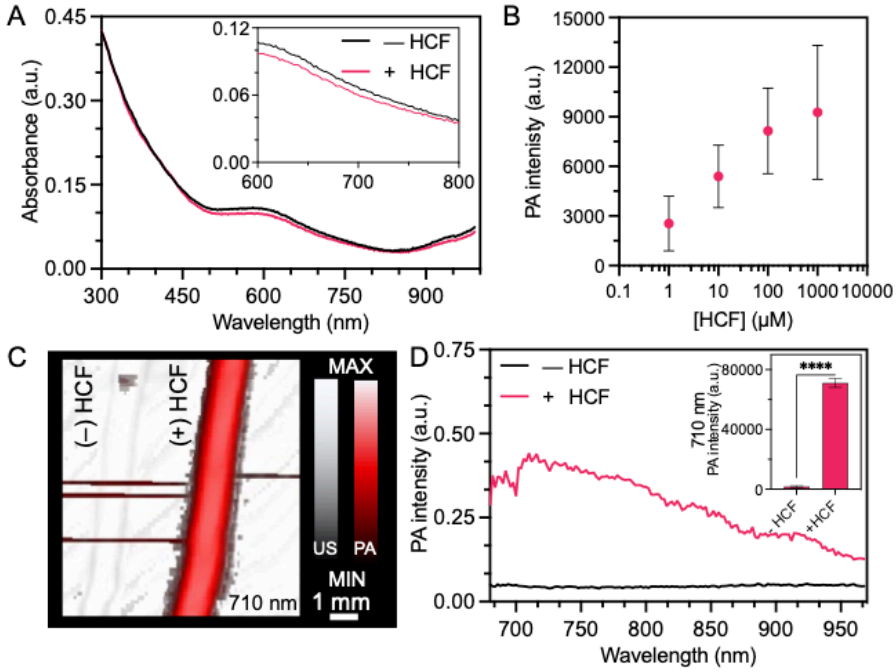

Figure 3. 2 HCF-mediated PA enhancement of Ag_2S/AuNR.
There was no change in absorbance but a 42-fold PA enhancement. **A.** HCF treatment of Ag_2S/AuNRs causes no significant changes in absorption spectrum. **B.** Ag_2S/AuNRs stabilized in 5 mM CTAB show an exponential PA enhancement with increasing amounts of HCF. **C-D.** HCF-treated particles show a significant (42-fold) PA enhancement at 710 nm ($p<0.0001$). **D**. The PA spectrum of untreated particles follows the low absorbance pattern in panel A. HCF-treated particles have peak PA signal at 710 nm. 710 nm is the LSPR of the core gold nanorod. The error bars represent the standard deviation of six ROIs.

Here, 50 μM HCF treatment has no significant effect on the absorption spectra of silver chalcogenide-coated AuNRs (**Figure 3.2A and 3.6C**). Conventional wisdom dictates that no change in absorbance should result in no PA change.[223] But HCF treatment of Ag_2S- and Ag_2Se-coated AuNRs results in an uncharacteristic 42- and 27-fold PA enhancement, respectively (**Figure 3.2C and 3.7B**). Furthermore, the PA spectrum shows enhanced PA in the NIR region (**Figure 3.2D and 3.7C**) whereas absorbance is lowest in the 700-800 nm range. Bare AuNRs showed no significant change in absorbance or PA enhancement on HCF treatment (**Figure 3.8 and 3.9**). The PA enhancement was specific to rod-shaped particles. Ag_2S coated gold spheres (AuSph) showed no change in absorbance or PA intensity after HCF addition (**Figure 3.10**).

The Grüneisen parameter (Γ, **Equation 3.1**) characterizes thermo-acoustic conversion efficiency. Γ is directly proportional to the particle's β.[96] Up to 93% of the PA signal generation can occur in the solvent surrounding the particle.[225] Others have reported the use of different solvents to modulate the PA intensity of gold nanoparticles.[95, 250, 255] Water is a unique solvent to decouple the PA signal generated by the particle from the PA signal generated by the solvent. The β of pure water goes to zero at 3.98 °C.[256] Hence, PA signal from water disappears at that temperature, thus allowing one to isolate the PA signal from the nanoparticle. The slope of the curve plotting PA intensity *vs.* temperature indirectly reports the Γ of the nanoparticle. Uncoated AuNRs exhibit characteristic PA behavior with water at low temperatures (**Figure 3.9D**). HCF treatment causes no significant change in the AuNRs' Γ value ($p>0.05$); both samples show zero PA signal in the 0-4 °C range. The slight deviation from 3.98 °C can be attributed to impurities such as excess CTAB and HCF in solution. Ag_2S/AuNRs show a unique PA response to changes in temperature (**Figure 3.3A-B**). Untreated nanoparticles have a low but linear PA response with zero PA signal at 10.8 °C. On the other hand, HCF-treated Ag_2S/AuNRs show an enhanced PA response with a 4-fold higher Γ value ($p<0.001$) and zero PA signal at -12.4 °C. The non-zero PA signal at 4 °C after HCF addition suggests that the PA enhancement is due to increased thermal confinement within the core-shell nanoparticle and is independent of the solvent. Coatings such as silica and polydimethylsiloxane have also shown thermal confinement effects on gold nanoparticles.[96, 99]

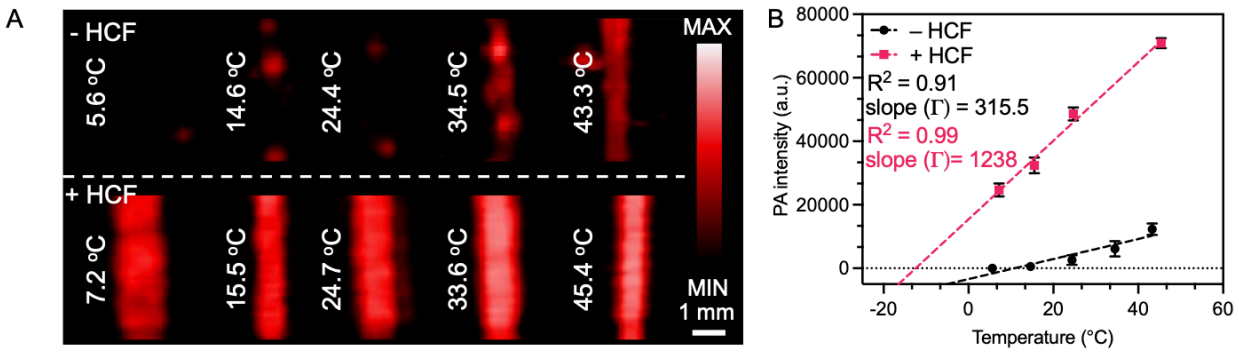

Figure 3. 3 Change in Grüneisen parameter (Γ) of Ag_2S/AuNR after HCF treatment.
A-B. HCF treated Ag_2S/AuNRs have non-zero PA intensity in the 0-4 °C range. This suggests that PA enhancement is independent of the solvent and due to thermal confinement with the nanoparticle and its shell. The slope in panel B represents Γ**.** HCF treated particles show a significant 4-fold enhancement in Γ ($p<0.001$).

The laser fluence (F, **Equation 3.1**) is directly proportional to PA intensity. We controlled laser fluence using a 1 cm thick agarose-based TiO_2 (0-8 mg/ml) filter as an optical scatterer.[253] **Figure 3.9A** shows the experimental setup to control laser fluence. HCF treatment had no effect on the linear response of AuNRs (**Figure 3.9B**). Silver chalcogenide-coated rods also showed a strong linear correlation between PA intensity and laser fluence (**Figure 3.9C-D**) on HCF treatment. Particles not treated with HCF showed low correlation, but this is attributed to extremely low PA intensity across all laser fluences. The higher PA intensity of HCF treated Ag_2S/Se/AuNRs at lower fluence could have applications for an LED-based PA system. LED-based systems are cheaper and more robust but operate at ~1000-fold lower fluence.[257] Low fluence means that more concentrated contrast agents are required to generate the same amount of contrast. Hence, engineering materials with enhanced PA contrast is extremely important. Photostability is also improved (6.5% and 9% decrease in PA intensity for S and Se respectively) when irradiated at the highest fluence of 18.2 ± 0.9 mJ/pulse for over 7 min (**Figure 3.10**). In contrast the low photostability of uncoated AuNRs is evident with 62% decrease in PA intensity. AuNRs are known to melt into more thermodynamically favorable spheres under high fluence irradiation.[223, 258]

3.4.3 Nanoparticle characterization after HCF treatment

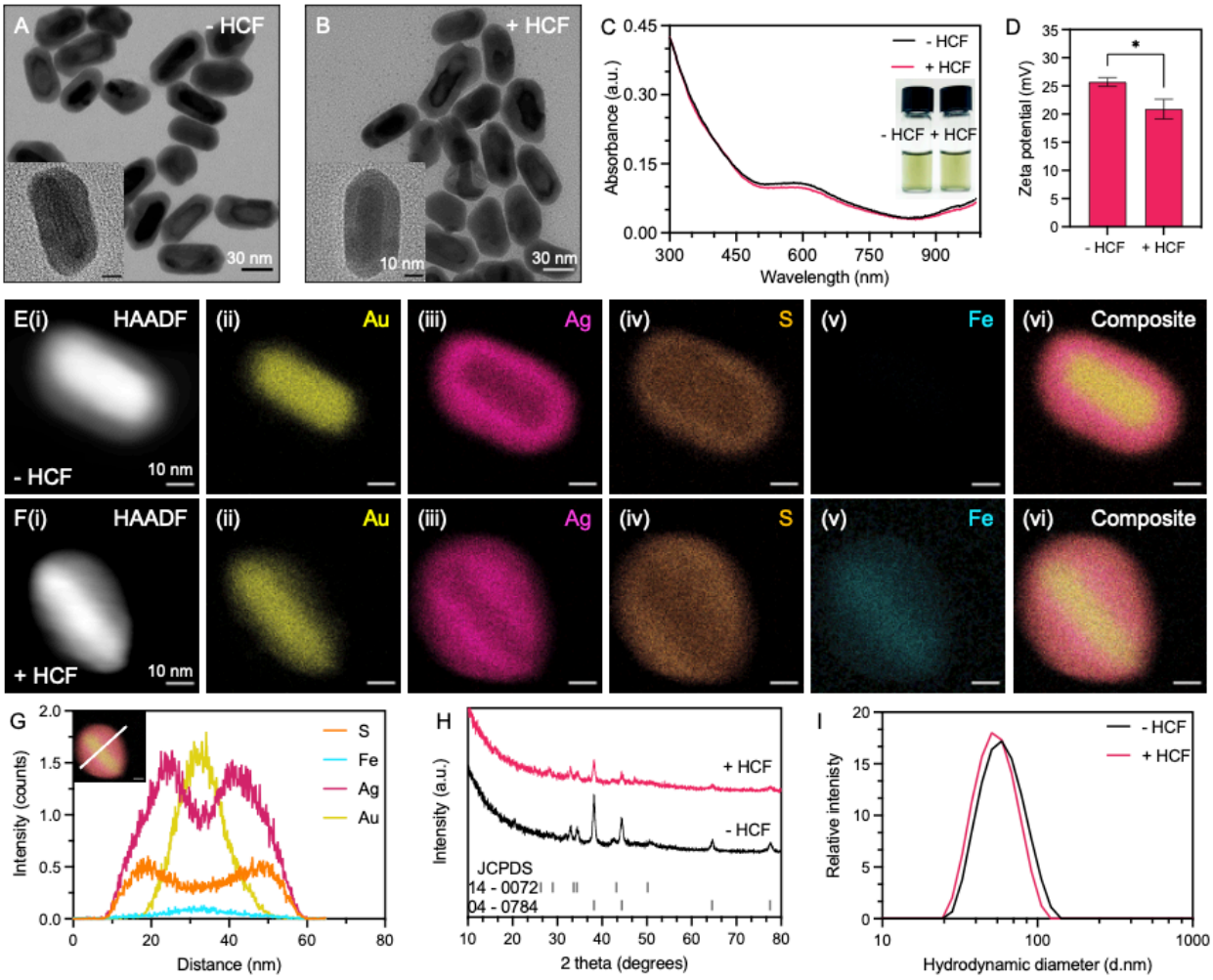

Figure 3. 4 Ag_2S/AuNR characterization after HCF treatment.
A-B. TEM images of Ag_2S/AuNR before and after HCF addition shows conservation of the core-shell structure, particle size, shell thickness, and colloidal stability. (Inset: HR-TEM). This contrasts with our previous work where the Ag shell was selectively oxidized using HCF.[71] Scale bars on low- and high-resolution images measures 30 and 10 nm respectively. **C**. Absorption spectra remains unchanged after HCF treatment. **D**. There is a significant ($p<0.05$) reduction in zeta potential due to the adsorption of negatively charged HCF on positively charged and CTAB-stabilized particles. **E-F**. EDX mapping of Ag_2S/AuNR before and after HCF treatment shows the surface adsorption of Fe representing $[Fe(CN)_6]^{3-}$. **G**. EDX mapping of HCF-treated Ag_2S/AuNR shows slight favoring of Fe adsorption along the longitudinal edge of the particle which is also seen in panel F(v). **H.** pXRD spectra showed no change in crystal structure on HCF treatment. **I**. DLS shows no significant change in particle hydrodynamic diameter after HCF treatment ($p>0.05$). Error bars in panel D represent standard deviation across six measurements.

PA enhancement can be driven by nanoparticle aggregation.[223] Aggregation can cause changes in absorbance or increase thermal flux into the solvent.[103] An increase in absorbance further enhances PA intensity. HCF treatment does not result in aggregation of coated or uncoated nanorods as seen in the TEM images, absorption spectra, and size distribution via DLS (**Figure**

3.4, 3.6 and 3.8). Therefore, aggregation or changes in optical absorption was excluded as a mechanism for the enhancement seen here. In our previous work with Ag/AuNRs, the Ag shell was selectively etched off using HCF as a positive control.[71] The shell etching resulted in AuNR LSPR recovery and PA signal increase. With Ag_2S and Ag_2Se coated AuNRs, the TEM images (**Figure 3.4 and 3.6**) indicate that shell layer remains unetched after HCF treatment. Since particle morphology is conserved, there is no change in absorption spectra. Hence, change in nanoparticle morphology was ruled out.

A high β of the material increases photoacoustic signal.[223] Importantly, different phases of crystals are known to have different β values. In our system, nanocrystalline Ag_2S can have three major phases: monoclinic acanthite (α-Ag_2S), body centered cubic argentite (β-Ag_2S), and FCC phase (γ-Ag_2S). α-Ag_2S is more common under ambient conditions; β and γ-Ag_2S are stable at 456 K and 865 K, respectively.[259] β-Ag_2S has the highest thermal expansion coefficient of the three phases.[259] We did not heat the nanoparticles to those temperatures, but others have shown that a phase transition in metal chalcogenides is possible via chemical modification[260]. For example, n-butyllithium-treated MoS_2 was reported to undergo a phase change due to the electrons injected by n-butyllithium treatment occupying the lowest energy states above the Fermi energy.[260] Thus, it is plausible that the HCF treatment is causing a phase change in our system, an increase in the β, and thus an increase in the photoacoustic signal. But we did not observe any change in crystal structure on HCF addition (**Figure 3.4H, 3.6D, and 3.8D**) in any of our particles. Hence this hypothesis was rejected.

Another hypothesis is that HCF displaces CTAB on the particle surface. CTAB is a positively charged surfactant commonly used to stabilize AuNRs.[261, 262] HCF is a negatively charged molecule hence the substitution of CTAB with HCF should change the particle's surface

charge. There is a significant reduction ($p<0.05$) in zeta potential for all particles as negatively charged $[Fe(CN)_6]^{3-}$ gets adsorbed onto the particle surface. The dynamic interaction between HCF and CTAB on the particle surface was further studied using ATR-FTIR (**Figures 3.5, 3.14, 3.17, and 3.18**). The experimental setup is illustrated in **Figure 3.13.**

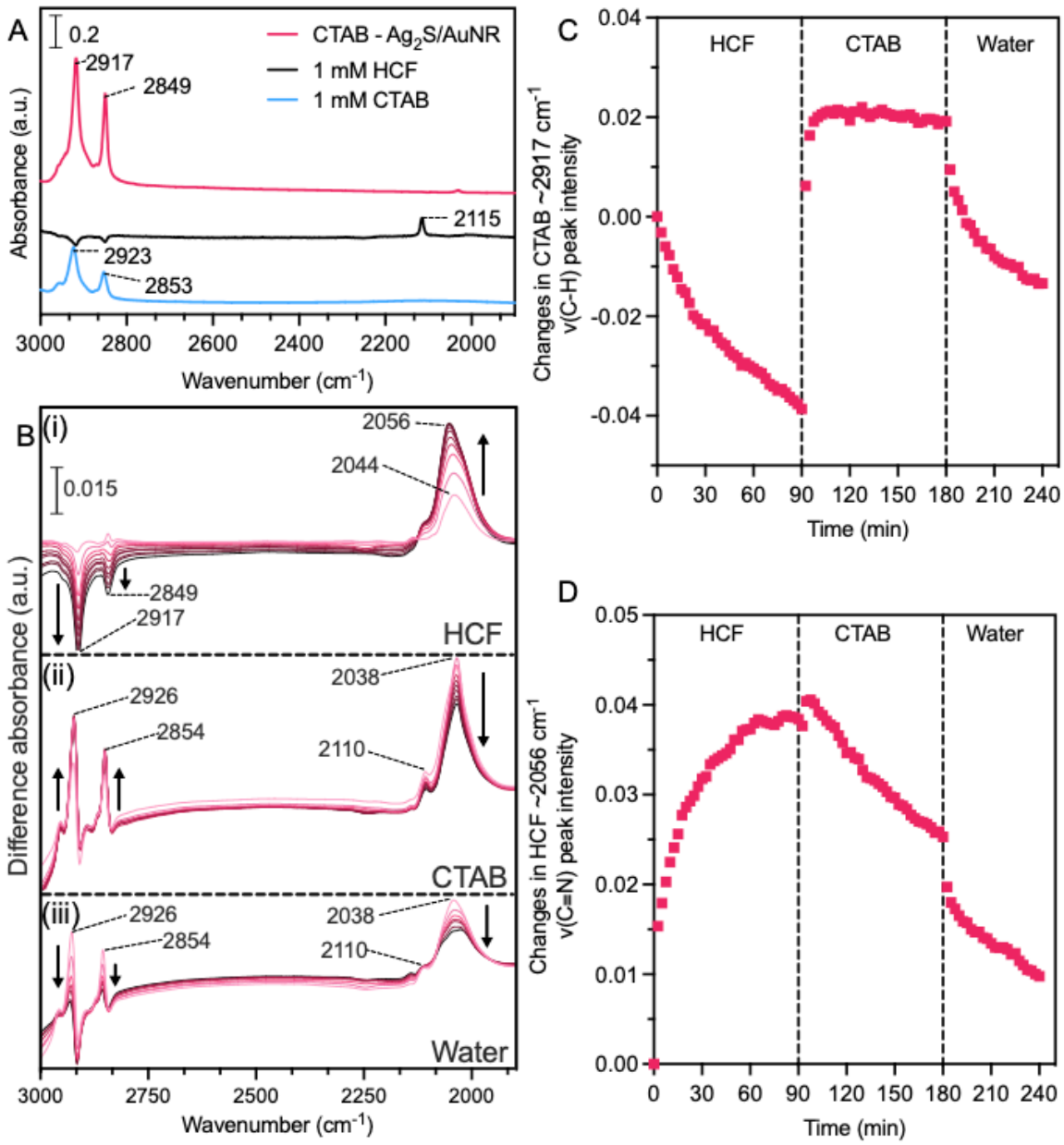

Figure 3. 5 Dynamic *in situ* ATR-FTIR spectra of Ag_2S/AuNR upon HCF treatment.
A. Reference spectra for a dried thin film of CTAB-stabilized Ag_2S/AuNR on an AMTIR crystal; 1 mM solution phase HCF and 1 mM solution phase CTAB are shown. **B.** Here, *in situ* time dependent ATR-FTIR difference spectra for a CTAB stabilized Ag_2S/AuNR following: **(i)** 50 µM HCF flow adsorption. Increase in the 2056 cm^{-1} ν(C≡N) band with the simultaneous decrease in the 2917 and 2849 cm^{-1} ν(C-H) bands as a function of time suggesting a displacement of CTAB with HCF; **(ii)** 50 µM CTAB flow adsorption following HCF adsorption. CTAB can partially desorb loosely bound HCF while forming multilayers on direct surface bound HCF as seen by a change in peak intensity as a function of time; and **(iii)** water desorption flow. These spectra show the desorption of multilayer CTAB and changes to the surface coordination of adsorbed HCF. Temporal spectra in B are collected every 10 minutes from light to dark coloration. **C.** Changes in the CTAB ~2917 cm^{-1} ν(C-H) peak intensity. **D.** Changes in the HCF 2056 cm^{-1} ν(C≡N) peak intensity.

Figure 3.5A and **3.17A** show the dried thin film spectrum of CTAB-stabilized Ag_2S/AuNR and Ag_2Se/AuNR, respectively. Significant ν(C-H) vibrations at 2917 and 2849 cm^{-1} from methyl and methylene groups from CTAB coatings are observed with both particles. The particles also had a strong positive zeta potential before HCF addition due to CTAB stabilization.[262] This suggests that a large amount CTAB was present in the colloidal suspension and that CTAB remained on the film when the suspension was dried. For the *in-situ* temporal adsorption spectra, water was initially flowed over the film to remove excess CTAB and loose particles (**Figure 3.14A**). CTAB related peaks decreased with minimal peak shifts, thus indicating the removal of excess CTAB only. Flowing water for 60 minutes results a plateau for CTAB peak intensity changes; the maximum amount of CTAB is removed from the particle surface at this point (**Figure 3.14B**).

Figure 3.5B shows the *in situ* ATR-FTIR spectra as HCF, CTAB, and water are flowed across the nanorod film (three consecutive flow streams after the initial water wash). The 2044 cm^{-1} peak appears as the HCF flowed over the Ag_2S/AuNR thin film while the CTAB ν(C-H) 2917 and 2849 cm^{-1} decreases (**Figure 3.5B(i)**). This suggests that HCF has higher affinity for the nanoparticle surface and displaces CTAB. Solution phase 50 μM HCF has negligible spectral absorbance values and minimally contributes to the adsorbed intensity (data not shown).

Surface interactions were determined using the 1 mM HCF solution phase spectra (**Figure 3.5A**) as a reference. The 2115 cm^{-1} peak for the 1 mM HCF solution phase is assigned to the ν(C≡N) vibration mode. The 2044 cm^{-1} peak appears when HCF is adsorbed onto Ag_2S/AuNR. Versus the 2115 cm^{-1} solution phase peak, the adsorbed 2044 cm^{-1} peak is broader and shifts to a lower peak position, thus indicating that HCF is complexing with the surface.

Solution phase HCF is a centrosymmetric molecule and when adsorbed onto the nanorod surface, the symmetry changes and new peaks appear.[263] The interaction with the surface also leads to broadening of the infrared peaks. The adsorption of HCF is further corroborated with the EDX spectra, thus showing Fe adsorption after HCF treatment (**Figure 3.4F**). EDX is a surface-weighted technique and cannot decipher between passive adsorption and complexation between HCF and Ag-chalcogenide. Previous studies also report strong interactions of ferro- and ferricyanide ions adsorbing onto Ag electrodes *via* a Ag-C≡N interaction.[264] At earlier time points and subsequently low surface coverage, the initially adsorbed HCF peak appears at 2044 cm^{-1}. The peak shifts to 2057 cm^{-1} at higher surface coverage. The peak shift as adsorption time increases could suggest a surface concentration-dependent interaction with the Ag_2S/AuNR surface. Hence, there is a strong positive correlation between PA amplitude and HCF concentration (**Figure 3.2B**).

Following the adsorption of HCF, CTAB was flowed over the film to observe any reversible displacement reactions (**Figure 3.5B(ii)**). Positive peaks at 2926 and 2854 cm^{-1} are now observed to increase in intensities and are assigned to CTAB ν(C-H). Interestingly, the 2926 and 2824 cm^{-1} peak more closely resemble solution phase CTAB but are different than the displaced peak positions at 2917 and 2854 cm^{-1} when flowed with HCF. This suggests that the CTAB is forming a multilayer on top of HCF rather than interacting directly with the Ag_2S/AuNR surface, supporting that HCF has a higher affinity to the surface than CTAB. As the CTAB layer grows on top of the HCF, PA enhancement is steadily lost (**Figure 3.15**). A slight decrease in the 2038 cm^{-1} HCF peak is observed and could be due to the desorption of loosely bound HCF. Additionally, the ν(C≡N) peak shape narrowed, and the position shifted from 2057 cm^{-1} to 2038 cm^{-1} when CTAB was flowed over the HCF-adsorbed film. Introducing CTAB into the aqueous flow caused multilayer interactions between HCF and CTAB. When particles are washed via centrifugation

instead of CTAB to remove the adsorbed HCF, the pellet still shows PA enhancement. The supernatant shows no PA contrast (**Figure 3.16**).

When the thin film is desorbed with pure water (**Figure 3.5B(iii)**), there is a drastic decrease in the ν(C-H) 2926 and 2854 cm^{-1} peak intensity indicating that the multilayer CTAB is reversibly adsorbed. HCF also desorbs as noted by the decrease in peak intensities. Peak broadening is also seen suggesting low surface coverage conditions.

Similar analyses can be made with Ag_2Se/AuNR (**Figure 3.17**). When the film is flowed with HCF, the surface-complexed HCF 2049 cm^{-1} peak appears while a loosely bound CTAB is displaced. With the CTAB and water desorption flow streams, HCF related peaks can be seen to decrease, indicating partial desorption. Multilayer reversible CTAB adsorption is observed with the ν(C-H) peak positions resembling solution phase positions and with intensities falling to baseline values. When comparing the adsorbed HCF spectra between Ag_2S/AuNR and Ag_2Se/AuNR, varying surface complexation modes are seen as noted by the HCF peak position and broadening. This suggests that the surface complexation mode is dependent on nanoparticle composition and surface coverage. The slight desorption of HCF from Ag_2Se/AuNRs (27-fold) could explain the lower PA enhancement compared to Ag_2S/AuNRs (42-fold).

Bare AuNRs show minimal adsorption of HCF and CTAB (**Figure 3.18**). When water is finally flowed over the AuNRs, all molecules are completely desorbed, thus suggesting a fully reversible physisorption process. Thus, HCF is directly complexed with the chalcogenide coating and not the core gold nanorod. This explains why AuNRs treated with HCF show no PA enhancement (**Figure 3.11**).

EDX mapping shows a slight preferential adsorption of HCF along the longitudinal edge of the nanoparticle surface (**Figure 3.4F-G**). This could explain why Ag_2S/AuSph show no PA

enhancement compared to coated nanorods (**Figure 3.10**). PA enhancement was specific to HCF (III). 50 μM potassium ferrocyanide (HCF (II)), KO_2, NaCN, NaH, and $KMnO_4$ had no effect on PA signal from Ag_2S/AuNR (**Figure 3.19**).

There are two possible hypotheses for how HCF adsorption causes an increase in the grüneisen parameter (Γ). Γ is a temperature dependent variable. Recently HCF was associated with excess heat production during a redox couple reaction.[265] It is also well known that HCF redox can be triggered by light absorption like the kind used in photoacoustics.[266, 267] Hence, it is possible that HCF adsorption and subsequent light absorption increases the temperature at the shell-HCF interface, resulting in 4-fold Γ enhancement.

Second, there could be enhanced electrostriction due to HCF adsorption. Electrostriction is a material property that results in a rapid shape change in the presence of an externally applied electric field.[268] An external electric field can displace electrons-hole pairs in opposite directions resulting in a bulk volumetric change.[269] Γ is directly proportional to the volumetric thermal expansion coefficient (β, **Equation 3.1**).[270] An increase in β will result in enhanced Γ. In the case of plasmonic nanoparticles, the excitation from the pulsed light source can result in rapid shape changes. PA generated from electrostriction and thermal expansion of the particle would be additive and result in PA enhancement. Usually, the electrostriction forces are negligible and hence excluded from **Equation 3.1**.[271, 272] But others have shown that ferricyanide, chalcogenophosphates, and layered materials can possess enhanced electrostriction properties.[271, 273-275] PA imaging is one of the best ways to characterize both these hypotheses and an independent characterization technique is needed to confirm our findings. Unfortunately, independent confirmation is extremely challenging due to instrument limitations.

3.5 Conclusion

In this work, we report the surprising PA enhancement of silver chalcogenide-coated gold nanorods upon treatment with HCF. HCF treated nanoparticles showed no changes in absorbance but a significant (up to 42-fold) PA enhancement. Ag_2S/AuNRs showed higher PA efficiency compared to Ag_2Se/AuNRs. Ag_2S coated gold nanospheres showed no PA enhancement. The PA enhancement was attributed to a 4-fold increase in the Grüneisen parameter (Γ) after HCF addition. We showed that the Γ enhancement was not due to aggregation, increased absorbance, or crystal phase change of the shell layer. Dynamic in situ interactions between HCF and the silver chalcogenide surfaced revealed the irreversible displacement of CTAB with HCF from the nanoparticle shell surface. Uncoated AuNRs showed minimal HCF adsorption resulting in no Γ enhancement. We include two possible mechanisms for Γ enhancement. First, the localized heating at the shell-HCF interface due to photoinduced HCF redox chemistry. Since Γ is temperature dependent, localized heating results in Γ enhancement. Second, there may be an enhanced electrostriction response due to ferricyanide adsorption on a layered plasmonic nanoparticle surface which increases the volumetric thermal expansion component of Γ.

3.5 Acknowledgements

Chapter 3, in part, has been submitted for publication of the material as it may appear in Photoacoustic enhancement of ferricyanide treated silver chalcogenide coated gold nanorods, 2022, Mantri, Yash; Sit, Izaac; Zhou, Jiajing; Grassian, Vicki H.; Jokerst, Jesse V. The dissertation author was the primary researcher and author of this paper.

3.6 Supplementary information

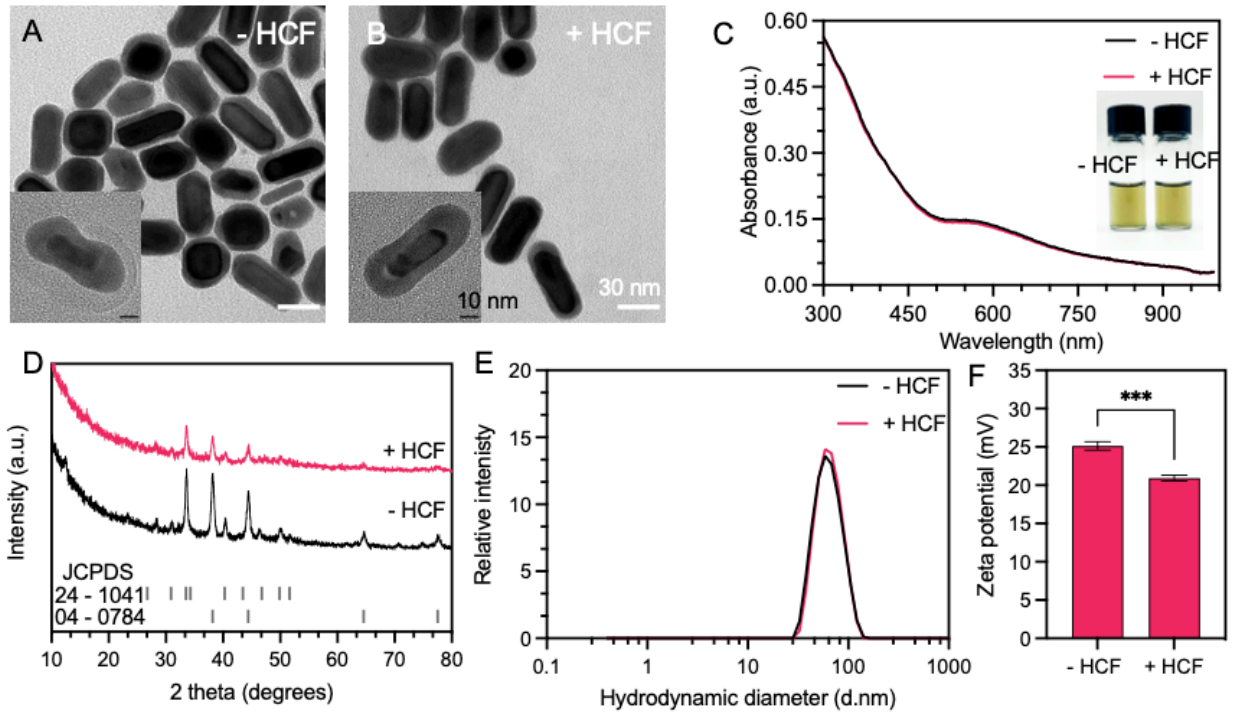

Figure 3. 6 Ag_2Se/AuNR synthesis and characterization before and after HCF treatment.
A-B. TEM and HRTEM show no change in particle morphology, size, and shell thickness on HCF treatment. Scale bars on low- and high-resolution images measures 30 and 10 nm respectively. **C.** Absorption spectra shows no change in LSPR after HCF treatment (Inset: no change in colloidal color). **D**. pXRD analysis shows characteristic peaks for Au and Ag_2Se that are unaffected by HCF addition. **E**. DLS shows no change in particle hydrodynamic diameter after HCF treatment. **F**. Addition of HCF significantly ($p<0.001$) reduces the zeta potential of the particle as negatively charged HCF gets adsorbed onto the particle surface. Error bars represent the standard deviation of six measurements.

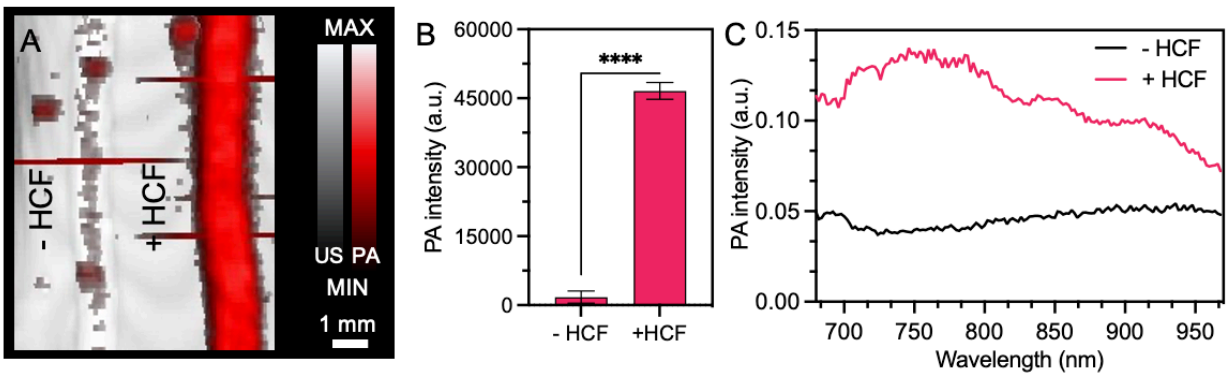

Figure 3. 7 HCF-mediated PA enhancement of Ag_2Se/AuNR.
A-B. 50 µM HCF treatment results in 27-fold PA enhancement. **C**. HCF treated particles show peak PA intensity at 740 nm.

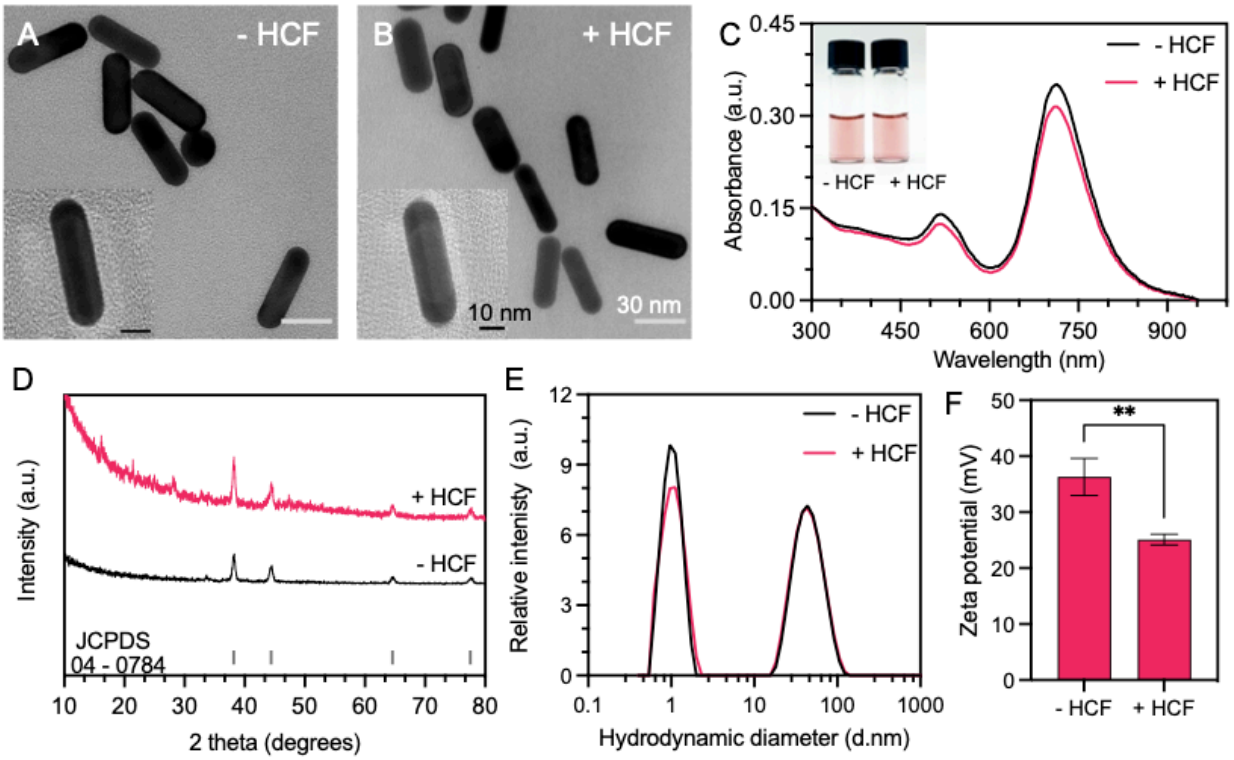

Figure 3. 8 AuNR characterization before and after HCF treatment.
A-B. TEM and HRTEM show no change in particle morphology and aspect ratio on HCF treatment. Scale bars on low- and high-resolution images measures 30 and 10 nm respectively. **C.** Absorption spectra shows no change in LSPR after HCF treatment (Inset: no change in colloidal color). **D**. pXRD analysis shows characteristic peaks for Au that are unaffected by HCF addition. **E**. DLS shows no change in particle hydrodynamic diameter after HCF treatment. **F**. Addition of HCF significantly ($p<0.001$) reduces the zeta potential of the particle as negatively charged HCF gets adsorbed onto the particle surface. Error bars represent the standard deviation of six measurements.

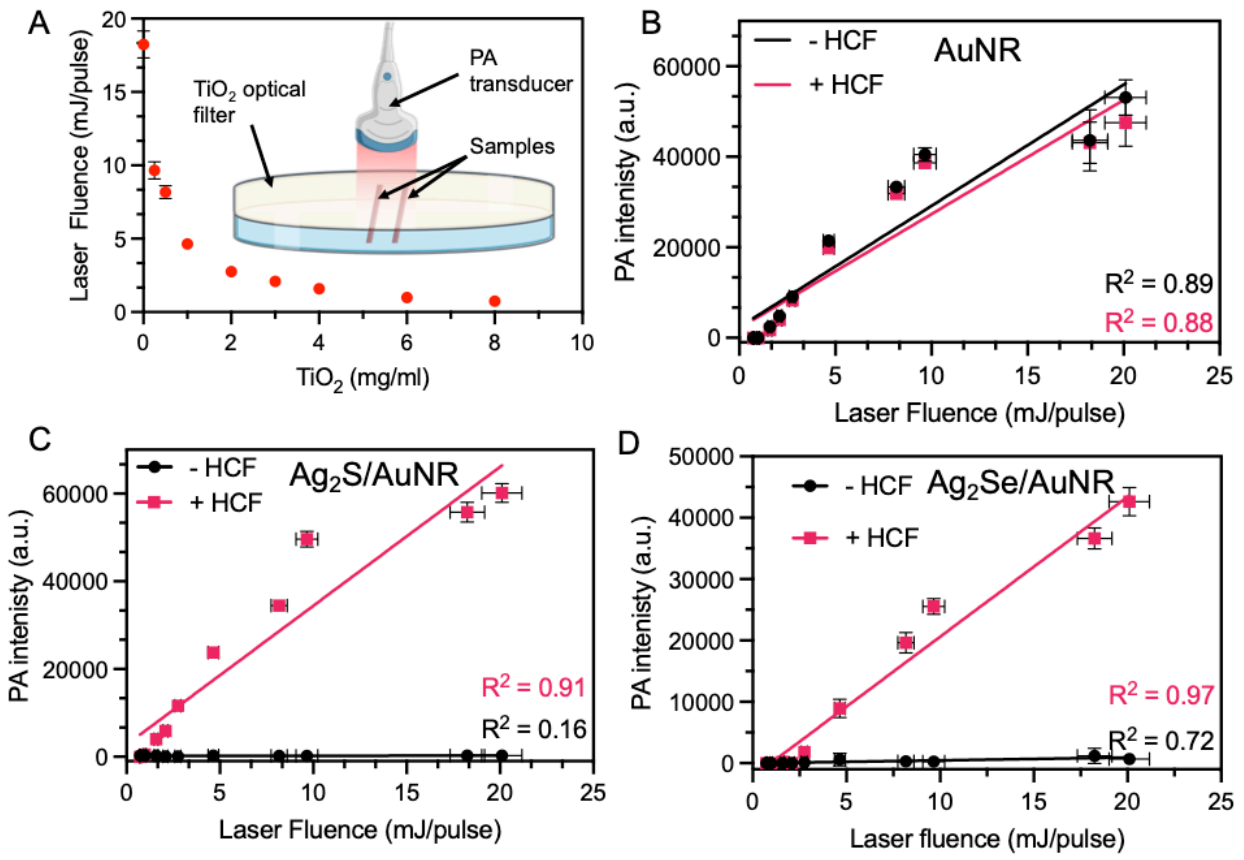

Figure 3. 9 Effect of laser fluence (F) on PA intensity.
A. (Inset)Experimental setup to control laser fluence using a 1 cm thick TiO_2 optical filter placed between the samples and PA transducer. An increase in TiO_2 concentration results in lower fluence for the sample. 0 mg/ml TiO_2 = 18.2 ± 0.9 mJ/pulse and 8 mg/ml TiO_2 = 0.73 ± 0.05 mJ/pulse. **B-D.** Both treated and untreated particles show a linear correlation between PA intensity and laser fluence. Error bars represent standard deviation in 6 ROIs for PA intensity and 3 separate measurements for fluence.

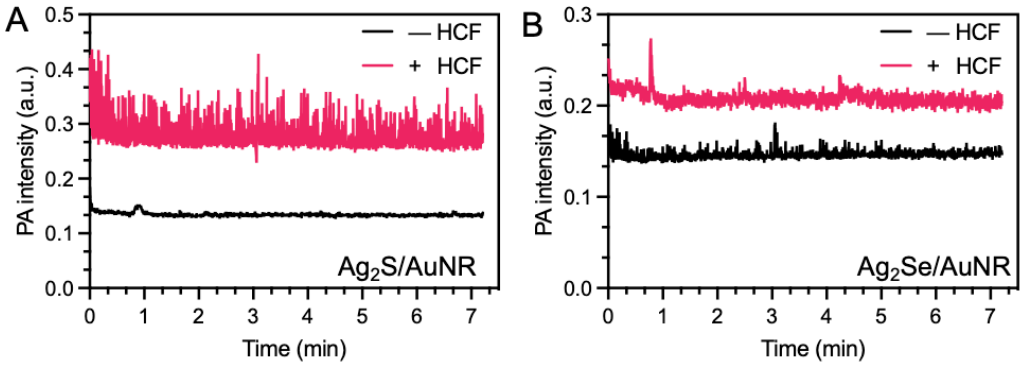

Figure 3. 10 Photostability of HCF treated and untreated particles.
A. Ag_2S/AuNR: Enhanced particles exhibit increased photostability with 6.5% decrease in PA signal after 7 min under the laser (18.2 ± 0.9 mJ/pulse). **B.** Ag_2Se/AuNR: HCF treated particles show a 9% decrease in PA intensity when irradiated for over 7 min with 18 mJ/pulse.

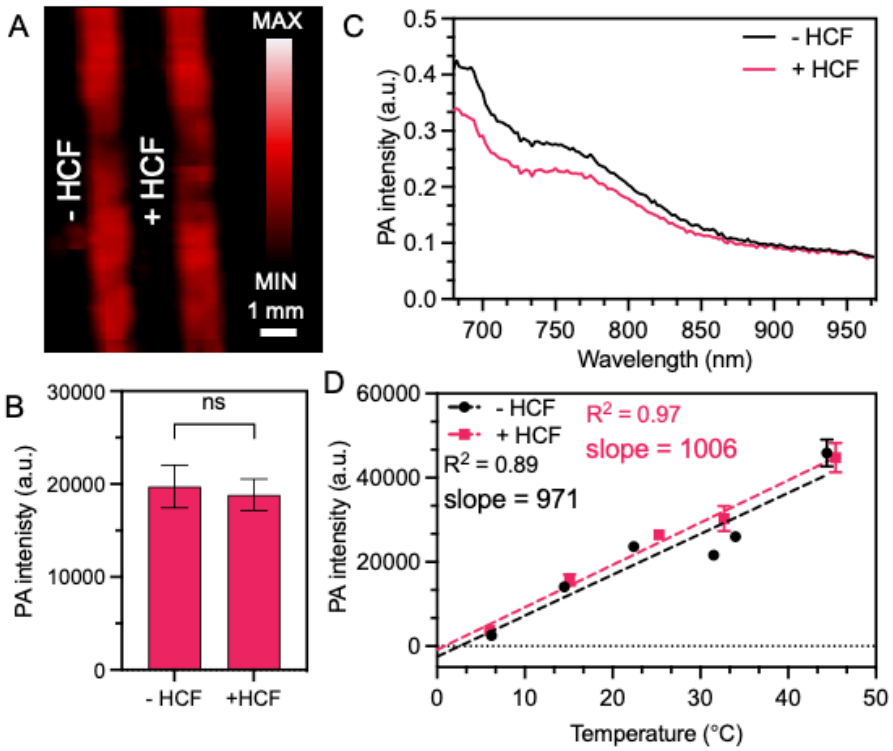

Figure 3. 11 PA characterization of AuNRs with HCF treatment.
A-C. AuNRs showed no PA enhancement after 50 µM HCF treatment. PA spectra showed peak PA intensity at 680 nm although AuNR LSPR was at 710 nm. The blue shift is attributed to rod reshaping under laser illumination. **D.** HCF treatment had no effect on the Grüneisen parameter (slope of PA vs. Temp). A simple linear regression showed zero PA signal at 0.8 ºC and 2.6 ºC with and without HCF addition respectively. The zero signal is expected as thermal expansion coefficient of water is minimum in the 0-4 ºC range.

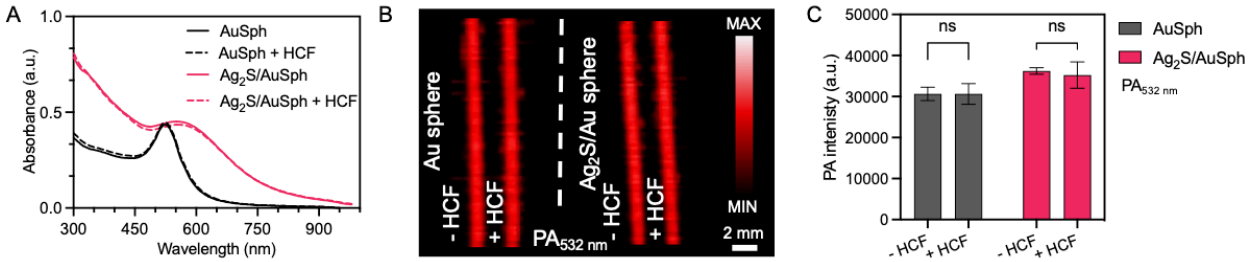

Figure 3. 12 Effect of shape on PA enhancement.
A. Ag_2S coated and uncoated AuSph have similar absorbance at 532 nm. Treatment with HCF causes no change in absorbance like AuNRs. **B-C.** No significant PA enhancement is seen in coated or uncoated AuSph after HCF addition ($p>0.05$). Error bars represent standard deviation in 6 measurements.

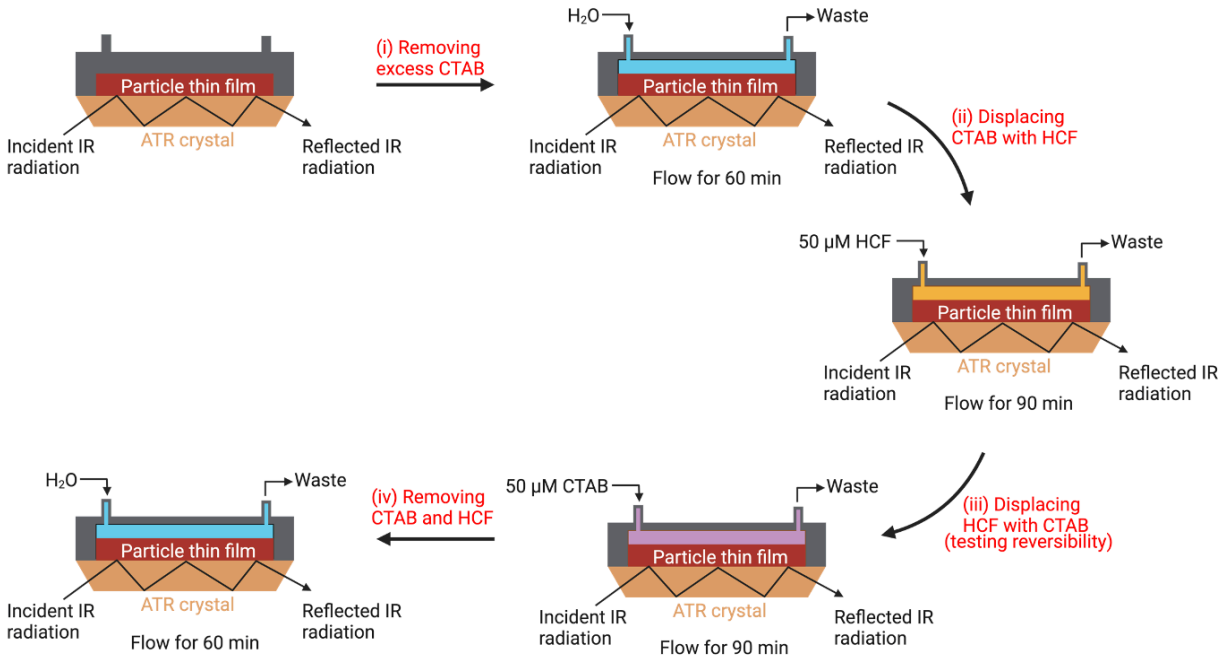

Figure 3. 13 Experimental setup for *in-situ* dynamic ATR-FTIR measurements.
A dry nanoparticle thin film was first created by drop casting 1 mL of a ~27 nM nanoparticle concentration onto the crystal and dried overnight with a continuous dry air purge. (i) For displacement reactions on silver chalcogenide coated-AuNRs, water was flowed at ~1 mL/min for 60 min to remove loose particles followed by a background scan. (ii) Next, 50 µM HCF was flowed over for the film for 90 min and another scan was taken. (iii) Then, 50 µM CTAB was flowed over the thin film for 90 min and another scan was taken. (iv) Finally for desorption, water was flowed over the film for 60 min.

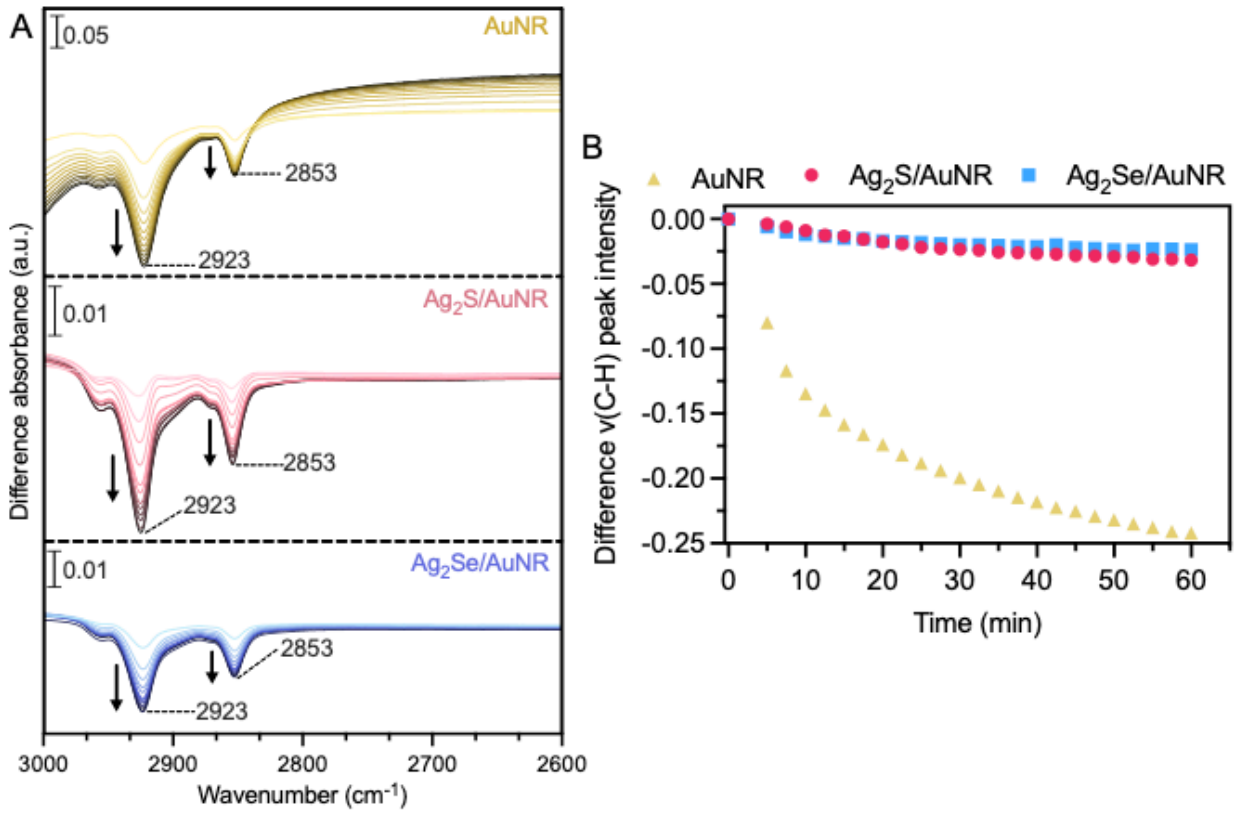

Figure 3. 14 Time dependent ATR-FTIR difference spectra for initial water wash show CTAB desorption.
A. ATR-FTIR spectra of 60 min water wash for AuNR (gold), Ag_2S/AuNR (pink), and Ag_2Se/AuNR (blue) show decrease in ν(C-H) peaks indicating CTAB desorption. Note the larger scale bar for AuNR, suggesting significant removal of CTAB compared to Ag_2S/AuNR and Ag_2Se/AuNR. **B.** Changes in the CTAB ~2923 cm^{-1} ν(C-H) peak intensity.

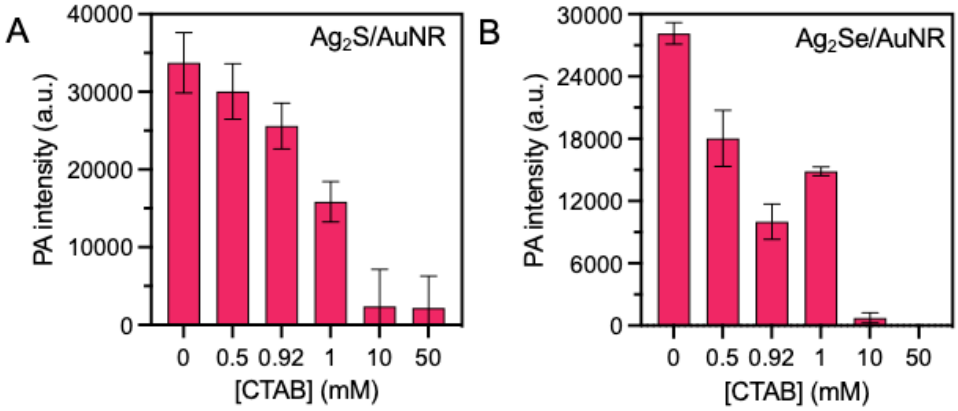

Figure 3. 15 PA enhancement is lost when particles are treated with CTAB after HCF addition.
A-B. Ag_2S/AuNR and Ag_2Se/AuNR show loss of PA enhancement when treated with increasing amounts of CTAB. CTAB was added after particles were enhanced with HCF. Enhancement is lost above the critical micelle concentration for CTAB (0.92 mM).

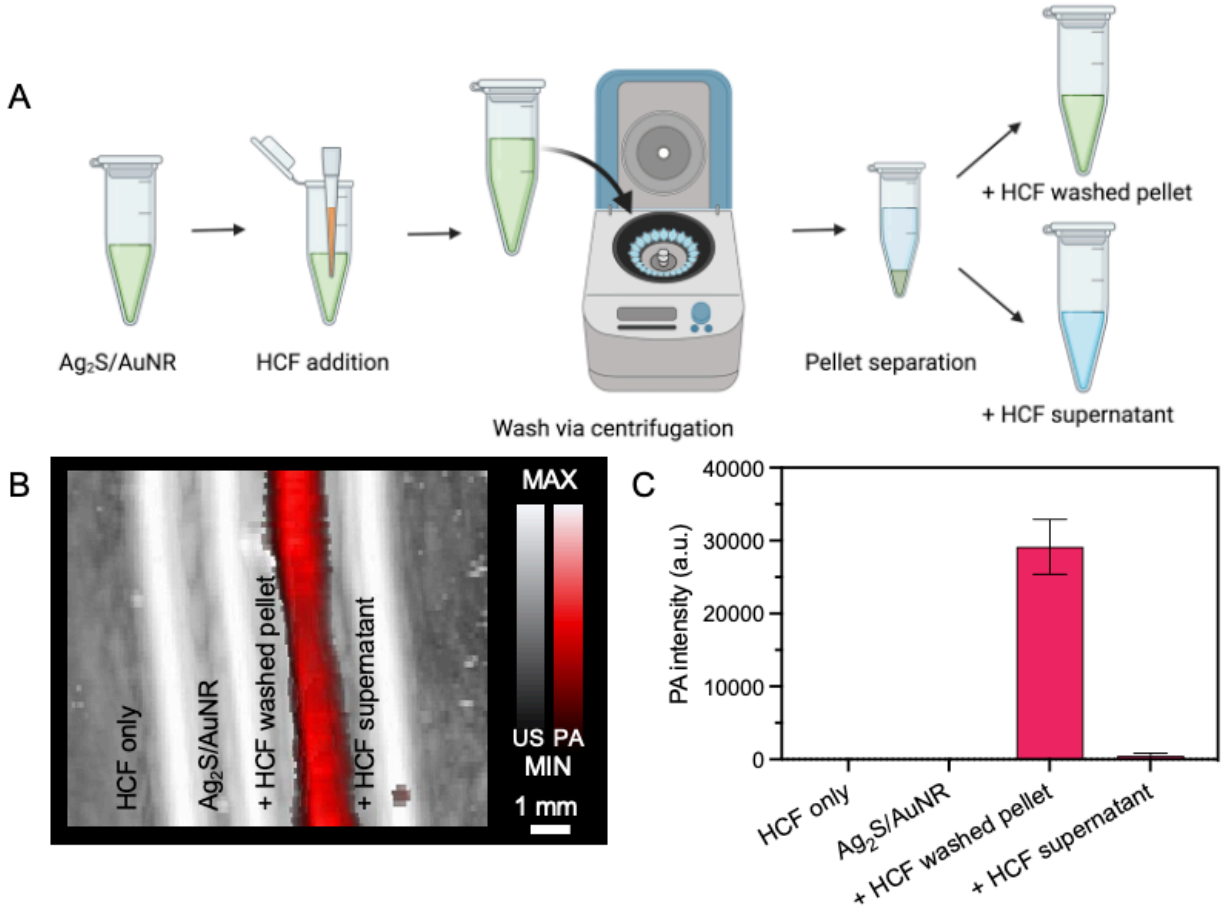

Figure 3. 16 PA enhancement is conserved even after washing.
A. Schematic representation of sample preparation. **B-C**. HCF treated Ag_2S/AuNR were washed via centrifugation and the pellet redispersed in distilled water. Washing and removal of excess HCF had no effect on PA enhancement showing the irreversible surface adsorption of HCF.

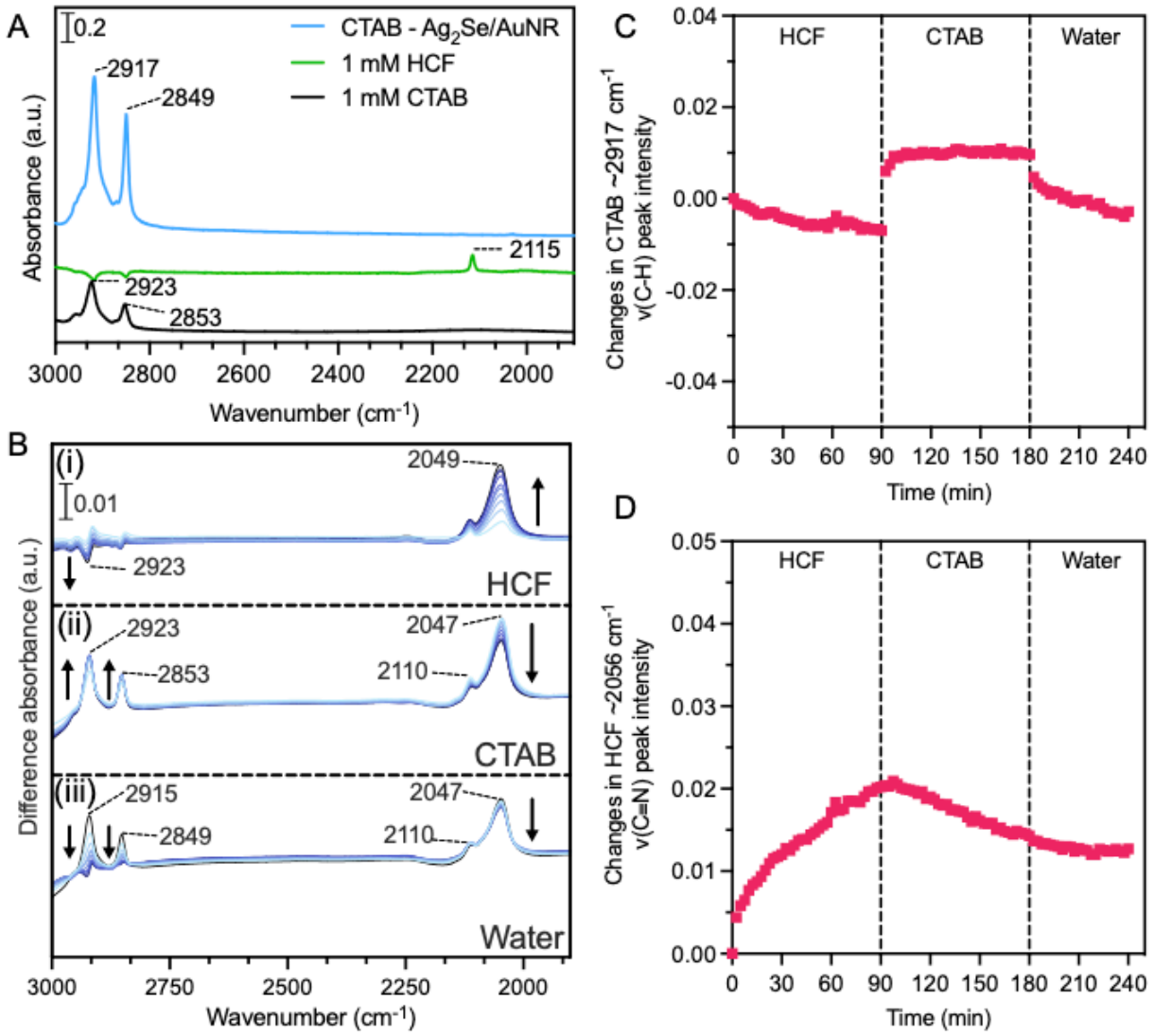

Figure 3. 17 Dynamic *in-situ* ATR-FTIR spectra of Ag_2Se/AuNR on HCF treatment.
A. Reference spectra for dried thin film of CTAB stabilized Ag2Se/AuNR on an AMTIR crystal, 1 mM solution phase HCF and 1 mM solution phase CTAB. **B.** *in-situ* time dependent ATR-FTIR difference spectra for a CTAB stabilized Ag_2Se/AuNR following: **(i)** 50 µM HCF flow adsorption. Increase in the 2049 cm^{-1} ν(C≡N) band with the simultaneous decrease in the 2923 cm^{-1} ν(C-H) bands as a function of time suggesting a displacement of CTAB with HCF. **(ii)** 50 µM CTAB flow adsorption following HCF adsorption. CTAB can partially desorb loosely bound HCF while forming multilayers on directly surface bound HCF as seen by a change in peak intensity as a function of time. **(iii)** water desorption flow. These spectra show the desorption of multilayer CTAB and changes to the surface coordination of adsorbed HCF. Temporal spectra in B are collected every 10 minutes from light to dark coloration. **C.** Changes in the CTAB ~2923 cm^{-1} ν(C-H) peak intensity. **D.** Changes in the HCF 2049 cm^{-1} ν(C≡N) peak intensity.

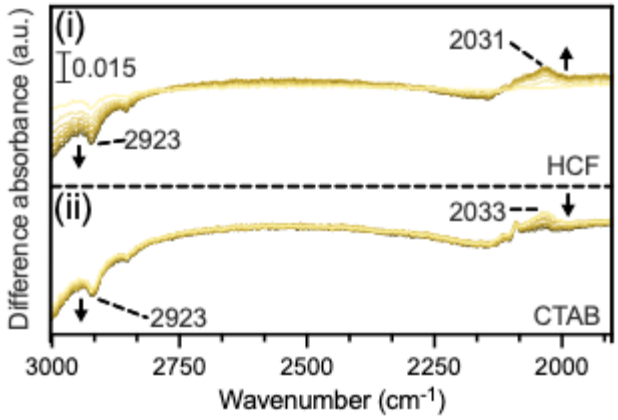

Figure 3. 18 Dynamic *in-situ* ATR-FTIR spectra of AuNR on HCF treatment.
(i) HCF is seen to displace CTAB noted by the positive 2031 cm^{-1} ν(C≡N) peak and negative 2923 cm^{-1} ν(C-H) peak. **(ii)** CTAB is seen to fully desorb HCF noted by the drastic decrease in the 2033 cm^{-1} peak intensity. This suggests that HCF is loosely bound to the AuNR surface and not directly coordinated. Spectra are shown every 10 minutes from light to dark coloration.

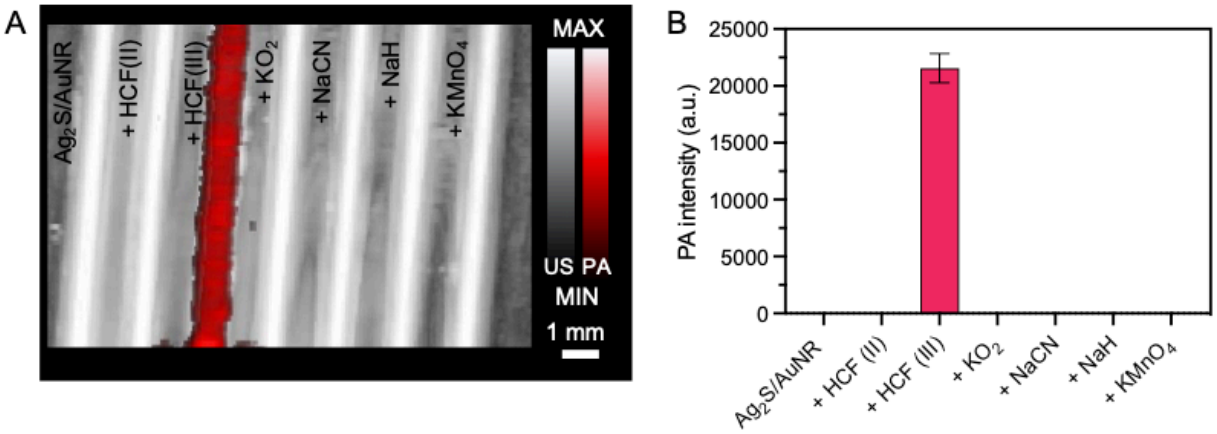

Figure 3. 19 PA enhancement is specific to HCF (III).
A-B. Ag_2S/AuNR treated with 50 µM Potassium ferrocyanide (HCF (II)), KO_2, NaCN, NaH, and $KMnO_4$ show no PA enhancement. The rationale for choosing these molecules was to serve as controls for different redox species.

Chapter 4: Point of care ultrasound as a tool to assess wound size and tissue regeneration after skin grafting

4.1 Abstract

Chronic wounds can be difficult to heal and are often accompanied by pain and discomfort. Multiple skin substitutes or Cellularized/Tissue based skin Products (CTPs) have been used in an attempt to facilitate closure of complex wounds. Allografts from cadaveric sources have been a viable option in achieving such closure. However, early assessment of graft incorporation has been difficult clinically, often with delayed evidence of failure. Visual cues to assess graft integrity have been limited and remain largely superficial at the skin surface. Furthermore, currently used optical imaging techniques can only penetrate a few millimeters deep into tissue. Ultrasound (US) imaging offers a potential solution to address this limitation. This work evaluates the use of US to monitor wound healing and allograft integration. We used a commercially available dual-mode (ultrasound and photoacoustic) scanner operating only in US mode. We compared the reported wound size from the clinic to the measured size using US in 45 patients. Two patients from this cohort received an allogenic skin graft and underwent multiple US scans over a 110-day period. All the data was processed by two independent analysts and one of them was blinded to the study. We measured change in US intensity and wound contraction as a function of time. Our results show a strong correlation (R^2 = 0.81, $p<0.0001$) between clinically and US measured wound sizes. Wound contraction greater than 91% was seen in both patients after skin grafting. An inverse relationship between wound size and US intensity (R^2 = 0.77, $p<0.0001$) showed that the echogenicity of the wound bed increases as healthy cells infiltrate the allograft matrix regenerating and leading to

healthy tissue and reepithelization. This work shows that US can be used to measure wound size and visualize tissue regeneration during the healing process.

4.2 Introduction

Wound healing is one of the most complex processes in the human body.[276] An ideally healed wound is an area that has been restored to normal anatomy, structure, functionality, and appearance after an injury.[276] Wounds can be classified into two broad categories, acute and chronic depending on underlying cause and how long they take to heal. An acute wound is a sudden injury to the skin that heals predictively within 8-12 weeks.[277] A chronic wound occurs due to a prolonged inflammatory response during healing which is difficult to heal, lasts longer than 12 weeks, and frequently reoccurs.[277] Poor perfusion into the wound site can significantly impair wound healing.[278] Access to expert wound care centers can promote evidence based wound care, leading to 45% faster healing rates and a more efficient use of health resources.[279, 280]

There are several wound treatment modalities. Standard wound care elements include serial debridement, compression therapy, judicious use of various wound dressings to control moisture balance, along with antimicrobial efforts to optimize the wound bed for successful healing.[281] These efforts also include minimizing pressure forces while optimizing vascular status to affected limb. Several additional advance adjunctive modalities exist. Negative pressure wound therapy device, adjunctive Hyperbaric Oxygen therapy, and cellularized/tissue based skin products (CTPs) are viable options. [282] CTPs or bioengineered skin grafts made of synthetic and/or biological materials are often used as aids to promote wound closure and restore skin function.[276, 283] The allograft skin substitutes provide a scaffold to the open wound defect. This scaffold will then become colonized by host immune cells as the healing cascade progresses. Clinicians often refer to the process of graft integration with the recipient area as “taking”. Healthy host cells infiltrate

the allograft matrix. These cells then differentiate into regenerated tissue ultimately integrating with surrounding healthy host tissue in a seamless fashion. Allograft take is typically dependent on the integrity of a healthy granular host wound base .[284, 285] A negative immune response, infection, excessive exudation, and compromised hemostasis can all endanger the survival of the allograft. Obstruction of adherence to granulating tissue and penetration of neo-capillaries can occur.[284, 286] Currently, clinicians rely on clinical experience and visual cues such as graft color, odor, texture, edema, drainage and necrosis to monitor the graft and the underlying wound health.[287, 288] However, visual inspection is limited to the skin surface whereas underlined edema and graft detachment can go unnoticed. Furthermore, studies have shown extensive heterogeneity in wound evaluations between different healthcare professionals. [289, 290] One study compared how nurses and clinicians evaluated one diabetic ulcer—there was significant discordance in wound evaluation with 62.5% describing the wound as reddened in contrast to 37.5% reporting the same wound as bland. Similar discordance was noted in their ability to quantify wound exudate with 62.5% describing exudate as moderate, 25% reporting no exudate, and 12.5% indicating that exudate could not be specified.[289] This underscores the necessity for a more objective wound assessment system that avoids this such observational variation.

Imaging is an indispensable tool to see what the eye cannot.[291] Digital imaging using standard cameras has helped size wounds more accurately and follow clinical progress after grafting.[292, 293] Ultraviolet light can visualize hidden wound features and has helped the field of forensics.[294] Spectral imaging and two-photon fluorescence microscopy have shown promise in visualizing vasculature and measure oxygen saturation in animal models; both are key parameters for optimal graft health.[295-298] Fluorescence imaging has also been used to detect bacterial infection in chronic wounds.[299] Unfortunately, all these techniques are optical and thus are limited by the

penetration depth of light through tissue (approx. 100 μm) while chronic wounds can exist much deeper (up to 2 cm).[289, 300] X-ray or magnetic resonance imaging (MRI) can be used to look deeper into diseased tissue but these either lack soft tissue contrast and risk radiation exposure (X-Ray) or are expensive, cannot be point-of-care, and lack resolution (MRI).

Ultrasound (US) imaging is a unique imaging modality that solves all these major limitations. It is a quick, inexpensive, non-radiative, non-invasive, and point-of-care imaging modality that can look deep into soft tissue (up to 10 cm).[301, 302] The use of ultrasound as a therapeutic tool to aid debridement and promote healing has been widely reported but there are very few reports of US imaging being used to monitor wound healing.[303-305] A recent small case series showed that US, doppler, and elastography could be used to determine wound morphology, biomechanics and proximity to other anatomical structures like bone and tendon.[306] Another case study in a 46-year old female with a stage IV sacral pressure ulcer showed that multiple two-dimensional US images could be reconstructed for three-dimensional visualization of the ulcer.[307] Photoacoustic imaging and high-resolution harmonic US has also been used to stage and track healing of pressure ulcers and burn wounds in animal models.[308, 309] Although these studies depict the advantages of US imaging like deeper imaging and elastography, a longitudinal human clinical study monitoring wound healing has not yet been reported. The ability to monitor a skin graft as it integrates would have high clinical significance and allow clinicians to make more informed therapeutic decisions. This work aims to evaluate the use of US to monitor wound healing and allograft integration.

4.3 Materials and methods

4.3.1 Patients

This study was approved by the Human Research Protections Program at the University of California San Diego (IRB #191998 and H191539X). Informed written consent from each patient was acquired before scanning. The inclusion criteria were as follows: (i) patients with ulcers not more than 15 cm^2 in area. ii) patients 18 years or older and be able to provide consent. Exclusion criteria included i) Patients with a blood-borne pathogen ii) patients with other lesions (e.g., Melanomas) at the wound site. iii) patients with orthopedic implants patients presenting with wounds between digits or in the pubic region; 63 patients (65 wounds) were recruited for this study. **Table 4.1** describes the patient demographic distribution. All patients were imaged.

Two patients (Patients A and B) who received allogenic skin grafts underwent multiple follow-up scans over a period of 110 days. Patient A was a 77-year-old non-diabetic female with a history of hypothyroidism. Patient A presented with an open, chronic, post-operative left knee wound with tendon involvement and chronic venous hypertension on both sides. Patient A was first scanned 103 days after presentation followed by 13 follow-up scans over a 110-day period. Patient B was a 33-year-old non-diabetic male with a history of renal transplant. Patient B presented with a left, anterior, lower limb, posttraumatic ulcer with chronic venous hypertension on the left side. Patient B was first scanned 33-days after presentation followed by 10 follow-up scans over a 106-day period.

This study did not involve any additional visits and was performed during a regularly scheduled wound care visit. The frequency of visit was independently decided by the wound specialist (CA) depending on the patient's needs. The wound site was prepared by removing any dressings and cleaning with sterile saline prior to scanning. Neighboring tissue was further cleaned using alcohol swabs to prevent infection. A photograph with a wound ruler was also taken to

correctly size the wound surface. To prevent cross contamination and infections, we used a new sterile CIV-Flex™ transducer cover for every scan (#921191 from AliMed Inc., Dedham, MA, USA).

4.3.2 Ultrasound imaging

We used a commercially available LED-based photoacoustic/ultrasound imaging system (AcousticX from CYBERDYNE Inc. (Tsukuba, Japan)).[257] In this study, we only used the ultrasound mode. The ultrasound transducer has 128 linearly arranged elements operating with a central frequency of 7 MHz, bandwidth of 80.9% and field of view of 4 cm. Sterile US gel (Aquasonic 100, Parker Laboratories Inc., Fairfield, NJ, USA) and a custom hydrophobic gel pad from CYBERDYNE INC. (Tsukuba, Japan) was used for US coupling between the transducer and skin surface. All US images were acquired at 30 frames per second.

Wounds smaller than 5 cm in length (Patient A) were scanned in a single sweep from inferior healthy tissue over the wound to superior healthy tissue. From these scans, we selected representative frames for inferior healthy tissue, two wound sites (site I and ii), and superior healthy tissue. For large wounds (Patient B), we selected three wounded sites at discrete distances from the inferior wound edge and tracked wound progression over time (**Fig 1A**). Inferior and superior sites to the wound were used as healthy controls. To monitor tissue regeneration, we measured changes in US intensity (mean gray value) and change in wound size as a function of time. All the images were acquired by YM only. It is important to note that all US scans were performed by hand. Thus, it is impossible to perfectly match US frames from the same site over multiple imaging sessions. To reduce the effects of this limitation, we matched the underlying bone morphology to compare similar spots over time. Patients with skin grafts went through the same imaging protocol with no added steps.

4.3.3 Image processing

All US frames were reconstructed and visualized using the custom software built for the AcousticX photoacoustic imaging system developed by CYBERDYNE Inc. (Tsukuba, Japan) version 2.00.10. B-mode, coronal cross-section images were exported as 8-bit gray scale images. The images were further processed to measure wound width, area, and US intensity using Fiji an ImageJ extension version 2.1.0/1.53c.[310] Data was plotted using Prism9 version 9.0.0. All measurements were made using custom region of interest (ROI) analysis for individual frames. Drawing ROIs by hand can be very subjective. Hence, all image quantification was independently confirmed by two analysts (YM and JT). JT was blinded to the study and only received B-mode US images to analyze the data.

To corroborate our method with the current gold standard eye measurements we compared reported wound size with size measured with US imaging. The reported wound size was provided by CA and his nursing team and was recorded as part of standard care. The wound width under US was measured using custom ROI analysis to outline the wound on a single frame. Wound width was defined as the widest region within the wound ROI (**Figure 4.1B**).

We quantified changes in US intensity over time in a constant ROI. A custom ROI (outline of wound site) was drawn for Patient A and B on day 1 and the US intensity within that ROI was tracked over time. Maintaining a constant ROI allows us to quantify tissue regeneration as the graft integrates into the wound bed. To further compare US intensity between wounded and healthy tissue, a dynamic baseline US intensity for healthy tissue was measured. We measured the mean gray value and its standard deviation (0.5 cm x 0.5 cm ROI) in two frames representing inferior and superior healthy tissue, for each time point. The healthy window was defined within one

standard deviation of the dynamic baseline. US intensities falling under and over this window were considered as wound and scar tissue respectively.

Finally, we monitored change in wound area under the skin graft. Custom ROIs were drawn for individual sites at each imaging time point. An area was considered to be a wound if its US intensity was significantly below the healthy window defined above.

4.3.4 Statistical testing

A Bland-Altman analysis was used to look for bias between clinically reported wound (gold standard) and US measured wound width. A mean bias more that 0.06 cm would be considered clinically significant as the lateral resolution of the US transducer ranges from 0.05-0.06 cm.[257]

To reduce the subjective nature of ROI-based analysis two independent analysts, YM and JT processed all the images. JT was blinded to the study. A Bland-Altman analysis was used to look for systemic bias between two independent analysis of the same images. For US intensity measurements a mean bias above 17 gray scale values (standard deviation in healthy tissue) would be considered clinically significant. For wound area measurements, a mean bias greater than 5% of the largest wound size would be considered clinically significant.

4.4 Results

Figure 4.1 A shows a typical US scan over a wound site. We show that US imaging can be used to reliably size wounds only limited by the width of the transducer. Skin graft integration, tissue regeneration, and changes in wound size can be easily visualized and quantified using US, which is not possible by eye. We also show that there is a significant negative correlation (R^2 = 0.77, $p<0.0001$) between wound size and US intensity.

Table 4. 1 Patient demographic distribution.

Category	Distribution
Age (mean ± standard deviation)	66.9 ± 14.6
Male/Female	31/32
Diabetic/Non-diabetic	19/44
Chronic venous hypertension (Yes/No)	37/26

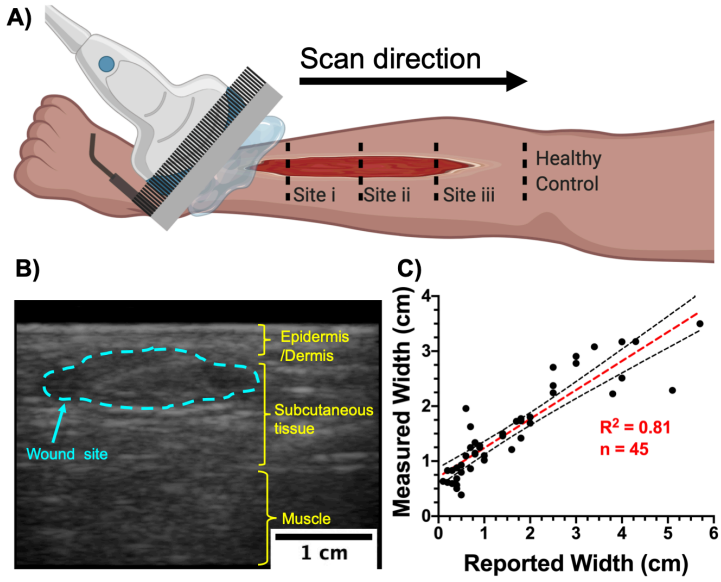

Figure 4. 1 Ultrasound imaging setup and wound width measurement.
A) Schematic representation of a typical ultrasound scan over a wound site. Small wounds (<5 cm in length) were scanned in one sweep from inferior to superior healthy tissue. Large wounds were imaged at discrete distances from the inferior wound edge. Superior and inferior tissue from the wound edge were considered as healthy controls. **B)** A typical B-mode US image showing coronal cross section of the lower limb. Wound width was measured at its widest point within the wound site (blue dotted line). **C)** Comparison between reported wound width at the point-of-care and measured wound width using US (n = 45) showed strong correlation ($R^2 = 0.81$, $p<0.0001$) between the gold standard and our method. Black dotted lines represent 95% confidence intervals.

4.4.1 Wound dimensions

Of the cohort of 63 patients with 65 wound sites, 20 wounds could not be sized with US: 15 wounds did not have a reported wound size from the clinic and were excluded; five wounds were located in regions with high curvature such as the lateral side of the toe or ankle, which makes US coupling difficult in these regions with a linear array transducer. Hence, 45 wounds were used to compare reported wound size with the US measured size. **Figure 4.1C** shows that there is a

strong correlation ($R^2 = 0.81$, $p<0.0001$) between reported and measured wound widths. A Bland-Altman analysis was used to check for any bias between the gold standard eye measurements and our US imaging technique (**Figure 4.6**). A calculated mean bias of -0.05 cm rejected our null hypothesis of clinical significance above 0.06 cm.

4.4.2 Wound regeneration after skin grafting

Figure 4.2 A-C depicts the wound progression and **Figure 4.2 D** shows the imaging and intervention/treatment timeline for patient A. **Figure 4.2 E-G** depicts the wound progression and **Figure 4.2 H** shows the imaging and intervention/treatment timeline for patient B.

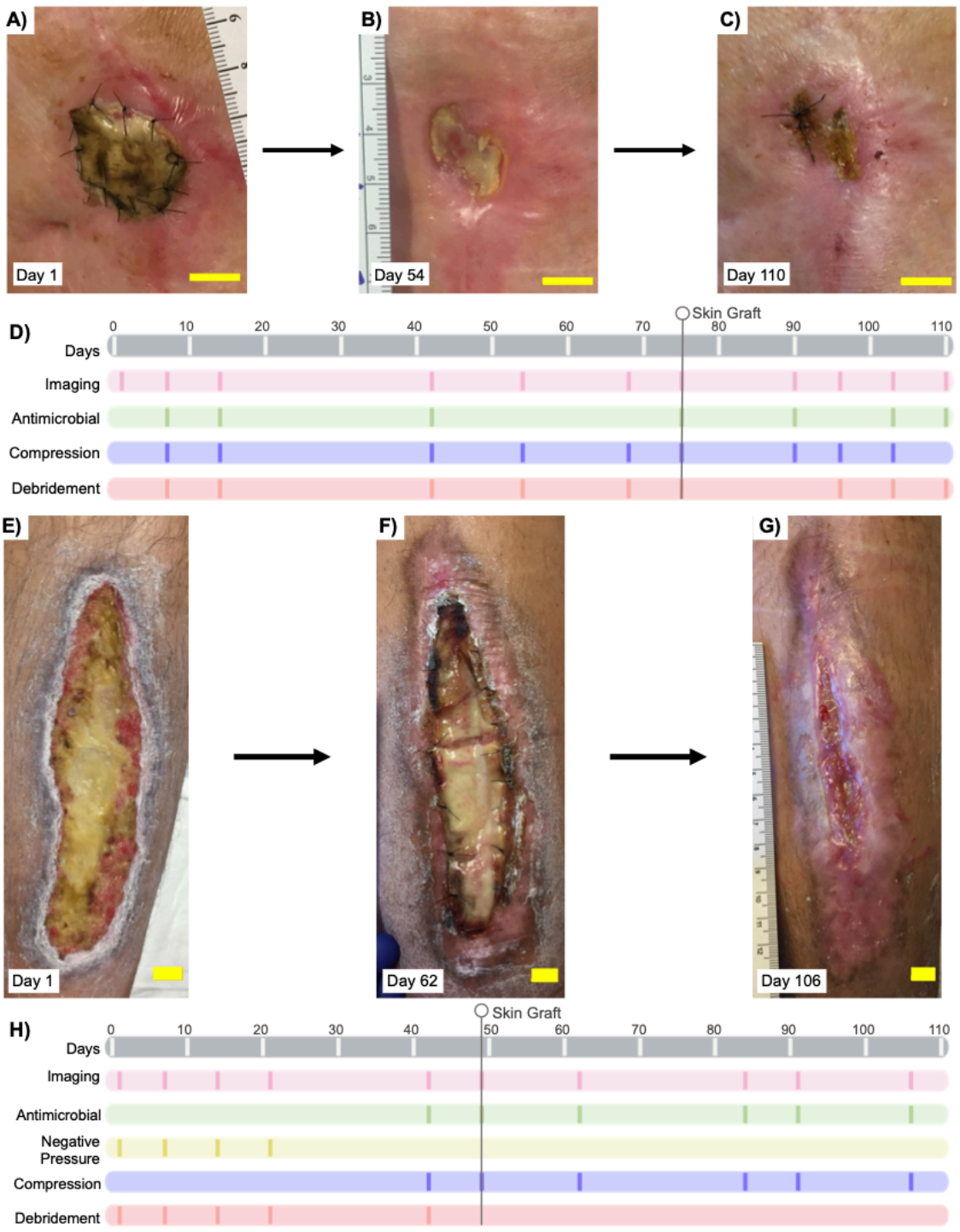

Figure 4. 2 Ultrasound imaging setup and wound width measurement.
A-C) Photographic progression of the wound site in Patient A, a 77-year-old female with a chronic left knee wound. **D)** Study and treatment timeline for Patient A, 13 scans over a 110-day period. Patient A received two skin grafts, 28 days before and 75 days after the start of this study. **E-G)** Photographic progression of the wound site in Patient B, a 33-year-old male with a chronic, left lower limb wound. **H)** Study and treatment timeline for Patient B, 10 scans over a 106-day period. Patient B received a skin graft 49 days into the study. All scale bars are 2 cm.

Patient A

Patient A had a left knee ulceration who underwent 13 US scans over 110-day-scan. Patient A received a human cadaver-derived, acellular dermal matrix (AlloDerm, Lifecell, Branchburg, NJ) skin graft 28 days prior to the first scan. A second tissue matrix allograft composed of dehydrated human amnion/chorion membrane (EpiFix, MiMedx, Marietta GA) was used 75-days after the first scan. **Figure 4.7 and 4.8** show the visual and US scan progression over two wounds and one healthy site. Imaging sites are marked i, ii, and healthy from inferior-superior regions. Wound pictures (**Figure 4.2 A-C**) show wound contraction and skin graft integration at the surface over time. An increase in tissue echogenicity is seen at both sites i and ii indicative of skin graft integration (**Figure 4.7**). The superior healthy control tissue remains unchanged over the study period.

Figure 4.3 C-F quantifies the US data for Patient A. The dynamic baseline for healthy tissue was measured over 13 independent scans. (73.5 ± 12.9 (unique for patient A)). Changes in US intensity over time for site i and ii showed that it took 90 days for site i and 96 days for site ii to achieve gray scale values similar to healthy tissue (**Figure 4.3 C and E**). Wound size under the skin graft showed varied rates of contraction for both sites. Site i showed an 89.2% and site ii showed a 96.0% reduction in size over 110 days (**Figure 4.3 D and F**). Wound contraction was slowest between days 14-68 which is consistent with the physician notes reporting slow improvements and signs of edema during the same period. Interestingly, wound contraction was fastest between days 68-90 which was also noted by the attending doctor.

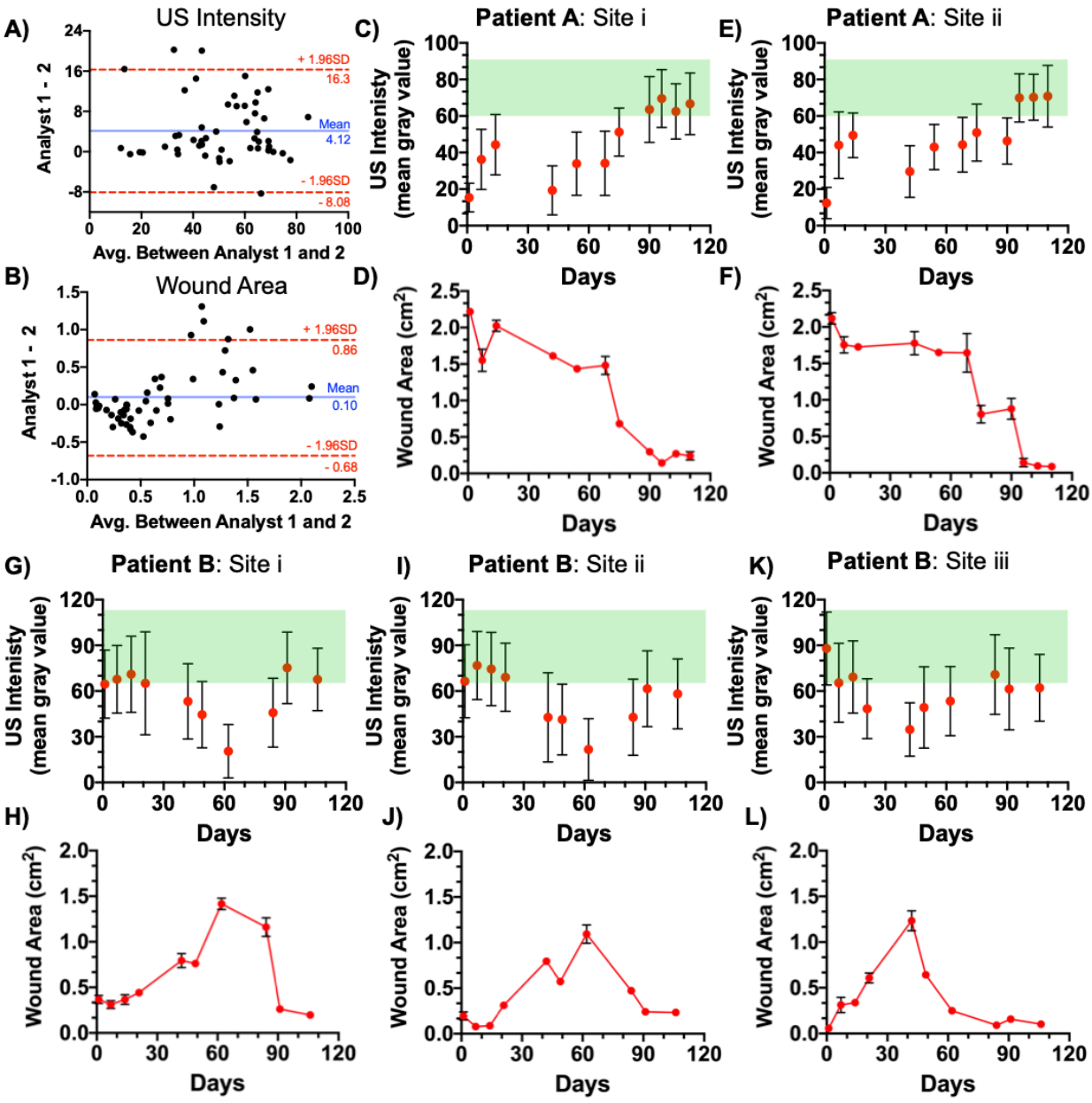

Figure 4. 3 Ultrasound imaging setup and wound width measurement.
A-B) Bland-Altman analysis between measurements made by two independent analysts using the same set of images. Statistical analysis of both US intensity (**A**) and wound area (**B**) showed no significant bias between the two analysts. **C-F)** Change in US intensity and wound area for patient A, sites i and ii. Site i and ii showed an 89.2% and 96.0% reduction in size respectively. **(G-L)** Change in US intensity and wound size for patient B, sites i, ii and iii showing an 86.1%, 78.6% and 91.7% contraction respectively. Error bars in panels C, E, G, I, and K, represent standard deviation of mean gray value in a single ROI. Error bars in panels D, F, H, J, and L represent standard deviation of area measured using 3 US frames.

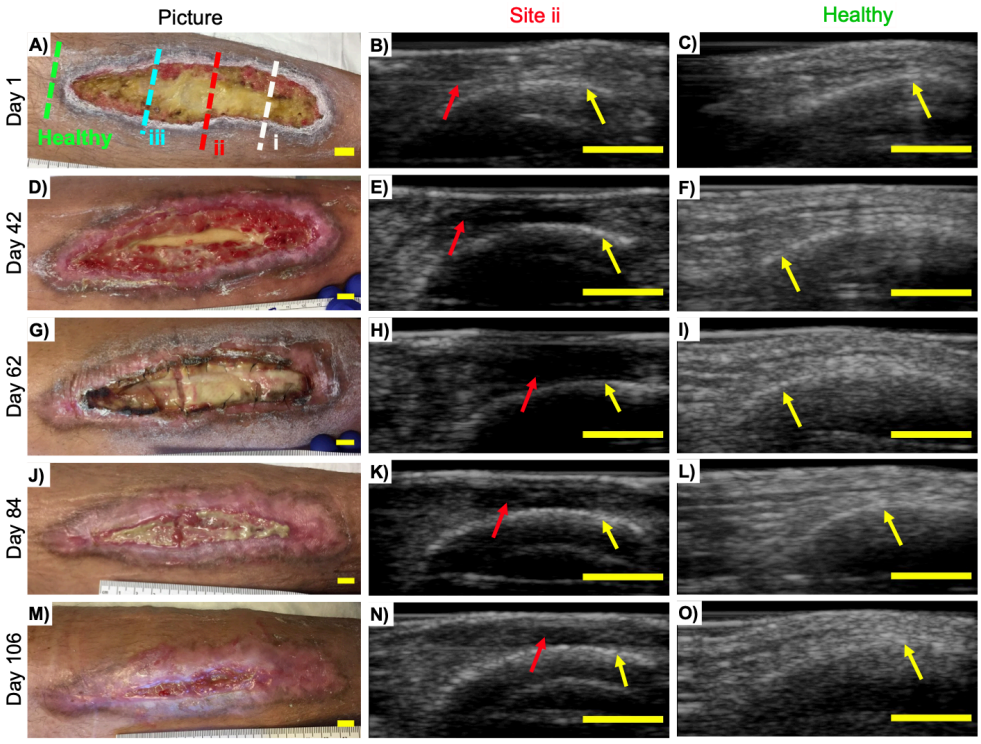

Figure 4. 4 Monitoring wound progression using ultrasound.
Patient B was a 33-year-old male with an anterior lower limb wound who received an allogenic skin graft 49 days into the study. Photographs and US images from Site ii (red dotted line) and superior healthy tissue (green dotted line) from **A-C)** Day 1, **D-F)** Day 42 **G-I),** Day 62, **J-L)** Day 84, and **M-O)** Day 106. Signs of tissue loss (**B**) can be seen using US while not visible to the eye (**A**). An increase in wound size, and hypoechoic regions were observed (**B, E, and H**) over the first 62 days indicating tissue loss even though skin grafting was done on day 49. An increase in echogenicity indicating tissue regeneration and wound contraction can be seen between days 62-106 (**K and N**). The ability to monitor tissue loss and regeneration under a skin graft between days 49-62 and 62-106 respectively, shows the main power of imaging over current methods. Superior healthy control tissue (green dotted line) remains fairly unremarkable and unchanged over the same time period. Red arrows show wound site, yellow arrows point to the tibia. All scale bars are 1 cm.

Patient B

Patient B was a 33-year-old male with an anterior, lower left limb ulceration who underwent 10 US scans over a 106-day period. Patient B received a human cadaver-derived, acellular dermal matrix (AlloDerm, Lifecell, Branchburg, NJ) skin graft 49 days after the first scan. We monitored wound progression at three wound sites i, ii, and iii (inferior, medial, and superior, respectively). **Figure 4.4** shows the differences between wound and healthy tissue while

focusing on site ii and superior healthy control only. Annotated images on site i and iii can be found in the supplementary section (**Figure 4.9 and 4.10**).

The average healthy gray value measured over 10 separate scans was 90.4 ± 21.5 (unique for patient B). All wound sites showed an increase in wound size and loss of US signal until skin grafting followed by a tissue regeneration and wound contraction period (**Figure 4.9**). Healthy control tissue remained unchanged over the same time period. Sites i and ii responded differently compared to site iii (**Figure 4.3G-L**). Between days 1-62, the wound area at site i increased from 0.37 cm^2 to 1.42 cm^2 while Site ii increased from 0.20 cm^2 to 1.10 cm^2. Both sites i and ii showed an increase in wound size and tissue loss up to 62 days into the study even though patient B was skin grafted on day 49 (**Figure 4.3H and J**). Site iii responded to treatment at a different rate. Wound area at site iii increased from 0.05 cm^2 to 1.23 cm^2 within the first 42 days followed by a healing period. By the end of the study, sites i, ii, and iii showed an 86.1%, 78.6%, and 91.7% contraction respectively. Photographic pictures clearly show that Patient B's wound had not completely healed by the end of the study (**Figure 4.4M**). Incomplete healing can be seen when US intensity was monitored over time (**Figure 4.3G-K**). The measured US intensities approach the healthy window but do not show complete regeneration after 110 days of treatment.

A plot of wound area vs. US intensity revealed an inverse relationship between the two variables with $R^2 = 0.77$ and 0.72 for patients A and B, respectively. A large wound with less tissue shows low US signal while a small wound with regenerated tissue showed high US signal (**Figure 4.5**).

All data quantification was done by two independent analysts (YM and JT). JT was blinded to the study while YM acquired and analyzed all the data. Bland-Altman analysis revealed no significant bias between the two analysts. For US intensity measurements, a mean bias of 4.12

gray values between the two analysts, rejected our null hypothesis of clinical significance above 17 gray values (standard deviation in healthy tissue). For wound area measurements, a mean bias of 0.10 cm^2 (4.4% of largest measured wound size) rejected our null hypothesis of clinical significance above 5% of the largest measured area.

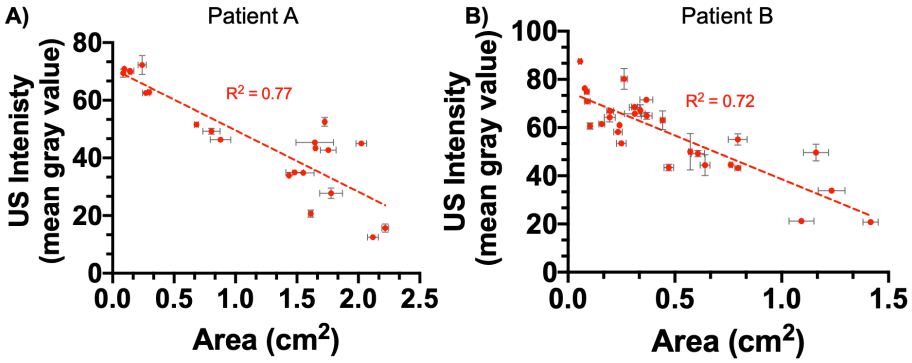

Figure 4. 5 Relationship between wound size and US intensity.
Wound size is negatively correlated to US intensity for both **A)** Patient A ($R^2 = 0.77$, $p<0.0001$) and **B)** Patient B ($R^2 = 0.72$, $p<0.0001$). As the skin graft takes, wound size reduces as healthy cells infiltrate the graft matrix. This infiltration results in tissue regeneration and an increase in US intensity. Error bars represent standard error of mean between three US frames.

4.5 Discussion

The fast, inexpensive, reliable, and pain free characteristics of point-of-care US imaging make it an ideal modality to monitor wound progression. Currently, wounds are sized by eye using a wound ruler as reference. Although more advanced sizing protocols using high definition cameras using complex edge detection and neural networks have been reported, their limited penetration into tissue makes depth measurements difficult.[311-313] Furthermore wounds may prematurely contract at the surface level only ahead of a voluminous deeper cavity defect.[314] This dimension is often neglected though it may further explain aberrant wound healing delays or cause of wound deterioration. The ability of US to non-invasively image under the skin surface make it an ideal imaging modality to solve such limitations. **Figure 4.1C** shows that wound width measured using US imaging has strong correlation ($R^2 = 0.81$) with the reported eye measured values. The Bland-Altman analysis also showed no clinically significant difference between

reported and measured values (**Figure 4.6**). One limitation is wounds above 4 cm in width are consistently undersized. This is because the US transducer used in this study has 128-elements each measuring 3.5 mm long with a pitch of 0.3 mm, giving it a lateral field of view of ~ 4 cm.[257] US imaging has value at estimating wound depth, but these are usually difficult to measure by eye and hence are rarely reported.

Tissue loss or edema accumulation results in hypoechoic regions on US images.[315, 316] On the other hand, scar tissue and edema reduction through use of compression modalities results in hyperechoic regions.[317] Patients have unique soft tissue density and collagen arrangements giving them unique baseline acoustic properties. It is important to measure healthy tissue US intensity separately for each case to distinguish between diseased, healthy, and scar tissue. With skin grafts, the ideal outcome is to restore anatomical continuity along with functionality while minimizing scarring. US imaging is an effective tool to visualize tissue regeneration because US intensity increases as the wound heals. This phenomenon is clearly visible with both patients A and B. **Figure 4.3** shows the change in US intensity and wound size over time. It is interesting to note an inverse relationship between wound size and US intensity for both patients (**Figure 4.5**). In both patients, the corresponding US intensity increases whenever wound size reduces. This is because healthy cells infiltrate into the graft matrix regenerating healthy tissue as the skin graft takes; this in turn increases US signal. Skin grafting did not lead to scar formation because the US intensity of regenerated tissue stayed within the defined healthy tissue window (**Figure 4.3 C, E, G, I, and K**). A high collagen orientation index in scar and keloid tissue leads to hyper-echogenicity under US imaging.[318, 319]

Sometimes wounds deteriorate secondary to a deeper unhealed voluminous defect. This defect often collects fluid and may evolve into a seroma or an abscess. [320] Such a defect is

particularly difficult to predict and visualize with current methods at the bedside. Therefore, visual clinical cues such as erythema, swelling, fluctuance and/or presence of pain can be used to predict tissue health under the skin.[288] Ultrasound imaging is especially effective in providing insight into deeper wound elements. The real time, high-resolution, high-depth penetration nature of ultrasound allows it to detect signs of edema and tissue loss before it is visible on the skin surface. The ability of US to predict tissue loss is seen in patient B (**Figure 4.4**) where site ii shows signs of tissue loss approximately 0.5 cm under the wound surface on day 1 (**Figure 4.4 B and S4**). The hypoechoic regions between the tibia and the US probe cover in **Figure 4.4 E and H** are indicative of further tissue loss which left the tibia exposed by day 42. The increase in wound size and loss of tissue was also corroborated by image analysis (**Figure 4.3 G-L**) where US intensity reduces, and wound area increases over the first 62 days.

Wound healing is an extremely complicated process that is affected by many variables such as age, local perfusion, moisture and patient compliance.[321, 322] Younger patients are more likely to heal faster than older patients.[323] Comparing the healing rates between patient A (77-year old) and patient B (33-year-old) in Fig. 3 shows that patient B exhibited faster wound contraction after skin grating compared to patient A. Patient A showed a 62% contraction within 103 days of the first skin graft placement. Patient B had a larger wound but 65% contraction within 42 days of skin grafting. Furthermore, patient A required a secondary skin graft (EpiFix, MiMedx, Marietta GA) 54 days into the study after which the wound contraction rate increased at both sites (Fig. 3 C-F). These results suggest that US imaging could be used to evaluate wound healing rate; however, a more comprehensive and well powered study is needed to draw conclusions.

Although US imaging is a powerful tool to monitor wound health, it has its limitations. US images are gray scale images, and it is difficult to distinguish between wound sites responding to

treatment and the surrounding healthy tissue. Furthermore, US images can provide high resolution structural imaging but lacks functional imaging capabilities.[324] Photoacoustic imaging is similar to US but uses light as an excitation source to produce pressure waves.[223] It has already shown promise in visualizing ulcers and neovascularization in mice,[309] which is key for wound healing and skin graft integration. Our future work will look to incorporate photoacoustic imaging to monitor neovascularization in human subjects.

4.6 Conclusion

Ultrasound imaging is a valuable tool to study skin graft integration used for chronic wound treatment. We first showed that wound width measurements made by US imaging are strongly correlated to measurements made visually. Second, a thorough investigation into two patients (5 wound sites), both receiving allogenic skin grafts showed that wound contraction, healing, and skin graft integration could be monitored using wound area and US intensity. The loss of tissue and inflammation resulted in hypoechoic regions on the ultrasound which healed after skin graft placement and integration in both patients. Over 110 days, patient A showed up to 96% wound contraction whereas patient B showed up to 91.7% contraction over a similar period. During the healing process, US intensities recovered into the healthy tissue window showing soft tissue regeneration under the skin graft.

4.7 Acknowledgements

Chapter 4, in full, is a reprint of the material as it appears in Point of Care ultrasound as a tool to assess wound size and tissue regeneration after skin grafting. Mantri, Yash; Tsujimoto, Jason; Penny, William F.; Garimella, Pranav S.; Anderson, Caesar A; Jokerst, Jesse V., Ultrasound in Medicine and Biology, 2021. The dissertation author was the primary investigator and author of this paper.

4.8 Supplementary information

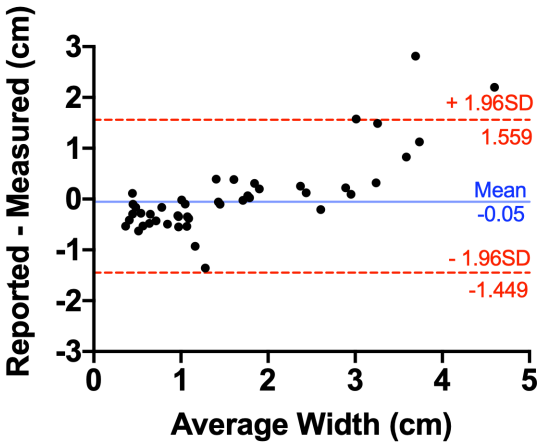

Figure 4. 6 Bland-Altman analysis.
Bland-Altman analysis of reported wound width and ultrasound (US) measured wound width in 45 patients. A mean bias of -0.05 cm rejected the null hypothesis of clinically significant difference above 0.06 cm.

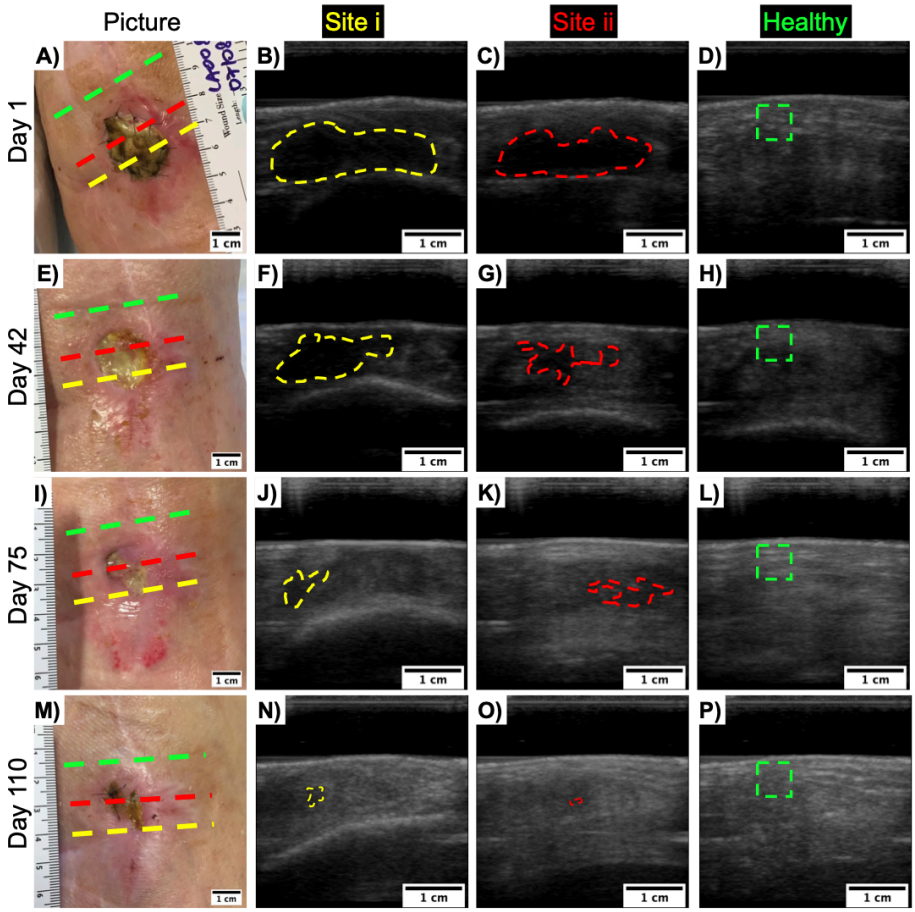

Figure 4. 7 ROI based analysis for Patient A.
Patient A, a 77-year-old female with an anterior left knee wound received an allogenic skin graft 28 days prior and 54 days into the study. Photographs and US images from sites i (yellow), ii (red), and superior healthy tissue (green) from **A-D)** Day 1, **E-H)** Day 42 **I-L),** Day 75, and **M-P)** Day 110. Site i and ii both showed slow healing periods between days 14-62. Wound contraction and tissue regeneration increased after the second skin graft placement. The superior healthy tissue (green dotted line) remained unchanged over the whole study period. Yellow and red lines correspond to ROIs used for wound size measurement. Dotted green lines represent ROI used for measuring US intensity of healthy tissue.

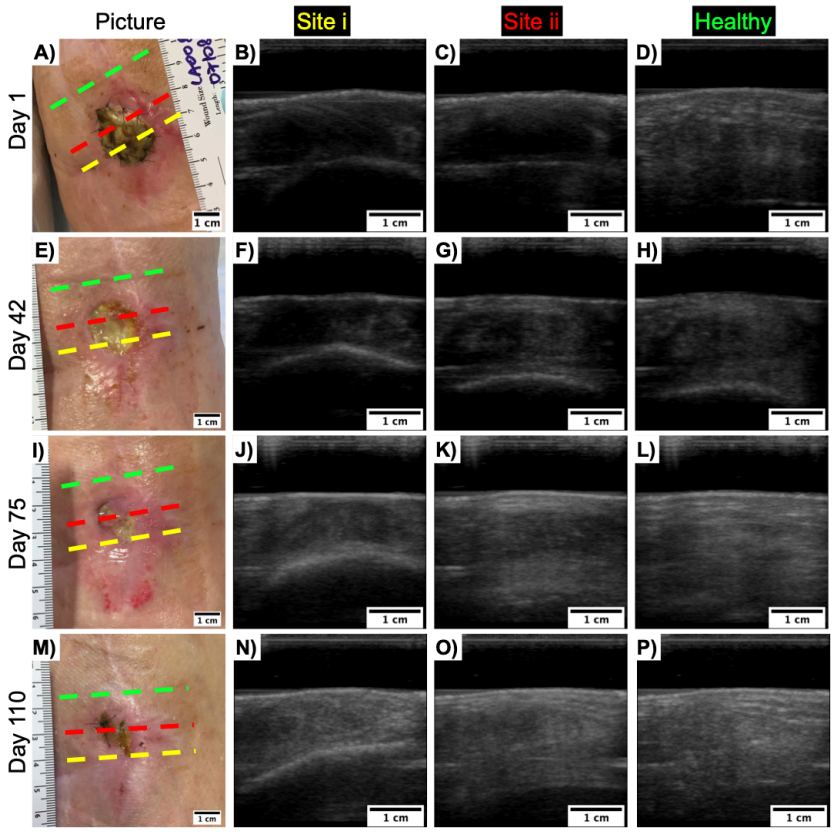

Figure 4. 8 Unannotated version of ROI based analysis for Patient A.

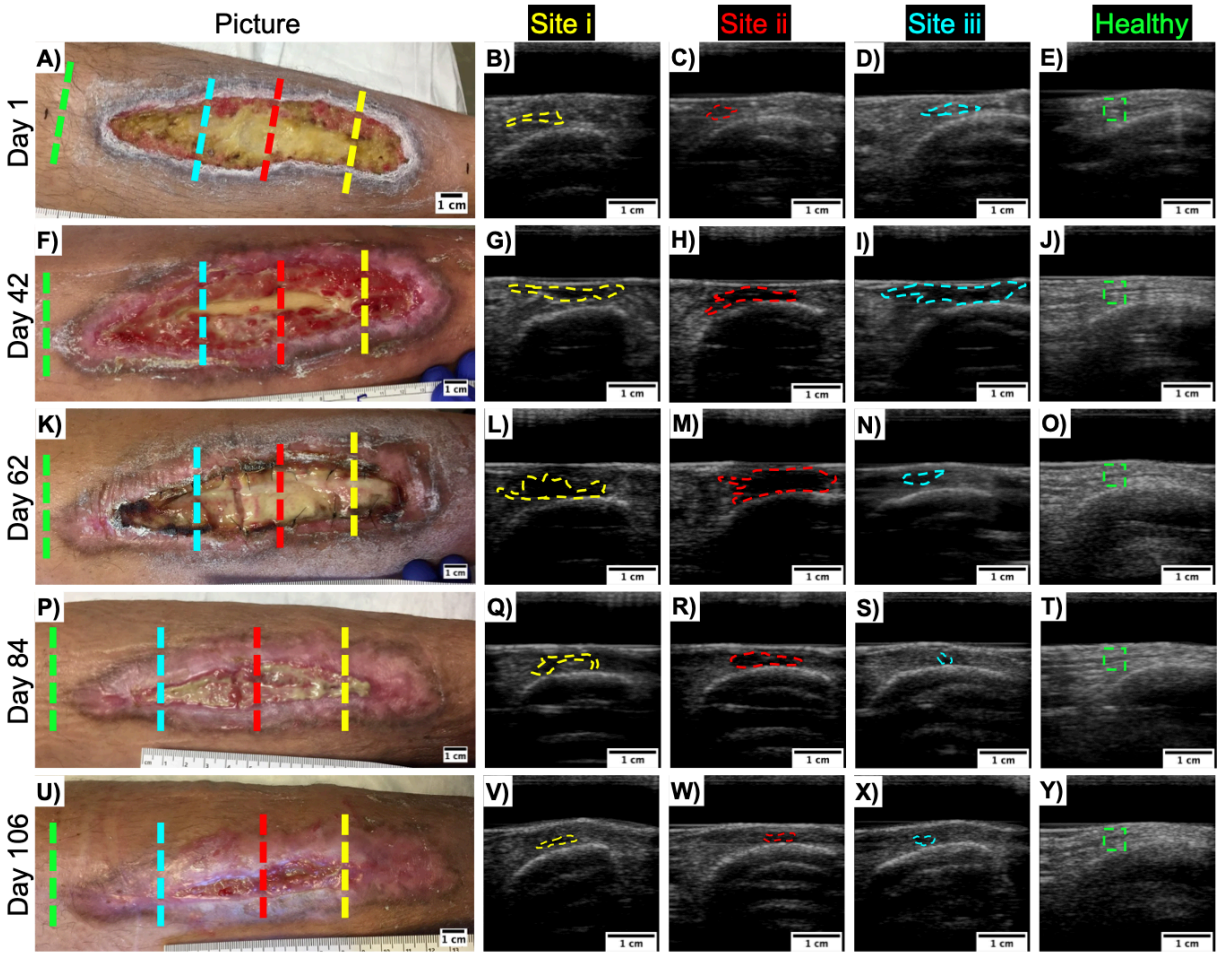

Figure 4. 9 ROI based analysis for Patient B.
Patient B, a 33-year-old male with a chronic anterior lower limb wound received an allogenic skin graft 49 days into the study. Photographs and US images of site i (yellow), ii (red), iii (blue), and superior healthy tissue (green) from **A-E)** Day 1, **F-J)** Day 42, **K-O)** Day 62, **P-T)** Day 84, and **U-Y)** Day 106. A consistent increase in wound size, and loss of tissue is seen in all three wound sites whereas superior healthy tissue remains the same. After skin grafting, site iii (starts healing first **(N)** whereas site i and ii still show further tissue loss **(L-M)**. This is particularly difficult to see by eye. By Day 84 and 106, an increase in US signal within the wound site shows that the skin graft has taken and wound size under the graft has reduced considerably for sites i, ii and iii. Superior healthy tissue (control) remains unchanged over the entire study period. Yellow, red, and blue dotted lines correspond to ROIs used for wound size measurement. Dotted green lines represent the ROIs used for measuring US intensity of healthy tissue.

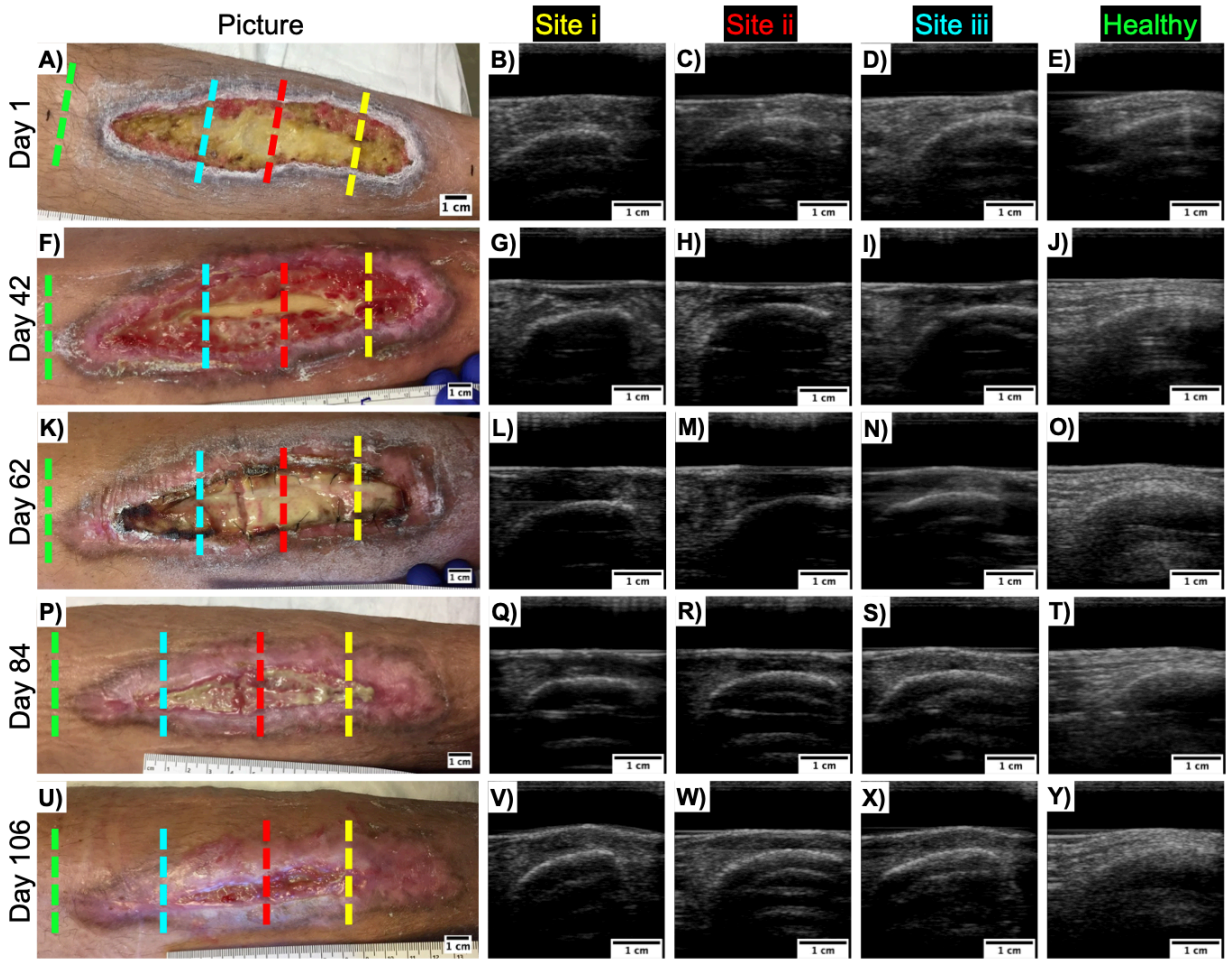

Figure 4. 10 Unannotated version of ROI based analysis for Patient B.

Chapter 5: Photoacoustic monitoring of angiogenesis predicts response to therapy in healing wounds

5.1 Abstract

Chronic wounds are a major health problem that cause the medical infrastructure billions of dollars every year. Chronic wounds are often difficult to heal and cause significant discomfort. Although wound specialists have numerous therapeutic modalities at their disposal, tools that could 3D-map wound bed physiology and guide therapy do not exist. Visual cues are the current standard but are limited to surface assessment; clinicians rely on experience to predict response to therapy. Photoacoustic (PA) ultrasound (US) is a non-invasive, hybrid imaging modality that can solve these major limitations. PA relies on the contrast generated by hemoglobin in blood which allows it to map local angiogenesis, tissue perfusion and oxygen saturation—all critical parameters for wound healing. This work evaluates the use of PA-US to monitor angiogenesis and stratify patients responding *vs.* not-responding to therapy. We imaged 19 patients with 22 wounds once a week for at least three weeks. Our findings suggest that PA imaging directly visualizes angiogenesis. Patients responding to therapy showed clear signs of angiogenesis and an increased rate of PA increase ($p = 0.002$). These responders had a significant and negative correlation between PA intensity and wound size. Hypertension was correlated to impaired angiogenesis in non-responsive patients. The rate of PA increase and hence the rate of angiogenesis was able to predict healing times within 30 days from the start of monitoring (power = 88%, alpha = 0.05) This early response detection system could help inform management and treatment strategies while improving outcomes and reducing costs.

5.2 Introduction

Chronic wounds are a major health problem, but there are no tools to diagnose these wounds before they have erupted and/or evaluate deep tissue response to therapy.[325] Chronic wounds cost the United States medical infrastructure up to $100B/year with a single diabetic ulcer costing nearly $50,000 — these numbers will increase as the population ages.[326] To decrease costs and improve quality of life, the community needs tools to predict and monitor response to therapy. Unfortunately, conventional methods are primarily based on visual inspection and cannot see beneath the skin surface — 3D mapping of physiology deep into the wound bed could better stratify wound risk and guide therapy but such tools do not exist. While the Braden/Norton scales and transcutaneous oximetry (TCOM) have shown promise, these systems offer an ensemble assessment of the affected area with no spatial details on the wound boundaries, wound depth, and interaction of wound with healthy tissue.[327, 328] Thus, the development of tools to map and measure imaging markers associated with wound risk and treatment response could have a major positive impact for patients with chronic wounds or at risk of developing such wounds.[309, 329, 330]

Ultrasound (US) imaging is non-invasive and rapid [331-336] and can make 3D maps of the wound. US is an affordable, high resolution, sensitive, non-ionizing, and real-time tool for imaging but its use is surprisingly rare in wound care despite being ideally suited to characterize soft tissue and bone surfaces.[337] Recently, we reported the use of US to assess wound size in 45 patients.[338] We also performed a longitudinal study of wound healing in patients who received allogenic skin grafts over a 110-day period. We showed that ultrasound imaging can predict wound exacerbation and tissue loss before it is seen by the eye.[338] However, ultrasound alone mostly provides anatomic information: There are few details on perfusion or oxygenation, which are *critical to wound formation and wound healing*. In contrast photoacoustic (PA) ultrasound is a “light in, sound out”

technique versus conventional "sound in, sound out" ultrasound. Contrast in photoacoustic s is generated by differential absorption of light: hemoglobin and deoxyhemoglobin are common absorbers.[2, 339-341] Thus, photoacoustic imaging can report tissue oxygenation and tissue *perfusion.*[342, 343] *The same scan also collects standard ultrasound images.*

Angiogenesis is the formation of new blood vessels from pre-existing vessels. It is well known that angiogenesis is crucial for wound healing.[344] The new blood vessels carry essential cytokines and oxygen for wound repair. Studies have shown that elevated glucose levels in diabetic patients hinders angiogenesis resulting in diabetic ulcer formation, poor wound healing, and limb loss.[345, 346] Treatment protocols such as hyperbaric oxygen therapy,[347] negative pressure wound therapy,[348] and debridement[349] can promote angiogenesis and improve healing outcomes. Hypertension can impair angiogenesis.[350] Hence, an early angiogenesis detection tool could help direct treatment protocols and drastically improve outcomes. Multi-photon microscopy techniques can visualize angiogenesis in vivo but these have micron-scale depth penetration. PA imaging is ideally suited for this application due to centimeter-scale depth penetration and the contrast generated by hemoglobin in blood vessels.[246, 351] Others have recently demonstrated the use of PA imaging to assess peripheral hemodynamic changes in humans[352-356], and thus we were motivated *to use photoacoustic imaging to visualize angiogenesis.* We show here that the rate of PA signal increase directly reports the rate of angiogenesis. We further show that the rate of PA change could be used to predict time to heal. This could help clinicians make early and better-informed decisions on whether a particular treatment regimen should be continued.

5.3 Materials and methods

5.3.1 Patients

This study was performed in accordance with the ethical rules for human experimentation stated in the 1975 Declaration of Helsinki and approved by the University of California San Diego's Human Research Protections Program (Institutional Review Board No. 191998 and 202019X). Informed written consent was acquired from all participants before scanning. Inclusion criteria were (i) age >18 years and be able to provide consent; (ii) wounds smaller than 15 cm^2; (iii) patients must undergo a minimum of three scans spaced at least one week apart from each other. Exclusion criteria included (i) presence of secondary lesions at the wound site (e.g., melanomas); (ii) blood-borne diseases; (iii) orthopedic implants near the wound site. Twenty-one patients (24 wounds) were recruited for this study at the UCSD Hyperbaric Medicine and Wound Care Center, Encinitas, CA, USA. Two patients were excluded from analysis due to poor US coupling reducing image quality. **Table 5.3** describes the patient demographic.

All patients were scanned during a routine wound care visit. Patients were scanned once a week for at least three weeks. C.A.A. was the independent wound specialist and decided the treatment regimen for all patients blinded to the results of the scan. Before scanning, all wound dressings were removed per standard of care, and the wound area was cleaned using sterile saline. Surrounding healthy tissue was cleaned using alcohol swabs to prevent infection. A sterile CIV-Flex transducer cover (Product no. 921191, AliMed Inc., Dedham, MA, USA) was used for every scan to prevent cross contamination.

5.3.2 Photoacoustic - Ultrasound imaging

We used a commercially available LED-based photoacoustic imaging system (AcousticX from Cyberdyne Inc., Tsukuba, Japan). The AcousticX system uses two LED-arrays operating at 850 nm, pulse width 70 ns, and 4 kHz repetition rate. The 128-element linear ultrasound transducer operates at a central frequency of 7 MHz, bandwidth of 80.9%, and a 4 cm field of view. We used a custom hydrophobic gel pad from Cyberdyne Inc. and sterile ultrasound coupling gel (Aquasonic 100, Parker Laboratories Inc., Fairfield NJ, USA) for coupling with the wound surface. All images were acquired at 30 frames/s.

All wounds were scanned in a single sweep from inferior healthy tissue to wound region to superior healthy tissue. All scans were performed by hand, and thus frame alignment between scans was extremely difficult. Due to limitations in image exportation from the software, and to minimize misalignment effects between scans, we chose three representative frames from the central region of the wound for processing. Clinicians also report size and healing assessment from the wound's center.[357] Furthermore, we matched the underlying bone pattern to compare similar spots over time. Y.M. acquired all the images.

5.3.3 Image processing

J.T. performed all the image processing and was blinded to wound photographs and healing times. J.T. only received US scans of the patients. All frames were reconstructed and visualized using the AcousticX software (Cyberdyne Inc.; Version 2.00.10). We exported 8-bit PA, B-mode, and overlayed coronal cross-section images. The images were further processed using Fiji, an ImageJ extension, version 2.1.0/1.53c. Frames with incomplete US coupling were excluded from analysis. Data was plotted using Prism version 9.0.0. We drew custom regions-of-interest (ROIs)

for every frame. We quantified changes in wound area, tissue regeneration, scar tissue development, and photoacoustic intensity as a function of time.

Wound area and tissue regeneration were quantified using a previously described method.[338] Briefly, we determined a dynamic baseline US intensity of healthy tissue for each patient. Areas with intensity lower or higher than baseline values were classified as wound and scar tissue respectively. Wound and scar area were measured using custom ROIs that fit the above classification criteria. Changes in PA intensity was measured using rectangular ROIs (4 cm wide x 1 cm deep). ROIs were drawn under the dermal layer (first 2 mm) hence avoiding PA signal from scabs and hyperpigmented regions of the skin. PA ROIs was made larger to cover the entire field of view of the transducer (4 cm). This is important so we did not miss any signs of angiogenesis from the periphery of the wound. ROIs for PA intensity measurements were also kept constant for all patients eliminating any concerns of inter-rater reliability. All US and PA quantification were carried out on the same frames.

5.3.4 Statistics

We measured wound area and PA intensity in three frames for each scan. The error bars in each figure represent the standard deviation within these three frames. A simple linear regression was fit to the data measuring changes in imaging markers over time; 95% confidence intervals for these fits are shown in each figure. Furthermore, we plotted the rate of PA change per day *vs.* the healing time for the study population and fit a one-phase exponential decay curve to it. We used a Pearson correlation test to determine the correlation between the time to heal (days) versus rate of PA increase comparing the null hypothesis that there is no correlation versus there is a negative correlation between these two variables. The statistical analyses were conducted at alpha = 0.05. A power analysis was also performed on this data. We used a two-tailed Fisher's exact test to look

for significant differences in clinical features between responders and non-responders. An area under the curve – receiver operating characteristic (AUC – ROC) analysis was performed to study the classification of therapeutic responders vs non-responders.

5.4 Results

Nineteen patients with 22 wounds were analyzed in this study. All patients underwent at least three scans spaced one week apart. We measured changes in wound area, PA intensity, and scar tissue formation over time. **Table 5.4** lists all the wound and relevant patient information. Nine wounds showed response to therapy. **Table 5.1** shows the clinical features of therapeutic responders and non-responders. Responders were patients who healed within 111 days.[358, 359] Hypertension was significantly ($p = 0.0001$) responsible for delayed healing. We noted no significant difference in other clinical features (age, sex, diabetes, smoking, body mass index (BMI), heart rate, blood pressure, and oxygen saturation) between the two groups. Extreme cases of wounds that had a swift, delayed and no response to therapy have been highlighted below.

Table 5. 1 Clinical features of responders (healing time < 111 days) and non-responders.
This data is from 19 patients with 22 wounds. Values are mean ± SD or number of subjects (%). * Marks significant difference ($p < 0.05$).

Category	Responders (n = 9 wounds)	Non-Responders (n = 13 wounds)	p values
Age (years)	68.1 ± 10.3	60.9 ± 15.1	0.31
Sex (male)	2 (29 %)	9 (75 %)	0.051
Diabetes	2 (22 %)	5 (38 %)	0.59
Hypertension	1 (11 %)	11 (85 %)	0.0001*
Smoker	2 (29 %)	4 (31 %)	0.39
BMI (kg/m^2)	28.2 ± 9.6	30.5 ± 5.9	0.63
Heart rate (bpm)	74 ± 12	92 ± 22	0.19
Blood Pressure (systolic/diastolic) (mm of Hg)	147/80 ± 22/6	154/91 ± 30/22	0.78
Oxygen saturation (%)	98.4 ± 0.97	97.7 ± 1.4	0.31
Rate of PA change (Intensity (a.u.)/day)	6698 ± 4217	2501 ± 2129	0.002*
Wound size on Day 1of imaging(cm^2)	0.931 ± 0.52	0.978 ± 0.70	0.33
Wound size on last day of imaging (cm^2)	0.454 ± 0.35	0.509 ± 0.25	0.43
Time of Initiation after first presentation (days)	Not controlled see **Table 5.4**.		

Figure 5.1 shows wound healing and angiogenesis in an 82-year-old female (Subject ID: PN1) presenting with a chronic, left posterolateral ankle ulcer. PN1 healed in 66 days. Wound healing was visible *via* photographs within the first 29 days of treatment (**Figure 5.1A-C**). US imaging showed a 33.3% reduction in wound size over 29 days from 0.48 cm^2 – 0.32 cm^2 (**Figure 5.1P**). The wound area reduced linearly as a function of time ($R^2 = 0.61$). PA imaging showed the formation of new blood vessels on day 7 (**Figure 5.1H**). PA intensity increased linearly at a rate of 4217 ± 1336 intensity a.u./day as the wound healed ($R^2 = 0.50$) (**Figure 5.1Q**). A sagittal maximum intensity projection (MIP) of the wound area showed angiogenesis into the wound bed (**Figure 5.1M-O**). Unannotated version of Figure 1 can be found in the supporting information (**Figure 5.5**). **Figure 5.1R** shows a negative correlation between wound area and PA intensity ($R^2 = 0.95$).

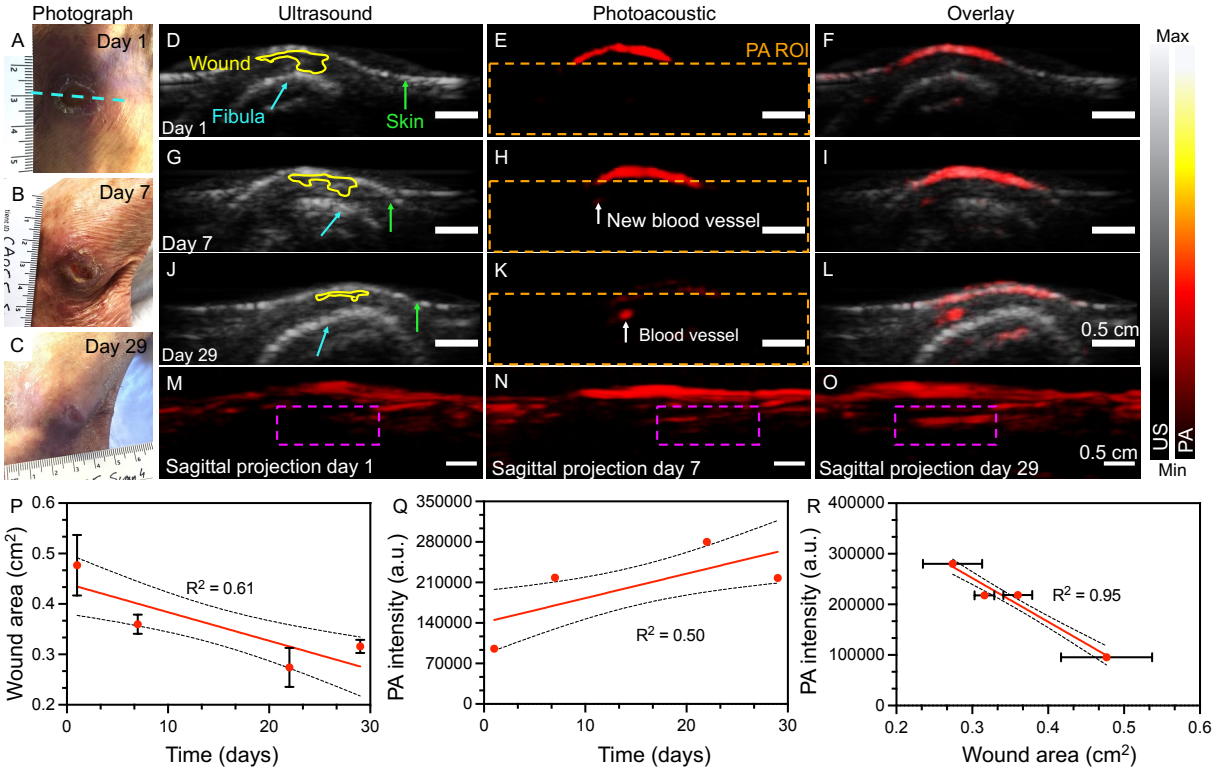

Figure 5. 1 Photoacoustic imaging monitoring of angiogenesis in a healing wound.
PN1, an 82-year-old female presenting with a chronic, left posterolateral ankle ulcer. **A-C**, Photographs showing the wound on days 1, 7, and 29 of the study. Blue dotted line indicates the imaging plane. **D-F**, **G-I**, and **J-L**, showing US, PA, and overlayed images of the wound on days 1, 7, and 29, respectively. Yellow ROI on the US outlines the wound. Green and blue arrows mark the skin surface and fibula respectively. White arrows (**H and K**) show new blood vessel formation *i.e.,* angiogenesis. Orange outline marks the ROI for PA intensity measurement. **M-O**, show the sagittal maximum intensity projection of the wound on days 1, 7 and 29 showing new blood vessels invading the wound bed (Purple box). All scale bars are 0.5 cm. **P**, negative correlation between wound area and time suggests wound closure ($R^2 = 0.61$). **Q**, Significant positive correlation between PA intensity and time suggests angiogenesis within the wound bed ($R^2 = 0.50$). Rate of PA increase 4217 ± 1336 intensity a.u./day. **R**, PA intensity increases linearly as the wound heals suggesting that angiogenesis is correlated to wound closure ($R^2 = 0.95$). Scale bars represent 0.5 cm. Error bars represent standard deviation in 3 representative frames from the center of the wound. Error bars for PA intensity in **Q** and **R** are too small to be shown.

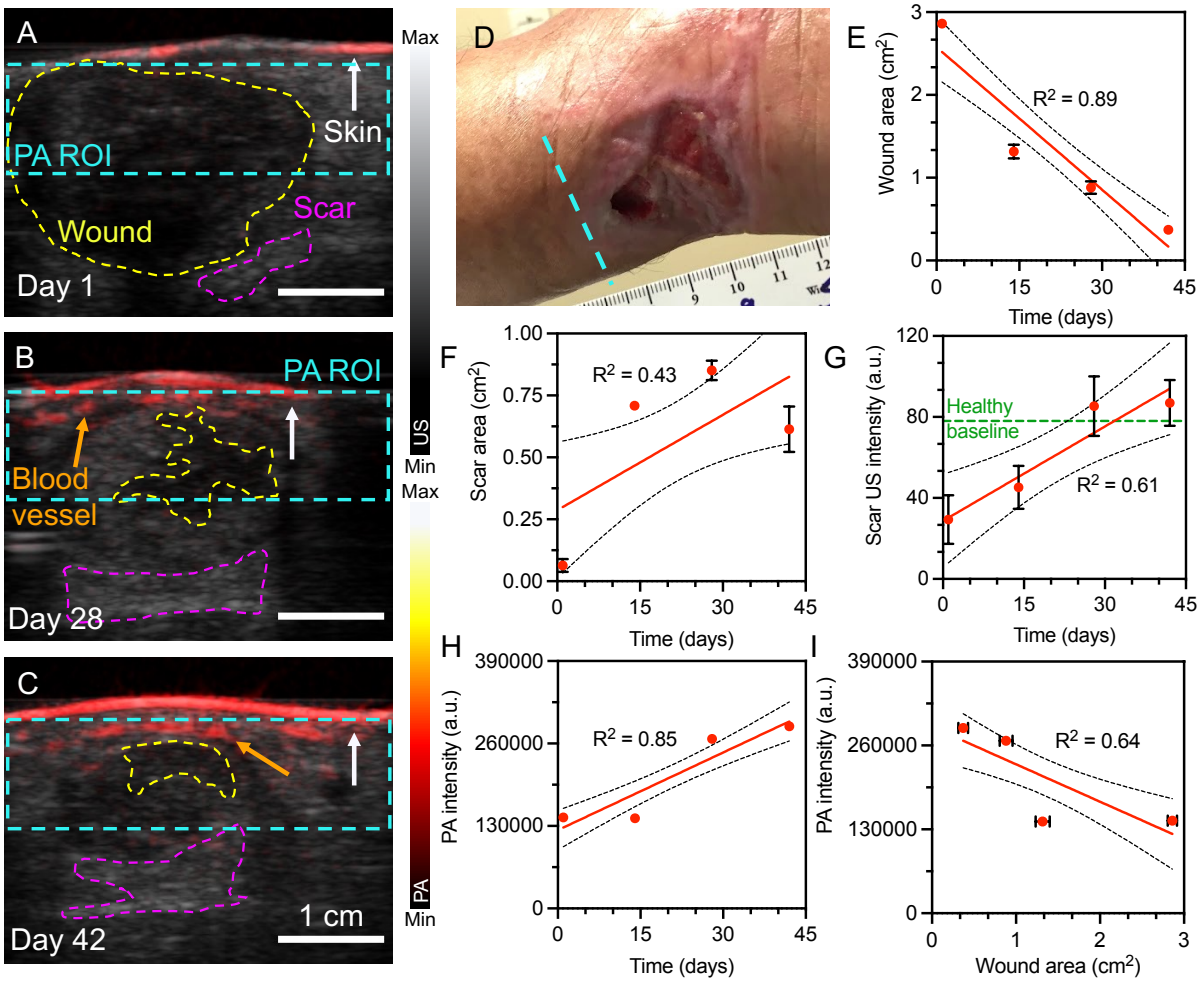

Figure 5. 2 Tunneling wounds; wound closure, scar tissue development and angiogenesis.
A-C, US-PA overlay of the wound on days 1, 28, and 42 of the study. Yellow, purple, and blue dotted lines in A-C represent wound, scar area, and PA ROI respectively. White and orange arrows represent skin surface and blood vessels respectively. **D**, Photographic image of wound in the left posterior ankle region. There is significant tunneling of the wound (not seen by eye). Blue dotted line in **D** indicates the relative imaging plane for panels A-C. **E**, 87% wound contraction is seen within 42-days. **F-G**, Scar tissue development is seen as hyperechoic regions at the wound bed. **H**, Significant increase in PA intensity over time indicates angiogenesis. **I**, A negative correlation between PA intensity and wound area suggests angiogenesis results in wound closure. Scale bars represent 1 cm. Error bars represent standard deviation in three frames at the center of the wound. Error bars for PA intensity in **H** and **I** are too small to be shown.

Figure 5.2 shows the progress of the wound healing indicators in PN2. PN2 was a 59-year-old male presenting with a chronic left ankle ulcer following a severed Achilles tendon repair surgery. PN2 underwent three scans (day 1, 14, 28, 42) and took 292 days to heal. Photographs show tunneling of the wound under healthy surface tissue superior to the wound (**Figure 5.2D**). Blue dotted lines represent the imaging plane. It is important to note that tunneling wounds cannot

be assessed non-invasively by the eye. **Figure 5.2A-C**, show wound progression over the 42-day study period. The wound tunnel showed 87% contraction by day 42 and wound area showed a strong negative correlation with treatment time ($R^2 = 0.89$) (**Figure 5.2E**). More importantly, this patient showed the development of scar tissue by day 28 that was also mentioned in the doctor's notes. Tissue was considered scarred if the mean US intensity was higher than healthy tissue baseline. Scar area was measured using custom ROIs with maximum size fitting the above criteria. Scar area and intensity increased linearly as a function of time ($R^2 = 0.43$ and 0.61 respectively) (**Figure 5.2F-G**). PA intensity in the wound area increased linearly at a rate of 4078 ± 534 intensity a.u./day, $R^2 = 0.85$ (**Figure 5.2H**). PA intensity was negatively proportional to wound area ($R^2 = 0.64$) (**Figure 5.2I**). An unannotated version of **Figure 5.2** can be found in the supporting information (**Figure 5.6**).

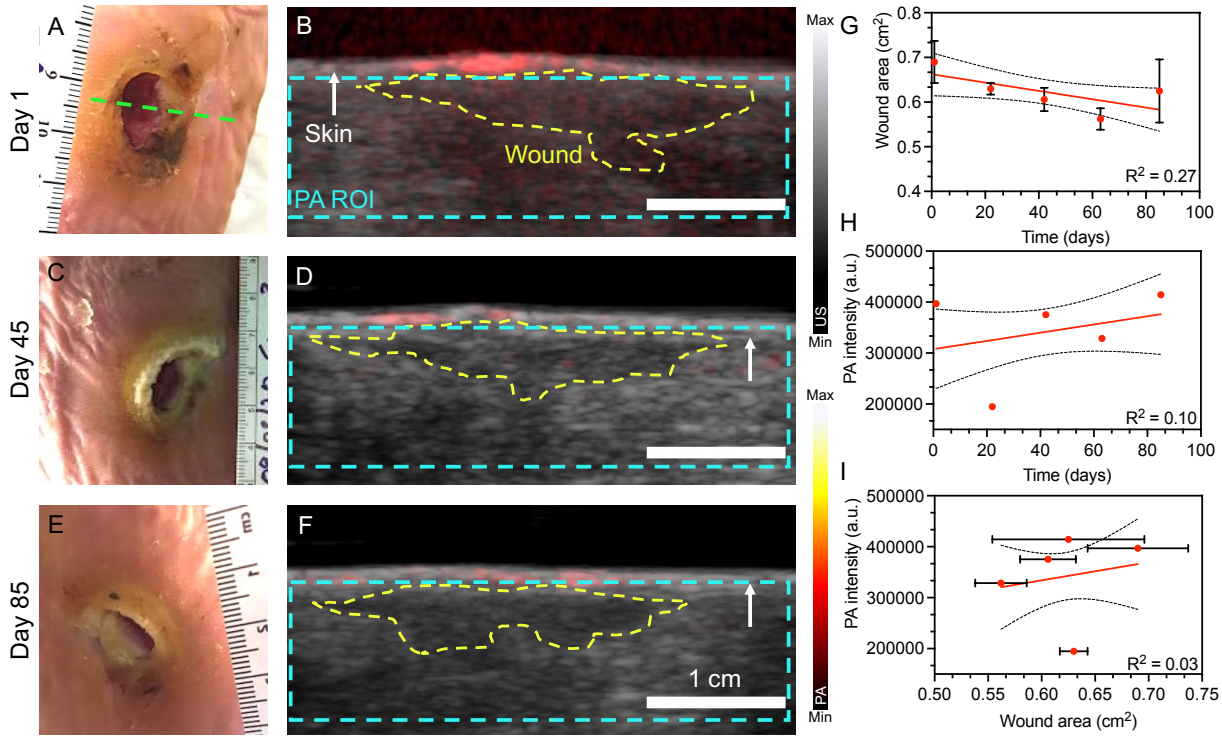

Figure 5. 3 Wound progression in a non-responding patient.
A-B, **C-D**, and **E-F**, photographs, and US – PA overlays on days 1, 45, and 85 of the study respectively. No significant changes in wound size can be seen in the pictures and US scans. Yellow and blue dotted line outlines the wound region and PA ROI used for processing. White arrow marks the skin surface. Green dotted line marks the imaging plane. **G**, mean wound area reduced by 9.4% in the 85-day period but this change was not statistically significant ($R^2 = 0.27$). **H,** PA intensity in the wound increased at a rate of 807.7 ± 706.7 intensity a.u./day, $R^2 = 0.10$ showing no significant correlation versus time. This suggests the absence of angiogenesis and the need for a different therapeutic approach. **I**, the plot of PA intensity *vs.* wound area showed no significant correlation ($R^2 = 0.03$). Scale bars represent 1 cm. Error bars represent standard deviation in three frames at the center of the wound. Error bars for PA intensity in **H** and **I** are too small to be shown.

Figure 5.3 shows progression in a non-healing wound. Subject PN3 was a 70-year-old female presenting with a stage III pressure ulcer on her left heel. PN3 took over 384 days to heal and was still receiving wound care during the preparation of this manuscript. PN3 underwent five scans over an 85-day period, and received standard wound care decided by the attending physician C.A.A. Photographs showed no visible contraction of the ulcer (**Figure 5.3 A, C, and E**). US imaging showed a 9.4% reduction in wound size over 85-days (**Figure 5.3G**). PA intensity increased by 4.2% during the same interval (**Figure 5.3H**). No clear signs of angiogenesis were visible at any point of the study. There was no significant correlation between PA intensity and

wound area, R^2 = 0.03 (**Figure 5.3I**). Unannotated version of **Figure 5.3** can be found in the supporting information (**Figure 5.7**).

Figure 5.4 shows population wide analysis for 17 patients with 20 wounds within the first 30 days of monitoring. The rate of PA increase was derived from the plot of PA intensity *vs.* time for each wound. Error bars represent the standard error of the slope. Healing times were noted from the patient charts as reported by the clinic and C.A.A. Two patients had scans more than 30 days apart and hence were dropped from the analysis in **Figure 5.4A.** The full-length monitoring period for all patients can be found in the **Figure 5.8** that shows a similar trend as in **Figure 5.4A**. The minimum amount of time needed to classify a patient is 30 days. A one-phase exponential decay curve was fit to the data with an R^2 = 0.76. The plateau was calculated to be 1738 intensity a.u./day. Wounds were classified into responders and non-responders using rate of PA change and healing time; 111 days was used as a cutoff for this classification based on previously reported values in literature.[358, 359] The green shaded region (n = 9 wounds) in **Figure 5.4A** shows wounds classified as responders to therapy. The other 11 wounds were classified as non-responders. A power analysis using the data in **Figure 5.4A** showed 80% power with an alpha of 0.05 with 17 wounds. The power was 80% with p = 0.0009 for 20 wounds (**Figure 5.4B**). Hence, the sample size was statistically sufficient to draw clinically significant conclusions. **Figure 5.4C** shows the AUC-ROC curves for discriminating responders *vs.* non-responders. Responders were patients with a rate of PA intensity increase greater than 1738 intensity a.u./day and healing time less than 111-days. The AUC-ROC value is 0.915, which is higher than other reported wound-prediction techniques (**Table 5.2**).

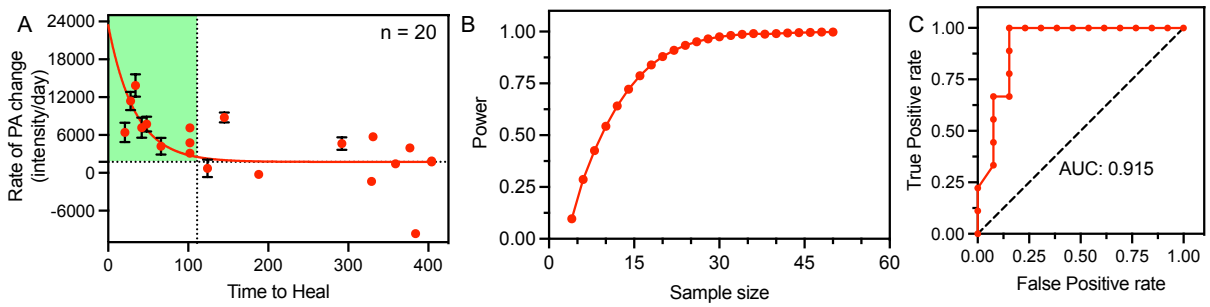

Figure 5. 4 Photoacoustic imaging to predict wound healing and response to therapy.
A, the rate of PA increase per day within the first 30 days is an effective imaging marker to predict wound healing time. Healing times reduce exponentially as a function of the rate of PA increase (n = 20). This could help classify patients as responders (green shaded area*) vs*. non-responders to a particular therapy. PA could help in the early identification of non-responders allowing clinicians to change their therapeutic approach and improve outcomes. **B**, Power analysis using the data used in panel A showed that 80% power with an alpha of 0.05 was achieved at n = 17. At n = 20 the power was 88%, p = 0.0009. Error bars in panel A represent standard error in the rate of PA change for each patient.

Table 5. 2 PA imaging has the highest AUC values compared to other commonly used wound healing prediction techniques.

Prediction technique	AUC	Reference
Photoacoustic imaging	0.915	Current work
Transcutaneous oxygen monitoring	0.805	[360]
Ankle brachial index	0.630	[361]
Toe brachial index	0.560	[361]
Multispectral imaging	0.700	[362]
Toe blood pressure	0.760	[363]
Demographics only	0.556	[364]
Demographic + clinical characteristics	0.605	[364]
Demographic + clinical characteristics + wound characteristics	0.712	[364]

5.5 Discussion

5.5.1 Imaging parameters

PA imaging is ideally suited to monitor local angiogenesis, perfusion, and oxygen saturation: These are all key parameters for wound healing.[365] Multiple studies have shown the use of PA tomography and microscopy to visualize the skin surface, superficial blood vessels, and blood flow with exceptional spatial resolution (< 100 μm, lateral resolution)[343, 366-369] The LED-

based PA system used in this study has much lower spatial resolution and fluence but is also less expensive and more robust/portable compared to conventional high energy laser-based systems. It employs low-energy LED illumination operating under the maximum permissible exposure limit ($2 – 9$ μJ/cm^2) with a lateral resolution between 550 – 590 μm.[257] Hand-held scans using the LED-based PA system allows easy mapping of wounds on contoured surfaces such as the ankle, thus making it ideal to visualize angiogenesis in complex wounds. The 850-nm excitation used in this study falls within the biological optical window and maximizes depth penetration while maintaining a relatively high signal-to-noise ratio (~ 35 dB).[370] Limitations of this LED-based system include a small cache: The system acquires 500 – 1500 frames per scan but the processing software only exports 180 representative frames per scan (1 exported frame for every 8 acquired frames). Hence, there is a large loss of data unless one scans multiple small areas separately. The image exportation limited us to analyze only three representative frames from the center of the wound.

One major strength of the study was that all image processing was carried out by J.T. who was blinded to the study. We used carefully considered criteria to define wound *vs.* scar *vs.* healthy tissue. Areas were classified as wound or scar tissue if the mean US intensity was lower or higher than healthy tissue baseline, respectively. Custom drawn ROIs analysis can be extremely subjective [371] but we have shown good inter-rater reliability (mean bias 4.4%) in our previous work that used US to quantify tissue regeneration and wound closure in skin grafted patients.[338] The PA intensity was quantified using a rectangular ROI measure 4 cm wide and 1 cm deep and excluding the skin surface. We used the integrated density measurement which adds the intensity of all the pixels in the ROI instead of mean PA intensity. The use of integrated density reduces the effects of poor coupling, if any and provides an absolute value of PA intensity. The PA intensity ROI was

maintained constant for all patients, eliminating concerns of subjectivity, and interferences due to skin tone.

5.5.2 Clinical significance

It is well established that angiogenesis is critical for wound healing. New blood vessels formed during the healing process deliver key cytokines and oxygen that reshape the wound matrix and result in wound closure.[365] Hence, angiogenesis can be a key imaging marker to predict response to therapy. The Centers for Medicare and Medicaid Services (CMS) in the United States re-evaluates coverage after 30 days from initial patient encounter. Patients needing advanced therapies need to be certified by the attending physician to enter a comprehensive plan of care in the medical record.[372] A recent high-powered study in 620,356 wounds showed that demographics, wound and clinical assessment could be used to predict wound healing in 84 days (AUC = 0.712, **Table 5.2**). But this is above the 30-day re-evaluation time limit set by CMS. [364]

The main clinical significance of this study is the ability to classify patients according to their response within 30 days from the start of therapy which aligns with the coverage re-evaluation time from CMS. Compared to other commonly employed techniques such as ankle brachial index, TCOM, *etc*., PA imaging is the best predictor for wound healing (AUC = 0.915, **Table 5.2**). PA classification could allow wound specialists to change their course of treatment if the wound is not responding to conventional treatment protocols.[281, 282, 338, 347] This would in turn improve outcomes, reduce amputations, healing time, and costs.

The rate of PA change is indicative of the rate of angiogenesis in the wound bed. The MIPs (**Figure 5.1M-O and Figure 5.10**) confirms the formation of new blood vessels into the wound bed. Responding patients had a mean rate of PA change 6698 ± 4217 intensity (a.u.)/day that was significantly higher ($p = 0.002$) than non-responders (2501 ± 2129 intensity (a.u.)/day). Within the

responding group, higher age and lower BMI were related to an increased rate of PA change (**Figure 5.9**). Age negatively impacts angiogenesis hence the age correlation is unexpected.[373, 374] The difference in treatment regimens like the use of cellularized tissue products to accelerate tissue regeneration could explain the age correlation. Blood pressure had no significant effect on the rate of PA change. Hypertension, diabetes, and smoking are also known to impair angiogenesis and hence wound repair.[322, 350, 375] The effect of hypertension on wound healing is visible in this cohort (**Table 5.1**): 12 of the 13 non-responsive wounds were hypertensive (92%), but only 1 of the 9 responsive wounds were hypertensive (14%). Hence non-hypertensive patients are more likely to develop new blood vessels and positively respond to therapy. Clinical factors alone can be used as a classifier but the use of PA imaging significantly improves prediction (**Table 5.2**).[364] A larger patient cohort could better illustrate the role of other risk factors that impair healing.

Traditionally, clinicians use surface cues such as color and presence of devitalized tissue to assess wound health.[338] In some cases, wound tunneling or cavitation can lengthen healing times and cause significant discomfort. Conventionally, probing tools are used to measure tunneling depth. Probing is invasive and can lead to further tissue injury. Accurately and safely assessing tunneling wounds is therefore quite difficult visually. PN2 presents as an ideal example of a tunnelling wound to show the power of imaging over conventional wound assessment methods. The US was not only able to measure wound reduction (87% in 42 days), but also monitor scar tissue formation in the wound bed. Scar tissue presents as hyperechoic regions on the US due to its high fibrotic nature.[317] The addition of PA imaging allows us to visualize angiogenesis around the healing wound. Angiogenesis can be clearly seen in **Figure 5.2B-C** sandwiched in between the wound and skin surface. Deeper blood vessels can be seen on the US in **Figure 5.2C,** but these have very low PA signal due to reduced light penetration through tissue. The presence of a sterile

sleeve between the transducer and skin surface also enhances light scattering, further reducing penetration depth. Using a higher wavelength of light could help visualize deeper vessels. The longer healing time compared to PN1 with similar rate of PA change can be attributed to the larger wound size, tunneling, and a different treatment regimen compared to PN1. PN1s wound was limited to skin breakdown whereas PN2s wound had full thickness soft tissue involvement.

Secondary trauma, insufficient off-loading, poor wound dressing practices, and poor patient compliance can significantly impair wound healing and increase healing time.[376] Nevertheless, with 88% power in our study, we believe there is enough statistical significance to draw clinically relevant conclusions from this PA data. Future work in this field will look at employing oximetry-based PA measurements to measure local oxygen tension within the wound. It would also be interesting to study how PA imaging performs in conjunction with other prediction tools. The specialty of hyperbaric medicine could potentially benefit from this study. Such knowledge about oxygenation could potentially improve the use of hyperbaric oxygen treatment, indicating whether it should be initiated, continued, or halted. Patients not responding to therapy can then be more efficiently directed to other wound treatment interventions or therapeutic modalities. Furthermore motion-compensation and deep learning algorithms could improve image stability, quality, and streamline image processing.[253, 377]

5.6 Conclusion

Angiogenesis is a key imaging marker for wound healing. PA-US imaging can be used to measure wound size, rate of angiogenesis, and scar tissue formation. A study of 19 patients with 22 wounds revealed that there is an inverse correlation between wound area and PA intensity. An increase in PA intensity correlates with wound closure due to the formation of new blood vessels. 3D MIP images confirmed blood vessel infiltration into the wound bed. Non-healing wounds

showed no correlation between PA intensity and wound area. A higher rate of PA increase was associated with an exponential reduction in healing times. Finally, PA imaging could be used to classify therapy responders and non-responders within 30-days from the start of treatment. With an AUC value of 0.915, PA imaging is the best wound prediction technique. This work could have clinical significance in helping doctors make more informed and early decisions about whether treatment should be initiated, continued, altered, or halted.

5.7 Acknowledgements

Chapter 5, in full, is a reprint of the material as it appears in Photoacoustic monitoring of angiogenesis predicts response to therapy in healing wounds. Mantri, Yash; Tsujimoto, Jason; Donovan, Brian; Fernandes, Christopher C.; Garimella, Pranav S.; Penny, William F.; Anderson, Caesar A; Jokerst, Jesse V., Wound Repair and Regeneration, 2021. The dissertation author was the primary investigator and author of this paper.

5.8 Supplementary information

Table 5. 3 Patient demographic distribution.

Category	Distribution
Total participants	19
Number of scanning events range	3 – 11 scans
Monitoring time range for individual patients	21 – 112 days
Average age (years)	63.5 ± 14.4
Sex (Male / Female)	11 / 8
Body mass index (kg/m^2)	29.4 ± 7.4
Diabetes (Y / N)	8 / 11
Hypertension (Y / N)	12 / 7
Smoker (Y/N)	8 / 11

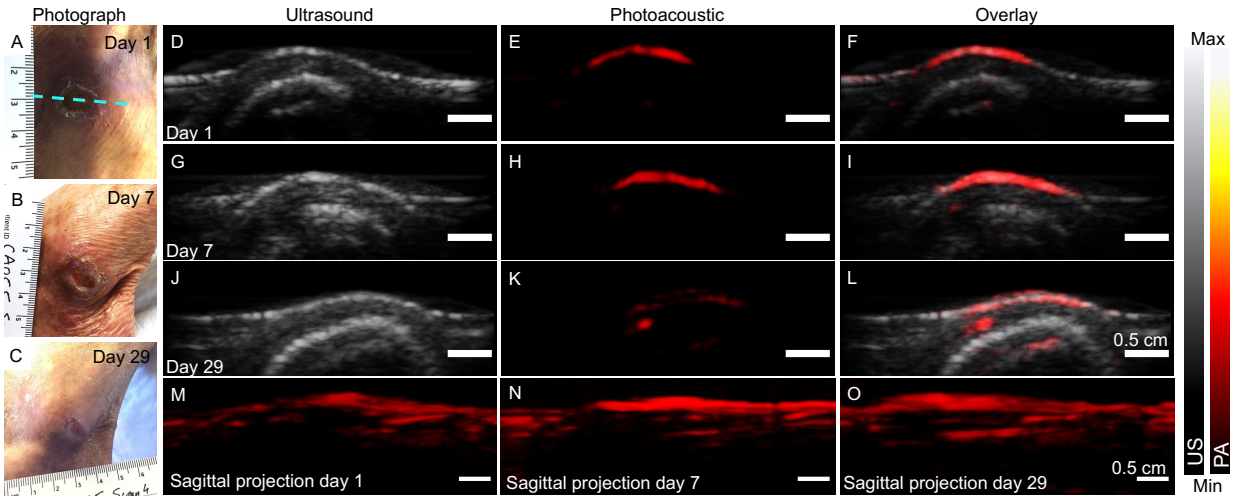

Figure 5. 5 Unannotated version of Figure 5.1
Blue dotted line marks the imaging plane.

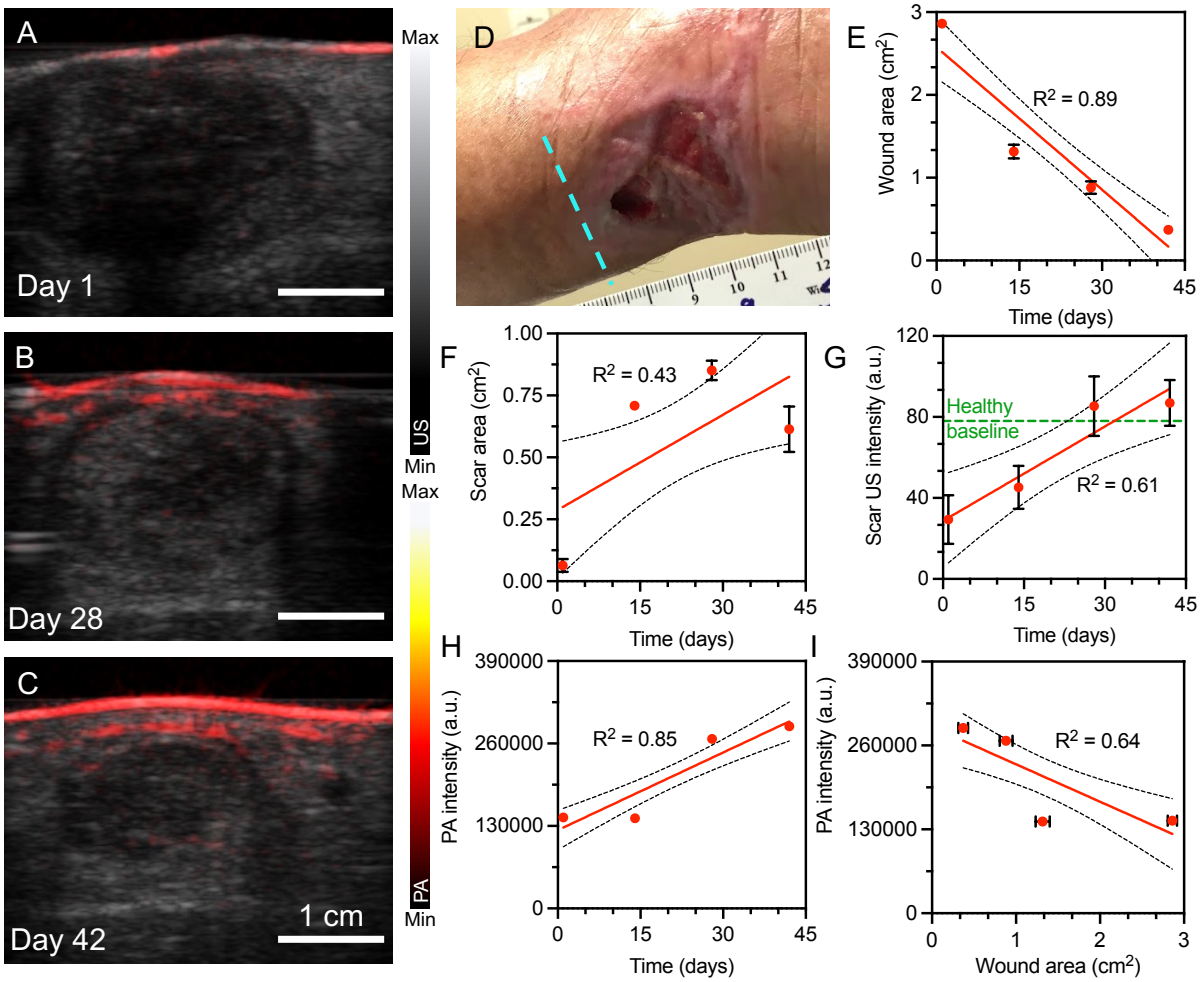

Figure 5. 6 Unannotated version of Figure 5.2.
Blue dotted line marks the imaging plane.

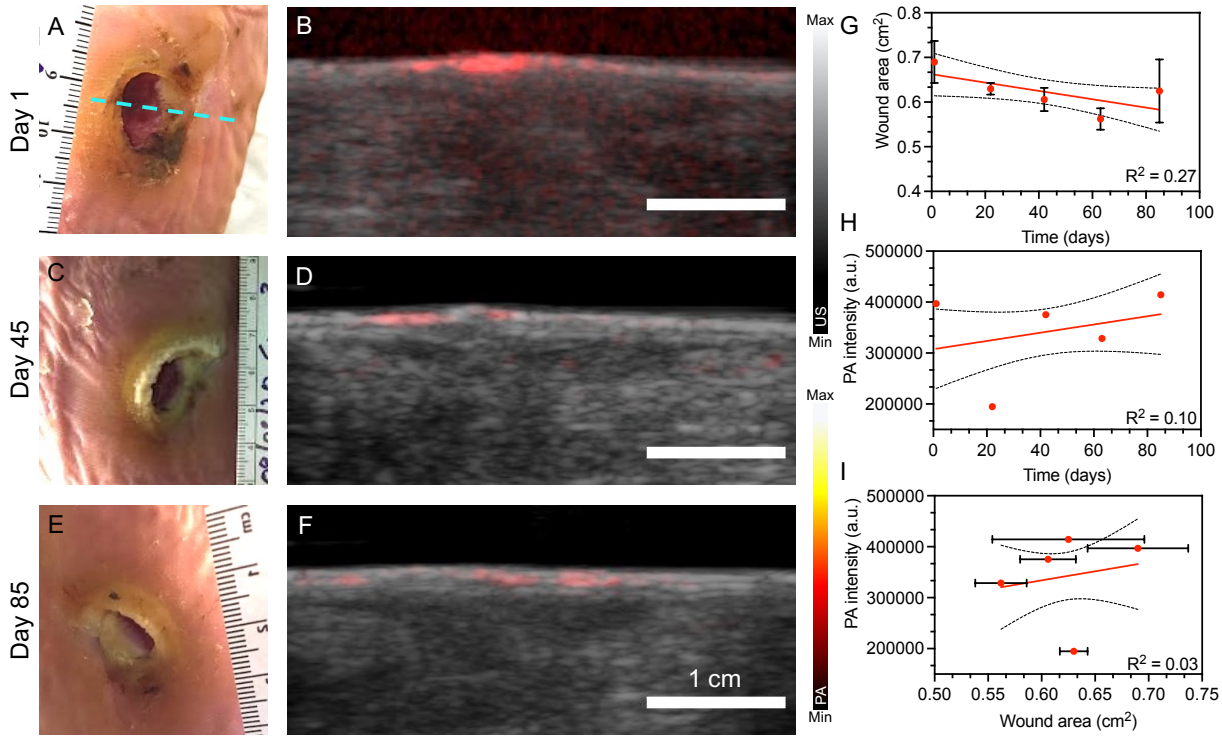

Figure 5. 7 Unannotated version of Figure 5.3.
Blue dotted line marks the imaging plane.

Table 5. 4 Patient and wound information.

Green highlights indicate patients who are non-hypertensive and show good response to therapy. * Indicates patients who were still receiving wound care at the time of submission. WA, B, and C, denote different wounds on the same patient.

Pateint Number	Age (yrs)	Sex (M/F)	Number of scans (Study period in days)	First imaging session after initial presentation (days)	Wound discription	Healing time (days)	Hypertensive (Y/N)	Response to therapy (Y/N)
PN1	82	F	4 (29)	18	Left posterolateral ankle	66	N	Y
PN2	59	M	4 (42)	7	Left posterior ankle	292	Y	N
PN3	70	F	5 (85)	175	Left heel	384	Y	N
PN4	70	M	6 (112)	110	Right Achilles ulcer	411*	Y	N
PN5	28	M	3 (118)	490	Inferior to the left knee	357	Y	N
PN6	77	M	11 (110)	103	Inferior to the left knee	124	Y	N
PN7 – WA	71	M	3 (21)	2252	Left dorsal ankle	404*	Y	N
PN7 – WB	71	M	3 (21)	2252	Left dorsal heel	404*	Y	N
PN8	56	M	4 (51)	32	Greater toe of right foot	331	Y	N
PN9 – WA	56	F	4 (35)	47	Lower anterior left leg	102	N	Y
PN9 – WB	56	F	4 (35)	47	Lower medial left leg	102	N	Y
PN9 – WC	56	F	4 (35)	47	Lower left leg	102	N	Y
PN10	72	M	7 (99)	229	Left posterior leg	329	Y	N
PN11	78	F	6 (98)	421	Lateral left ankle	188	Y	N
PN12	33	M	10 (106)	33	Lower anterior left leg	145	Y	N
PN13	67	F	4 (34)	32	Toe of left foot	34	N	Y
PN14	62	M	4 (77)	740	Left plantar great toe	377*	Y	N
PN15	54	M	4 (76)	329	Mid-lateral right foot	359	N	N
PN16	62	F	3 (21)	35	Right lower leg	21	N	Y
PN17	82	F	4 (28)	12	Right lower leg	28	N	Y
PN18	60	M	6 (42)	14	Right medial ankle	42	Y	Y
PN19	68	M	3 (22)	43	Right plantar region	48	N	Y

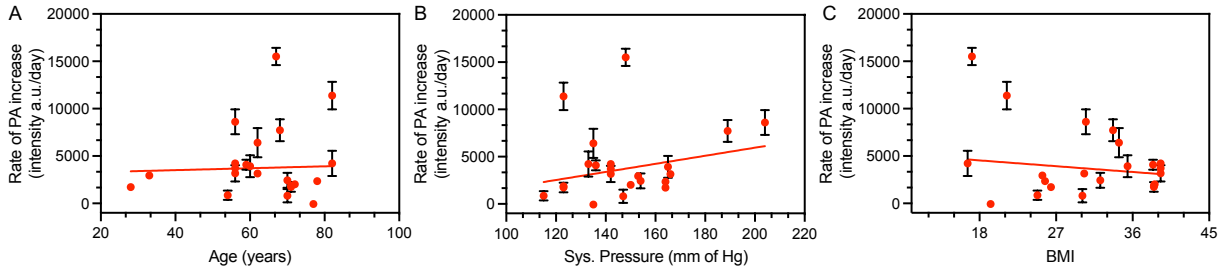

Figure 5. 8 Confounding variables for the entire cohort.
A, Effect of age (years), **B**, systolic blood pressure (mm of Hg), and **C**, body mass index (BMI) for the entire cohort on the rate of PA change shows no significant correlation.

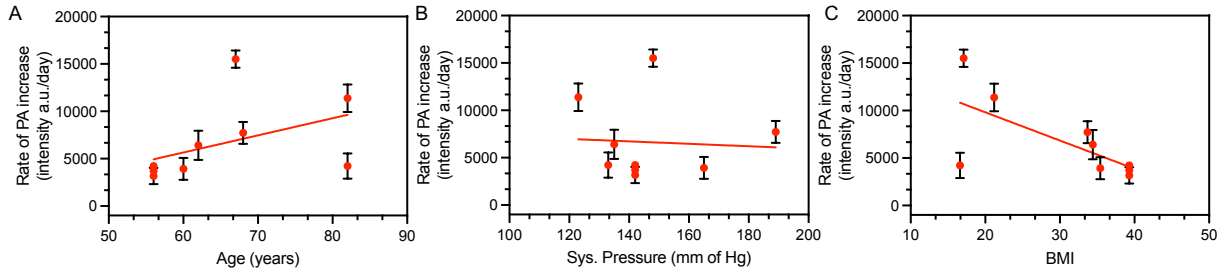

Figure 5. 9 Confounding variables for the therapy responders.
A, Effect of age (years), **B**, systolic blood pressure (mm of Hg), and **C**, body mass index (BMI) for the responders on the rate of PA change. Higher age and lower BMI are related to increased rate of change in PA intensity. Blood pressure had no significant effect on the rate of PA change.

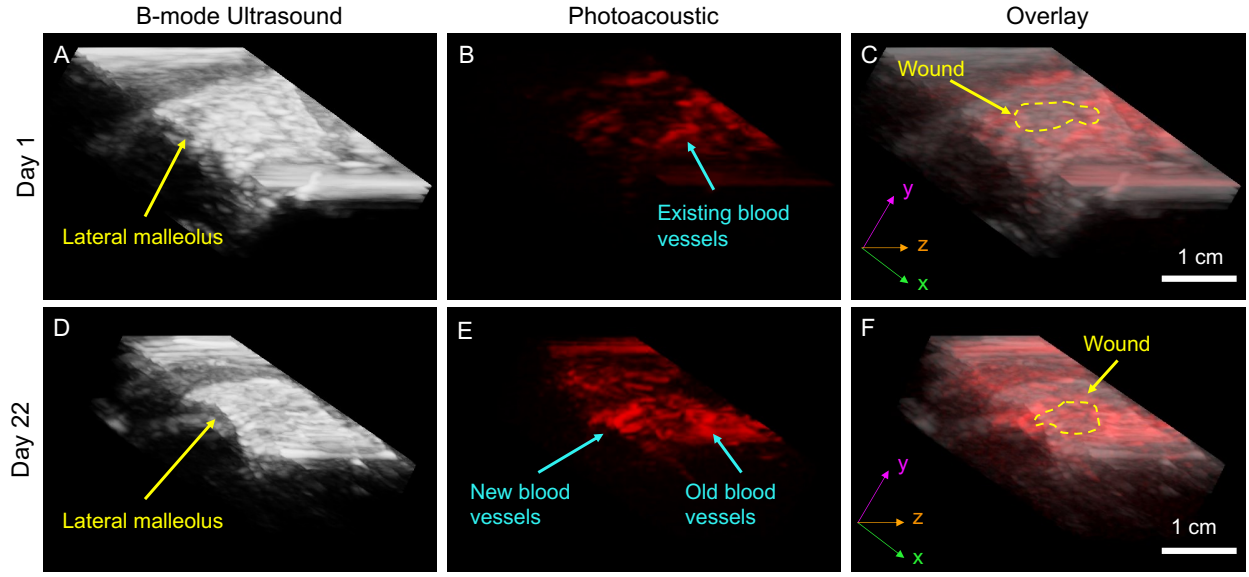

Figure 5. 10 3D mapping of angiogenesis.
Photoacoustic 3D mapping of the wound bed for PN1. (A – C) wounded region on Day 1 shows lack of blood vessels in the wound bed marked by yellow dotted lines in C. A few peripheral blood vessels can be seen on Day 1 in panel B. (D – F) wounded region on Day 22. Newly formed blood vessels can be seen in E. Scale bars represents 1 cm.

Chapter 6: Monitoring peripheral hemodynamic response to changes in blood pressure via photoacoustic imaging

6.1 Abstract

Chronic wounds and amputations are common in chronic kidney disease patients needing hemodialysis (HD). HD is often complicated by drops in blood pressure (BP) called intra-dialytic hypotension. Whether intra-dialytic hypotension is associated with detectable changes in foot perfusion, a risk factor for wound formation and impaired healing remains unknown. Photoacoustic (PA) imaging is ideally suited to study perfusion changes. We scanned the feet of 20 HD and 11 healthy subjects. HD patients were scanned before and after a dialysis session whereas healthy subjects were scanned twice at rest and once after a 10 min exercise period while BP was elevated. Healthy ($r=0.70$, $p<0.0001$) and HD subjects ($r=0.43$, $p<0.01$) showed a significant correlation between PA intensity and systolic BP. Furthermore, HD cohort showed a significantly reduced PA response to changes in BP compared to the healthy controls ($p<0.0001$). Hence showing that PA can monitor hemodynamic changes due to changes in BP.

6.2 Introduction

Chronic kidney disease (CKD) affects more than 9% of the global population.[378, 379] An estimated two million of these patients with CKD progress to end-stage kidney disease (ESKD) and must undergo kidney replacement therapies such as a kidney transplant or dialysis.[378] Rates of non-traumatic lower limb amputations are ~4.3/100 person-years for ESKD patients and reach 13.8/100 person-years for the diabetic subpopulation.[380] Foot ulcers usually precede 84% of amputations with half occurring in diabetic patients.[381] Worse, diabetic dialysis patients develop foot ulcers at five-fold higher rate than even diabetic chronic kidney disease patients.[382] Foot ulceration is a significant risk factor for limb loss, and thus prevention—along with timely diagnosis and treatment—may translate to a reduced amputation rate. There is an urgent need to develop novel, non-invasive techniques to diagnose risk factors for ulceration and prevent limb loss in persons with ESKD.

Clinically, tissue perfusion is often inferred using measurements of blood pressure (BP),[383] blood oxygen saturation,[384] and lactate levels.[385] Measurements of full body hemodynamic parameters fail to reflect changes in peripheral microcirculation.[386] Transcutaneous oxygen monitoring (TcOM),[387] functional magnetic resonance imaging (fMRI),[388] laser doppler imaging (LDI)[389], and spatial frequency domain imaging (SFDI)[390] can measure local perfusion and oxygenation in specialized care settings. TcOM is a non-invasive skin oxygen tension measurement system used for infants and adults.[387] But TcOM suffers from long acquisition times (15-20 min) and is susceptible to calibration errors and poor inter-rater usability.[391] fMRI can non-invasively image difficult to access areas like the brain and produce perfusion maps.[388] But fMRI has poor temporal resolution (5 sec) and reproducibility.[392, 393] LDI can provide real-time and continuous perfusion monitoring but is sensitive to all movements resulting in erroneous readings,

and it can only penetrate a few millimeters into tissue.[394] SFDI can provide a large field of view and rapid imaging but is limited to surface tissues and still needs to be developed further for clinical use.[390]

Photoacoustic (PA) imaging is a hybrid imaging modality that can solve these major limitations. PA imaging uses pulsed light to generate sound waves via thermal expansion that can be overlaid with conventional ultrasound (US) data.[223] PA employs the difference in light absorption between oxygenated and deoxygenated hemoglobin to measure oxygen saturation, map vasculature and tissue perfusion in real time.[1]

n pre-clinical settings, PA is used to measure disease biomarkers,[395] oxidative stress,[8, 230] blood oxygen saturation,[342] and image chronic wounds.[246, 309] Clinically PA is used for diagnosing and monitoring breast cancer progression, [396, 397] vascular dynamics in human fingers, [398] inflammatory bowel disease, [399] and many more diseased states.[400-403] Recently, we demonstrated the ability of PA imaging to monitor angiogenesis and predict wound healing.[404] The non-invasive, real-time, and enhanced penetration depth (>4 cm) of PA imaging make it an ideal tool to map peripheral tissue perfusion as a risk factor for the development of limb complications.

Here, we aimed to explore the use of PA to measure changes in peripheral blood perfusion in a cohort of HD patients before and after dialysis. We hypothesized that the change in PA signal would be dependent on changes in blood pressure given the intradialytic hypotension that often occurs in patients.[405-409] The loss of pressure is followed by peripheral vasoconstriction and reduced peripheral perfusion because blood flow is redirected towards the vital organs.[410] This controlled change in blood pressure in a resting patient without medication or exercise is unique to HD patients. Hence HD patients make an exquisite cohort to study the effects of blood pressure on peripheral photoacoustic signals and tissue perfusion.

6.3 Materials and Methods

6.3.1 Patients

This study was performed in accordance with the ethical guidelines for human experimentation stated in the 1975 Declaration of Helsinki. The study was approved by the University of California San Diego's Human Research Protections Program and was given Institutional Review Board approval (IRB# 191998). Written informed consent was obtained from all subjects before participation. All subjects were ≥18 years old and able to provide consent. Those in the CKD group were all on hemodialysis. Exclusion criteria were: (i) presence of bloodborne pathogens and (ii) presence of implants in the imaging region. Dialysis patients (n=22) were recruited consecutively for this study at the outpatient Hemodialysis Unit, UC San Diego Health System. Eleven healthy volunteers, with no known vascular disease history were recruited at UC San Diego.

The dialysis patients were each scanned twice: once at the start of HD (pre-dialysis), and again at the completion of HD (post-dialysis). Blood pressure and ultrafiltration volume were recorded by the Fresenius 2008T dialyzer (Fresenius Medical Care, Waltham, MA, USA). Two of the 22 dialysis patients were subsequently excluded from the analysis due to complications during HD (unrelated to imaging) preventing a post HD scan.

The 11 healthy subjects were each scanned three times: 1) at baseline; 2) after 3 hours of rest and no pressure changes (negative control (test/re-test), pre-exercise); and 3) after 10 minutes of exercise to elevate blood pressure (positive control, post-exercise). We monitored body temperature, heart rate, and blood pressure at all imaging time points. **Figure 6.1** illustrates the study protocol for the two groups. **Table 6.1** describes the CKD/HD and healthy group demographics.

Table 6. 1 CKD/HD and Healthy group demographics.

Category	CKD/HD group (n = 22)	Healthy group (n = 11)
Age (mean ± SD)	59.2 ± 14.3 years	26.5 ± 4.1 years
Male/Female	7/15	11/0
Diabetic/non-diabetic	14/8	0/11
Average UF removed	2732.3 ± 1109 ml	N.A.

6.3.2 Blood pressure measurements

Blood pressure (BP) for the HD patients was measured internally by the dialyzer. We also noted their ultrafiltration volume at the end of the HD session. Patients were at rest sitting in semi-Fowler's position at the time of measurement. BP measurements were made just before and at completion of the HD session (**Figure 6.1D**). Change in systolic pressure was defined as the difference between BP_{HDend} and $BP_{HDstart}$.

For the healthy group we used an electronic blood pressure monitor (Omcron Healthcare Inc., Lake Forest, IL, USA, Model no: BP742N). The cuff was placed on the left upper arm and the subjects were sitting up straight for all measurements. We recorded BP twice at rest (T=0 and T=3 hrs) and once after 10 min of exercise (**Figure 6.1C**). The T=3 hrs time point was chosen to mimic the length of a typical HD session without changes in BP, serving as a negative control. Exercise consisted of climbing up and down stairs for 10 min to simulate an increase in blood pressure (positive control). Changes in systolic BP were calculated as differences between (i) $BP_{pre\text{-}exercise}$ and $BP_{baseline}$; and (ii) $BP_{post\text{-}exercise}$ - $BP_{pre\text{-}exercise}$.

6.3.3 Photoacoustic imaging

All the PA imaging was done using the AcousticX from Cyberdyne Inc. (Tsukuba, Japan). This LED-based PA scanner operates at 850 nm wavelength with an LED repetition rate of 4 kHz, pulse width of 70 ns, and operating at 2.6 μJ/cm^2 per pulse.[257] It employs a 128-element linear

array transducer with a 0.38 x 6 cm field of view, 7 MHz central frequency, and a bandwidth of 80.9%.[411] We used a custom hydrophobic gel pad from Cyberdyne Inc. along with sterile US coupling gel (Aquasonic 100, Parker Laboratories Inc. Fairfield NJ, USA) to couple the transducer with the skin surface. A sterile sleeve (CIV-Flex™ #921191 from AliMed Inc., Dedham, MA, USA) covered the transducer during imaging. All images were acquired at 30 frames/s in a single handheld sweep.

We scanned two spots on each foot (except for one patient in whom only one foot was scanned due to a left lower limb amputation). The plantar area was scanned in a medial-lateral direction and the heel area in an inferior-superior direction (**Figure 6.1B**). It must be noted that since all the scans are done manually, precise control of the scan area was extremely difficult. But the same general area was scanned for every patient. CKD/HD patients were scanned once before and once after an HD session (**Figure 6.1D**). Healthy subjects (the control group) were scanned three times (**Figure 6.1C**). BP measurements and PA imaging were carried out simultaneously.

6.3.4 Image processing

All scans were reconstructed and visualized using the proprietary AcousticX software (Cyberdyne Inc. version 2.00.10); 8-bit PA, B-mode, and PA+US overlayed coronal cross-sectional images were exported. We used the proprietary software developed by the PA system's manufacturer for image reconstruction. The system reconstructs PA images using Fourier transform analysis.[257] All the processing was done manually. Scans ranged between 45 – 180 frames governed by scan distance and length. PA signal was quantified using region of interest (ROI) analysis *via* ImageJ (with Fiji extension), version 2.1.0/1.53c. We drew a 4-cm-wide and 1-cm-deep rectangular ROI that was kept constant across all frames. PA signal from the skin was excluded from analysis to minimize the impact of variable melanin concentration in different skin

tones. Integrated density function was used to quantify the PA signal within the ROI. Global PA intensity was defined as the mean integrated PA density of all four imaging regions (**Figure 6.1B**).

6.3.5 Statistics

We measured changes in PA intensity as a function of changes in systolic BP. Simple linear regression was used to fit this data and plotted with 95% confidence intervals. We used a paired, two-tailed t-test to compare PA intensities pre-and-post exercise and HD for the healthy and diseased groups, respectively. We also used a student's t-test to compare the hemodynamic response to changes in blood pressure for HD *vs.* healthy subjects. A p-value < 0.05 was considered significant. We tested equality of the two population variances (Healthy *vs.* CKD/HD group) using a one-tailed F-test with an alpha = 0.05. The difference was considered significant if the F-value was less than the $F_{critical}$ value. We also ran two separate multivariate linear regressions (CKD/HD and healthy group) to study the effect of other confounding variables such as body mass index (BMI in kg/m^2), diabetic status (Y/N), UF removed (ml), age (years), sex (M/F). A covariance matrix was also calculated to study the effect of the confounding variables on each other. Future work will evaluate heart rate and body temperature in this multivariate analysis.

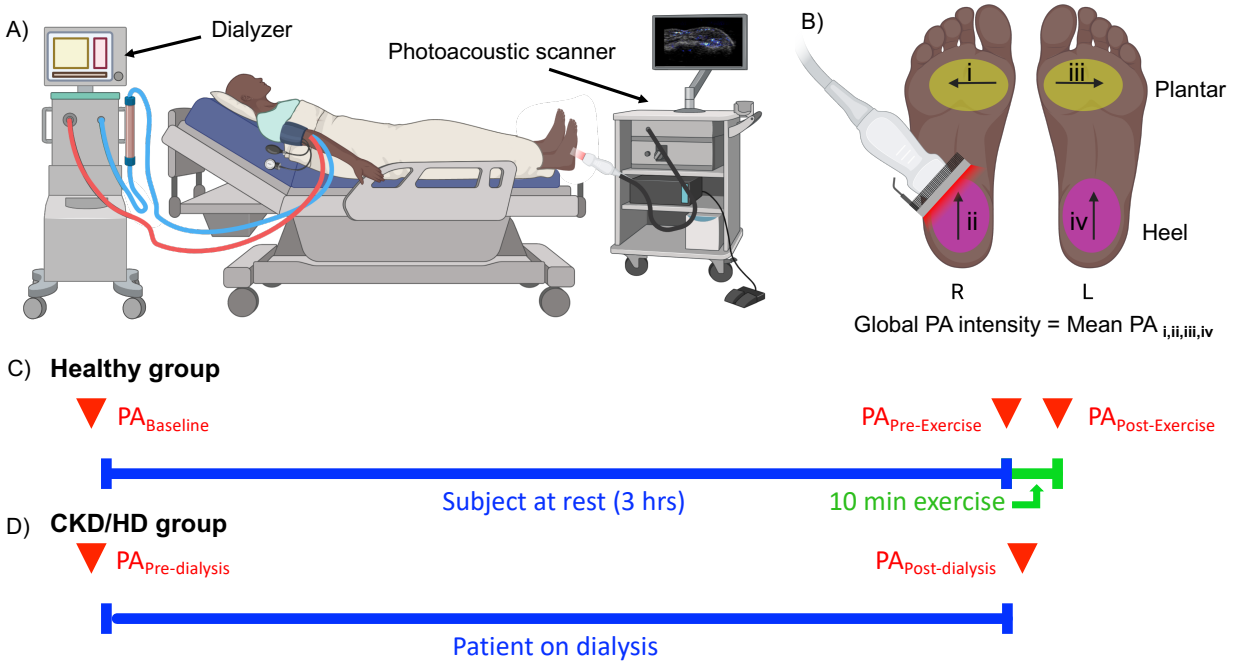

Figure 6. 1 Photoacoustic monitoring of peripheral perfusion; study design and timeline.
A. The CKD/HD group consisted of patients on hemodialysis (HD). **B**. We scanned the plantar and heel area in a medial-lateral and inferior-superior direction, respectively. Global PA intensity was defined as the mean PA intensity of all four imaging regions. **C.** Healthy subjects were scanned at baseline (T = 0 hrs), pre-exercise (T = 3 hrs), and immediately after 10 min of exercise (post-exercise). **D.** HD patients were scanned pre-and-post their HD session. Red downward triangles represent imaging time points. Blue line indicated healthy subjects at rest for 3 hrs and CKD/HD patients on dialysis. Green denotes the 10 min exercise period to increase blood pressure in healthy subjects.

6.4 Results

A total of 33 subjects were recruited for this study. All subjects were pseudonymized with an identification code at the start of the study. The healthy and the CKD/HD group are referred as HC 0XX and CKD/HD 0YY respectively. Patient demographics and BP data can be found in **Tables S1** (Healthy) and **S2** (CKD/HD).

6.4.1 Healthy control group

Eleven subjects (26.5 ± 4.1 years old) with no history of cardiovascular or other disease were recruited at UCSD. Subjects were scanned at baseline (T = 0 hrs), pre-exercise at rest (T = 3 hrs), and immediately post-exercise (**Figure 6.2A**). Exercising consisted of climbing up and down

stairs for 10 minutes. We monitored BP, heart rate, and body temperature at each imaging time point (**Table 6.2**). **Figure 6.2** shows PA data from the healthy cohort.

The PA signal under the skin surface increased by 47% ($p<0.01$), and the average BP increased by 27.6 ± 18.2 mmHg immediately post-exercise relative to baseline (**Figure 6.2 B-C**). The change in PA intensity was directly ($r = 0.81$) and significantly ($p<0.0001$) proportional to the change in systolic BP (**Figure 6.2D**). PA intensity was significantly ($p<0.0001$) higher after exercise when BP was elevated (**Figure 6.2C**). As a negative control, the subjects were maintained at rest for 3 hrs, simulating the length of a typical HD session. There were no significant changes in BP and PA intensity (baseline - pre-exercise) during the rest period ($p = 0.18$).

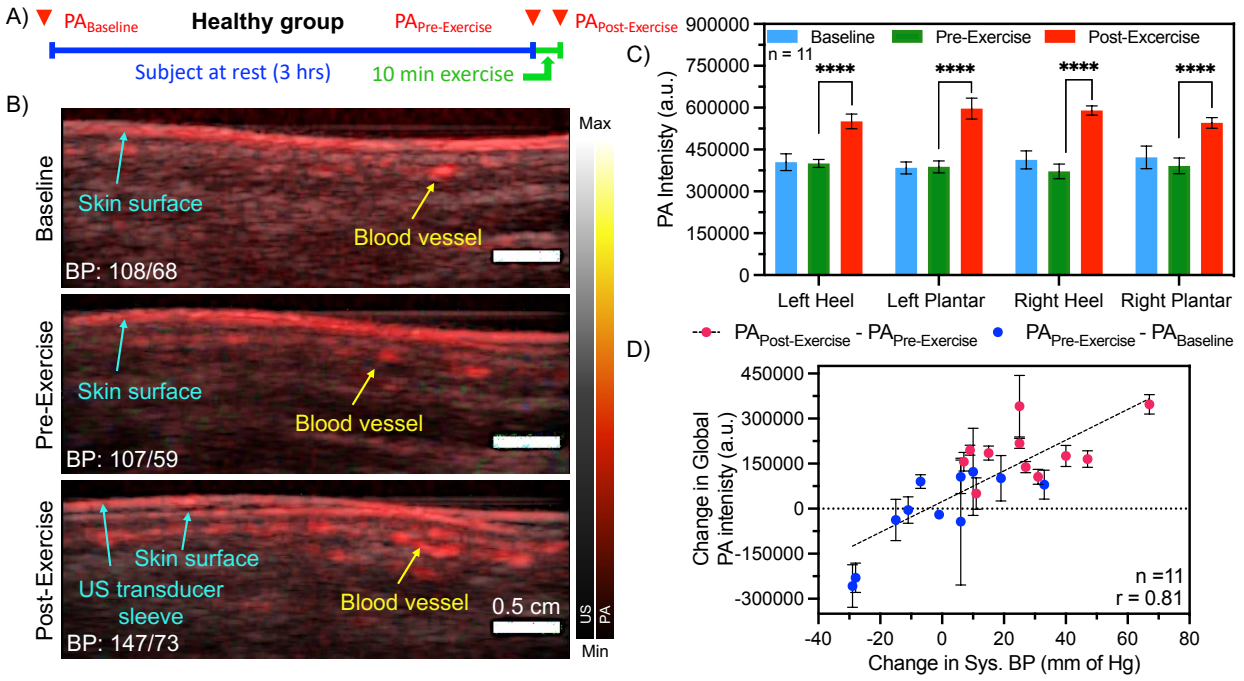

Figure 6. 2 Hemodynamic response to changes in blood pressure for healthy subjects.
A. Study design for the healthy group. Subjects were scanned at baseline (T = 0 hrs), pre-exercise at rest (T = 3 hrs), and immediately post-exercise. **B**. PA and US overlay of the left heel (HC 002). Blood vessels appear as distinct red dots marked by the yellow arrow. The skin surface is labelled in blue. At rest there was negligible change in systolic BP between baseline and pre-exercise. After a 10 min exercise session, blood pressure increased by 40 mm of Hg accompanied by a higher PA signal. PA intensity was quantified using a rectangular ROI measuring 4 cm x 1 cm. The skin surface was excluded from analysis. The ROI annotated images can be found in the supplementary information. Scale bar represents 0.5 cm. **C**. PA intensity was significantly higher after exercise (****, $p<0.0001$, n= 11) at each imaging site. There were no significant differences between $PA_{Baseline}$ and $PA_{Pre\text{-}Exercise}$. This rest period served as a negative control for the healthy group. **D.** The change in global PA intensity in the healthy group correlated with the change in systolic BP ($r = 0.81$, $p<0.001$). The 22 data points reflect changes between $PA_{Pre\text{-}Exercise} - PA_{Baseline}$ (Blue) and $PA_{Post\text{-}Exercise} - PA_{Pre\text{-}Exercise}$ (Pink) (n=11). Error bars in panel C represent standard deviation between 11 subjects and in panel D at least 90 frames.

6.4.2 CKD/HD group

Twenty-two HD patients were enrolled in this cohort (59.2 ± 14.3 years old). Two patients developed hypotension-related complications preventing a second scan and were not included the analysis due to incomplete data acquisition (**Table 6.3**). The complications were independent of the imaging study. Patients were scanned before and after a routine HD session (**Figure 6.3B**).

On average PA signal and systolic BP reduced by 11% and 16.6 ± 19.8 mm of Hg respectively. PA intensity and hence perfusion was significantly lower after dialysis (**Figure 6.3C,**

p<0.01). PA intensity in different imaging regions trended lower after dialysis but the difference was not statistically significant. PA intensity showed a positive correlation to changes in BP during an HD session (r = 0.43, p<0.01, **Figure 6.3E**). PA signal and hence perfusion was higher pre-dialysis when BP was higher. The UF removed showed a positive correlation with BP but did not directly correlate with the change in PA intensity (**Figure 6.8**).

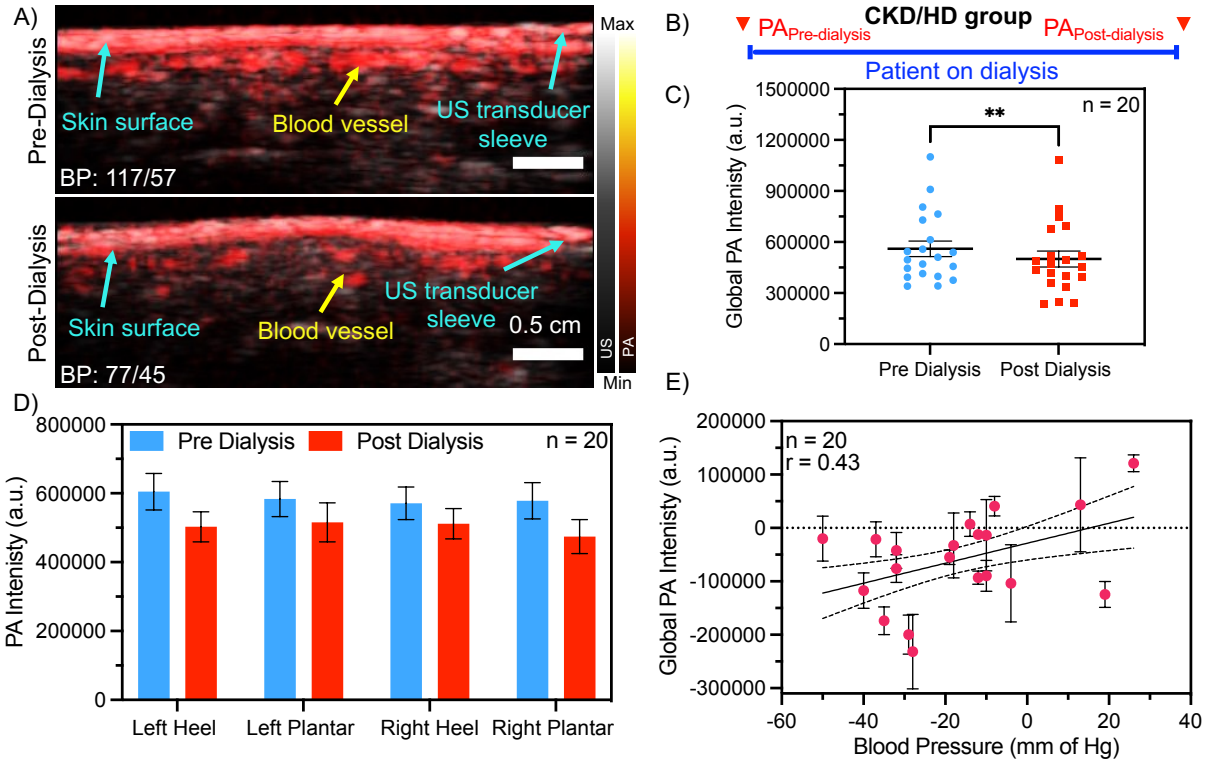

Figure 6. 3 Changes in peripheral tissue perfusion during hemodialysis.
A. PA and US overlay of the left heel in subject CKD/HD 012. Blood perfusion into the heel is considerably lower after dialysis when BP is low. Scale bar represents 0.5 cm. **B.** CKD/HD patients were scanned just before and after a routine dialysis session. **C**. A paired t-test showed a significant decrease in global PA signal and hence perfusion after dialysis (**, p<0.01). **D**. PA intensity at individual imaging areas were lower (not significantly) after dialysis. **E**. Hemodynamic response of the CKD group to changes in BP during dialysis showed a positive correlation (r = 0.43, p<0.01). Error bars in panel C-D represent standard deviation among 20 patients and in panel E at least 90 frames.

6.4.3 Healthy vs. CKD/HD subjects

HD patients showed a significantly different PA response to changes in BP compared to healthy controls (**Figure 6.4**). The mean PA intensity was significantly higher for the HD group (**Figure 6.4A**, p<0.01). More importantly, the data spread (standard deviation) for the diseased

group was significantly wider (F = 0.045; $F_{critical}$ = 0.63). The hemodynamic response to changes in BP was characterized using the slope of changing PA as a function of changing systolic pressure (**Figure 6.4B**). The slope for the HD group (1870 a.u. intensity/mm Hg) was significantly (p = 0.0001) lower than the healthy group (5116 a.u. intensity/mm Hg).

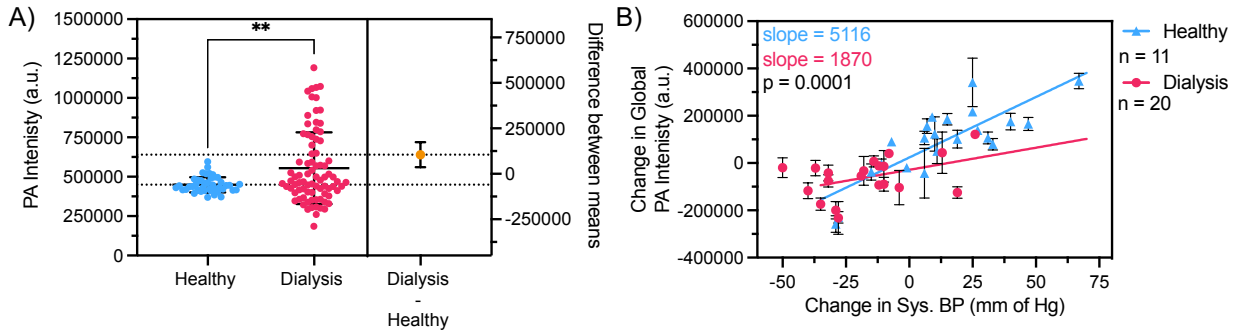

Figure 6. 4 Comparing hemodynamic response to changes in BP in health *vs.* dialysis patients.
A. PA intensities of the healthy and diseased group for all scans. CKD/HD show a significantly wider PA distribution (F = 0.045; $F_{critical}$ = 0.63) compared to the healthy group. Dialysis patients also showed a significantly higher (**, p<0.01) mean PA intensity compared to healthy control group due to higher mean BP. **B**. Healthy subjects showed a significantly higher slope (significant difference between slopes; p = 0.0001) to changes in BP compared to the CKD/HD patients. The slope of the simple linear regression characterizes the hemodynamic response to changes in BP. Error bars in panel A represent standard deviation among all scans ($n_{healthy}$ = 44; $n_{diseased}$ = 80) and in panel B at least 90 frames.

6.5 Discussion

This cohort study explored the use of photoacoustic imaging to compare changes in peripheral perfusion in response to varying BP in HD patients *vs.* healthy controls. Our data suggests that HD patients show a significantly reduced PA response (p = 0.0001) to changes in BP compared to healthy controls.

The removal of excess fluid during dialysis as UF increases hematocrit.[405] Since PA leverages hemoglobin in red blood cells to generate contrast, the increase in hematocrit should increase PA intensity after dialysis.[412, 413] But we observed the opposite effect: The global PA intensity significantly decreases after HD (**Figure 6.3C**, p<0.01). This can be attributed to the loss of BP after dialysis. A sudden loss in blood pressure results in peripheral vasoconstriction as blood

is shunted towards the vital organs to preserve their function.[414] Vasoconstriction results in reduced peripheral perfusion that is observed as lower PA intensity after HD. Hypertension is present in 68% of HD patients, and this further reduces peripheral perfusion.[415] The changes in peripheral perfusion can exacerbate the risk of developing complications such as ulceration, amputations, and cardiovascular morbidity.[416-418]

The management of BP in HD patients is challenging but extremely important. A sudden drop in BP can leave patients lethargic and weak.[419] Some patients show a paradoxical rise in blood pressure after dialysis due to an increased cardiac output and hematocrit.[420, 421] Three HD patients (13.6%) showed a paradoxical rise in BP in the HD cohort, which might explain why individual imaging regions showed no significant difference before and after dialysis (**Figure 6.3D**). Instead, a paired comparison of the global PA intensity in **Figure 6.3C** showed a statistically significant difference ($p<0.01$).

The main clinical finding of this work is that photoacoustic imaging can be used to differentiate between a healthy and diseased response to changes in BP (**Figure 6.4B**). The slopes characterize the change in perfusion as a function of BP. The healthy control cohort showed a significantly higher perfusion ($p = 0.0001$) when BP was elevated compared to the CKD/HD cohort. HD patients had a significantly wider distribution of PA intensities due to higher variability in BP compared to the control group (HD: 135.4 ± 29.1 mm of Hg; Healthy: 137.3 ± 19.4 mm of Hg, **Figure 6.4A**). Although this cohort study was not age and gender matched, we have 85% power in our results (**Figure 6.9**). Furthermore, the healthy group showed a significant positive correlation between global PA intensity and absolute systolic BP (**Figure 6.10**, $r = 0.70$, $p<0.05$) at baseline. The CKD/HD group showed no significant correlation which can be attributed to varying disease etiologies and progression. Hence, this work suggests that PA imaging can be used

to monitor peripheral tissue perfusion, a risk factor for wound formation and impaired healing.[422, 423] Others have also shown the use of PA imaging to visualize tissue perfusion but most studies use high-powered lasers which are expensive, bulky, and pose an exposure risk above the maximum permissible exposure limit.[398, 424, 425]

Whether these changes in perfusion pose a significant risk to CKD/HD patients remains to be seen. A future longitudinal study predicting wound formation and correlating changes in perfusion with wound healing will help clinicians tailor therapeutic regimes to best serve each patient. For example, patients with poor perfusion can be provided advanced therapies such as hyperbaric oxygen therapy (HBOT) that are known to promote angiogenesis, perfusion, and wound healing.[426]

Changes in BP are also dependent on other confounding factors such as BMI,[427] diabetic status,[428] age[429] etc. A multivariate linear regression (**Figure 6.11**) shows a strong positive correlation (R = 0.72) accounting for seven such confounding variables. Furthermore, the covariance matrix shows that the volume of UF removed has strong and positive covariance with the change in systolic pressure. Patients who had high volumes of UF removed, tended to show higher changes in pressure. In the healthy group (**Figure 6.12**), the main contributing variable was the change in systolic BP (R = 0.81) whereas all the other confounding variables had relatively low covariance with each other. This means that the contributor to PA change was the change in systolic BP ($p = 0.0019$). Melanin, the molecule that gives skin its characteristic color is also a major absorber and source of PA signal.[430] Our group recently studied the effect of skin tone on PA oximetry.[430] In this work, we excluded any signals from the skin surface and since patients serve as their own controls between scans, and we only evaluated the change between scans; thus, skin tone should have minimal impacts. Furthermore, this study recruited a diverse set of CKD/HD

patients and HD subjects from all possible skin types (Fitzpatrick scores 1-6) to account for skin tone bias. Other confounding variables could be changes in vascular physiology (increased resistance, calcification etc.) due to chronic diseased states in the CKD/HD groups,[431] but these are extremely difficult to account for.

6.6 Limitations

The LED-based PA system used in this work is an inexpensive, portable, and non-invasive imaging system. The LEDs used in this system operate 1000-fold under the maximum permissible exposure limit of 20 mJ/cm^2.[432] But the system is limited in data processing as it condenses the number of frames between acquisition and export. Since we used a handheld scanner for all scans, it is difficult to generate 3D maps of the imaging area even though the system is capable to do so. The use of motion compensation and deep-learning algorithms to reduce noise and align frames could help map perfusion and oxygenation of the tissue.[253, 377] Future work will look to map tissue oxygenation in real time.

Within the CKD/HD group, hematocrit readings could help normalize PA intensity changes for variable fluid loss between patients. But not all dialyzers were equipped to measure hematocrit in real time limiting our analysis.

6.7 Conclusion

The management of BP and peripheral perfusion in dialysis patients is extremely important and challenging to monitor. Peripheral perfusion measurements are rare at the point-of-care. In this work, we imaged peripheral perfusion in 20 HD patients and 11 healthy subjects using PA imaging. We compared the peripheral tissue perfusion response to changes in blood pressure due to dialysis or exercise. The healthy group showed a positive correlation to changes in BP. The CKD/HD group also showed a positive correlation to BP changes during a dialysis session. In

comparison, the CKD/HD group showed a significantly reduced PA response to changes in blood pressure compared to healthy controls.

6.8 Acknowledgements

Chapter 6, in full, is a reprint of the material as it appears in Monitoring peripheral hemodynamic response to changes in blood pressure via photoacoustic imaging. Mantri, Yash; Dorobek, Tyler R.; Tsujimoto, Jason; Penny, William F; Garimella, Pranav S.; Jokerst, Jesse V., Photoacoustics, 2022. The dissertation author was the primary investigator and author of this paper.

6.9 Supplementary information

Table 6. 2 Healthy control group.

Blood pressure, heart rate, and temperature at baseline, pre-exercise, and post exercise.

Subject demographics			Baseline (T = 0 hrs)				Pre-exercise (T = 3 hrs)				Post-exercise			
Subject ID	Age	Sex	Systolic (mm of Hg)	Diastolic (mm of Hg)	Heart Rate (bpm)	Temp (°C)	Systolic (mm of Hg)	Diastolic (mm of Hg)	Heart Rate (bpm)	Temp (°C)	Systolic (mm of Hg)	Diastolic (mm of Hg)	Heart Rate (bpm)	Temp (°C)
HC 001	25	M	132	79	65	35.2	138	81	68	35.2	149	86	139	34.9
HC 002	26	M	108	68	66	35.3	107	59	72	34.0	147	73	122	35.0
HC 003	24	M	163	87	84	34.6	135	83	90	34.2	160	86	94	31.7
HC 004	29	M	128	93	84	34.7	121	80	96	34.6	168	84	126	33.0
HC 005	24	M	124	109	104	34.0	130	84	124	34.5	139	93	135	30.1
HC 006	33	M	133	91	80	35.0	122	73	81	34.6	153	94	114	31.4
HC 007	25	M	136	64	69	34.4	121	67	64	30.0	188	85	115	31.0
HC 008	28	M	112	79	72	34.8	122	81	79	31.2	147	80	120	30.9
HC 009	29	M	118	77	102	34.0	137	80	74	30.1	152	93	99	29.2
HC 010	31	M	155	93	72	34.0	126	81	67	30.8	133	88	121	34.5
HC 011	18	M	112	70	92	34.0	145	85	80	34.0	172	75	137	32.9

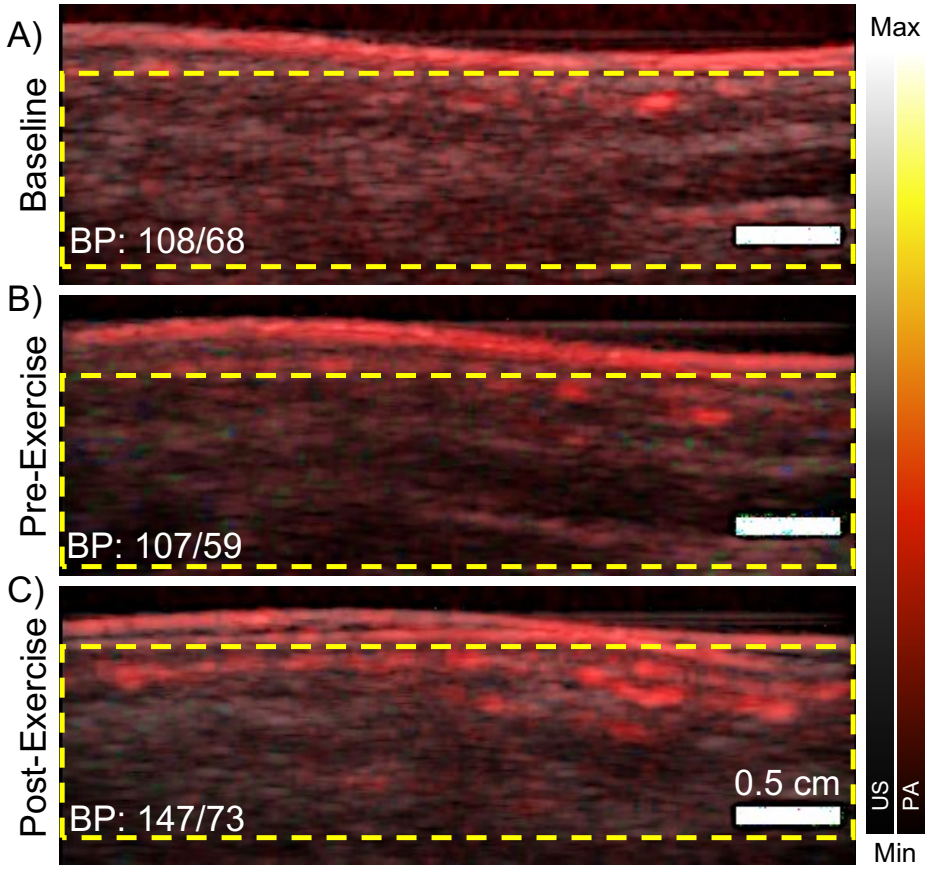

Figure 6. 5 ROI analysis for the healthy group.
Region of interest analysis for quantifying PA intensity for healthy subjects (HC 002 in this figure). We used a 4 cm wide and 1 cm deep rectangular ROI that was kept constant for all scans. The skin layer was excluded from the analysis. Scale bars measure 0.5 cm. PA intensity and therefore perfusion increased with a rise in BP (40 mm of Hg increase after exercise). Scale bar represents 0.5 cm.

Table 6. 3 CKD/HD group.

22 patients on hemodialysis were recruited for this study. We recorded blood pressure and ultrafiltrate removed (UF removed) before and after a dialysis session. Two patients (marked in red) were excluded from analysis due to complications independent of imaging during the session.

Patient demographics			Pre-dialysis		Post-dialysis		UF Removed (ml)
Patient ID	Age	Sex	Systolic (mm of Hg)	Diastolic (mm of Hg)	Systolic (mm of Hg)	Diastolic (mm of Hg)	
CKD/HD 001	70	M	134	65	97	59	3200
CKD/HD 002	64	M	132	68	NA	NA	N/A
CKD/HD 003	80	F	161	68	142	65	3100
CKD/HD 004	49	F	115	72	87	52	2457
CKD/HD 005	48	F	135	68	127	67	1246
CKD/HD 006	73	F	126	80	116	86	3125
CKD/HD 007	61	M	161	70	143	83	2895
CKD/HD 008	71	F	174	59	124	55	3890
CKD/HD 009	55	F	209	72	166	78	4253
CKD/HD 010	61	F	188	107	156	69	2497
CKD/HD 011	70	M	168	76	154	62	3180
CKD/HD 012	61	F	117	57	77	45	5491
CKD/HD 013	68	F	154	69	173	77	1459
CKD/HD 014	67	F	159	65	149	56	1885
CKD/HD 015	53	M	133	72	121	58	3869
CKD/HD 016	62	F	119	68	90	55	2362
CKD/HD 017	23	F	131	114	96	65	692
CKD/HD 018	34	F	138	88	134	91	3057
CKD/HD 019	58	M	156	87	169	95	1674
CKD/HD 020	77	F	154	87	122	59	2165
CKD/HD 021	62	M	94	57	120	50	1887
CKD/HD 022	35	F	107	91	95	78	2995

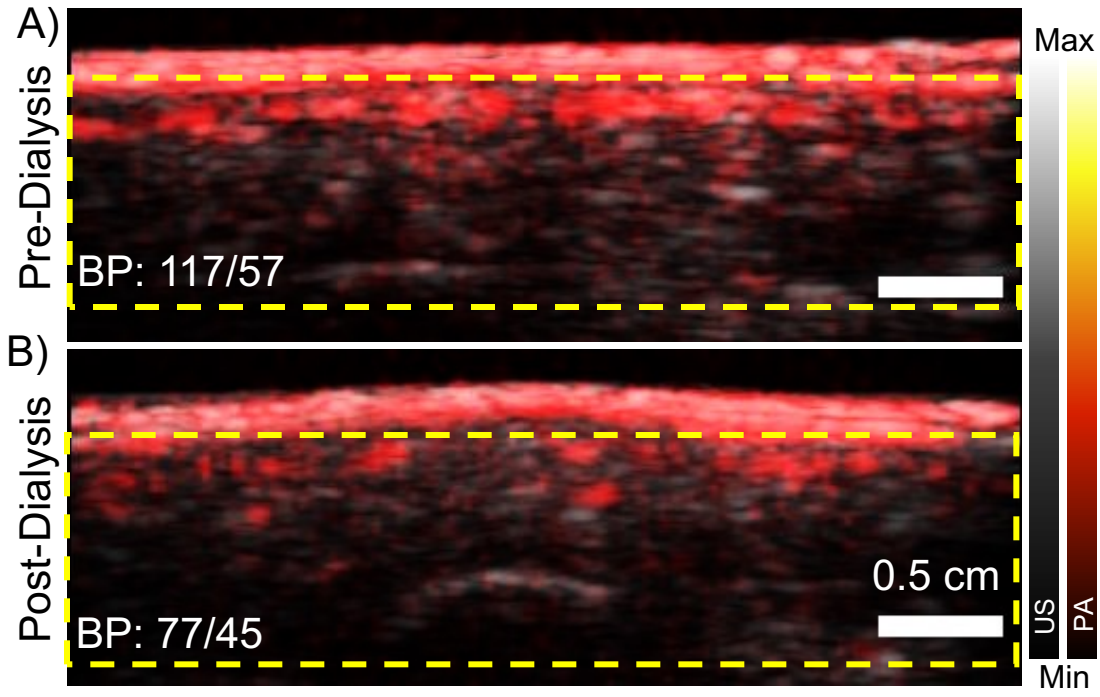

Figure 6. 6 ROI analysis for the CKD/HD group.
ROI analysis for the diseased group (CKD/HD 012 in this figure). These images are from the left heel. After dialysis (panel B), PG 012 experienced a 40-mm-Hg drop in BP resulting in reduced PA signal and perfusion. Scale bars represents 0.5 cm.

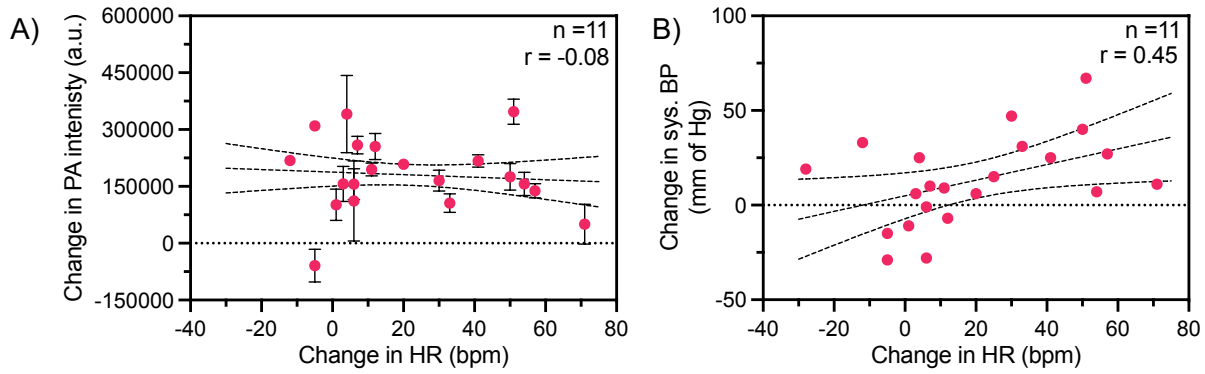

Figure 6. 7 Effect of heart rate (HR) on perfusion and systolic BP in the healthy cohort.
A. The change in HR had no significant effect on the change in PA intensity. **B.** The change in BP was positively correlated to an increasing HR due to exercise.

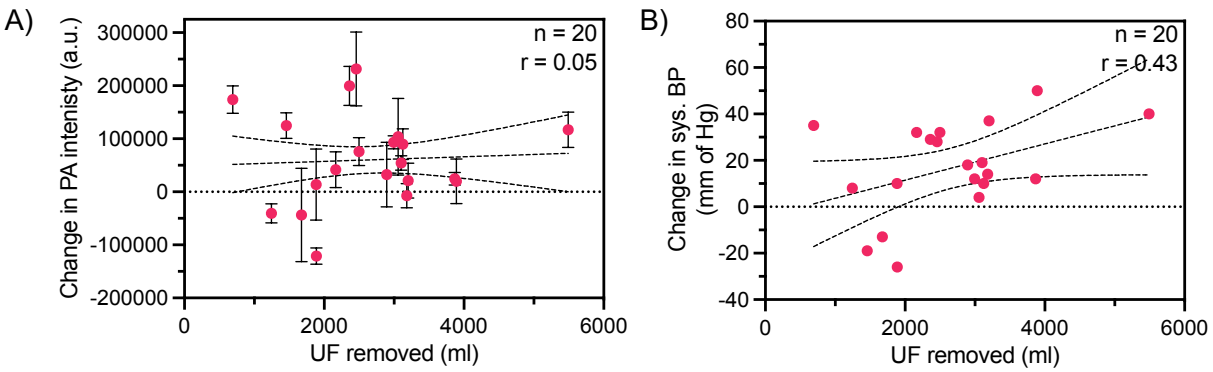

Figure 6. 8 Effect of ultrafiltrate (UF) removed on perfusion and blood pressure.
A. Changes in PA and perfusion were independent of the UF removed. **B.** The change in systolic BP was not significantly correlated to the amount of UF removed.

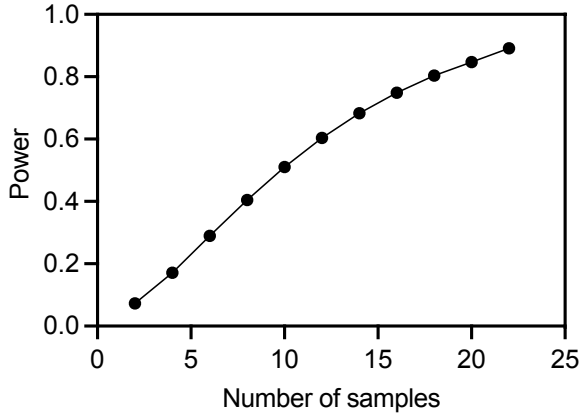

Figure 6. 9 Power analysis.
Power curve for the dialysis patients shows 85% power with n = 20.

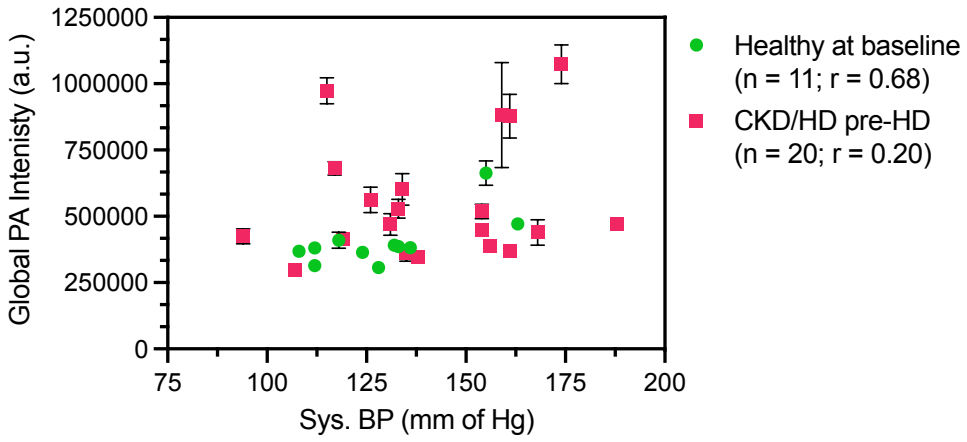

Figure 6. 10 Correlation between global PA intensity and absolute systolic BP at rest / baseline.
The healthy group shows a significant positive correlation ($r = 0.68$; $p<0.05$) compared to the CKD/HD group ($r = 0.20$, $p>0.05$).

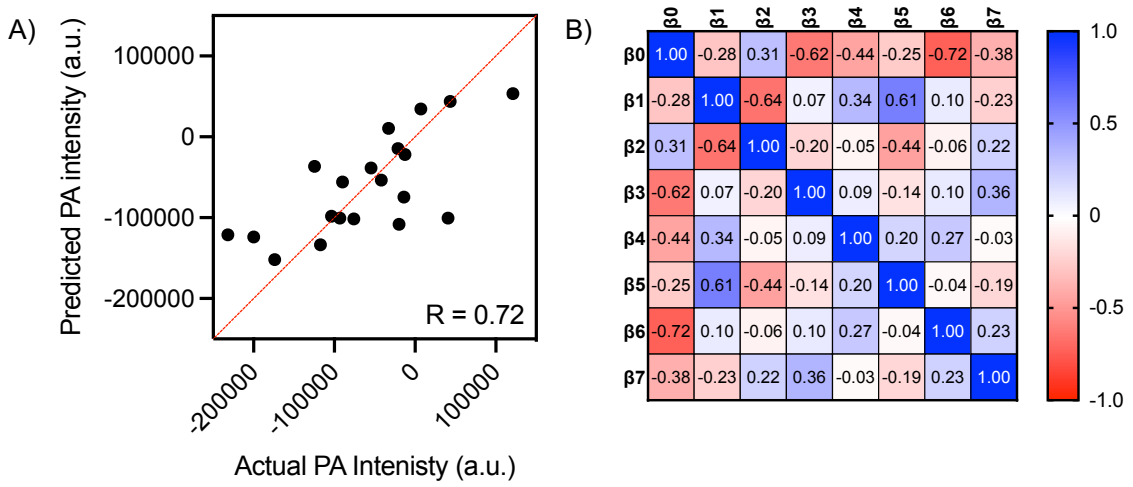

Figure 6. 11 Multivariate linear regression analysis for the CKD/HD group.
A. The coefficient of multiple correlation (R = 0.72) with 7 independent variables shows PA intensity can be predicted using the below-mentioned confounders. **B.** Covariance matrix reporting the degree of intertwining between the confounding variables. **B0** = Intercept (mean response when all the variables = 0)**; β1** = change in Sys BP (mm of Hg); **β2** = change in Dia. BP (mm of Hg); **β3** = age (years); **β4** = sex (Female/Male); **β5** = UF removed (ml); **β6** = BMI (kg/m^2); and **β7** = diabetic status (No/Yes). Higher positive values indicate strong covariance between those variables. For example, between **β5** and **β1** = 0.61 indicates that when a higher volume of UF is removed, the change in systolic pressure during an HD session also tends to be higher. Similarly, between **β7** and **β4** = -0.03 indicates that the patients BMI and sex are not related to each other.

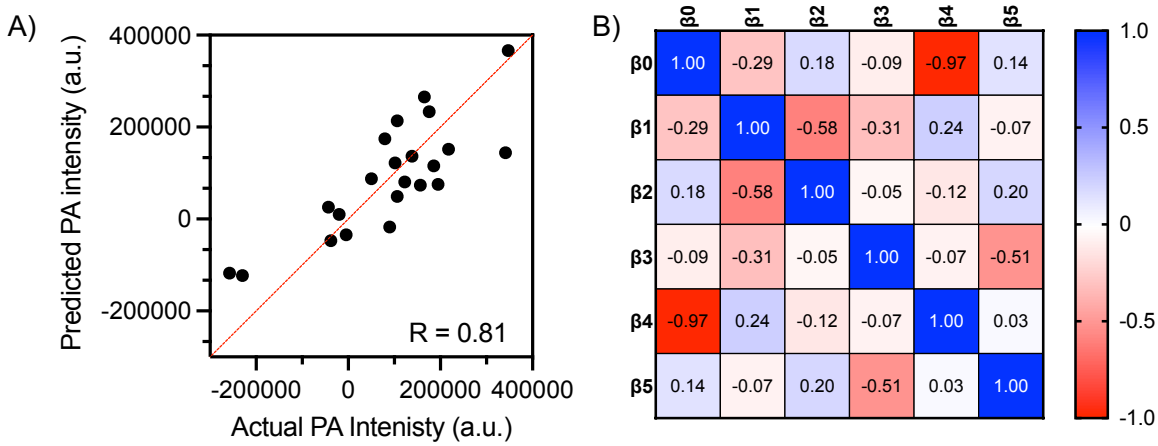

Figure 6. 12 Multivariate linear regression analysis for the healthy group.
A. The coefficient of multiple correlation (R = 0.81) with five independent variables shows PA intensity can be predicted using the below-mentioned confounders. **B.** Covariance matrix reporting the degree of intertwining between the confounding variables. **B0** = Intercept (mean response when all the variables = 0)**; β1** = change in Sys BP (mm of Hg); **β2** = change in Dia. BP (mm of Hg); **β3** =change in heart rate (BPM); **β4** = Age (yrs); **β5** = change in body temperature (°C). Age showed a strong negative correlation with the intercept, meaning younger subjects showed higher PA signals. The covariance between all other parameters was low in the control group. This means that the main contributor to the correlation in panel A is the change in systolic BP (p = 0.0019).

Chapter 7: The impact of skin tone on photoacoustic oximetry and tools to minimize bias

7.1 Abstract

The major optical absorbers in tissue are melanin and oxy/deoxy-hemoglobin, but the impact of skin tone and pigmentation on biomedical optics is still not completely understood or adequately addressed. Melanin largely governs skin tone with higher melanin concentration in subjects with darker skin tones. Recently, there has been extensive debate on the bias of pulse oximeters when used with darker subjects. Photoacoustic (PA) imaging can measure oxygen saturation similarly as pulse oximeters and could have value in studying this bias. More importantly, it can deconvolute the signal from the skin and underlying tissue. Here, we studied the impact of skin tone on PA signal generation, depth penetration, and oximetry. Our results show that subjects with darker skin tones exhibit significantly higher PA signal at the skin surface, reduced penetration depth, and lower oxygen saturation compared to subjects with lighter skin tones. We then suggest a simple way to compensate for these signal differences.

7.2 Introduction

Biomedical optics play an increasingly powerful role in human health, but the impact that skin tone and skin pigmentation have on optical imaging and diagnostics is not completely understood or adequately addressed. Melanin governs skin tone and is a strong light-absorbing pigment; thus, darker skin absorbs more photons leaving less light to probe the deeper tissues of interest. The primary challenge for optical medical devices is that variations in skin pigmentation can alter measurements between subjects in ways that the device was not designed to anticipate. Variable melanin content/skin tone has been reported to adversely affect the performance of a broad range of optical medical devices including pulse oximeters,[433] cerebral tissue oximeters,[434] hyperspectral reflectance imagers,[435] bilirubinometers,[436] wearable photoplethysmography,[437] other "wearables" in the consumer market (e.g., smart watches),[438, 439] and photoacoustic (PA) imagers.[440] In one recent high-powered example,[433] 48,000 pulse oximetry readings in 8,675 white subjects and 1,326 black subjects were compared with arterial oxygen saturation measurements. The results, while controversial,[441] showed that Black subjects were 3.2-fold more likely to have undiagnosed hypoxemia, and potentially not get needed supplemental oxygen. This can lead to differences in health outcomes because Black people, Hispanics, and others often have darker skin tones. This disparity in health outcomes illustrates the importance of investigating the impact of skin pigmentation during, not after, medical device development.

Hypoxemia is an abnormal decrease in partial pressure of oxygen in the blood – a key parameter in clinical decision making in diseases including cancer,[442-444] COVID,[445, 446] wound care,[447-449] chronic kidney disease,[450, 451] aging,[452, 453] *etc*. Measuring blood oxygen saturation (sO_2) can be relatively straightforward due to the differences in absorption between oxy-and-deoxy-hemoglobin. But melanin is also a major optical absorber in tissue. Clinically, dermatologists use

the Fitzpatrick scale to classify people with different skin tones.[454] The Fitzpatrick scale is a numerical classification system (1 (pale white) – 6 (black/very dark brown)) to estimate the response of different skin types to ultraviolet light (**Figure 7.1A**).[455] Currently, few biomedical devices actively measure or compensate for changes in skin color between subjects.

Tissue optical absorption is quantified by the local absorption coefficient ($\boldsymbol{\mu_a}$). A higher μ_a means that more photons are absorbed, which reduces the light penetrance into tissue. Tissue μ_a is a linear summation of the absorption of all chromophores present, weighed by chromophore concentration, **Equation 7.1**. Here $\boldsymbol{\mu_a}$ denotes the absorption coefficient (cm^{-1}); $\boldsymbol{\lambda_i}$ is the imaging wavelength (nm); $\mathbf{HbO_2}$ and **Hb** denote oxy-and-deoxy-hemoglobin respectively. In tissue, $\boldsymbol{\mu_a}$ varies significantly with wavelength due to the inherent spectral absorption properties of constituent molecules like hemoglobin and melanin (**Figure 7.1B**).[456, 457] Other absorbing species in tissue include lipids, proteins, collagen, water *etc*.[458] But these have minimal absorption in the biological optical window (700 – 900 nm).[1, 459] Many biomedical optics devices do not consider potential variation or uncertainty in $\mu_{a,skin}$ and thus unexpected differences in tissue light transport can compromise performance of optical technologies including pulse oximetry, fluorescence, PA, *etc*.[460]

$$\boldsymbol{\mu_{a,skin}}(\boldsymbol{\lambda_i}) = \mu_{a,HbO_2}(\lambda_i)[HbO_2] + \mu_{a,Hb}(\lambda_i)[Hb] + \mu_{a,melanin}(\lambda_i)[melanin] + \mu_{a,other\ absorbers}(\lambda_i)[other\ absorbers] \quad \text{Equation (7.1)}$$

PA produces signal as a function of $\boldsymbol{\mu_a}$.[461] PA imaging delivers diffused light through tissue, where the photons are absorbed by dominant chromophores (hemoglobin and melanin) and converted to sound waves for acoustic imaging.[1, 223] The intensity of PA signal is directly proportional to $\boldsymbol{\mu_a}$.[223] Vasculature and blood oxygen saturation (sO_2) can be mapped in 3D using multiple wavelengths. While many optical oximetry techniques offer an ensemble or point-based

value of oxygenation, PA imaging offers a 3D map that can measure oxygenation through many centimeters of tissue.[342, 425, 462, 463] Furthermore, PA can also deconvolute the skin layer from the tissue layer[247, 309, 464], and the first FDA-approved system was recently launched (Seno Medical).[465-467]

This work is an observational case series that aims to measure photoacoustic signal and oxygenation differences in healthy human subjects as a function of skin tone. We performed PA imaging and oximetry on nine healthy volunteers with a Fitzpatrick skin type of 1,4, and 6 (**Figure 7.1C-D;** n=3 per skin type).[455] Our data shows significant changes in PA signal as a function of skin tone. Using the training data from the nine volunteers, we formulated a compensation equation that was tested on new Fitzpatrick type 3 and 5 subjects. Our case series shows that compensating for differences in skin tone is possible for photoacoustic oximetry.

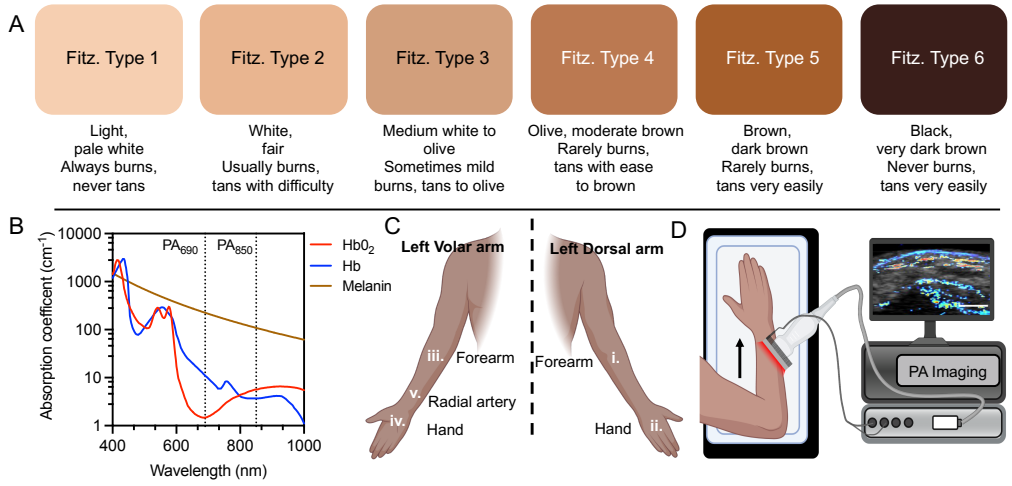

Figure 7. 1 Skin tone classification.
Classification of skin tone based on the Fitzpatrick scale.[455] Fitzpatrick 1 is lightest and 6 is the darkest skin tone. **B.** Absorption coefficient (μ_a in cm^{-1}) of oxy-deoxyhemoglobin and melanin in the visible and near infrared region. Data from ref. [457] and [456]. PA imaging was done at 690 and 850 nm. **C.** Nine volunteers classified as Fitzpatrick 1, 4, and 6 were scanned at 5 locations on the left arm. **D.** Typical scan of the dorsal forearm using a handheld photoacoustic transducer. Arrow annotates the scan direction.

7.3 Materials and methods

7.3.1 Subjects

This work was performed in compliance with the ethical rules for human experimentation stated in the 1975 Declaration of Helsinki and approved by the University of California San Diego's Human Research Protections program. Eleven volunteers were recruited for this study. Subjects signed an informed written consent prior to participation. Inclusion criteria were (i) subjects >18 years old and able to provide informed written consent, (ii) pulse oximetry reading >96% on the left index finger at rest,[468] and (iii) a body mass index ranging from 18.5 – 25 kg/m^2.[469] Exclusion criteria were (i) subjects with known cardiovascular disease history, (ii) on medications that alter hemodynamic status such as blood pressure, oxygenation *etc*. (iii) presence of wounds in the imaging area, and (iv) previous history of skin disorders.

All subjects were scanned over five locations on the left arm: (i) dorsal forearm, (ii) dorsal hand, (iii) volar forearm, (iv) volar hand, and (v) radial artery. An area measuring approximately 4 cm x 3 cm was scanned at imaging spots i – iv. The radial artery oxygenation was scanned in a single imaging plane. Before scanning, the imaging area was cleaned using alcohol. Pulse oximetry was done using a finger pulse oximeter from ZAcurate, Texas, USA. Subjects were classified into different Fitzpatrick skin types subjectively by Y.M. and objectively using the ITA scale. The calculations for determining ITA score can be found elsewhere.[470] The skin color quantification was done using a commercially available WR10QC portable colorimeter from Fru, China. The colorimeter used a D65 light source, CIE 10^o observer, and measured CIEL*a*b color space.

7.3.2 Photoacoustic-ultrasound imaging

We used two commercially available PA imaging systems: one LED-based and one laser-based. The LED-based system was the AcousticX from Cyberdyne Inc., Tsukuba, Japan. The AcousticX system uses two LED-arrays operating with a pulse width of 70 ns and 4 KHz repetition rate. The illumination wavelengths used for imaging points i – iv were 850 and 690 nm separately. The radial artery was imaged using a combination of 850 and 690 nm illumination to measure oxygen saturation. The AcousticX employs a 128-element ultrasound transducer operating at a central frequency of 9 MHz, bandwidth of 80.9%, and with a 4-cm field-of-view. We used the proprietary AcousticX software for image acquisition and visualization.

The laser-based system was the VisualSonics Vevo 2100 LAZR from FUJIFILM VisualSonics Inc., Toronto, Canada. We scanned with a LZ250 transducer with a central frequency of 21 MHz. Images were acquired at 850 and 690 nm. PA spectra was acquired between 680 – 970 nm with a step size of 2 nm. PA oximetry was carried out using the in-built OxyHemo function using 750 and 850 nm illumination. Doppler imaging on this system was used to confirm the position of the radial artery.

We used sterile ultrasound coupling gel (Aquasonic 100, Parker Laboratories Inc. Fairfield NJ, USA) for coupling with the skin surface. All images were acquired at 30 frames/s. Image acquisition settings such as gain, dynamic range, and averaging were kept consistent for each machine between all Fitzpatrick skin types. A minimum of 80 frames were acquired for each scan. All scans were done using a hand-held transducer in a proximal-distal direction.

7.3.3 Image processing

All the image processing was done using Fiji, an ImageJ extension, version 2.1.0/1.53c. Data was plotted using Prism version 9.0.0. A minimum of 80 frames were processed for each

scan. For the two wavelengths (690 and 850 nm), we processed a minimum of 640 frames for regions i-iv. For the radial artery, a minimum of 30 frames were acquired. Both the LED and laser-based systems acquire oximetry images in a step-by-step function of PA at wavelength 1 – 2 followed by B-mode US. Internally, the processing is done using a pixel-by-pixel analysis using the manufacturer's software and algorithms. The LED-based system does offer more control over weighing signal from each wavelength and the extinction coefficients of oxy-deoxy-hemoglobin that can help to correct for differences in skin absorption.

Data was quantified using custom ROI analysis for each 80-frame scan. The ROI outline followed the contour of the skin, and we quantified the mean PA intensity within the ROI. We were careful to include only the skin surface using the B-mode US. The ROI was dynamically changed for every frame of the scan. To quantify subdermal PA signal, we drew a standard ROI measuring 1cm deep and 4 cm wide. This ROI was held constant throughout the 80 frames while ensuring exclusion of the skin surface. We quantified the integrated PA intensity, i.e., the sum of all pixel intensities within the ROI. The integrated intensity was chosen to quantify net noise and clutter, and reduce the effect of dark pixels on the PA.

To measure oxygen saturation, we drew custom ROIs on the oximetry images taken under default settings from both scanners. We averaged the s_aO_2 across 30 frames. PA at the superior edge of the vessel was representative of the arterial sO_2 .

The compensation equation was formed by plotting the compensation factor *vs.* the Fitzpatrick scale. The compensation factor was defined as the ratio between pulse oximetry sO_2 and PA s_aO_2. We calculated a unique compensation factor for each subject. The compensation factor for each skin type was an average of three subjects. The correction factors for all the

Fitzpatrick types were calculated by solving the compensation equation. The correction factors were then tested on two new subjects (Fitzpatrick types 3 and 5).

7.3.4 Statistics

The error bars in all plots represents standard deviation. Standard deviation in grouped analysis of n = 9 for Fitzpatrick types 1, 4, and 6 (3 each) was propagated from each patient where we quantified a minimum of 80-frames each. A simple linear regression was fit to the data measuring changes in PA signal and sO_2 as a function of Fitzpatrick skin type. All significance testing was done using a 2-tailed, unpaired student's t-test; p-value < 0.05 was considered significant.

7.4 Results

7.4.1 Effect of skin tone on surface photoacoustic signal

We imaged the dorsal and volar forearm and hand of nine subjects with Fitzpatrick skin type of 1, 4, and 6 (n=3 each) (**Table 7.2, Figure 7.1C**). The forearm and hand were selected because they have a relatively uniform distribution of melanin (**Figure 7.6**), are relatively flat to facilitate scanning, and are relatively free of hair that can compromise imaging. **Figure 7.2** shows the change in PA intensity as a function of Fitzpatrick skin type at 850 nm. PA intensity increases significantly ($p<0.0001$, $R^2 = 0.81$) between Fitzpatrick scales 1 – 4 (104%) and 4 – 6 (47%). Subjects with darker skin tones showed considerably more streaking artifacts, noise, and clutter (**Figure 7.2D-F and H**).[471] Within skin types, we observed significant changes ($p = 0.016$, Fitz. 4; $p = 0.008$, Fitz. 6) in PA intensity between the dorsal and volar hand of skin types 4 and 6 (at 850 nm) (**Figure 7.7**). Dorsal areas were both darker and had higher signal. The dorsal and volar forearm within skin types 1, 4, and 6 showed no significant change ($p>0.05$) in photoacoustic

intensity, which is consistent with reports of similar melanin content in photo-protected skin.[472] The region-of-interest (ROI) outlines used for quantification can be found in the supplementary information (**Figure 7.8**).

PA imaging at 690 nm also followed an increasing trend as a function of skin type ($p<0.01$, $R^2 = 0.68$) (**Figure 7.8**). Although the PA signal was consistently higher at 850 than 690 nm, this difference was not statistically significant ($p>0.05$) (**Figure 7.8I)**. The slopes of PA intensity *vs.* Fitzpatrick scale at 850 and 690 nm have no significant difference ($p = 0.14$). Depth penetration into tissue was reduced at 690 nm as shorter wavelengths scatter more.

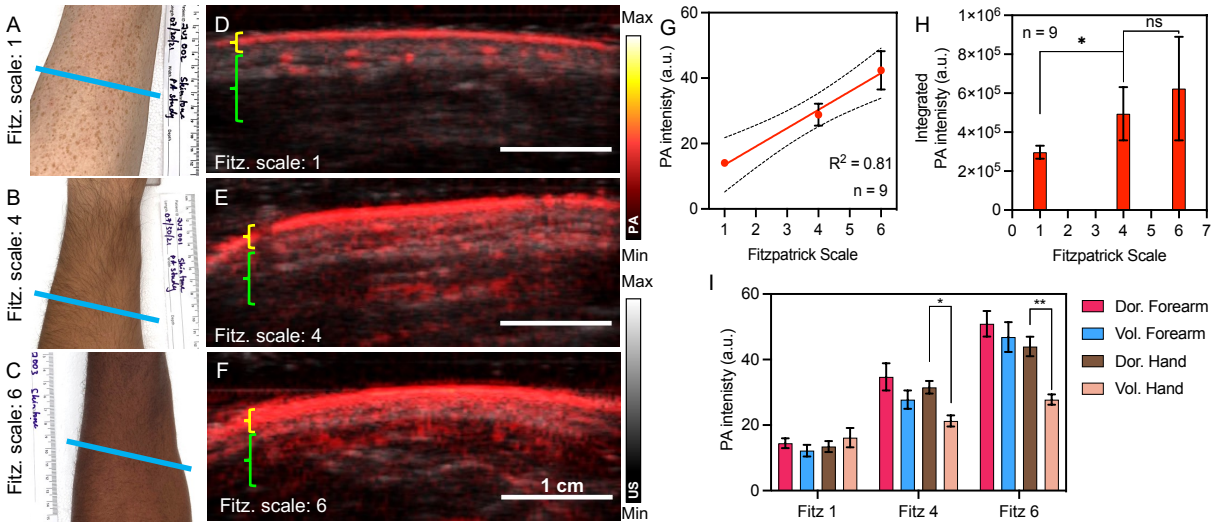

Figure 7. 2 Photoacoustic signal at 850 nm increases as a function of skin tone.
Photographic images of the dorsal forearm of Fitzpatrick scale 1, 4, and 6 healthy volunteers. **D-F**. PA and US overlay from the blue imaging plane in A-C shows increase in PA signal and clutter from the skin surface. Yellow and green brackets mark skin and subdermal tissue respectively. **G.** PA intensity is linearly correlated with skin tone on the Fitzpatrick scale ($R^2 = 0.81$, $n = 9$). **H**. Integrated PA intensity of 1 cm subdermal tissue shows an increase in noise and clutter in subjects with darker skin tone. **I**. PA intensity is significantly different ($p< 0.05$) between dorsal and volar hand in the same group (Fitz 4, and 6 $n = 3$ each). Error bars represent standard deviation between the three subjects in each group, and scale bars in D-F denote 1 cm. These images were acquired on the LED-based PA system.

7.4.2 Effect of skin tone on photoacoustic depth penetration

We also investigated the effect of skin tone on penetration depth to visualize deep blood vessels beneath the skin (**Figure 7.3**). Blood vessels were easily mapped in the subject with Type 1 skin (**Figure 7.3C and E**), but the high surface absorption in the Type 6 subject reduced light

penetrance and thus contrast detectability of the underlying blood vessels (**Figure 7.3D and F**). With the skin signal removed the signal-to-noise ratio for Fitz. 1 was 12.6 dB and Fitz. 6 was 3.2 dB (**Figure 7.9**). Furthermore, a power analysis with 9 subjects and a null hypothesis that the true mean photoacoustic signal between each of the Fitzpatrick skin tone groups are equal shows 88% power in our study (alpha = 0.05, **Figure 7.10**).

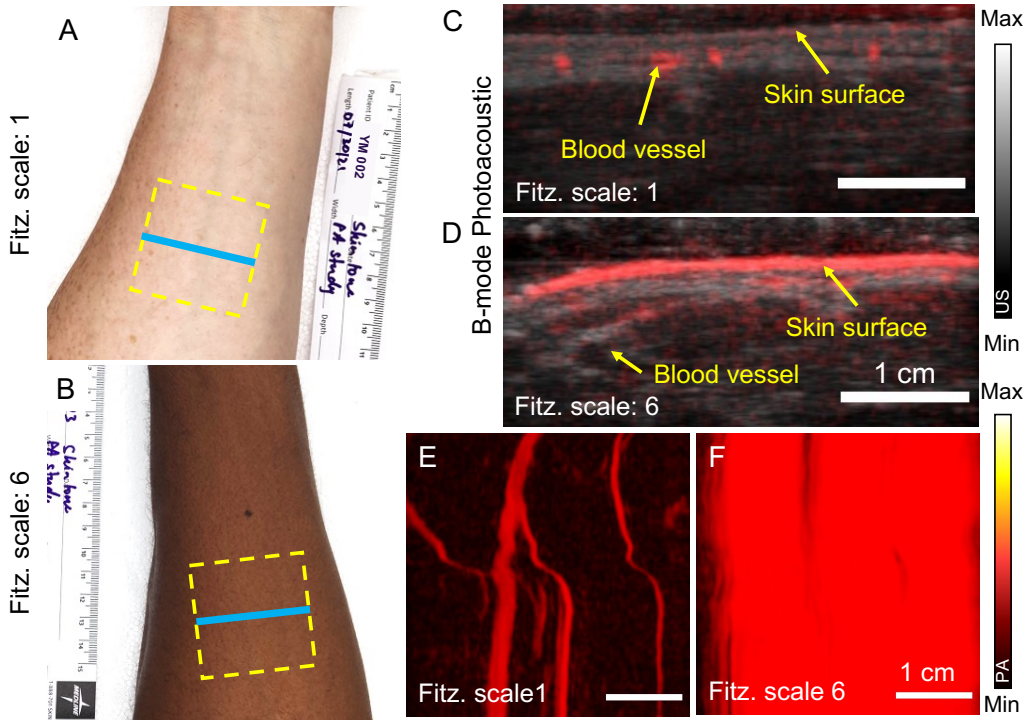

Figure 7. 3 High melanin in darker skin subjects obscures the underlying blood vessels in PA imaging (850 nm). **A-B.** Volar forearm of a Fitz. 1 and 6 subject respectively. Blue line are the planes imaged in panels **C/D**. **C**. Blood vessels are clearly visible in Fitz. 1 subject because light can penetrate through the skin. **D.** High melanin concentration in a Fitz. 6 subject reduces penetration depth and obscures underlying blood vessels which are visible on the US. **E-F.** Maximum intensity projection of all planes in the box shown as dashed square in **A/B** shows the map of blood vessels on a Fitz. 1 subject. The strong surface signal in the Fitz. 6 subject masks the vasculature underneath. These images were acquired on the LED-based PA system.

7.4.3 Photoacoustic oximetry of the radial artery

Clinically, the radial artery is a commonly used sampling site for blood gas measurements.[473] The radial artery should also include highly oxygenated blood in these healthy subjects (All subjects enrolled in this study had an sO_2 range between 96 – 100% measured via pulse oximetry (**Table 7.2**). Hence, we used PA imaging to non-invasively measure arterial sO_2 in

the radial artery as a function of skin tone. The position of the radial artery was confirmed using doppler-ultrasound (**Fig. S6**), and arterial pulsation was visible on conventional grayscale ultrasound (US). We used a combination of 850 and 690 nm illumination on the LED-based PA system to measure oxygen saturation.

Subjects with darker skin tones showed significantly lower PA s_aO_2 (Fitz. 4: -7.98%; Fitz 6: 18.2%) compared to pulse oximetry ($p<0.01$) (**Figure 7.4**). The increase in melanin content in subjects with darker skin tones linearly increases the perceived sO_2 at the skin surface (**Figure 7.4H**). The PA sO_2 measurements from the nine subjects were used as a training set to formulate a skin tone compensation equation (inset **Figure 7.4I**). We assumed that the pulse oximeter readings were the ground truth and defined a correction factor to compensate for the deviated measurements using PA (**Figure 7.4I**). The compensation factor was defined as a ratio between the pulse oximeter sO_2 (%)**:** PA measured s_aO_2 (%).

While a recent NEJM article showed a bias in pulse oximetry measurements,[433] in our case series, pulse oximeter measurements showed no significant differences between different Fitzpatrick skin types (**Figure 7.4J**). This could be due to a small sample size and because we only measured young and healthy volunteers (mean age: 26.7 ± 3.7 years; BMI range: 19-24 kg/m^2). The PA sO_2 measurements were significantly lower compared to pulse oximetry for darker skin types ($p<0.01$) (4 and 6, **Figure 7.4J**)

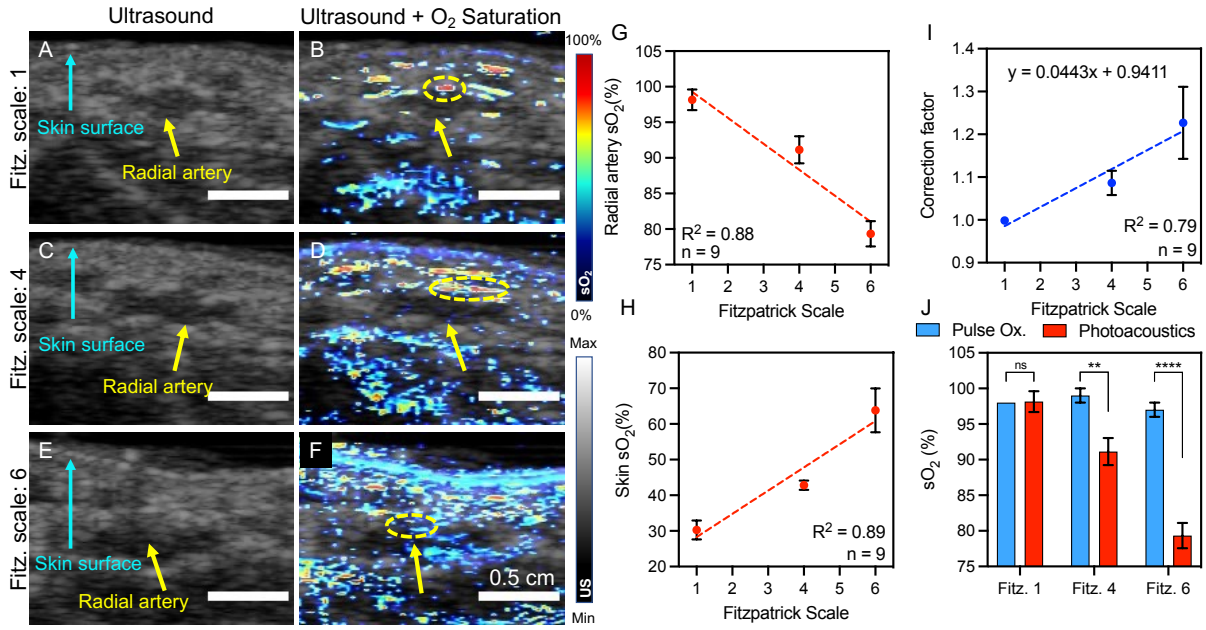

Figure 7. 4 Effect of skin tone on photoacoustic oximetry of the radial artery.
A-B. Low melanin concentration in Fitz. 1 subjects facilitates deeper and more accurate oxygen saturation measurements. **C-F.** An increase in melanin concentration in darker skin tones presents as high skin surface sO_2. The high skin signal reduces measurement accuracy in deeper blood vessels. Blue and yellow arrows point to the skin surface and radial artery respectively. Yellow dashed region in **B/D/F** represents the ROI used for s_aO_2 measurements. There is considerably more clutter and noise in darker skin toned subjects **D** and **F,** which obscures signal from the radial artery. **G.** PA measured oxygen saturation of the radial artery decreases linearly as a function of skin tone. **H.** The oxygen saturation on the skin surface increases linearly with increasing melanin concentration. **I.** The bias in the PA measurement can be compensated using a correction factor defined by the inset equation. **J**. The pulse oximeter shows no significant differences in sO_2 between different skin types contradicting the NEJM article.[433] But this study was done on a younger, healthier, and smaller cohort of patients. PA showed significant reduction in s_aO_2 for Fitz. 4 and 6 subjects due to increased melanin absorption at the skin surface. The pulse oximeter measures sO_2 peripherally where skin is thinnest compared to the radial artery where skin is considerably thicker. Scale bars measure 0.5 cm. error bars represent standard deviation between three subjects. These Images were acquired on the LED-based PA system.

Table 7. 1 Correction factors for PA oximetry for varying Fitzpatrick skin types.

Fitzpatrick Scale	Correction factor	Percent correction
1	0.99	- 0.01%
2	1.029	2.9 %
3	1.074	7.4 %
4	1.118	11.8 %
5	1.163	16.3 %
6	1.207	20.7 %

7.4.4 Compensating for differences in skin tone for photoacoustic oximetry

The equation in **Figure 7.4I** defined the correction factor for all Fitzpatrick skin types listed in **Table 7.1**. We tested these values in 2 new subjects with a Fitzpatrick rating of 3 and 5 (**Figure 7.5**). The darker Fitzpatrick type 5 subject showed a significantly lower s_aO_2 reading compared to the lighter Fitzpatrick type 3 subject ($p<0.001$). Using the correction factors defined in **Table 7.1**, we were able to compensate for skin absorption and amend measurements to within ±2.24% error compared to the pulse oximeter (**Figure 7.5C**). The corrected sO_2 is a product of the PA s_aO_2 and the correction factor for the Fitzpatrick skin type.

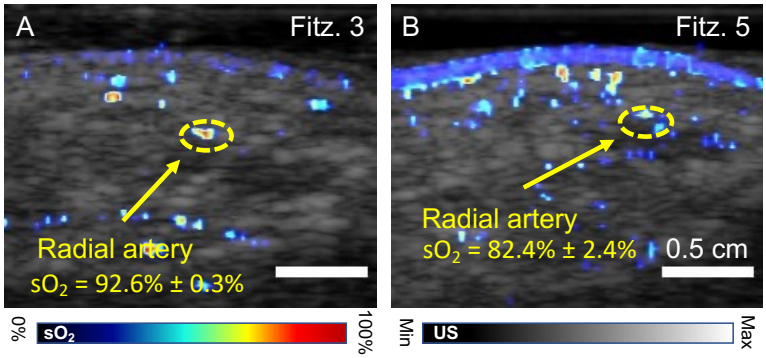

C

Skin type	Pulse Ox. sO_2	PA sO_2	Corrected sO_2	Percent Error
Fitz. 3	98 %	92.6 %	99.5 %	+ 1.53 %
Fitz. 5	98 %	82.4 %	95.8 %	- 2.24 %

Figure 7. 5 Compensating for differences in skin tone for photoacoustic oximetry.
A-B. PA oximetry of the left radial artery in Fitz. 1 and 5 subjects respectively. The darker skin toned subject showed reduced sO_2 readings even though pulse oximetry measured 98% saturation in both cases. **C**. The previously defined correction factors were able to compensate for lack of signal in both subjects. Images were acquired at 690 and 850 nm. Standard deviation is measured over 30 frames. Yellow dotted circles outline the ROI for s_aO_2 quantification. Yellow arrow marks the radial artery. Scale bar measures 0.5 cm. These Images were acquired on the LED-based PA system.

7.4.5 Difference in LED or Laser-based photoacoustics

Finally, we studied the effect of the illumination source (LED *vs.* laser) on photoacoustic evaluation of different skin tones. The LED source operates at a 100-200-fold lower energy

compared to the laser.[253] The laser-based PA of the skin surface showed a positive correlation (R^2 = 0.70, $p<0.001$) similar to the LED-based PA. There was a 12.5% and 71.1% increase in PA signal between Fitzpatrick type 1 – 4 and 4 – 6 subjects respectively (**Figure 7.12**).

PA oximetry using the laser-based system was done at 850 and 750 nm. The sO_2 measurements are independent of the imaging wavelengths. Like the LED system, the laser-based system also showed a decrease in radial artery oxygenation for darker subjects (**Figure 7.13**). The absorption by melanin in the Fitzpatrick type 6 subject was so high that the PA s_aO_2 dropped to 1.3%. The Fitzpatrick 1 subject also showed a lower s_aO_2 (59.2%) in comparison to the LED-system (97.8%). This could be because of the reconstruction algorithms used to reduce noise and calculate sO_2.[474]

7.5 Discussion

The young and healthy subjects recruited in this study had no previous history of cardiovascular disorders and were not on any medications that altered their oxygenation and perfusion status. Hence, the main significant difference between subjects with varying Fitzpatrick skin types was the concentration of melanin in their skin. Melanosomes are subcellular organelles that synthesize and store melanin. Studies have shown that subjects with darker skin tones have significantly more isolated, larger, and higher concentrations of melanosomes than subjects with lighter skin tones.[475, 476] The larger and more concentrated melanosomes increase the absorption cross section of melanin resulting in enhanced light absorption (higher $\boldsymbol{\mu_a}$ of melanin in **Equation 7.1**). The increase in melanin μ_a leads to higher PA signal at the skin surface and reduced depth penetration. Furthermore, larger melanosomes in darker subjects (1.44 ± 0.67 μm^2, from Thong *et al.*[476]) tend to scatter more near infrared light (NIR) than smaller melanosomes (0.94 ± 0.48 μm^2, from Thong *et al.*[476]) found in lighter skin toned patients.

PA imaging relies heavily on NIR illumination,[477] and thus increased scattering in this region further impedes light penetration through tissue.[30] With fewer photons making it through the skin in darker subjects, PA depth penetration is also reduced. The strong skin absorption and PA in Fitzpatrick type 6 subjects makes it difficult to visualize underlying vasculature (**Figure 7.3D/F**). Even in Fitzpatrick 1 subjects, PA imaging with 690 nm did not penetrate deeper than the skin surface (**Figure 7.8D**) as melanin has a higher μ_a at 690 nm (**Figure 7.1B**).[456] Time gain compensation to boost deeper signals coupled with noise reduction algorithms could help perform deeper PA imaging.[478] The smaller melanosomes in darker subjects could also enhance PA by increasing the surface area to volume ratio of the melanosomes. (Increasing surface-area-to-volume ratios is known to result in PA enhancement.[90, 223])

The increase in PA at the skin surface in darker subjects results in streaking and clutter artifacts (**Figure 7.2D-F**). Although there is reduced light penetrance through the skin, subdermal (1 cm under skin surface) PA signal is significantly higher in Fitzpatrick type 6 than type 1 subjects ($p<0.01$). The increased subdermal PA signal is attributed to streaking and clutter artifacts. The use of a single linear array of transducers and the presence of strong absorbers like melanin in darker subjects results in streaking artifacts.[471] Streaking artifacts can be reduced using filtered back projection or PA computed tomography.[479] Clutter is a phenomenon caused by multipath reverberations or off-axis scatterers. It leads to a static cloud of echo signals occluding the tissue regions of interest.[471, 480, 481] Higher PA signal in darker subjects leads to stronger reverberations and increased clutter in subdermal tissue. Furthermore, streaking and clutter cloak physiological PA signals from blood vessels making it difficult to differentiate between signal and noise (**Figure 7.2E-F**). This cloaking is only exacerbated during PA oximetry that combines data from two wavelengths (**Figure 7.4B/D/F**). Fluence correction,[482] plane wave ultrasound from different

angles,[483] focused ultrasound,[484] spatial weighting,[485] and deep learning[253] have shown promise in reducing noise and clutter in PA images.

The sO_2 measurements are dependent on PA signal at both 850 and 690 nm, the lack of PA depth penetration at 690 nm results in erroneous sO_2 readings. Furthermore, the increase in clutter and noise in darker skin toned subjects also interferes with their s_aO_2 evaluation (**Figure 7.4 B, D, and F**). The clutter in Fitzpatrick type 4 and 6 subjects makes ROI analysis difficult. Due to these perturbations, darker skin toned subjects show false signs of hypoxemia.

Pulse oximetry is a cheap, quick, and non-invasive oxygenation measurement technique but is limited to only peripheral sO_2 measurements where skin is relatively thin.[486] The arterial blood gas test is the most accurate way of determining the partial pressure of oxygen in blood, but is an invasive technique often resulting in various complications ranging from spasms, occlusions, infections *etc*.[487] PA imaging is advantageous because it is provides non-invasive local oxygen saturation and tissue perfusion map in real time. It is important to assess oxygen saturation locally to better understand the diseased state and to take more informed clinical decisions.

Other optical oximetry techniques such as pulse oximeters are often calibrated with a wide range of skin types, but the measurement inherently discards the concentration and $\boldsymbol{\mu_a}$ of melanin and other absorbers in **Equation 7.1,** resulting in erroneous readings.[488, 489] Although a short case series, this study shows that skin tone has a significant impact on the interaction of light with tissue, and that it must be studied in more detail.

Compensating for the under reporting of s_aO_2 in higher Fitzpatrick skin type subjects is a critical finding. The equation and correction factors in **Figure 7.4** and **Table 7.1** represent a small cohort of subjects. Nevertheless, this proof-of-concept study shows that compensating for different skin tones could be as simple as a software update for these imaging systems. Future work will

evaluate these conclusions in larger cohorts including subjects with arterial blood gas measurements. Ideally, we would objectively measure skin color using a colorimeter or reflectance spectroscopy before any clinical measurements.[490] This color measurement would further inform the image processing tool to compensate for changes in signal due to skin color by changing the weights for PA signal at each imaging wavelength.

Finally, the difference in oximetry results using the LED-based and laser-based systems could be explained by the different absorption spectra of oxy-deoxy-hemoglobin used by these commercial systems.[474] The laser-based system consistently under reports oxygenation values, but follows the same trends of decreasing s_aO_2 as a function of Fitzpatrick skin type.

7.6 Conclusion

The effect of skin tone on PA imaging was explored in this study. Our findings show that subjects with darker skin tones show increased absorption of light at the skin surface. This increase in surface absorption leads to reduced penetration depth and obscures underlying blood vessels. PA imaging is an ideal tool to study the transportation of light through tissue, because it can deconvolute signal from the skin surface. PA oximetry of the radial artery showed that under the same imaging conditions, subjects with darker skin tones exhibit lower arterial oxygen saturation. This technical bias was attributed to the increase in melanin concentration in darker subjects. The bias against darker skin toned subjects could be easily corrected by formulating an equation describing the change in oxygen saturation as a function of Fitzpatrick skin type. This correcting equation was able to compensate for the reduced PA signal in two test subjects with <2% error compared to pulse oximeter readings. Finally, the use of two independent PA systems confirmed our trends and showed that the laser-based system had an even more profound impact on PA oximetry compared to the LED-based system.

7.7 Acknowledgements

Chapter 7, in full, is a reprint of the material as it appears in The impact of skin tone on photoacoustic oximetry and tools to minimize bias. Mantri, Yash; Jokerst, Jesse V., Biomedical Optics Express, 2022. The dissertation author was the primary investigator and author of this paper.

7.8 Supplementary information

Table 7. 2 Subject demographic and arterial oxygen saturation.

11 volunteers were enrolled in this study. The average age was 26.7 ± 3.7 years. All subjects were healthy with no active or history of cardiovascular or skin conditions that could affect perfusion, oxygenation, or imaging. YM 001 – 009 were used as the training set and YM 010 - 011 were used as the test subjects for the correction equation. PsO2% is oxygen saturation measured by the pulse oximeter, PAsaO2% is the photoacoustic measured arterial oxygen saturation using the LED-based PA system

Subject ID	Age (years)	Sex (M/F)	Fitzpatrick Scale	PsO_2 (%)	PAs_aO_2 (%)
YM 001	25	M	4	99	90.4 ± 0.9
YM 002	20	M	1	98	98.5 ± 1.2
YM 003	32	M	6	98	86.2 ± 1.0
YM 004	26	F	4	100	90.1 ± 1.7
YM 005	31	M	6	97	78.1 ± 2.0
YM 006	24	F	1	98	98.2 ± 1.0
YM 007	27	M	6	96	73.7 ± 2.1
YM 008	23	M	4	98	92.9 ± 2.7
YM 009	26	M	1	98	97.8 ± 2.0
YM 010	31	M	3	98	92.6 ± 0.3
YM 011	24	M	5	98	82.4 ± 2.4

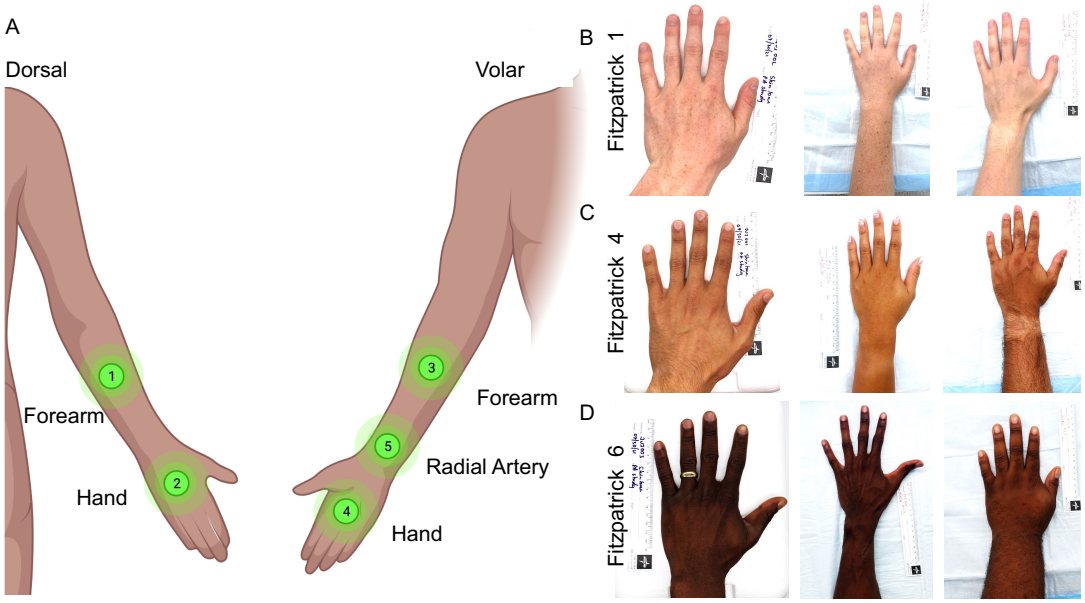

Figure 7. 6 Imaging areas and subject photographs.
A. Imaging points on the dorsal and volar hand. B-D. Photographic images of the dorsal hand of the nine subjects, representing Fitzpatrick skin types 1, 4, and 6 respectively. These were used in the training set (YM 001-09). These regions were selected because they have a relatively uniform distribution of melanin, are relatively flat to facilitate scanning, and are relatively free of hair that can compromise imaging.

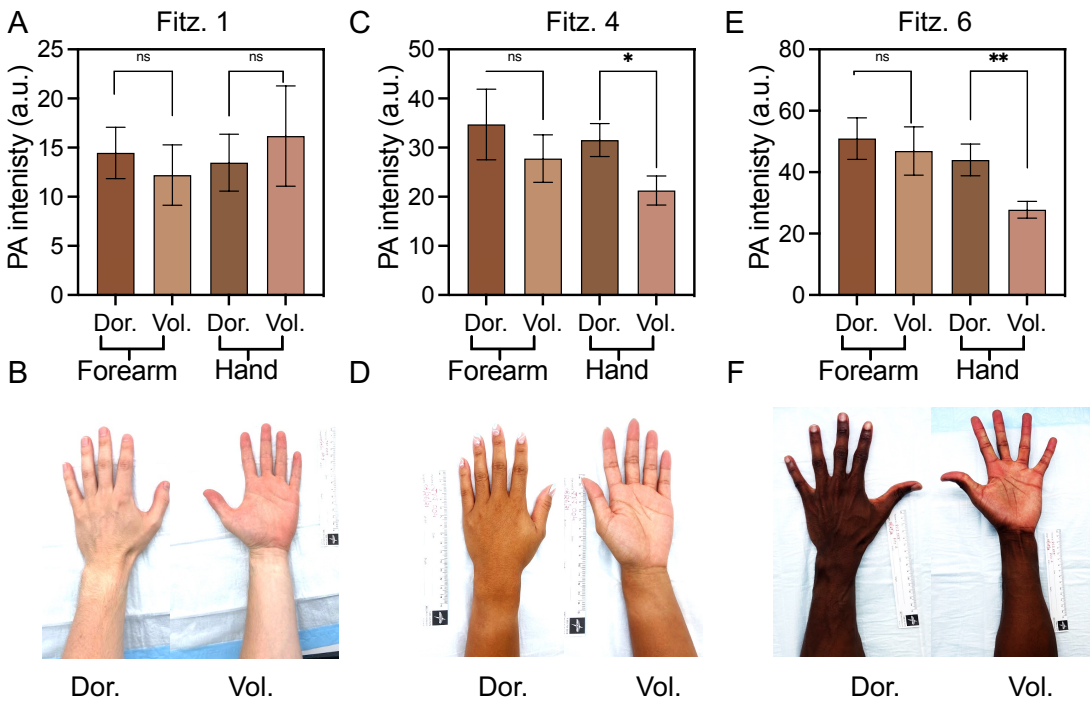

Figure 7. 7 Volar *vs.* dorsal PA.
A-B, C-D, and D-E. Differences in PA signal at 850 nm and photographs of dorsal and volar regions of the forearm and hand of Fitzpatrick type 1, 4, and 6 respectively. Fitz. 1 subjects showed similar melanin distributions on both sides hence there was no significant difference in PA intensity. Fitz. 4 and 6 subjects showed similar pigmentation on both sides of the forearm, but their volar hand was lighter compared to the other regions. The lighter skin tone in this region results in a significant drop in PA intensity compared to the dorsal side. The differences in the Fitz. 6 subjects are greater than that in the Fitz. 4 subjects. Error bars represent standard deviation in 3 subjects.

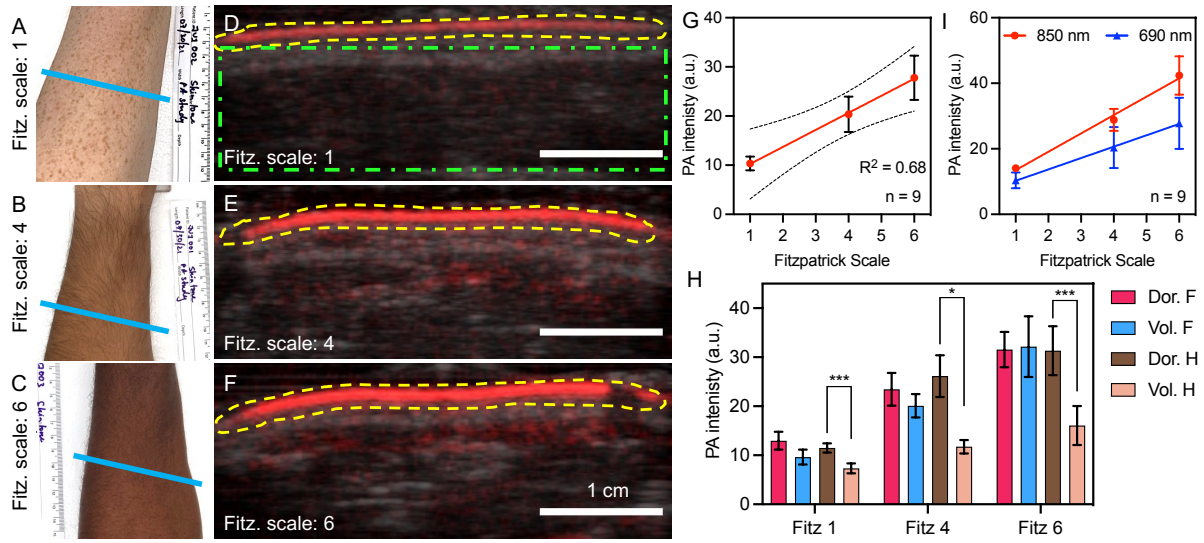

Figure 7. 8 Photoacoustic signal at 690 nm increases as a function of skin tone.
A-C. Photographic images of the dorsal forearm of Fitz. 1, 4, and 6 subjects. These are the same subjects from Fig. 2, imaged under similar settings with the only difference being the illumination wavelength of 690 nm. **D-E**. With increasing melanin concentration in darker skin toned subjects, the PA signal at the skin surface also increases. Since 690 nm is more prone to scattering compared to 850 nm, the penetration depth even for the Fitz.1 subjects is limited to only a few millimeters of the skin surface. Yellow and green dashed regions outline ROIs for skin surface and subdermal PA quantification respectively. **G**. PA signal at the skin surface increases as a function of Fitzpatrick skin type. **H.** Differences in the PA signal at different imaging areas shows a similar trend compared to 850 nm. The only difference seen is between the dorsal and volar hand where pigmentation varies most. **I.** PA signal at 850 nm is consistently higher *vs.* 690 nm but not significantly different. The slopes of both curves are not significantly different either. Hence the trends of increasing PA due to an increase in skin tone is conserved across wavelengths. Error bars represent standard deviation in three subjects of each skin type. Scale bar measures 1 cm. These images were acquired on the LED-based PA system.

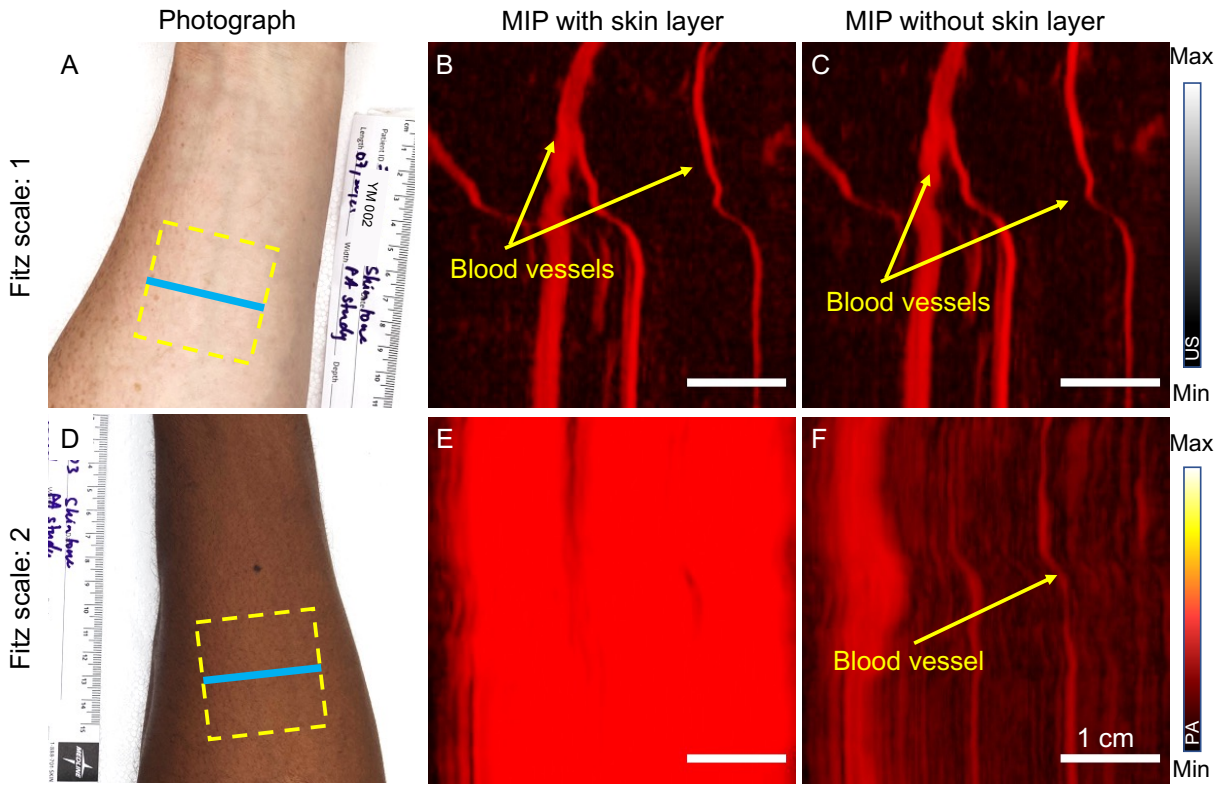

Figure 7. 9 High melanin in darker skin toned subjects reduces signal-to-noise ratio for subdermal imaging. **A-C.** Volar forearm of a Fitz. 1 subject and corresponding MIP PA maps with and without the skin layer. **D-F**. Volar forearm of Fitz. 6 subject and corresponding MIP PA maps with and without the skin layer. A high melanin concentration in darker skin toned subjects results in high skin PA signal. The high skin PA signal reduces light penetration into tissue obscuring underlying vasculature and reducing SNR. SNR for Fitz. 1 = 12.6 dB; and Fitz. 6 = 3.2 dB.

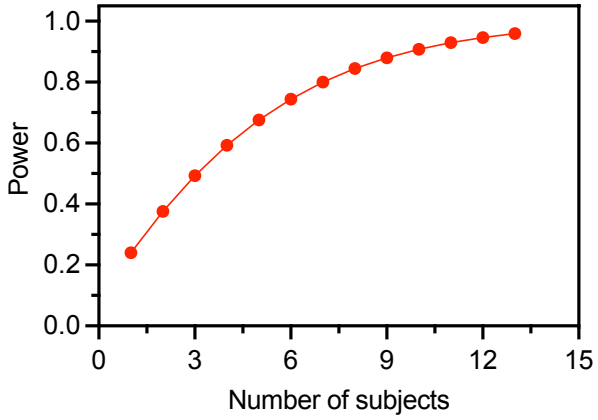

Figure 7. 10 Power analysis.
With a total of 9 subjects there is 88% power in our data (alpha = 0.05).

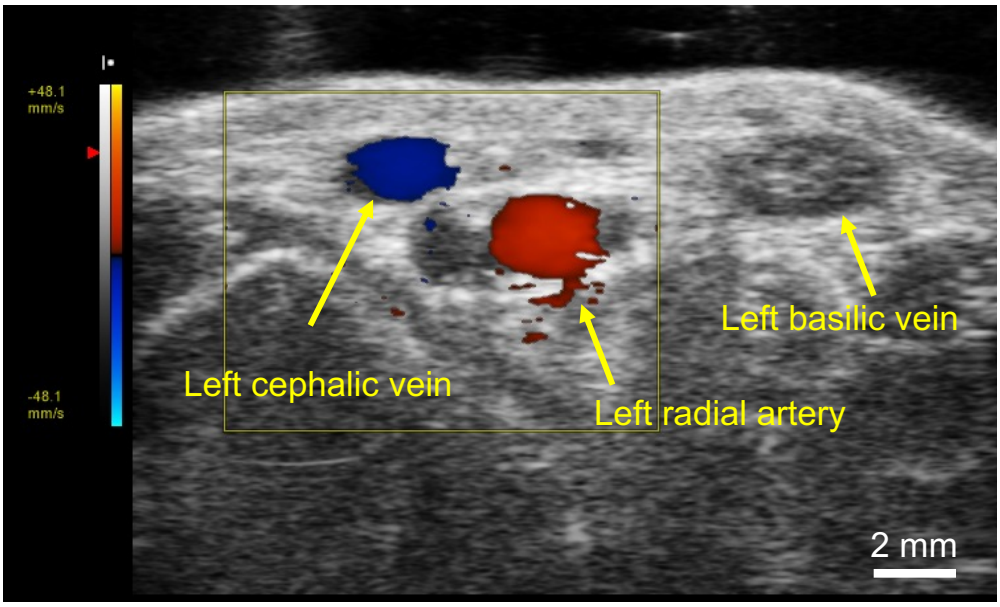

Figure 7. 11 Radial artery confirmation using ultrasound-doppler imaging.
Ultrasound doppler imaging to confirm the location of the radial artery. The red coloration indicated blood flowing towards the transducer in the artery, and blue indicates blood flowing away from the transducer in the vein. The left basilic vein is not colored because it is placed outside the doppler window (yellow box). Scale bar measures 2 mm. This Images was acquired on the laser-based PA system.

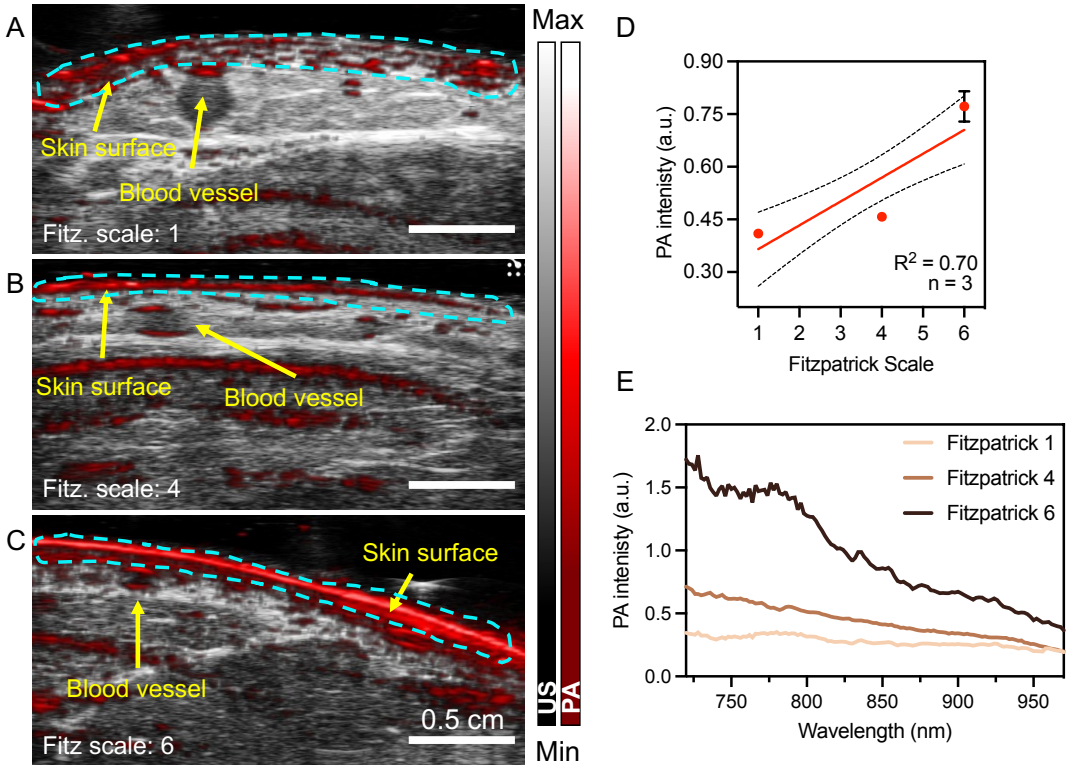

Figure 7. 12 Laser-based PA imaging of different skin tones.
A-C. PA and US overlay of the dorsal forearm of subjects with Fitzpatrick type 1, 4, and 6 skin. **D.** PA intensity of the skin surface is significantly and positively correlated to the Fitzpatrick skin type. **E.** PA spectra of the three types of skin shows that PA intensity is higher due to the increase in melanin concentration from Fitz. 1 – 6 skin types. The spectral pattern follows the μ_a of melanin in Fig 1. Error bars represent standard deviation in >80 frames per subject. Scale bar measures 0.5 cm. These images were acquired on the laser-based PA system.

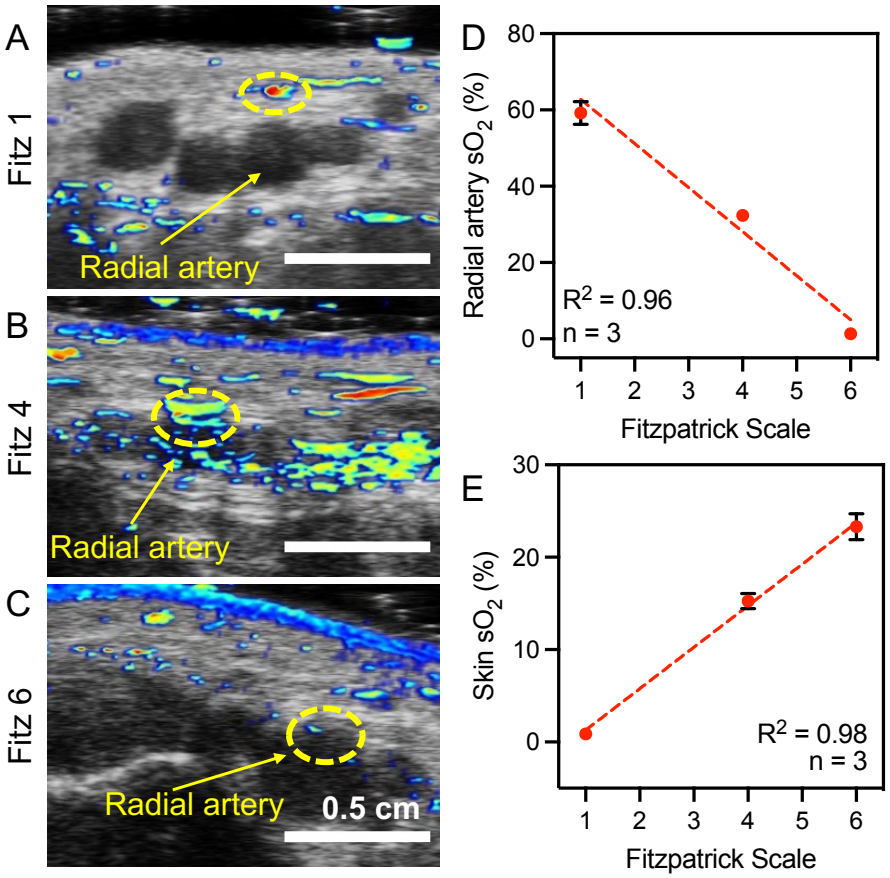

Figure 7. 13 Laser-based PA oximetry of subjects with varying skin type.
A-C. PA and US overlay of the left radial artery of subjects with Fitzpatrick type 1, 4, and 6 skin. These subjects all had sO_2 >98% as measured by pulse oximetry. **D.** PA s_aO_2 was significantly reduced for subjects with darker skin tones. This was because of the enhanced absorption by melanin present in higher concentrations in darker skin toned subjects. **E**. High melanin concentration results in a higher perceived skin sO_2. Yellow dashed region represents ROI for image analysis. These images were acquired on the laser-based PA system.

REFERENCES

1. Xu, M.; Wang, L. V., Photoacoustic imaging in biomedicine. *Review of scientific instruments* **2006,** *77* (4), 041101.

2. Beard, P., Biomedical photoacoustic imaging. *Interface focus* **2011,** *1* (4), 602-631.

3. Wang, X.; Xie, X.; Ku, G.; Wang, L. V.; Stoica, G., Noninvasive imaging of hemoglobin concentration and oxygenation in the rat brain using high-resolution photoacoustic tomography. *Journal of biomedical optics* **2006,** *11* (2), 024015.

4. Hester, S. C.; Kuriakose, M.; Nguyen, C. D.; Mallidi, S., Role of Ultrasound and Photoacoustic Imaging in Photodynamic Therapy for Cancer. *Photochemistry and Photobiology* **2020**.

5. Wang, J.; Jeevarathinam, A. S.; Humphries, K.; Jhunjhunwala, A.; Chen, F.; Hariri, A.; Miller III, B. R.; Jokerst, J. V., A mechanistic investigation of methylene blue and heparin interactions and their photoacoustic enhancement. *Bioconjugate chemistry* **2018,** *29* (11), 3768-3775.

6. Cheng, H.-B.; Li, Y.; Tang, B. Z.; Yoon, J., Assembly strategies of organic-based imaging agents for fluorescence and photoacoustic bioimaging applications. *Chemical Society Reviews* **2020,** *49* (1), 21-31.

7. Jeevarathinam, A. S.; Lemaster, J. E.; Chen, F.; Zhao, E.; Jokerst, J., Photoacoustic Imaging Quantifies Drug Release from Nanocarriers via Redox Chemistry of Dye-Labeled Cargo. *Angewandte Chemie International Edition* **2019**.

8. Hariri, A.; Zhao, E.; Jeevarathinam, A. S.; Lemaster, J.; Zhang, J.; Jokerst, J. V., Molecular imaging of oxidative stress using an LED-based photoacoustic imaging system. *Scientific reports* **2019,** *9* (1), 1-10.

9. Zhang, J.; Zhen, X.; Upputuri, P. K.; Pramanik, M.; Chen, P.; Pu, K., Activatable photoacoustic nanoprobes for in vivo ratiometric imaging of peroxynitrite. *Advanced Materials* **2017,** *29* (6), 1604764.

10. Pu, K.; Huang, J., Activatable Molecular Probes for Second Near-Infrared Fluorescence, Chemiluminescence, and Photoacoustic Imaging. *Angewandte Chemie* **2020**.

11. Lemaster, J. E.; Jokerst, J. V., What is new in nanoparticle-based photoacoustic imaging? *Wiley Interdisciplinary Reviews: Nanomedicine and Nanobiotechnology* **2017,** *9* (1), e1404.

12. Jokerst, J. V.; Cole, A. J.; Van de Sompel, D.; Gambhir, S. S., Gold nanorods for ovarian cancer detection with photoacoustic imaging and resection guidance via Raman imaging in living mice. *ACS nano* **2012,** *6* (11), 10366-10377.

13. Mantri, Y.; Davidi, B.; Lemaster, J. E.; Hariri, A.; Jokerst, J. V., Iodide-doped Precious Metal Nanoparticles: Measuring Oxidative Stress in vivo via Photoacoustic Imaging. *Nanoscale* **2020**.

14. Weber, J.; Beard, P. C.; Bohndiek, S. E., Contrast agents for molecular photoacoustic imaging. *Nature methods* **2016,** *13* (8), 639-650.

15. Dixon, A. J.; Hu, S.; Klibanov, A. L.; Hossack, J. A., Oscillatory Dynamics and In Vivo Photoacoustic Imaging Performance of Plasmonic Nanoparticle-Coated Microbubbles. *Small* **2015,** *11* (25), 3066-3077.

16. Shrestha, B.; DeLuna, F.; Anastasio, M. A.; Yong Ye, J.; Brey, E. M., Photoacoustic Imaging in Tissue Engineering and Regenerative Medicine. *Tissue Engineering Part B: Reviews* **2020**.

17. Upputuri, P. K.; Pramanik, M., Recent advances in photoacoustic contrast agents for in vivo imaging. *Wiley Interdisciplinary Reviews: Nanomedicine and Nanobiotechnology* **2020**.

18. Meng, Z.; Zhou, X.; She, J.; Zhang, Y.; Feng, L.; Liu, Z., Ultrasound-Responsive Conversion of Microbubbles to Nanoparticles to Enable Background-Free in Vivo Photoacoustic Imaging. *Nano letters* **2019,** *19* (11), 8109-8117.

19. Wang, S.; Fu, L.; Xin, J.; Wang, S.; Yao, C.; Zhang, Z.; Wang, J., Photoacoustic response induced by nanoparticle-mediated photothermal bubbles beyond the thermal expansion for potential theranostics. *Journal of biomedical optics* **2018,** *23* (12), 125002.

20. Wilson, K.; Homan, K.; Emelianov, S., Biomedical photoacoustics beyond thermal expansion using triggered nanodroplet vaporization for contrast-enhanced imaging. *Nature communications* **2012,** *3* (1), 1-10.

21. Wang, L. V.; Hu, S., Photoacoustic tomography: in vivo imaging from organelles to organs. *Science* **2012,** *335* (6075), 1458-1462.

22. Wilson, K.; Homan, K.; Emelianov, S., Biomedical photoacoustics beyond thermal expansion using triggered nanodroplet vaporization for contrast-enhanced imaging. *Nature Comm.* **2012,** *3*, 618.

23. Hashimoto, S.; Werner, D.; Uwada, T., Studies on the interaction of pulsed lasers with plasmonic gold nanoparticles toward light manipulation, heat management, and nanofabrication. *Journal of Photochemistry and Photobiology C: Photochemistry Reviews* **2012,** *13* (1), 28-54.

24. Dreaden, E. C.; Alkilany, A. M.; Huang, X.; Murphy, C. J.; El-Sayed, M. A., The golden age: gold nanoparticles for biomedicine. *Chemical Society Reviews* **2012,** *41* (7), 2740-2779.

25. Alkilany, A. M.; Murphy, C. J., Toxicity and cellular uptake of gold nanoparticles: what we have learned so far? *Journal of nanoparticle research* **2010,** *12* (7), 2313-2333.

26. Alkilany, A. M.; Abulateefeh, S. R.; Murphy, C. J., Facile Functionalization of Gold Nanoparticles with PLGA Polymer Brushes and Efficient Encapsulation into PLGA Nanoparticles: Toward Spatially Precise Bioimaging of Polymeric Nanoparticles. *Particle & Particle Systems Characterization* **2019,** *36* (2), 1800414.

27. Sun, X.; Liu, Z.; Welsher, K.; Robinson, J. T.; Goodwin, A.; Zaric, S.; Dai, H., Nano-graphene oxide for cellular imaging and drug delivery. *Nano research* **2008,** *1* (3), 203-212.

28. Irvine, W. M.; Pollack, J. B., Infrared optical properties of water and ice spheres. *Icarus* **1968,** *8* (1-3), 324-360.

29. Vogt, W. C.; Jia, C.; Wear, K. A.; Garra, B. S.; Pfefer, T. J., Biologically relevant photoacoustic imaging phantoms with tunable optical and acoustic properties. *Journal of biomedical optics* **2016,** *21* (10), 101405.

30. Evanoff, D. D.; Chumanov, G., Size-controlled synthesis of nanoparticles. 2. Measurement of extinction, scattering, and absorption cross sections. *The Journal of Physical Chemistry B* **2004,** *108* (37), 13957-13962.

31. Pang, G. A.; Laufer, J.; Niessner, R.; Haisch, C., Photoacoustic signal generation in gold nanospheres in aqueous solution: signal generation enhancement and particle diameter effects. *The Journal of Physical Chemistry C* **2016,** *120* (48), 27646-27656.

32. Park, J.; Kang, H.; Kim, Y. H.; Lee, S.-W.; Lee, T. G.; Wi, J.-S., Physically-synthesized gold nanoparticles containing multiple nanopores for enhanced photothermal conversion and photoacoustic imaging. *Nanoscale* **2016,** *8* (34), 15514-15520.

33. Khan, D.; Gajula, D.; Bayram, F.; Kim, S.; Koley, G. In *Effect of Plasmonic Absorption on Photoacoustic Signal Generation*, 2018 IEEE 13th Nanotechnology Materials and Devices Conference (NMDC), IEEE: 2018; pp 1-4.

34. Tao, C.; An, L.; Lin, J.; Tian, Q.; Yang, S., Surface Plasmon Resonance–Enhanced Photoacoustic Imaging and Photothermal Therapy of Endogenous H2S-Triggered Au@ Cu2O. *Small* **2019,** *15* (44), 1903473.

35. Xu, W.; Leskinen, J.; Tick, J.; Happonen, E.; Tarvainen, T.; Lehto, V.-P., Black mesoporous silicon as contrast agent for LED-based 3D photoacoustic tomography. *ACS Applied Materials & Interfaces* **2020**.

36. Lemaster, J. In *Gold nanorods with size-controlled polydopamine coating for spectral imaging (Conference Presentation)*, Reporters, Markers, Dyes, Nanoparticles, and Molecular Probes for Biomedical Applications XII, International Society for Optics and Photonics: 2020; p 112560A.

37. Zhou, J.; Jiang, Y.; Hou, S.; Upputuri, P. K.; Wu, D.; Li, J.; Wang, P.; Zhen, X.; Pramanik, M.; Pu, K., Compact plasmonic blackbody for cancer theranosis in the near-infrared II window. *ACS nano* **2018,** *12* (3), 2643-2651.

38. Repenko, T.; Rix, A.; Nedilko, A.; Rose, J.; Hermann, A.; Vinokur, R.; Moli, S.; Cao-Milàn, R.; Mayer, M.; von Plessen, G., Strong photoacoustic signal enhancement by coating gold nanoparticles with melanin for biomedical imaging. *Advanced Functional Materials* **2018,** *28* (7), 1705607.

39. He, L.; Mao, C.; Brasino, M.; Harguindey, A.; Park, W.; Goodwin, A. P.; Cha, J. N., TiO2-capped gold nanorods for plasmon-enhanced production of reactive oxygen species and photothermal delivery of chemotherapeutic agents. *ACS applied materials & interfaces* **2018,** *10* (33), 27965-27971.

40. Sreejith, S.; Joseph, J.; Nguyen, K. T.; Murukeshan, V. M.; Lye, S. W.; Zhao, Y., Graphene oxide wrapping of gold–silica core–shell nanohybrids for photoacoustic signal generation and bimodal imaging. *ChemNanoMat* **2015,** *1* (1), 39-45.

41. Moon, H.; Kumar, D.; Kim, H.; Sim, C.; Chang, J.-H.; Kim, J.-M.; Kim, H.; Lim, D.-K., Amplified photoacoustic performance and enhanced photothermal stability of reduced graphene oxide coated gold nanorods for sensitive photoacoustic imaging. *ACS nano* **2015,** *9* (3), 2711-2719.

42. Song, J.; Yang, X.; Jacobson, O.; Lin, L.; Huang, P.; Niu, G.; Ma, Q.; Chen, X., Sequential drug release and enhanced photothermal and photoacoustic effect of hybrid reduced graphene oxide-loaded ultrasmall gold nanorod vesicles for cancer therapy. *ACS nano* **2015,** *9* (9), 9199-9209.

43. Leng, C.; Zhang, X.; Xu, F.; Yuan, Y.; Pei, H.; Sun, Z.; Li, L.; Bao, Z., Engineering Gold Nanorod–Copper Sulfide Heterostructures with Enhanced Photothermal Conversion Efficiency and Photostability. *Small* **2018,** *14* (12), 1703077.

44. Yamaoka, Y.; Takamatsu, T. In *Enhancement of multiphoton excitation-induced photoacoustic signals by using gold nanoparticles surrounded by fluorescent dyes*, Photons Plus Ultrasound: Imaging and Sensing 2009, International Society for Optics and Photonics: 2009; p 71772A.

45. Ferrauto, G.; Carniato, F.; Di Gregorio, E.; Tei, L.; Botta, M.; Aime, S., Large photoacoustic effect enhancement for ICG confined inside MCM-41 mesoporous silica nanoparticles. *Nanoscale* **2017,** *9* (1), 99-103.

46. Gao, C.; Deng, Z.-J.; Peng, D.; Jin, Y.-S.; Ma, Y.; Li, Y.-Y.; Zhu, Y.-K.; Xi, J.-Z.; Tian, J.; Dai, Z.-F., Near-infrared dye-loaded magnetic nanoparticles as photoacoustic contrast agent for enhanced tumor imaging. *Cancer biology & medicine* **2016,** *13* (3), 349.

47. Novoselova, M. V.; Bratashov, D. N.; Sarimollaoglu, M.; Nedosekin, D. A.; Harrington, W.; Watts, A.; Han, M.; Khlebtsov, B. N.; Galanzha, E. I.; Gorin, D. A., Photoacoustic and fluorescent effects in multilayer plasmon-dye interfaces. *Journal of biophotonics* **2019,** *12* (4), e201800265.

48. de la Zerda, A.; Bodapati, S.; Teed, R.; May, S. Y.; Tabakman, S. M.; Liu, Z.; Khuri-Yakub, B. T.; Chen, X.; Dai, H.; Gambhir, S. S., Family of enhanced photoacoustic imaging agents for high-sensitivity and multiplexing studies in living mice. *ACS nano* **2012,** *6* (6), 4694-4701.

49. Zerda, A. d. l.; Liu, Z.; Bodapati, S.; Teed, R.; Vaithilingam, S.; Khuri-Yakub, B. T.; Chen, X.; Dai, H.; Gambhir, S. S., Ultrahigh sensitivity carbon nanotube agents for photoacoustic molecular imaging in living mice. *Nano letters* **2010,** *10* (6), 2168-2172.

50. Liu, Y.; Bhattarai, P.; Dai, Z.; Chen, X., Photothermal therapy and photoacoustic imaging via nanotheranostics in fighting cancer. *Chemical Society Reviews* **2019,** *48* (7), 2053-2108.

51. Halas, N. J.; Lal, S.; Chang, W.-S.; Link, S.; Nordlander, P., Plasmons in strongly coupled metallic nanostructures. *Chemical reviews* **2011,** *111* (6), 3913-3961.

52. Jain, P. K.; El-Sayed, M. A., Plasmonic coupling in noble metal nanostructures. *Chemical Physics Letters* **2010,** *487* (4-6), 153-164.

53. Hohenester, U., Particle Plasmons. In *Nano and Quantum Optics*, Springer: 2020; pp 207-257.

54. Tsai, C.-Y.; Lin, J.-W.; Wu, C.-Y.; Lin, P.-T.; Lu, T.-W.; Lee, P.-T., Plasmonic coupling in gold nanoring dimers: observation of coupled bonding mode. *Nano letters* **2012,** *12* (3), 1648-1654.

55. Rasskazov, I. L.; Wang, L.; Murphy, C. J.; Bhargava, R.; Carney, P. S., Plasmon-enhanced upconversion: engineering enhancement and quenching at nano and macro scales. *Optical Materials Express* **2018,** *8* (12), 3787-3804.

56. He, L.; Dragavon, J.; Cho, S.; Mao, C.; Yildirim, A.; Ma, K.; Chattaraj, R.; Goodwin, A. P.; Park, W.; Cha, J. N., Self-assembled gold nanostar–NaYF 4: Yb/Er clusters for multimodal imaging, photothermal and photodynamic therapy. *Journal of Materials Chemistry B* **2016,** *4* (25), 4455-4461.

57. Funston, A. M.; Novo, C.; Davis, T. J.; Mulvaney, P., Plasmon coupling of gold nanorods at short distances and in different geometries. *Nano letters* **2009,** *9* (4), 1651-1658.

58. Bohren, C. F.; Huffman, D. R., *Absorption and scattering of light by small particles*. John Wiley & Sons: 2008.

59. Chen, T.; Pourmand, M.; Feizpour, A.; Cushman, B.; Reinhard, B. r. M., Tailoring plasmon coupling in self-assembled one-dimensional Au nanoparticle chains through simultaneous control of size and gap separation. *The journal of physical chemistry letters* **2013,** *4* (13), 2147-2152.

60. Liu, Y.; He, J.; Yang, K.; Yi, C.; Liu, Y.; Nie, L.; Khashab, N. M.; Chen, X.; Nie, Z., Folding up of gold nanoparticle strings into plasmonic vesicles for enhanced photoacoustic imaging. *Angewandte Chemie International Edition* **2015,** *54* (52), 15809-15812.

61. Huang, P.; Lin, J.; Li, W.; Rong, P.; Wang, Z.; Wang, S.; Wang, X.; Sun, X.; Aronova, M.; Niu, G., Biodegradable gold nanovesicles with an ultrastrong plasmonic coupling effect for photoacoustic imaging and photothermal therapy. *Angewandte Chemie International Edition* **2013,** *52* (52), 13958-13964.

62. Yang, Z.; Song, J.; Dai, Y.; Chen, J.; Wang, F.; Lin, L.; Liu, Y.; Zhang, F.; Yu, G.; Zhou, Z., Self-assembly of semiconducting-plasmonic gold nanoparticles with enhanced optical property for photoacoustic imaging and photothermal therapy. *Theranostics* **2017,** *7* (8), 2177.

63. Park, J. H.; Dumani, D. S.; Arsiwala, A.; Emelianov, S.; Kane, R. S., Tunable aggregation of gold-silica janus nanoparticles to enable contrast-enhanced multiwavelength photoacoustic imaging in vivo. *Nanoscale* **2018,** *10* (32), 15365-15370.

64. Lu, S. Z.; Guo, X. Y.; Zou, M. S.; Zheng, Z. Q.; Li, Y. C.; Li, X. D.; Li, L. L.; Wang, H., Bacteria-Instructed In Situ Aggregation of AuNPs with Enhanced Photoacoustic Signal for Bacterial Infection Bioimaging. *Advanced healthcare materials* **2020,** *9* (1), 1901229.

65. Murphy, C. J.; Sau, T. K.; Gole, A. M.; Orendorff, C. J.; Gao, J.; Gou, L.; Hunyadi, S. E.; Li, T., Anisotropic metal nanoparticles: synthesis, assembly, and optical applications. ACS Publications: 2005.

66. Li, W.; Chen, X., Gold nanoparticles for photoacoustic imaging. *Nanomedicine* **2015,** *10* (2), 299-320.

67. Jokerst, J. V.; Miao, Z.; Zavaleta, C.; Cheng, Z.; Gambhir, S. S., Affibody-functionalized gold–silica nanoparticles for Raman molecular imaging of the epidermal growth factor receptor. *Small* **2011,** *7* (5), 625-633.

68. Wu, X.; Ming, T.; Wang, X.; Wang, P.; Wang, J.; Chen, J., High-photoluminescence-yield gold nanocubes: for cell imaging and photothermal therapy. *ACS nano* **2010,** *4* (1), 113-120.

69. Peng, Y.; Liu, Y.; Lu, X.; Wang, S.; Chen, M.; Huang, W.; Wu, Z.; Lu, G.; Nie, L., Ag-hybridized plasmonic Au-triangular nanoplates: highly sensitive photoacoustic/Raman evaluation and improved antibacterial/photothermal combination therapy. *Journal of Materials Chemistry B* **2018,** *6* (18), 2813-2820.

70. Mantri, Y.; Jokerst, J. V. In *Ferricyanide meditated photoacoustic enhancement of metal chalcogenide-coated gold nanorods.(Conference Presentation)*, Photons Plus Ultrasound: Imaging and Sensing 2020, International Society for Optics and Photonics: 2020; p 1124019.

71. Kim, T.; Zhang, Q.; Li, J.; Zhang, L.; Jokerst, J. V., A gold/silver hybrid nanoparticle for treatment and photoacoustic imaging of bacterial infection. *ACS nano* **2018,** *12* (6), 5615-5625.

72. Jana, N. R.; Gearheart, L.; Murphy, C. J., Wet chemical synthesis of high aspect ratio cylindrical gold nanorods. *The Journal of Physical Chemistry B* **2001,** *105* (19), 4065-4067.

73. Moon, G. D.; Choi, S.-W.; Cai, X.; Li, W.; Cho, E. C.; Jeong, U.; Wang, L. V.; Xia, Y., A new theranostic system based on gold nanocages and phase-change materials with unique features for photoacoustic imaging and controlled release. *Journal of the American Chemical Society* **2011,** *133* (13), 4762-4765.

74. Li, W.; Brown, P. K.; Wang, L. V.; Xia, Y., Gold nanocages as contrast agents for photoacoustic imaging. *Contrast media & molecular imaging* **2011,** *6* (5), 370-377.

75. Yang, X.; Skrabalak, S. E.; Li, Z.-Y.; Xia, Y.; Wang, L. V., Photoacoustic tomography of a rat cerebral cortex in vivo with Au nanocages as an optical contrast agent. *Nano letters* **2007,** *7* (12), 3798-3802.

76. Xiang, L.; Xing, D.; Gu, H.; Yang, D.; Zeng, L.; Yang, S. In *Gold nanoshell-based photoacoustic imaging application in biomedicine*, 2006 International Symposium on Biophotonics, Nanophotonics and Metamaterials, IEEE: 2006; pp 76-79.

77. Liu, M.; Guyot-Sionnest, P., Preparation and optical properties of silver chalcogenide coated gold nanorods. *Journal of Materials Chemistry* **2006,** *16* (40), 3942-3945.

78. Chen, H.; Kou, X.; Yang, Z.; Ni, W.; Wang, J., Shape-and size-dependent refractive index sensitivity of gold nanoparticles. *Langmuir* **2008,** *24* (10), 5233-5237.

79. Zhang, X.-L.; Zheng, C.; Zhang, Y.; Yang, H.-H.; Liu, X.; Liu, J., One-pot synthesis of gold nanostars using plant polyphenols for cancer photoacoustic imaging and photothermal therapy. *Journal of Nanoparticle Research* **2016,** *18* (7), 174.

80. Grześkiewicz, B.; Ptaszyński, K.; Kotkowiak, M., Near and far-field properties of nanoprisms with rounded edges. *Plasmonics* **2014,** *9* (3), 607-614.

81. Huang, W.; Qian, W.; El-Sayed, M. A.; Ding, Y.; Wang, Z. L., Effect of the lattice crystallinity on the electron− phonon relaxation rates in gold nanoparticles. *The Journal of Physical Chemistry C* **2007,** *111* (29), 10751-10757.

82. Link, S.; Burda, C.; Mohamed, M.; Nikoobakht, B.; El-Sayed, M., Femtosecond transient-absorption dynamics of colloidal gold nanorods: Shape independence of the electron-phonon relaxation time. *Physical Review B* **2000,** *61* (9), 6086.

83. Liu, J. G.; Zhang, H.; Link, S.; Nordlander, P., Relaxation of plasmon-induced hot carriers. *ACS Photonics* **2017,** *5* (7), 2584-2595.

84. He, W.; Wang, X.; Gao, X.; Lu, Z.; Song, J. In *Application of gold nanoparticles in photoacoustic imaging*, IOP Conference Series: Materials Science and Engineering, IOP Publishing: 2020; p 012086.

85. García-Álvarez, R.; Chen, L.; Nedilko, A.; Sánchez-Iglesias, A.; Rix, A.; Lederle, W.; Pathak, V.; Lammers, T.; von Plessen, G.; Kostarelos, K., Optimizing the geometry of photoacoustically active gold nanoparticles for biomedical imaging. *ACS Photonics* **2020,** *7* (3), 646-652.

86. Knights, O. B.; Ye, S.; Ingram, N.; Freear, S.; McLaughlan, J. R., Optimising gold nanorods for photoacoustic imaging in vitro. *Nanoscale Advances* **2019,** *1* (4), 1472-1481.

87. Jiang, Y.; Upputuri, P. K.; Xie, C.; Lyu, Y.; Zhang, L.; Xiong, Q.; Pramanik, M.; Pu, K., Broadband absorbing semiconducting polymer nanoparticles for photoacoustic imaging in second near-infrared window. *Nano letters* **2017,** *17* (8), 4964-4969.

88. Cao, Z.; Feng, L.; Zhang, G.; Wang, J.; Shen, S.; Li, D.; Yang, X., Semiconducting polymer-based nanoparticles with strong absorbance in NIR-II window for in vivo photothermal therapy and photoacoustic imaging. *Biomaterials* **2018,** *155*, 103-111.

89. Wu, J.; You, L.; Lan, L.; Lee, H. J.; Chaudhry, S. T.; Li, R.; Cheng, J. X.; Mei, J., Semiconducting polymer nanoparticles for centimeters-deep photoacoustic imaging in the second near-infrared window. *Advanced Materials* **2017,** *29* (41), 1703403.

90. Chen, Y.-S.; Zhao, Y.; Yoon, S. J.; Gambhir, S. S.; Emelianov, S., Miniature gold nanorods for photoacoustic molecular imaging in the second near-infrared optical window. *Nature nanotechnology* **2019,** *14* (5), 465-472.

91. Oldenburg, S.; Averitt, R.; Westcott, S.; Halas, N., Nanoengineering of optical resonances. *Chemical Physics Letters* **1998,** *288* (2-4), 243-247.

92. Wang, S.; Xu, H.; Ye, J., Plasmonic rod-in-shell nanoparticles for photothermal therapy. *Physical Chemistry Chemical Physics* **2014,** *16* (24), 12275-12281.

93. Vijayaraghavan, P.; Chiang, C. S.; Chiang, H. K.; Li, M. L.; Hwang, K. C., Multi-Branched Plasmonic Gold Nanoechinus-Based Triple Modal Bioimaging: An Efficient NIR-to-NIR Up and Down-Conversion Emission and Photoacoustic Imaging. *Advanced Materials Technologies* **2016,** *1* (7), 1600107.

94. Ge, X.; Fu, Q.; Bai, L.; Chen, B.; Wang, R.; Gao, S.; Song, J., Photoacoustic imaging and photothermal therapy in the second near-infrared window. *New Journal of Chemistry* **2019,** *43* (23), 8835-8851.

95. Chen, Y. S.; Frey, W.; Aglyamov, S.; Emelianov, S., Environment-dependent generation of photoacoustic waves from plasmonic nanoparticles. *Small* **2012,** *8* (1), 47-52.

96. Shi, Y.; Qin, H.; Yang, S.; Xing, D., Thermally confined shell coating amplifies the photoacoustic conversion efficiency of nanoprobes. *Nano Research* **2016,** *9* (12), 3644-3655.

97. Shahbazi, K.; Frey, W.; Chen, Y.-S.; Aglyamov, S.; Emelianov, S., Photoacoustics of core–shell nanospheres using comprehensive modeling and analytical solution approach. *Communications Physics* **2019,** *2* (1), 119.

98. Jokerst, J. V.; Thangaraj, M.; Kempen, P. J.; Sinclair, R.; Gambhir, S. S., Photoacoustic imaging of mesenchymal stem cells in living mice via silica-coated gold nanorods. *ACS nano* **2012,** *6* (7), 5920-5930.

99. Chen, Y.-S.; Frey, W.; Kim, S.; Kruizinga, P.; Homan, K.; Emelianov, S., Silica-coated gold nanorods as photoacoustic signal nanoamplifiers. *Nano letters* **2011,** *11* (2), 348-354.

100. Chen, Y.-S.; Frey, W.; Kim, S.; Homan, K.; Kruizinga, P.; Sokolov, K.; Emelianov, S., Enhanced thermal stability of silica-coated gold nanorods for photoacoustic imaging and image-guided therapy. *Optics express* **2010,** *18* (9), 8867-8878.

101. Gao, F.; Bai, L.; Liu, S.; Zhang, R.; Zhang, J.; Feng, X.; Zheng, Y.; Zhao, Y., Rationally encapsulated gold nanorods improving both linear and nonlinear photoacoustic imaging contrast in vivo. *Nanoscale* **2017,** *9* (1), 79-86.

102. Ju, K.-Y.; Kang, J.; Pyo, J.; Lim, J.; Chang, J. H.; Lee, J.-K., pH-Induced aggregated melanin nanoparticles for photoacoustic signal amplification. *Nanoscale* **2016,** *8* (30), 14448-14456.

103. Bayer, C. L.; Nam, S. Y.; Chen, Y.-S.; Emelianov, S. Y., Photoacoustic signal amplification through plasmonic nanoparticle aggregation. *Journal of biomedical optics* **2013,** *18* (1), 016001.

104. Chen, Y.-S.; Yoon, S. J.; Frey, W.; Dockery, M.; Emelianov, S., Dynamic contrast-enhanced photoacoustic imaging using photothermal stimuli-responsive composite nanomodulators. *Nature communications* **2017,** *8* (1), 1-10.

105. Alkurdi, A.; Lombard, J.; Detcheverry, F.; Merabia, S., Enhanced Heat Transfer with Metal-Dielectric Core-Shell Nanoparticles. *Physical Review Applied* **2020,** *13* (3), 034036.

106. Kumar, D.; Ghai, D. P.; Soni, R., Simulation Studies of Photoacoustic Response from Gold-Silica Core-Shell Nanoparticles. *Plasmonics* **2018,** *13* (6), 1833-1841.

107. Pang, G. A.; Poisson, F.; Laufer, J.; Haisch, C.; Bossy, E., Theoretical and experimental study of photoacoustic excitation of silica-coated gold nanospheres in water. *The Journal of Physical Chemistry C* **2019**.

108. Hu, M.; Wang, X.; Hartland, G. V.; Salgueiriño-Maceira, V.; Liz-Marzán, L. M., Heat dissipation in gold–silica core-shell nanoparticles. *Chemical Physics Letters* **2003,** *372* (5-6), 767-772.

109. Rodríguez-Roldán, G.; Cruz-Orea, A.; Suaste-Gómez, E., Thermal Characterization of a PPy/PLA Composite by Photoacoustic Calorimetry and Photopyroelectric Techniques. *International Journal of Thermophysics* **2019,** *40* (2), 16.

110. Hatef, A.; Darvish, B.; Dagallier, A.; Davletshin, Y. R.; Johnston, W.; Kumaradas, J. C.; Rioux, D.; Meunier, M., Analysis of photoacoustic response from gold–silver alloy nanoparticles irradiated by short pulsed laser in water. *The Journal of Physical Chemistry C* **2015,** *119* (42), 24075-24080.

111. Nam, S. Y.; Ricles, L. M.; Suggs, L. J.; Emelianov, S. Y., Nonlinear photoacoustic signal increase from endocytosis of gold nanoparticles. *Optics letters* **2012,** *37* (22), 4708-4710.

112. Masim, F. C. P.; Liu, H.-L.; Porta, M.; Yonezawa, T.; Balčytis, A.; Juodkazis, S.; Hsu, W.-H.; Hatanaka, K., Enhanced photoacoustics from gold nano-colloidal suspensions under femtosecond laser excitation. *Optics express* **2016,** *24* (13), 14781-14792.

113. Langer, G.; Bouchal, K.-D.; Grün, H.; Burgholzer, P.; Berer, T., Two-photon absorption-induced photoacoustic imaging of Rhodamine B dyed polyethylene spheres using a femtosecond laser. *Optics express* **2013,** *21* (19), 22410-22422.

114. Masim, F. C. P.; Hsu, W.-H.; Liu, H.-L.; Yonezawa, T.; Balčytis, A.; Juodkazis, S.; Hatanaka, K., - Photoacoustic signal enhancements from gold nano-colloidal suspensions excited by a pair of time-delayed femtosecond pulses. **2017**.

115. Huang, K.; Zhang, Y.; Lin, J.; Huang, P., Nanomaterials for photoacoustic imaging in the second near-infrared window. *Biomaterials science* **2019,** *7* (2), 472-479.

116. Petronijevic, E.; Leahu, G.; Belardini, A.; Centini, M.; Voti, R. L.; Hakkarainen, T.; Koivusalo, E.; Piton, M. R.; Suomalainen, S.; Guina, M., Photo-acoustic spectroscopy reveals extrinsic optical chirality in GaAs-based nanowires partially covered with gold. *International Journal of Thermophysics* **2018,** *39* (4), 46.

117. Jeong, H.-H.; Mark, A. G.; Alarcón-Correa, M.; Kim, I.; Oswald, P.; Lee, T.-C.; Fischer, P., Dispersion and shape engineered plasmonic nanosensors. *Nature communications* **2016,** *7* (1), 1-7.

118. Petronijević, E.; Leahu, G.; Li Voti, R.; Belardini, A.; Scian, C.; Michieli, N.; Cesca, T.; Mattei, G.; Sibilia, C., Photo-acoustic detection of chirality in metal-polystyrene metasurfaces. *Applied Physics Letters* **2019,** *114* (5), 053101.

119. Nishi, H.; Asami, K.; Tatsuma, T., CuS nanoplates for LSPR sensing in the second biological optical window. *Optical Materials Express* **2016,** *6* (4), 1043-1048.

120. Lei, D. Y.; Appavoo, K.; Ligmajer, F.; Sonnefraud, Y.; Haglund Jr, R. F.; Maier, S. A., Optically-triggered nanoscale memory effect in a hybrid plasmonic-phase changing nanostructure. *ACS photonics* **2015,** *2* (9), 1306-1313.

121. Yildirim, A.; Chattaraj, R.; Blum, N. T.; Goodwin, A. P., Understanding acoustic cavitation initiation by porous nanoparticles: toward nanoscale agents for ultrasound imaging and therapy. *Chemistry of Materials* **2016,** *28* (16), 5962-5972.

122. Hariri, A.; Alipour, K.; Mantri, Y.; Schulze, J. P.; Jokerst, J. V., Deep Learning Improves Contrast in Low-Fluence Photoacoustic Imaging. *arXiv preprint arXiv:2004.08782* **2020**.

123. Phan, T. T. V.; Bui, N. Q.; Moorthy, M. S.; Lee, K. D.; Oh, J., Synthesis and in vitro performance of polypyrrole-coated iron–platinum nanoparticles for photothermal therapy and photoacoustic imaging. *Nanoscale research letters* **2017,** *12* (1), 570.

124. Lee, D. Y.; Kim, J. Y.; Lee, Y.; Lee, S.; Miao, W.; Kim, H. S.; Min, J. J.; Jon, S., Black Pigment Gallstone Inspired Platinum-Chelated Bilirubin Nanoparticles for Combined Photoacoustic Imaging and Photothermal Therapy of Cancers. *Angewandte Chemie* **2017,** *129* (44), 13872-13876.

125. Homan, K. A.; Souza, M.; Truby, R.; Luke, G. P.; Green, C.; Vreeland, E.; Emelianov, S., Silver nanoplate contrast agents for in vivo molecular photoacoustic imaging. *ACS nano* **2012,** *6* (1), 641-650.

126. Silvestri, B.; Armanetti, P.; Sanità, G.; Vitiello, G.; Lamberti, A.; Calì, G.; Pezzella, A.; Luciani, G.; Menichetti, L.; Luin, S., Silver-nanoparticles as plasmon-resonant enhancers for eumelanin's photoacoustic signal in a self-structured hybrid nanoprobe. *Materials Science and Engineering: C* **2019,** *102*, 788-797.

127. Ku, G.; Zhou, M.; Song, S.; Huang, Q.; Hazle, J.; Li, C., Copper sulfide nanoparticles as a new class of photoacoustic contrast agent for deep tissue imaging at 1064 nm. *ACS nano* **2012,** *6* (8), 7489-7496.

128. Song, X. R.; Wang, X.; Yu, S. X.; Cao, J.; Li, S. H.; Li, J.; Liu, G.; Yang, H. H.; Chen, X., Co9Se8 nanoplates as a new theranostic platform for photoacoustic/magnetic resonance Dual-Modal-Imaging-Guided Chemo-Photothermal combination therapy. *Advanced Materials* **2015,** *27* (21), 3285-3291.

129. Cheng, L.; Liu, J.; Gu, X.; Gong, H.; Shi, X.; Liu, T.; Wang, C.; Wang, X.; Liu, G.; Xing, H., PEGylated WS2 nanosheets as a multifunctional theranostic agent for in vivo dual-modal CT/photoacoustic imaging guided photothermal therapy. *Advanced materials* **2014,** *26* (12), 1886-1893.

130. Yu, X.; Li, A.; Zhao, C.; Yang, K.; Chen, X.; Li, W., Ultrasmall semimetal nanoparticles of bismuth for dual-modal computed tomography/photoacoustic imaging and synergistic thermoradiotherapy. *ACS nano* **2017,** *11* (4), 3990-4001.

131. Zhang, Y. S.; Wang, Y.; Wang, L.; Wang, Y.; Cai, X.; Zhang, C.; Wang, L. V.; Xia, Y., Labeling human mesenchymal stem cells with gold nanocages for in vitro and in vivo tracking by two-photon microscopy and photoacoustic microscopy. *Theranostics* **2013,** *3* (8), 532.

132. Thakur, S. N.; Guo, D.; Kundu, T.; Goodman, L., Two-photon photoacoustic spectroscopy of acetone 3p Rydberg states. *Chemical physics letters* **1992,** *199* (3-4), 335-340.

133. Nie, L.; Chen, M.; Sun, X.; Rong, P.; Zheng, N.; Chen, X., Palladium nanosheets as highly stable and effective contrast agents for in vivo photoacoustic molecular imaging. *Nanoscale* **2014,** *6* (3), 1271-1276.

134. Wang, L.; Jiang, X.; Ji, Y.; Bai, R.; Zhao, Y.; Wu, X.; Chen, C., Surface chemistry of gold nanorods: origin of cell membrane damage and cytotoxicity. *Nanoscale* **2013,** *5* (18), 8384-8391.

135. Alkilany, A. M.; Nagaria, P. K.; Hexel, C. R.; Shaw, T. J.; Murphy, C. J.; Wyatt, M. D., Cellular uptake and cytotoxicity of gold nanorods: molecular origin of cytotoxicity and surface effects. *small* **2009,** *5* (6), 701-708.

136. Jokerst, J. V.; Lobovkina, T.; Zare, R. N.; Gambhir, S. S., Nanoparticle PEGylation for imaging and therapy. *Nanomedicine* **2011,** *6* (4), 715-728.

137. Takahashi, H.; Niidome, Y.; Niidome, T.; Kaneko, K.; Kawasaki, H.; Yamada, S., Modification of gold nanorods using phosphatidylcholine to reduce cytotoxicity. *Langmuir* **2006,** *22* (1), 2-5.

138. Yasun, E.; Li, C.; Barut, I.; Janvier, D.; Qiu, L.; Cui, C.; Tan, W., BSA modification to reduce CTAB induced nonspecificity and cytotoxicity of aptamer-conjugated gold nanorods. *Nanoscale* **2015,** *7* (22), 10240-10248.

139. Lee, Y. J.; Ahn, E.-Y.; Park, Y., Shape-dependent cytotoxicity and cellular uptake of gold nanoparticles synthesized using green tea extract. *Nanoscale research letters* **2019,** *14* (1), 1-14.

140. Rastinehad, A. R.; Anastos, H.; Wajswol, E.; Winoker, J. S.; Sfakianos, J. P.; Doppalapudi, S. K.; Carrick, M. R.; Knauer, C. J.; Taouli, B.; Lewis, S. C., Gold nanoshell-localized photothermal ablation of prostate tumors in a clinical pilot device study. *Proceedings of the National Academy of Sciences* **2019,** *116* (37), 18590-18596.

141. Viator, J. A.; Svaasand, L. O.; Aguilar, G.; Choi, B.; Nelson, J. S. In *Photoacoustic measurement of epidermal melanin*, Biomedical optoacoustics IV, International Society for Optics and Photonics: 2003; pp 14-20.

142. Zhang, H. F.; Maslov, K.; Stoica, G.; Wang, L. V., Functional photoacoustic microscopy for high-resolution and noninvasive in vivo imaging. *Nature biotechnology* **2006,** *24* (7), 848-851.

143. West, J. L.; Halas, N. J., Engineered nanomaterials for biophotonics applications: improving sensing, imaging, and therapeutics. *Annual review of biomedical engineering* **2003,** *5* (1), 285-292.

144. Lal, S.; Clare, S. E.; Halas, N. J., Nanoshell-enabled photothermal cancer therapy: impending clinical impact. *Accounts of chemical research* **2008,** *41* (12), 1842-1851.

145. Apel, K.; Hirt, H., Reactive oxygen species: metabolism, oxidative stress, and signal transduction. *Annu Rev Plant Biol* **2004,** *55*, 373-99.

146. Murphy, M. P., How mitochondria produce reactive oxygen species. *Biochemical journal* **2009,** *417* (1), 1-13.

147. Schieber, M.; Chandel, N. S., ROS function in redox signaling and oxidative stress. *Current biology* **2014,** *24* (10), R453-R462.

148. Scherz-Shouval, R.; Elazar, Z., ROS, mitochondria and the regulation of autophagy. *Trends in cell biology* **2007,** *17* (9), 422-427.

149. Boonstra, J.; Post, J. A., Molecular events associated with reactive oxygen species and cell cycle progression in mammalian cells. *Gene* **2004,** *337*, 1-13.

150. Fleury, C.; Mignotte, B.; Vayssière, J.-L., Mitochondrial reactive oxygen species in cell death signaling. *Biochimie* **2002,** *84* (2-3), 131-141.

151. Nathan, C.; Cunningham-Bussel, A., Beyond oxidative stress: an immunologist's guide to reactive oxygen species. *Nature Reviews Immunology* **2013,** *13* (5), 349.

152. Carden, D. L.; Granger, D. N., Pathophysiology of ischaemia–reperfusion injury. *The Journal of pathology* **2000,** *190* (3), 255-266.

153. Medzhitov, R., Origin and physiological roles of inflammation. *Nature* **2008,** *454* (7203), 428.

154. Pedersen, J. T.; Chen, S. W.; Borg, C. B.; Ness, S.; Bahl, J. M.; Heegaard, N. H.; Dobson, C. M.; Hemmingsen, L.; Cremades, N.; Teilum, K., Amyloid-β and α-synuclein decrease the level of metal-catalyzed reactive oxygen species by radical scavenging and redox silencing. *Journal of the American Chemical Society* **2016,** *138* (12), 3966-3969.

155. Sverdlov, A. L.; Elezaby, A.; Qin, F.; Behring, J. B.; Luptak, I.; Calamaras, T. D.; Siwik, D. A.; Miller, E. J.; Liesa, M.; Shirihai, O. S., Mitochondrial reactive oxygen species mediate cardiac structural, functional, and mitochondrial consequences of diet-induced metabolic heart disease. *Journal of the American Heart Association* **2016,** *5* (1), e002555.

156. Mailloux, R. J.; McBride, S. L.; Harper, M.-E., Unearthing the secrets of mitochondrial ROS and glutathione in bioenergetics. *Trends in biochemical sciences* **2013,** *38* (12), 592-602.

157. Degli Esposti, M., Measuring mitochondrial reactive oxygen species. *Methods* **2002,** *26* (4), 335-340.

158. Weidinger, A.; Kozlov, A. V., Biological activities of reactive oxygen and nitrogen species: oxidative stress versus signal transduction. *Biomolecules* **2015,** *5* (2), 472-484.

159. Bhattacharyya, A.; Chattopadhyay, R.; Mitra, S.; Crowe, S. E., Oxidative stress: an essential factor in the pathogenesis of gastrointestinal mucosal diseases. *Physiological reviews* **2014,** *94* (2), 329-354.

160. Merksamer, P. I.; Trusina, A.; Papa, F. R., Real-time redox measurements during endoplasmic reticulum stress reveal interlinked protein folding functions. *Cell* **2008,** *135* (5), 933-947.

161. Tanaka, K.; Miura, T.; Umezawa, N.; Urano, Y.; Kikuchi, K.; Higuchi, T.; Nagano, T., Rational design of fluorescein-based fluorescence probes. Mechanism-based design of a maximum fluorescence probe for singlet oxygen. *Journal of the American Chemical Society* **2001,** *123* (11), 2530-2536.

162. Gomes, A.; Fernandes, E.; Lima, J. L., Fluorescence probes used for detection of reactive oxygen species. *Journal of biochemical and biophysical methods* **2005,** *65* (2-3), 45-80.

163. Hicks, J.; Halkerston, R.; Silman, N.; Jackson, S.; Aylott, J.; Rawson, F., Real-time bacterial detection with an intracellular ROS sensing platform. *Biosensors and Bioelectronics* **2019**, 111430.

164. Van de Bittner, G. C.; Dubikovskaya, E. A.; Bertozzi, C. R.; Chang, C. J., In vivo imaging of hydrogen peroxide production in a murine tumor model with a chemoselective bioluminescent reporter. *Proceedings of the National Academy of Sciences* **2010,** *107* (50), 21316-21321.

165. Taruttis, A.; Ntziachristos, V., Advances in real-time multispectral optoacoustic imaging and its applications. *Nature photonics* **2015,** *9* (4), 219.

166. Razansky, D.; Vinegoni, C.; Ntziachristos, V., Multispectral photoacoustic imaging of fluorochromes in small animals. *Optics letters* **2007,** *32* (19), 2891-2893.

167. Fu, T.; Chen, Y.; Hao, J.; Wang, X.; Liu, G.; Li, Y.; Liu, Z.; Cheng, L., Facile preparation of uniform FeSe2 nanoparticles for PA/MR dual-modal imaging and photothermal cancer therapy. *Nanoscale* **2015,** *7* (48), 20757-20768.

168. Chen, F.; Zhao, E. R.; Hu, T.; Shi, Y.; Sirbuly, D. J.; Jokerst, J. V., Silicon carbide nanoparticles as a photoacoustic and photoluminescent dual-imaging contrast agent for long-term cell tracking. *Nanoscale Advances* **2019**.

169. Moore, C.; Chen, F.; Wang, J.; Jokerst, J. V., Listening for the therapeutic window: Advances in drug delivery utilizing photoacoustic imaging. *Advanced drug delivery reviews* **2019**.

170. Miao, Q.; Pu, K., Emerging designs of activatable photoacoustic probes for molecular imaging. *Bioconjugate chemistry* **2016,** *27* (12), 2808-2823.

171. Yang, X.; Stein, E. W.; Ashkenazi, S.; Wang, L. V., Nanoparticles for photoacoustic imaging. *Wiley interdisciplinary reviews: nanomedicine and nanobiotechnology* **2009,** *1* (4), 360-368.

172. Yang, Z.; Dai, Y.; Yin, C.; Fan, Q.; Zhang, W.; Song, J.; Yu, G.; Tang, W.; Fan, W.; Yung, B. C., Activatable semiconducting theranostics: simultaneous generation and ratiometric photoacoustic imaging of reactive oxygen species in vivo. *Advanced Materials* **2018,** *30* (23), 1707509.

173. Pu, K.; Shuhendler, A. J.; Jokerst, J. V.; Mei, J.; Gambhir, S. S.; Bao, Z.; Rao, J., Semiconducting polymer nanoparticles as photoacoustic molecular imaging probes in living mice. *Nature nanotechnology* **2014,** *9* (3), 233.

174. Chen, Y.-S.; Zhao, Y.; Yoon, S. J.; Gambhir, S. S.; Emelianov, S., Miniature gold nanorods for photoacoustic molecular imaging in the second near-infrared optical window. *Nature nanotechnology* **2019,** *14* (5), 465.

175. Tian, L.; Chen, E.; Gandra, N.; Abbas, A.; Singamaneni, S., Gold nanorods as plasmonic nanotransducers: distance-dependent refractive index sensitivity. *Langmuir* **2012,** *28* (50), 17435-17442.

176. Kim, F.; Song, J. H.; Yang, P., Photochemical synthesis of gold nanorods. *Journal of the American Chemical Society* **2002,** *124* (48), 14316-14317.

177. Gou, L.; Murphy, C. J., Fine-tuning the shape of gold nanorods. *Chemistry of materials* **2005,** *17* (14), 3668-3672.

178. Murphy, C. J.; Jana, N. R., Controlling the aspect ratio of inorganic nanorods and nanowires. *Advanced Materials* **2002,** *14* (1), 80-82.

179. Gandra, N.; Singamaneni, S., Bilayered Raman-intense gold nanostructures with hidden tags (BRIGHTs) for high-resolution bioimaging. *Advanced Materials* **2013,** *25* (7), 1022-1027.

180. Zhang, Z.; Wang, J.; Chen, C., Gold nanorods based platforms for light-mediated theranostics. *Theranostics* **2013,** *3* (3), 223.

181. Yilmaz, H.; Bae, S. H.; Cao, S.; Wang, Z.; Raman, B.; Singamaneni, S., Gold Nanorod-based Plasmonic Nose for Analysis of Chemical Mixtures. *ACS Applied Nano Materials* **2019**.

182. Levi, J.; Kothapalli, S. R.; Ma, T.-J.; Hartman, K.; Khuri-Yakub, B. T.; Gambhir, S. S., Design, synthesis, and imaging of an activatable photoacoustic probe. *Journal of the American Chemical Society* **2010,** *132* (32), 11264-11269.

183. Wang, S.; Sheng, Z.; Yang, Z.; Hu, D.; Long, X.; Feng, G.; Liu, Y.; Yuan, Z.; Zhang, J.; Zheng, H., Activatable Small-Molecule Photoacoustic Probes that Cross the Blood-Brain Barrier for Visualization of Copper (II) in Mice with Alzheimer's Disease. *Angewandte Chemie (International ed. in English)* **2019,** *58* (36), 12415-12419.

184. Yang, Z.; Song, J.; Tang, W.; Fan, W.; Dai, Y.; Shen, Z.; Lin, L.; Cheng, S.; Liu, Y.; Niu, G., Stimuli-Responsive Nanotheranostics for Real-Time Monitoring Drug Release by Photoacoustic Imaging. *Theranostics* **2019,** *9* (2), 526.

185. Weber, J.; Bollepalli, L.; Belenguer, A. M.; Di Antonio, M.; De Mitri, N.; Joseph, J.; Balasubramanian, S.; Hunter, C. A.; Bohndiek, S. E., An Activatable Cancer-Targeted Hydrogen Peroxide Probe for Photoacoustic and Fluorescence Imaging. *Cancer research* **2019,** *79* (20), 5407-5417.

186. Lu, X.; Zhao, M.; Chen, P.; Fan, Q.; Wang, W.; Huang, W., Enhancing hydrophilicity of photoacoustic probes for effective ratiometric imaging of hydrogen peroxide. *Journal of Materials Chemistry B* **2018,** *6* (27), 4531-4538.

187. Reinhardt, C. J.; Zhou, E. Y.; Jorgensen, M. D.; Partipilo, G.; Chan, J., A ratiometric acoustogenic probe for in vivo imaging of endogenous nitric oxide. *Journal of the American Chemical Society* **2018,** *140* (3), 1011-1018.

188. Wang, S.; Li, Z.; Liu, Y.; Feng, G.; Zheng, J.; Yuan, Z.; Zhang, X., Activatable photoacoustic and fluorescent probe of nitric oxide for cellular and in vivo imaging. *Sensors and Actuators B: Chemical* **2018,** *267*, 403-411.

189. Reinhardt, C. J.; Xu, R.; Chan, J., Nitric oxide imaging in cancer enabled by steric relaxation of a photoacoustic probe platform. *Chemical Science* **2020**.

190. Zhang, J.; Zhen, X.; Zeng, J.; Pu, K., A dual-modal molecular probe for near-infrared fluorescence and photoacoustic imaging of peroxynitrite. *Analytical chemistry* **2018,** *90* (15), 9301-9307.

191. Xie, C.; Zhen, X.; Lyu, Y.; Pu, K., Nanoparticle regrowth enhances photoacoustic signals of semiconducting macromolecular probe for in vivo imaging. *Advanced Materials* **2017,** *29* (44), 1703693.

192. Zhang, Q.; Cobley, C. M.; Zeng, J.; Wen, L.-P.; Chen, J.; Xia, Y., Dissolving Ag from Au− Ag Alloy Nanoboxes with H2O2: A Method for Both Tailoring the Optical Properties and Measuring the H2O2 Concentration. *The Journal of Physical Chemistry C* **2010,** *114* (14), 6396-6400.

193. Varma, S. D.; Devamanoharan, P., Excretion of hydrogen peroxide in human urine. *Free radical research communications* **1990,** *8* (2), 73-78.

194. Varma, S.; Devamanoharan, P., Hydrogen peroxide in human blood. *Free radical research communications* **1991,** *14* (2), 125-131.

195. Giblin, F. J.; McCready, J. P.; Kodama, T.; Reddy, V. N., A direct correlation between the levels of ascorbic acid and H2O2 in aqueous humor. *Experimental eye research* **1984,** *38* (1), 87-93.

196. Liu, P.; Xu, B.; Quilley, J.; Wong, P. Y.-K., Peroxynitrite attenuates hepatic ischemia-reperfusion injury. *American Journal of Physiology-Cell Physiology* **2000,** *279* (6), C1970-C1977.

197. Tan, Y. T., Silver halides in photography. *MRS Bulletin* **1989,** *14* (5), 13-16.

198. Shankar, C.; Dao, A. T.; Singh, P.; Higashimine, K.; Mott, D. M.; Maenosono, S., Chemical stabilization of gold coated by silver core–shell nanoparticles via electron transfer. *Nanotechnology* **2012,** *23* (24), 245704.

199. Mott, D. M.; Anh, D. T. N.; Singh, P.; Shankar, C.; Maenosono, S., Electronic transfer as a route to increase the chemical stability in gold and silver core–shell nanoparticles. *Advances in colloid and interface science* **2012,** *185*, 14-33.

200. Linnert, T.; Mulvaney, P.; Henglein, A., Surface chemistry of colloidal silver: surface plasmon damping by chemisorbed iodide, hydrosulfide (SH-), and phenylthiolate. *The Journal of Physical Chemistry* **1993,** *97* (3), 679-682.

201. Cappel, C. R., Silver compounds. *Kirk-Othmer Encyclopedia of Chemical Technology* **2000**.

202. Singh, P.; Thuy, N. T.; Aoki, Y.; Mott, D.; Maenosono, S., Intensification of surface enhanced Raman scattering of thiol-containing molecules using Ag@ Au core@ shell nanoparticles. *Journal of Applied Physics* **2011,** *109* (9), 094301.

203. Ibrahim, H.; Mohammed, S.; Amin, A., Comparative studies of the electrochemical behavior of silver electrode in chloride, bromide and iodide aqueous solutions. *Int. J. Electrochem. Sci* **2010,** *5*, 278-294.

204. Ghosh, S.; Saraswathi, A.; Indi, S.; Hoti, S.; Vasan, H., Ag@ AgI, core@ shell structure in agarose matrix as hybrid: synthesis, characterization, and antimicrobial activity. *Langmuir* **2012,** *28* (22), 8550-8561.

205. Kato, Y.; Ono, L. K.; Lee, M. V.; Wang, S.; Raga, S. R.; Qi, Y., Silver iodide formation in methyl ammonium lead iodide perovskite solar cells with silver top electrodes. *Advanced Materials Interfaces* **2015,** *2* (13), 1500195.

206. Pedersen, D. B.; Wang, S.; Duncan, E. S.; Liang, S. H., Adsorbate− Induced Diffusion of Ag and Au Atoms Out of the Cores of Ag@ Au, Au@ Ag, and Ag@ AgI Core− Shell Nanoparticles. *The Journal of Physical Chemistry C* **2007,** *111* (37), 13665-13672.

207. Liu, M.; Guyot-Sionnest, P., Synthesis and optical characterization of Au/Ag core/shell nanorods. *The Journal of Physical Chemistry B* **2004,** *108* (19), 5882-5888.

208. Mulvaney, P., Surface plasmon spectroscopy of nanosized metal particles. *Langmuir* **1996,** *12* (3), 788-800.

209. Xie, K.; Yu, Y.; Zhang, Z.; Liu, W.; Pei, Y.; Xiong, L.; Hou, L.; Wang, G., Hydrogen gas improves survival rate and organ damage in zymosan-induced generalized inflammation model. *Shock* **2010,** *34* (5), 495-501.

210. Xiang, Y.; Wu, X.; Liu, D.; Li, Z.; Chu, W.; Feng, L.; Zhang, K.; Zhou, W.; Xie, S., Gold nanorod-seeded growth of silver nanostructures: from homogeneous coating to anisotropic coating. *Langmuir* **2008,** *24* (7), 3465-3470.

211. Liu, H.; Pierre-Pierre, N.; Huo, Q., Dynamic light scattering for gold nanorod size characterization and study of nanorod–protein interactions. *Gold bulletin* **2012,** *45* (4), 187-195.

212. Gonzalez, A.; Noguez, C.; Ortiz, G.; Rodriguez-Gattorno, G., Optical absorbance of colloidal suspensions of silver polyhedral nanoparticles. *The Journal of Physical Chemistry B* **2005,** *109* (37), 17512-17517.

213. Grzelczak, M.; Sánchez-Iglesias, A.; Rodríguez-González, B.; Alvarez-Puebla, R.; Pérez-Juste, J.; Liz-Marzán, L. M., Influence of iodide ions on the growth of gold nanorods: tuning tip curvature and surface plasmon resonance. *Advanced Functional Materials* **2008,** *18* (23), 3780-3786.

214. Millstone, J. E.; Wei, W.; Jones, M. R.; Yoo, H.; Mirkin, C. A., Iodide ions control seed-mediated growth of anisotropic gold nanoparticles. *Nano letters* **2008,** *8* (8), 2526-2529.

215. Smith, D. K.; Miller, N. R.; Korgel, B. A., Iodide in CTAB prevents gold nanorod formation. *Langmuir* **2009,** *25* (16), 9518-9524.

216. Walsh, M. J.; Barrow, S. J.; Tong, W.; Funston, A. M.; Etheridge, J., Symmetry breaking and silver in gold nanorod growth. *ACS nano* **2015,** *9* (1), 715-724.

217. Grzelczak, M.; Pérez-Juste, J.; Rodríguez-González, B.; Liz-Marzán, L. M., Influence of silver ions on the growth mode of platinum on gold nanorods. *Journal of Materials Chemistry* **2006,** *16* (40), 3946-3951.

218. Zhang, A.; Tie, X.; Zhang, J.; An, Y.; Li, L., Adsorption of iodide and iodate on colloidal silver surface. *Applied Surface Science* **2008,** *255* (5), 3184-3187.

219. Saunders, J. A.; Rogers, L. C.; Klomsiri, C.; Poole, L. B.; Daniel, L. W., Reactive oxygen species mediate lysophosphatidic acid induced signaling in ovarian cancer cells. *Free Radical Biology and Medicine* **2010,** *49* (12), 2058-2067.

220. Hileman, E. O.; Liu, J.; Albitar, M.; Keating, M. J.; Huang, P., Intrinsic oxidative stress in cancer cells: a biochemical basis for therapeutic selectivity. *Cancer chemotherapy and pharmacology* **2004,** *53* (3), 209-219.

221. Fahrenholtz, C. D.; Swanner, J.; Ramirez-Perez, M.; Singh, R. N., Heterogeneous responses of ovarian cancer cells to silver nanoparticles as a single agent and in combination with cisplatin. *Journal of nanomaterials* **2017,** *2017*.

222. Link, S.; Burda, C.; Nikoobakht, B.; El-Sayed, M. A., Laser-induced shape changes of colloidal gold nanorods using femtosecond and nanosecond laser pulses. *The Journal of Physical Chemistry B* **2000,** *104* (26), 6152-6163.

223. Mantri, Y.; Jokerst, J. V., Engineering Plasmonic Nanoparticles for Enhanced Photoacoustic Imaging. *ACS nano* **2020,** *14* (8), 9408-9422.

224. Manohar, S.; Ungureanu, C.; Van Leeuwen, T. G., Gold nanorods as molecular contrast agents in photoacoustic imaging: the promises and the caveats. *Contrast media & molecular imaging* **2011,** *6* (5), 389-400.

225. Shahbazi, K.; Frey, W.; Chen, Y.-S.; Aglyamov, S.; Emelianov, S., Photoacoustics of core–shell nanospheres using comprehensive modeling and analytical solution approach. *Communications Physics* **2019,** *2* (1), 1-11.

226. Lohse, S. E.; Murphy, C. J., The quest for shape control: a history of gold nanorod synthesis. *Chemistry of Materials* **2013,** *25* (8), 1250-1261.

227. Dhada, K. S.; Hernandez, D. S.; Suggs, L. J., In vivo photoacoustic tracking of mesenchymal stem cell viability. *ACS nano* **2019,** *13* (7), 7791-7799.

228. Guo, D.; Huang, Y.; Jin, X.; Zhang, C.; Zhu, X., A Redox-Responsive, In-situ polymerized polyplatinum (IV)-coated gold nanorod as an amplifier of tumor accumulation for enhanced thermo-chemotherapy. *Biomaterials* **2021,** *266*, 120400.

229. Li, P.-C.; Wei, C.-W.; Liao, C.-K.; Chen, C.-D.; Pao, K.-C.; Wang, C.-R. C.; Wu, Y.-N.; Shieh, D.-B., Photoacoustic imaging of multiple targets using gold nanorods. *ieee transactions on ultrasonics, ferroelectrics, and frequency control* **2007,** *54* (8), 1642-1647.

230. Mantri, Y.; Davidi, B.; Lemaster, J. E.; Hariri, A.; Jokerst, J. V., Iodide-doped precious metal nanoparticles: measuring oxidative stress in vivo via photoacoustic imaging. *Nanoscale* **2020,** *12* (19), 10511-10520.

231. Cavigli, L.; Centi, S.; Borri, C.; Tortoli, P.; Panettieri, I.; Streit, I.; Ciofini, D.; Magni, G.; Rossi, F.; Siano, S., 1064-nm-resonant gold nanorods for photoacoustic theranostics within permissible exposure limits. *Journal of biophotonics* **2019,** *12* (10), e201900082.

232. Luke, G. P.; Yeager, D.; Emelianov, S. Y., Biomedical applications of photoacoustic imaging with exogenous contrast agents. *Annals of biomedical engineering* **2012,** *40* (2), 422-437.

233. Xu, M.; Yim, W.; Zhou, J.; Zhou, J.; Jin, Z.; Moore, C.; Borum, R.; Jorns, A.; Jokersta, J. V., The Application of Organic Nanomaterials for Bioimaging, Drug Delivery, and Therapy: Spanning various domains. *IEEE Nanotechnology Magazine* **2021**.

234. Fu, Q.; Zhu, R.; Song, J.; Yang, H.; Chen, X., Photoacoustic imaging: contrast agents and their biomedical applications. *Advanced Materials* **2019,** *31* (6), 1805875.

235. Upputuri, P. K.; Pramanik, M., Recent advances in photoacoustic contrast agents for in vivo imaging. *Wiley Interdisciplinary Reviews: Nanomedicine and Nanobiotechnology* **2020,** *12* (4), e1618.

236. Masim, F. C. P.; Hsu, W.-H.; Liu, H.-L.; Yonezawa, T.; Balčytis, A.; Juodkazis, S.; Hatanaka, K., Photoacoustic signal enhancements from gold nano-colloidal suspensions excited by a pair of time-delayed femtosecond pulses. *Optics Express* **2017,** *25* (16), 19497-19507.

237. Zhong, J.; Wen, L.; Yang, S.; Xiang, L.; Chen, Q.; Xing, D., Imaging-guided high-efficient photoacoustic tumor therapy with targeting gold nanorods. *Nanomedicine: Nanotechnology, Biology and Medicine* **2015,** *11* (6), 1499-1509.

238. Khanal, A.; Ullum, C.; Kimbrough, C. W.; Garbett, N. C.; Burlison, J. A.; McNally, M. W.; Chuong, P.; El-Baz, A. S.; Jasinski, J. B.; McNally, L. R., Tumor targeted mesoporous silica-coated gold nanorods facilitate detection of pancreatic tumors using Multispectral optoacoustic tomography. *Nano Research* **2015,** *8* (12), 3864-3877.

239. Huff, T. B.; Tong, L.; Zhao, Y.; Hansen, M. N.; Cheng, J.-X.; Wei, A., Hyperthermic effects of gold nanorods on tumor cells. **2007**.

240. Chen, J.; Liang, H.; Lin, L.; Guo, Z.; Sun, P.; Chen, M.; Tian, H.; Deng, M.; Chen, X., Gold-nanorods-based gene carriers with the capability of photoacoustic imaging and photothermal therapy. *ACS applied materials & interfaces* **2016,** *8* (46), 31558-31566.

241. Yim, W.; Borum, R. M.; Zhou, J.; Mantri, Y.; Wu, Z.; Zhou, J.; Jin, Z.; Creyer, M.; Jokerst, J. V., Ultrasmall gold nanorod-polydopamine hybrids for enhanced photoacoustic imaging and photothermal therapy in second near-infrared window. *Nanotheranostics* **2022,** *6* (1), 79.

242. Yim, W.; Zhou, J.; Mantri, Y.; Creyer, M. N.; Moore, C. A.; Jokerst, J. V., Gold nanorod–melanin hybrids for enhanced and prolonged photoacoustic imaging in the near-infrared-II window. *ACS Applied Materials & Interfaces* **2021,** *13* (13), 14974-14984.

243. Cavigli, L.; Milanesi, A.; Khlebtsov, B. N.; Centi, S.; Ratto, F.; Khlebtsov, N. G.; Pini, R., Impact of Kapitza resistance on the stability and efficiency of photoacoustic conversion from gold nanorods. *Journal of Colloid and Interface Science* **2020,** *578*, 358-365.

244. Pang, G. A.; Poisson, F.; Laufer, J.; Haisch, C.; Bossy, E., Theoretical and experimental study of photoacoustic excitation of silica-coated gold nanospheres in water. *The Journal of Physical Chemistry C* **2019,** *124* (1), 1088-1098.

245. Nguyen, S. C.; Zhang, Q.; Manthiram, K.; Ye, X.; Lomont, J. P.; Harris, C. B.; Weller, H.; Alivisatos, A. P., Study of heat transfer dynamics from gold nanorods to the environment via time-resolved infrared spectroscopy. *Acs Nano* **2016,** *10* (2), 2144-2151.

246. Wang, Y.; Zhan, Y.; Harris, L. M.; Khan, S.; Xia, J., A portable three-dimensional photoacoustic tomography system for imaging of chronic foot ulcers. *Quantitative imaging in medicine and surgery* **2019,** *9* (5), 799.

247. Moore, C.; Jokerst, J. V., Strategies for image-guided therapy, surgery, and drug delivery using photoacoustic imaging. *Theranostics* **2019,** *9* (6), 1550.

248. Sit, I.; Wu, H.; Grassian, V. H., Environmental Aspects of Oxide Nanoparticles: Probing Oxide Nanoparticle Surface Processes Under Different Environmental Conditions. *Annual Review of Analytical Chemistry* **2021,** *14*.

249. Sit, I.; Sagisaka, S.; Grassian, V. H., Nucleotide Adsorption on Iron (III) Oxide Nanoparticle Surfaces: Insights into Nano–Geo–Bio Interactions Through Vibrational Spectroscopy. *Langmuir* **2020,** *36* (51), 15501-15513.

250. Villanueva, Y.; Hondebrink, E.; Petersen, W.; Steenbergen, W., Photoacoustic measurement of the Grüneisen parameter using an integrating sphere. *Review of scientific instruments* **2014,** *85* (7), 074904.

251. Mallidi, S.; Emelianov, S., Photoacoustic technique to measure beam profile of pulsed laser systems. *Review of Scientific Instruments* **2009,** *80* (5), 054901.

252. Yao, D.-K.; Zhang, C.; Maslov, K. I.; Wang, L. V., Photoacoustic measurement of the Grüneisen parameter of tissue. *Journal of biomedical optics* **2014,** *19* (1), 017007.

253. Hariri, A.; Alipour, K.; Mantri, Y.; Schulze, J. P.; Jokerst, J. V., Deep learning improves contrast in low-fluence photoacoustic imaging. *Biomedical optics express* **2020,** *11* (6), 3360-3373.

254. Katz-Boon, H.; Walsh, M.; Dwyer, C.; Mulvaney, P.; Funston, A. M.; Etheridge, J., Stability of crystal facets in gold nanorods. *Nano letters* **2015,** *15* (3), 1635-1641.

255. Petrova, E.; Liopo, A.; Oraevsky, A. A.; Ermilov, S. A., Temperature-dependent optoacoustic response and transient through zero Grüneisen parameter in optically contrasted media. *Photoacoustics* **2017,** *7*, 36-46.

256. Xu, S.; Scherer, G. W.; Mahadevan, T.; Garofalini, S. H., Thermal expansion of confined water. *Langmuir* **2009,** *25* (9), 5076-5083.

257. Hariri, A.; Lemaster, J.; Wang, J.; Jeevarathinam, A. S.; Chao, D. L.; Jokerst, J. V., The characterization of an economic and portable LED-based photoacoustic imaging system to facilitate molecular imaging. *Photoacoustics* **2018,** *9*, 10-20.

258. Cavigli, L.; Khlebtsov, B. N.; Centi, S.; Khlebtsov, N. G.; Pini, R.; Ratto, F., Photostability of contrast agents for photoacoustics: The case of gold nanorods. *Nanomaterials* **2021,** *11* (1), 116.

259. Sadovnikov, S.; Gusev, A., Thermal expansion, heat capacity and phase transformations in nanocrystalline and coarse-crystalline silver sulfide at 290–970 K. *Journal of Thermal Analysis and Calorimetry* **2018,** *131* (2), 1155-1164.

260. Sun, L.; Yan, X.; Zheng, J.; Yu, H.; Lu, Z.; Gao, S.-p.; Liu, L.; Pan, X.; Wang, D.; Wang, Z., Layer-dependent chemically induced phase transition of two-dimensional MoS2. *Nano letters* **2018,** *18* (6), 3435-3440.

261. Smith, D. K.; Korgel, B. A., The importance of the CTAB surfactant on the colloidal seed-mediated synthesis of gold nanorods. *Langmuir* **2008,** *24* (3), 644-649.

262. He, J.; Unser, S.; Bruzas, I.; Cary, R.; Shi, Z.; Mehra, R.; Aron, K.; Sagle, L., The facile removal of CTAB from the surface of gold nanorods. *Colloids and Surfaces B: Biointerfaces* **2018,** *163*, 140-145.

263. Cheah, M. H.; Chernev, P., Electrochemical oxidation of ferricyanide. *Scientific reports* **2021,** *11* (1), 1-7.

264. Loo, B.; Lee, Y.; Liang, E.; Kiefer, W., Surface-enhanced Raman scattering from ferrocyanide and ferricyanide ions adsorbed on silver and copper colloids. *Chemical physics letters* **1998,** *297* (1-2), 83-89.

265. Sugiyama, A.; Miura, M.; Oshikiri, Y.; Kim, Y.; Morimoto, R.; Miura, M.; Osaka, T.; Mogi, I.; Yamauchi, Y.; Aogaki, R., Excess heat production in the redox couple reaction of ferricyanide and ferrocyanide. *Scientific reports* **2020,** *10* (1), 1-12.

266. Chang, C. C.; Bocarsly, A. B., Oxidation of halides by redox enhanced ferricyanide in the [FeII□ CN□ PtIV] n coordination polymer: an optically triggered process. *Journal of Electroanalytical Chemistry* **1999,** *470* (2), 99-113.

267. Ramalingam, K.; Liang, M.; Pyae, N. L. W.; Aung, S. H.; Oo, T. Z.; Srimuk, P.; Ma, J.; Presser, V.; Chen, F.; Waite, T. D., Self-sustained visible-light-driven electrochemical redox desalination. *ACS Applied Materials & Interfaces* **2020,** *12* (29), 32788-32796.

268. Kay, H., Electrostriction. *Reports on Progress in Physics* **1955,** *18* (1), 230.

269. Villafañe, V.; Sesin, P.; Soubelet, P.; Anguiano, S.; Bruchhausen, A. E.; Rozas, G.; Carbonell, C. G.; Lemaître, A.; Fainstein, A., Optoelectronic forces with quantum wells for cavity optomechanics in GaAs/AlAs semiconductor microcavities. *Physical Review B* **2018,** *97* (19), 195306.

270. Wang, X.; Nie, S.; Li, J.; Clinite, R.; Wartenbe, M.; Martin, M.; Liang, W.; Cao, J., Electronic Grüneisen parameter and thermal expansion in ferromagnetic transition metal. *Applied Physics Letters* **2008,** *92* (12), 121918.

271. Knyazev, G.; Ignatyeva, D.; Sopko, I.; Belotelov, V.; Romanov, O., Amplification of the electrostriction mechanism of photoacoustic conversion in layered media. *Journal of Physics D: Applied Physics* **2020,** *53* (47), 475101.

272. Heritier, J.-M., Electrostrictive limit and focusing effects in pulsed photoacoustic detection. *Optics Communications* **1983,** *44* (4), 267-272.

273. Feitelson, J.; Mauzerall, D., Enthalpy and electrostriction in the electron-transfer reaction between triplet zinc uroporphyrin and ferricyanide. *The Journal of Physical Chemistry B* **2002,** *106* (37), 9674-9678.

274. Autrey, T.; Foster, N. S.; Klepzig, K.; Amonette, J. E.; Daschbach, J. L., A new angle into time-resolved photoacoustic spectroscopy: A layered prism cell increases experimental flexibility. *Review of scientific instruments* **1998,** *69* (6), 2246-2258.

275. Dziaugys, A.; Kelley, K.; Brehm, J. A.; Tao, L.; Puretzky, A.; Feng, T.; O'Hara, A.; Neumayer, S.; Chyasnavichyus, M.; Eliseev, E. A., Piezoelectric domain walls in van der Waals antiferroelectric CuInP2Se6. *Nature communications* **2020,** *11* (1), 1-7.

276. Tottoli, E. M.; Dorati, R.; Genta, I.; Chiesa, E.; Pisani, S.; Conti, B., Skin Wound Healing Process and New Emerging Technologies for Skin Wound Care and Regeneration. *Pharmaceutics* **2020,** *12* (8), 735.

277. Martin, P.; Nunan, R., Cellular and molecular mechanisms of repair in acute and chronic wound healing. *British Journal of Dermatology* **2015,** *173* (2), 370-378.

278. Holmer, A.; Marotz, J.; Wahl, P.; Dau, M.; Kämmerer, P. W., Hyperspectral imaging in perfusion and wound diagnostics–methods and algorithms for the determination of tissue parameters. *Biomedical Engineering/Biomedizinische Technik* **2018,** *63* (5), 547-556.

279. Innes-Walker, K.; Parker, C.; Finlayson, K.; Brooks, M.; Young, L.; Morley, N.; Maresco-Pennisi, D.; Edwards, H., Improving patient outcomes by coaching primary health general practitioners and practice nurses in evidence based wound management at on-site wound clinics. *Collegian* **2019,** *26* (1), 62-68.

280. Edwards, H.; Finlayson, K.; Courtney, M.; Graves, N.; Gibb, M.; Parker, C., Health service pathways for patients with chronic leg ulcers: identifying effective pathways for facilitation of evidence based wound care. *BMC health services research* **2013,** *13* (1), 86.

281. Vinkel, J.; Holm, N. F. R.; Jakobsen, J. C.; Hyldegaard, O., Effects of adding adjunctive hyperbaric oxygen therapy to standard wound care for diabetic foot ulcers: a protocol for a systematic review with meta-analysis and trial sequential analysis. *BMJ open* **2020,** *10* (6), e031708.

282. Greer, N.; Foman, N. A.; MacDonald, R.; Dorrian, J.; Fitzgerald, P.; Rutks, I.; Wilt, T. J., Advanced wound care therapies for nonhealing diabetic, venous, and arterial ulcers: a systematic review. *Annals of internal medicine* **2013,** *159* (8), 532-542.

283. Augustine, R.; Kalarikkal, N.; Thomas, S., Advancement of wound care from grafts to bioengineered smart skin substitutes. *Progress in biomaterials* **2014,** *3* (2-4), 103-113.

284. Adams, D. C.; Ramsey, M. L., Grafts in dermatologic surgery: review and update on full- and split-thickness skin grafts, free cartilage grafts, and composite grafts. *Dermatologic surgery* **2005,** *31*, 1055-1067.

285. Andreassi, A.; Bilenchi, R.; Biagioli, M.; D'Aniello, C., Classification and pathophysiology of skin grafts. *Clinics in dermatology* **2005,** *23* (4), 332-337.

286. Benichou, G.; Yamada, Y.; Yun, S.-H.; Lin, C.; Fray, M.; Tocco, G., Immune recognition and rejection of allogeneic skin grafts. *Immunotherapy* **2011,** *3* (6), 757-770.

287. Zamfirescu, D.; Owen, E.; Lascar, I.; Molitor, M.; Zegrea, I.; Popescu, M.; Bishop, G.; Lauer, C.; Simionescu, M.; Climov, M. In *Sentinel skin allograft—a reliable marker for monitoring of composite tissue transplant rejection*, Transplantation proceedings, Elsevier: 2009; pp 503-508.

288. Ren, S.-Y.; Liu, Y.-S.; Zhu, G.-J.; Liu, M.; Shi, S.-H.; Ren, X.-D.; Hao, Y.-G.; Gao, R.-D., Strategies and challenges in the treatment of chronic venous leg ulcers. *World Journal of Clinical Cases* **2020,** *8* (21), 5070-5085.

289. Stremitzer, S.; Wild, T.; Hoelzenbein, T., How precise is the evaluation of chronic wounds by health care professionals? *International wound journal* **2007,** *4* (2), 156-161.

290. Gartlan, J.; Smith, A.; Clennett, S.; Walshe, D.; Tomlinson-Smith, A.; Boas, L.; Robinson, A., An audit of the adequacy of acute wound care documentation of surgical inpatients. *Journal of Clinical nursing* **2010,** *19* (15-16), 2207-2214.

291. Dargaville, T. R.; Farrugia, B. L.; Broadbent, J. A.; Pace, S.; Upton, Z.; Voelcker, N. H., Sensors and imaging for wound healing: a review. *Biosensors and Bioelectronics* **2013,** *41*, 30-42.

292. Quan, S. Y.; Lazarus, G. S.; Kohli, A. R.; Kapoor, R.; Margolis, D. J., Digital imaging of wounds: are measurements reproducible among observers? *The International Journal of Lower Extremity Wounds* **2007,** *6* (4), 245-248.

293. Papazoglou, E. S.; Zubkov, L.; Mao, X.; Neidrauer, M.; Rannou, N.; Weingarten, M. S., Image analysis of chronic wounds for determining the surface area. *Wound repair and regeneration* **2010,** *18* (4), 349-358.

294. Barsley, R. E.; West, M. H.; Fair, J. A., Forensic photography: ultraviolet imaging of wounds on skin. *The American journal of forensic medicine and pathology* **1990,** *11* (4), 300-308.

295. Yanez, C. O.; Morales, A. R.; Yue, X.; Urakami, T.; Komatsu, M.; Järvinen, T. A.; Belfield, K. D., Deep vascular imaging in wounds by two-photon fluorescence microscopy. *PLoS One* **2013,** *8* (7), e67559.

296. Schmidt, A.; Nießner, F.; von Woedtke, T.; Bekeschus, S., Hyperspectral imaging of wounds reveals augmented tissue oxygenation following cold physical plasma treatment in vivo. *IEEE Transactions on Radiation and Plasma Medical Sciences* **2020**.

297. Kennedy, G. T.; Stone, R.; Kowalczewski, A. C.; Rowland, R. A.; Chen, J. H.; Baldado, M. L.; Ponticorvo, A.; Bernal, N. P.; Christy, R. J.; Durkin, A. J., Spatial frequency domain imaging: a quantitative, noninvasive tool for in vivo monitoring of burn wound and skin graft healing. *Journal of biomedical optics* **2019,** *24* (7), 071615.

298. Yudovsky, D.; Nouvong, A.; Pilon, L., Hyperspectral imaging in diabetic foot wound care. SAGE Publications Sage CA: Los Angeles, CA: 2010.

299. Rennie, M.; Lindvere-Teene, L.; Tapang, K.; Linden, R., Point-of-care fluorescence imaging predicts the presence of pathogenic bacteria in wounds: a clinical study. *Journal of Wound Care* **2017,** *26* (8), 452-460.

300. Wilson, B. C.; Adam, G., A Monte Carlo model for the absorption and flux distributions of light in tissue. *Medical physics* **1983,** *10* (6), 824-830.

301. Ng, A.; Swanevelder, J., Resolution in ultrasound imaging. *Continuing Education in Anaesthesia Critical Care & Pain* **2011,** *11* (5), 186-192.

302. Szabo, T. L.; Lewin, P. A., Ultrasound transducer selection in clinical imaging practice. *Journal of Ultrasound in Medicine* **2013,** *32* (4), 573-582.

303. Driver, V. R.; Fabbi, M., Recent Advances in the Use of Ultrasound in Wound Care. **2010**.

304. Ennis, W. J.; Lee, C.; Plummer, M.; Meneses, P., Current status of the use of modalities in wound care: electrical stimulation and ultrasound therapy. *Plastic and reconstructive surgery* **2011,** *127*, 93S-102S.

305. Kavros, S. J.; Miller, J. L.; Hanna, S. W., Treatment of ischemic wounds with noncontact, low-frequency ultrasound: the Mayo clinic experience, 2004-2006. *Advances in skin & wound care* **2007,** *20* (4), 221-226.

306. Henshaw, F. R.; Reid, I. B.; Spencer, A. M.; Turner, D. E., Point of care ultrasound imaging as a wound assessment tool in diabetic foot ulcers: a case series. *Journal of Wound Care* **2020,** *29* (Sup8), S28-S34.

307. Yabunaka, K.; Iizaka, S.; Nakagami, G.; Fujioka, M.; Sanada, H., Three-dimensional ultrasound imaging of the pressure ulcer. A case report. *Medical ultrasonography* **2015,** *17* (3), 404-406.

308. Gnyawali, S. C.; Barki, K. G.; Mathew-Steiner, S. S.; Dixith, S.; Vanzant, D.; Kim, J.; Dickerson, J. L.; Datta, S.; Powell, H.; Roy, S., High-resolution harmonics ultrasound imaging for non-invasive characterization of wound healing in a pre-clinical swine model. *PLoS One* **2015,** *10* (3), e0122327.

309. Hariri, A.; Chen, F.; Moore, C.; Jokerst, J. V., Noninvasive staging of pressure ulcers using photoacoustic imaging. *Wound Repair and Regeneration* **2019,** *27* (5), 488-496.

310. Schindelin, J.; Arganda-Carreras, I.; Frise, E.; Kaynig, V.; Longair, M.; Pietzsch, T.; Preibisch, S.; Rueden, C.; Saalfeld, S.; Schmid, B., Fiji: an open-source platform for biological-image analysis. *Nature methods* **2012,** *9* (7), 676-682.

311. Chino, D. Y.; Scabora, L. C.; Cazzolato, M. T.; Jorge, A. E.; Traina-Jr, C.; Traina, A. J., Segmenting skin ulcers and measuring the wound area using deep convolutional networks. *Computer Methods and Programs in Biomedicine* **2020,** *191*, 105376.

312. Malone, M.; Schwarzer, S.; Walsh, A.; Xuan, W.; Al Gannass, A.; Dickson, H. G.; Bowling, F. L., Monitoring wound progression to healing in diabetic foot ulcers using three-dimensional wound imaging. *Journal of Diabetes and its Complications* **2020,** *34* (2), 107471.

313. Toygar, I.; Simsir, I. Y.; Cetinkalp, S., Evaluation of three different techniques for measuring wound area in diabetic foot ulcers: a reproducibility study. *Journal of Wound Care* **2020,** *29* (9), 518-524.

314. Medina, A.; Scott, P. G.; Ghahary, A.; Tredget, E. E., Pathophysiology of chronic nonhealing wounds. *Journal of Burn Care & Rehabilitation* **2005,** *26* (4), 306-319.

315. Terslev, L.; Torp-Pedersen, S.; Savnik, A.; Von der Recke, P.; Qvistgaard, E.; Danneskiold-Samsøe, B.; Bliddal, H., Doppler ultrasound and magnetic resonance imaging of synovial inflammation of the hand in rheumatoid arthritis: a comparative study. *Arthritis & Rheumatism: Official Journal of the American College of Rheumatology* **2003,** *48* (9), 2434-2441.

316. Ripollés, T.; Rausell, N.; Paredes, J. M.; Grau, E.; Martínez, M. J.; Vizuete, J., Effectiveness of contrast-enhanced ultrasound for characterisation of intestinal inflammation in Crohn's disease: a comparison with surgical histopathology analysis. *Journal of Crohn's and Colitis* **2013,** *7* (2), 120-128.

317. Ackerman, J. E.; Studentsova, V.; Myers, M.; Buckley, M. R.; Richards, M. S.; Loiselle, A. E., Non-invasive ultrasound quantification of scar tissue volume identifies early functional changes during tendon healing. *Journal of Orthopaedic Research®* **2019,** *37* (11), 2476-2485.

318. Verhaegen, P. D.; Van Zuijlen, P. P.; Pennings, N. M.; Van Marle, J.; Niessen, F. B.; Van Der Horst, C. M.; Middelkoop, E., Differences in collagen architecture between keloid, hypertrophic scar, normotrophic scar, and normal skin: an objective histopathological analysis. *Wound Repair and Regeneration* **2009,** *17* (5), 649-656.

319. Timar-Banu, O.; Beauregard, H.; Tousignant, J.; Lassonde, M.; Harris, P.; Viau, G.; Vachon, L.; Levy, E.; Abribat, T., Development of noninvasive and quantitative methodologies

for the assessment of chronic ulcers and scars in humans. *Wound Repair and Regeneration* **2001,** *9* (2), 123-132.

320. Landis, S. J., Chronic wound infection and antimicrobial use. *Advances in skin & wound care* **2008,** *21* (11), 531-540.

321. Valencia, I. C.; Falabella, A.; Kirsner, R. S.; Eaglstein, W. H., Chronic venous insufficiency and venous leg ulceration. *Journal of the American Academy of Dermatology* **2001,** *44* (3), 401-424.

322. Guo, S. a.; DiPietro, L. A., Factors affecting wound healing. *Journal of dental research* **2010,** *89* (3), 219-229.

323. Gould, L. J.; Abadir, P. M.; White-Chu, E. F., Age, frailty, and impaired wound healing. *Principles and practice of geriatric surgery* **2020**, 465-482.

324. Kim, J.; Park, E.-Y.; Park, B.; Choi, W.; Lee, K. J.; Kim, C., Towards clinical photoacoustic and ultrasound imaging: Probe improvement and real-time graphical user interface. *Experimental Biology and Medicine* **2020,** *245* (4), 321-329.

325. Eming, S. A.; Martin, P.; Tomic-Canic, M., Wound repair and regeneration: mechanisms, signaling, and translation. *Science translational medicine* **2014,** *6* (265), 265sr6-265sr6.

326. Han, G.; Ceilley, R., Chronic wound healing: a review of current management and treatments. *Advances in therapy* **2017,** *34* (3), 599-610.

327. Pang, S. M.-c.; Wong, T. K.-s., Predicting pressure sore risk with the Norton, Braden, and Waterlow scales in a Hong Kong rehabilitation hospital. *Nursing Research* **1998,** *47* (3), 147-153.

328. Balzer, K.; Pohl, C.; Dassen, T.; Halfens, R., The Norton, Waterlow, Braden, and Care Dependency ScalesL Comparing Their Validity When Identifying Patients' Pressure Sore Risk. *Journal of Wound Ostomy & Continence Nursing* **2007,** *34* (4), 389-398.

329. Cox, J., Predictors of pressure ulcers in adult critical care patients. *American journal of critical care* **2011,** *20* (5), 364-375.

330. Nouvong, A.; Hoogwerf, B.; Mohler, E.; Davis, B.; Tajaddini, A.; Medenilla, E., Evaluation of diabetic foot ulcer healing with hyperspectral imaging of oxyhemoglobin and deoxyhemoglobin. *Diabetes care* **2009,** *32* (11), 2056-2061.

331. Langevin, H. M.; Konofagou, E. E.; Badger, G. J.; Churchill, D. L.; Fox, J. R.; Ophir, J.; Garra, B. S., Tissue displacements during acupuncture using ultrasound elastography techniques. *Ultrasound in medicine & biology* **2004,** *30* (9), 1173-1183.

332. Ferrara, K.; Pollard, R.; Borden, M., Ultrasound microbubble contrast agents: fundamentals and application to gene and drug delivery. *Annu. Rev. Biomed. Eng.* **2007,** *9*, 415-447.

333. Lindner, J. R., Microbubbles in medical imaging: current applications and future directions. *Nature reviews Drug discovery* **2004,** *3* (6), 527-533.

334. Kim, K.; Zhang, S.; Salazar, G.; Jiang, X., Design, fabrication and characterization of high temperature piezoelectric vibration sensor using YCOB crystals. *Sensors and Actuators A: Physical* **2012,** *178*, 40-48.

335. Yang, J.-M.; Favazza, C.; Chen, R.; Yao, J.; Cai, X.; Maslov, K.; Zhou, Q.; Shung, K. K.; Wang, L. V., Simultaneous functional photoacoustic and ultrasonic endoscopy of internal organs in vivo. *Nature medicine* **2012,** *18* (8), 1297-1302.

336. Chen, Z.; Song, X.; Lei, L.; Chen, X.; Fei, C.; Chiu, C. T.; Qian, X.; Ma, T.; Yang, Y.; Shung, K., 3D printing of piezoelectric element for energy focusing and ultrasonic sensing. *Nano Energy* **2016,** *27*, 78-86.

337. Aoi, N.; Yoshimura, K.; Kadono, T.; Nakagami, G.; Iizuka, S.; Higashino, T.; Araki, J.; Koshima, I.; Sanada, H., Ultrasound assessment of deep tissue injury in pressure ulcers: possible prediction of pressure ulcer progression. *Plastic and reconstructive surgery* **2009,** *124* (2), 540-550.

338. Mantri, Y.; Tsujimoto, J.; Penny, W. F.; Garimella, P. S.; Anderson, C. A.; Jokerst, J. V., Point-of-Care Ultrasound as a Tool to Assess Wound Size and Tissue Regeneration after Skin Grafting. *Ultrasound in Medicine & Biology* **2021**.

339. Wang, L. V., *Photoacoustic imaging and spectroscopy*. CRC press: 2009.

340. Laufer, J. G.; Zhang, E. Z.; Treeby, B. E.; Cox, B. T.; Beard, P. C.; Johnson, P.; Pedley, B., In vivo preclinical photoacoustic imaging of tumor vasculature development and therapy. *Journal of biomedical optics* **2012,** *17* (5), 056016.

341. Weber, J.; Beard, P. C.; Bohndiek, S. E., Contrast agents for molecular photoacoustic imaging. *Nature methods* **2016,** *13* (8), 639.

342. Hariri, A.; Wang, J.; Kim, Y.; Jhunjhunwala, A.; Chao, D. L.; Jokerst, J. V., In vivo photoacoustic imaging of chorioretinal oxygen gradients. *Journal of biomedical optics* **2018,** *23* (3), 036005.

343. Attia, A. B. E.; Moothanchery, M.; Li, X.; Yew, Y. W.; Thng, S. T. G.; Dinish, U.; Olivo, M., Microvascular imaging and monitoring of hemodynamic changes in the skin during arterial-venous occlusion using multispectral raster-scanning optoacoustic mesoscopy. *Photoacoustics* **2021,** *22*, 100268.

344. Tonnesen, M. G.; Feng, X.; Clark, R. A. In *Angiogenesis in wound healing*, Journal of Investigative Dermatology Symposium Proceedings, Elsevier: 2000; pp 40-46.

345. Jonsson, K.; Jensen, J. A.; Goodson 3rd, W.; Scheuenstuhl, H.; West, J.; Hopf, H. W.; Hunt, T. K., Tissue oxygenation, anemia, and perfusion in relation to wound healing in surgical patients. *Annals of surgery* **1991,** *214* (5), 605.

346. Kolluru, G. K.; Bir, S. C.; Kevil, C. G., Endothelial dysfunction and diabetes: effects on angiogenesis, vascular remodeling, and wound healing. *International journal of vascular medicine* **2012,** *2012*.

347. Huang, X.; Liang, P.; Jiang, B.; Zhang, P.; Yu, W.; Duan, M.; Guo, L.; Cui, X.; Huang, M.; Huang, X., Hyperbaric oxygen potentiates diabetic wound healing by promoting fibroblast cell proliferation and endothelial cell angiogenesis. *Life Sciences* **2020,** *259*, 118246.

348. Liu, Y.; Tang, N.; Cao, K.; Wang, S.; Tang, S.; Su, H.; Zhou, J., Negative-pressure wound therapy promotes wound healing by enhancing angiogenesis through suppression of NLRX1 via miR-195 upregulation. *The international journal of lower extremity wounds* **2018,** *17* (3), 144-150.

349. Sun, X.; Zhang, J.; Wang, W.; Sun, J.; Wang, A., Maggot debridement therapy promotes diabetic foot wound healing by up-regulating endothelial cell activity. *Journal of Diabetes and its Complications* **2016,** *30* (2), 318-322.

350. Kiefer, F.; Neysari, S.; Humar, R.; Li, W.; Munk, V.; Battegay, E., Hypertension and angiogenesis. *Current pharmaceutical design* **2003,** *9* (21), 1733-1744.

351. Petri, M.; Stoffels, I.; Jose, J.; Leyh, J.; Schulz, A.; Dissemond, J.; Schadendorf, D.; Klode, J., Photoacoustic imaging of real-time oxygen changes in chronic leg ulcers after topical application of a haemoglobin spray: a pilot study. *Journal of wound care* **2016,** *25* (2), 87-91.

352. Yang, J.; Zhang, G.; Wu, M.; Shang, Q.; Huang, L.; Jiang, H., Photoacoustic assessment of hemodynamic changes in foot vessels. *Journal of biophotonics* **2019,** *12* (6), e201900004.

353. Yang, J.; Zhang, G.; Shang, Q.; Wu, M.; Huang, L.; Jiang, H., Detecting hemodynamic changes in the foot vessels of diabetic patients by photoacoustic tomography. *Journal of biophotonics* **2020,** *13* (8), e202000011.

354. Wu, M.; Shang, Q.; Yang, J.; Huang, L.; Jiang, H. In *In vivo Monitoring Hemodynamic Changes in Finger Vessels Using Photoacoustic Tomography*, Proceedings of the 2020 2nd International Conference on Intelligent Medicine and Image Processing, 2020; pp 13-18.

355. Choi, W.; Park, E.; Jeon, S.; Cho, S.; Ahn, J.; Park, B.; Kim, C. In *3D multi-structural foot imaging using dual-modal photoacoustic and ultrasound imaging*, Photons Plus Ultrasound: Imaging and Sensing 2021, International Society for Optics and Photonics: 2021; p 116420P.

356. Cheng, Z.; Ma, H.; Wang, Z.; Yang, S., In vivo volumetric monitoring of revascularization of traumatized skin using extended depth-of-field photoacoustic microscopy. *Frontiers of Optoelectronics* **2020,** *13* (4), 307-317.

357. Langemo, D.; Anderson, J.; Hanson, D.; Hunter, S.; Thompson, P., Measuring wound length, width, and area: which technique? *Advances in skin & wound care* **2008,** *21* (1), 42-45.

358. Zimny, S.; Schatz, H.; Pfohl, M., Determinants and estimation of healing times in diabetic foot ulcers. *Journal of Diabetes and its Complications* **2002,** *16* (5), 327-332.

359. Vas, P.; Rayman, G.; Dhatariya, K.; Driver, V.; Hartemann, A.; Londahl, M.; Piaggesi, A.; Apelqvist, J.; Attinger, C.; Game, F., Effectiveness of interventions to enhance healing of chronic foot ulcers in diabetes: a systematic review. *Diabetes/metabolism research and reviews* **2020,** *36*, e3284.

360. Feldman-Idov, Y.; Melamed, Y.; Linn, S.; Ore, L., Prognostic factors predicting ischemic wound healing following hyperbaric oxygenation therapy. *Wound Repair and Regeneration* **2013,** *21* (3), 418-427.

361. Reed, G. W.; Young, L.; Bagh, I.; Maier, M.; Shishehbor, M. H., Hemodynamic assessment before and after endovascular therapy for critical limb ischemia and association with clinical outcomes. *JACC: Cardiovascular Interventions* **2017,** *10* (23), 2451-2457.

362. Squiers, J. J.; Thatcher, J. E.; Bastawros, D.; Applewhite, A. J.; Baxter, R. D.; Yi, F.; Quan, P.; Yu, S.; DiMaio, J. M.; Gable, D. R., Machine learning analysis of multispectral imaging and clinical risk factors to predict amputation wound healing. *Journal of Vascular Surgery* **2021**.

363. Tehan, P. E.; Barwick, A. L.; Sebastian, M.; Chuter, V. H., Diagnostic accuracy of resting systolic toe pressure for diagnosis of peripheral arterial disease in people with and without diabetes: a cross-sectional retrospective case-control study. *Journal of foot and ankle research* **2017,** *10* (1), 1-7.

364. Cho, S. K.; Mattke, S.; Gordon, H.; Sheridan, M.; Ennis, W., Development of a model to predict healing of chronic wounds within 12 weeks. *Advances in wound care* **2020,** *9* (9), 516-524.

365. Barrientos, S.; Stojadinovic, O.; Golinko, M. S.; Brem, H.; Tomic-Canic, M., Growth factors and cytokines in wound healing. *Wound repair and regeneration* **2008,** *16* (5), 585-601.

366. Yew, Y. W.; Amma, D. U. K. S.; Kuan, A. H. Y.; Li, X.; Dev, K.; Attia, A. B. E.; Bi, R.; Moothanchery, M.; Balasundaram, G.; Aguirre, J., Raster-scanning optoacoustic mesoscopy imaging as an objective disease severity tool in atopic dermatitis patients. *Journal of the American Academy of Dermatology* **2021,** *84* (4), 1121-1123.

367. Toi, M.; Asao, Y.; Matsumoto, Y.; Sekiguchi, H.; Yoshikawa, A.; Takada, M.; Kataoka, M.; Endo, T.; Kawaguchi-Sakita, N.; Kawashima, M., Visualization of tumor-related blood vessels in human breast by photoacoustic imaging system with a hemispherical detector array. *Scientific reports* **2017,** *7* (1), 1-11.

368. Matsumoto, Y.; Asao, Y.; Yoshikawa, A.; Sekiguchi, H.; Takada, M.; Furu, M.; Saito, S.; Kataoka, M.; Abe, H.; Yagi, T., Label-free photoacoustic imaging of human palmar vessels: a structural morphological analysis. *Scientific reports* **2018,** *8* (1), 1-8.

369. Hariri, A.; Moore, C.; Mantri, Y.; Jokerst, J. V., Photoacoustic imaging as a tool for assessing hair follicular organization. *Sensors* **2020,** *20* (20), 5848.

370. Moore, C.; Chen, F.; Wang, J.; Jokerst, J. V., Listening for the therapeutic window: advances in drug delivery utilizing photoacoustic imaging. *Advanced drug delivery reviews* **2019,** *144*, 78-89.

371. Poldrack, R. A., Region of interest analysis for fMRI. *Social cognitive and affective neuroscience* **2007,** *2* (1), 67-70.

372. Nussbaum, S. R.; Carter, M. J.; Fife, C. E.; DaVanzo, J.; Haught, R.; Nusgart, M.; Cartwright, D., An economic evaluation of the impact, cost, and medicare policy implications of chronic nonhealing wounds. *Value in Health* **2018,** *21* (1), 27-32.

373. Rivard, A.; Fabre, J.-E.; Silver, M.; Chen, D.; Murohara, T.; Kearney, M.; Magner, M.; Asahara, T.; Isner, J. M., Age-dependent impairment of angiogenesis. *Circulation* **1999,** *99* (1), 111-120.

374. Nijhawans, P.; Behl, T.; Bhardwaj, S., Angiogenesis in obesity. *Biomedicine & Pharmacotherapy* **2020,** *126*, 110103.

375. Anderson, K.; Hamm, R. L., Factors that impair wound healing. *Journal of the American College of Clinical Wound Specialists* **2012,** *4* (4), 84-91.

376. Hallett, C. E.; Austin, L.; Caress, A.; Luker, K. A., Community nurses' perceptions of patient 'compliance'in wound care: A discourse analysis. *Journal of Advanced Nursing* **2000,** *32* (1), 115-123.

377. Mozaffarzadeh, M.; Moore, C.; Golmoghani, E. B.; Mantri, Y.; Hariri, A.; Jorns, A.; Fu, L.; Verweij, M. D.; Orooji, M.; de Jong, N., Motion-compensated noninvasive periodontal health monitoring using handheld and motor-based photoacoustic-ultrasound imaging systems. *Biomedical Optics Express* **2021,** *12* (3), 1543-1558.

378. Webster, A. C.; Nagler, E. V.; Morton, R. L.; Masson, P., Chronic kidney disease. *The lancet* **2017,** *389* (10075), 1238-1252.

379. Bikbov, B.; Purcell, C. A.; Levey, A. S.; Smith, M.; Abdoli, A.; Abebe, M.; Adebayo, O. M.; Afarideh, M.; Agarwal, S. K.; Agudelo-Botero, M., Global, regional, and national burden of chronic kidney disease, 1990–2017: a systematic analysis for the Global Burden of Disease Study 2017. *The Lancet* **2020,** *395* (10225), 709-733.

380. Eggers, P. W.; Gohdes, D.; Pugh, J., Nontraumatic lower extremity amputations in the Medicare end-stage renal disease population. *Kidney Int* **1999,** *56* (4), 1524-33.

381. Pecoraro, R. E.; Reiber, G. E.; Burgess, E. M., Pathways to diabetic limb amputation. Basis for prevention. *Diabetes Care* **1990,** *13* (5), 513-21.

382. Ndip, A.; Rutter, M. K.; Vileikyte, L.; Vardhan, A.; Asari, A.; Jameel, M.; Tahir, H. A.; Lavery, L. A.; Boulton, A. J., Dialysis treatment is an independent risk factor for foot ulceration in patients with diabetes and stage 4 or 5 chronic kidney disease. *Diabetes Care* **2010,** *33* (8), 1811-6.

383. Magder, S., The meaning of blood pressure. *Critical Care* **2018,** *22* (1), 1-10.

384. Vincent, J.-L.; Moraine, J.-J.; Van Der Linden, P., Toe temperature versus transcutaneous oxygen tension monitoring during acute circulatory failure. *Intensive care medicine* **1988,** *14* (1), 64-68.

385. Zampieri, F. G.; Damiani, L. P.; Bakker, J.; Ospina-Tascón, G. A.; Castro, R.; Cavalcanti, A. B.; Hernandez, G., Effects of a resuscitation strategy targeting peripheral perfusion status versus serum lactate levels among patients with septic shock. A Bayesian Reanalysis of the ANDROMEDA-SHOCK Trial. *American journal of respiratory and critical care medicine* **2020,** *201* (4), 423-429.

386. Lima, A.; Bakker, J., Noninvasive monitoring of peripheral perfusion. *Applied physiology in intensive care medicine* **2006**, 131-141.

387. Kmiec, M. M.; Hou, H.; Lakshmi Kuppusamy, M.; Drews, T. M.; Prabhat, A. M.; Petryakov, S. V.; Demidenko, E.; Schaner, P. E.; Buckey, J. C.; Blank, A., Transcutaneous oxygen measurement in humans using a paramagnetic skin adhesive film. *Magnetic resonance in medicine* **2019,** *81* (2), 781-794.

388. Aguirre, G. K.; Detre, J. A.; Wang, J., Perfusion fMRI for functional neuroimaging. *Int Rev Neurobiol* **2005,** *66*, 213-236.

389. Leahy, M.; De Mul, F.; Nilsson, G.; Maniewski, R., Principles and practice of the laser-Doppler perfusion technique. *Technology and health care* **1999,** *7* (2-3), 143-162.

390. Gioux, S.; Mazhar, A.; Cuccia, D. J., Spatial frequency domain imaging in 2019: principles, applications, and perspectives. *Journal of biomedical optics* **2019,** *24* (7), 071613.

391. Ercengiz, A.; Mutluoglu, M., Hyperbaric Transcutaneous Oximetry. **2017**.

392. Specht, K., Current challenges in translational and clinical fMRI and future directions. *Frontiers in psychiatry* **2020,** *10*, 924.

393. Bennett, C. M.; Miller, M. B.; Wolford, G. L., Neural correlates of interspecies perspective taking in the post-mortem Atlantic Salmon: An argument for multiple comparisons correction. *Neuroimage* **2009,** *47* (Suppl 1), S125.

394. Fagrell, B.; Nilsson, G., Advantages and limitations of one-point laser Doppler perfusion monitoring in clinical practice. *Vascular medicine review* **1995,** (2), 97-101.

395. Moore, C.; Borum, R. M.; Mantri, Y.; Xu, M.; Fajtová, P.; O'Donoghue, A. J.; Jokerst, J. V., Activatable Carbocyanine Dimers for Photoacoustic and Fluorescent Detection of Protease Activity. *ACS sensors* **2021**.

396. Nyayapathi, N.; Xia, J., Photoacoustic imaging of breast cancer: a mini review of system design and image features. *Journal of biomedical optics* **2019,** *24* (12), 121911.

397. Nyayapathi, N.; Zhang, H.; Zheng, E.; Nagarajan, S.; Bonaccio, E.; Takabe, K.; Fan, X. C.; Xia, J., Photoacoustic dual-scan mammoscope: results from 38 patients. *Biomedical Optics Express* **2021,** *12* (4), 2054-2063.

398. Ahn, J.; Kim, J. Y.; Choi, W.; Kim, C., High-resolution functional photoacoustic monitoring of vascular dynamics in human fingers. *Photoacoustics* **2021,** *23*, 100282.

399. Waldner, M. J.; Knieling, F.; Egger, C.; Morscher, S.; Claussen, J.; Vetter, M.; Kielisch, C.; Fischer, S.; Pfeifer, L.; Hagel, A., Multispectral optoacoustic tomography in Crohn's disease: noninvasive imaging of disease activity. *Gastroenterology* **2016,** *151* (2), 238-240.

400. Regensburger, A. P.; Wagner, A. L.; Claussen, J.; Waldner, M. J.; Knieling, F., Shedding light on pediatric diseases: multispectral optoacoustic tomography at the doorway to clinical applications. *Molecular and cellular pediatrics* **2020,** *7* (1), 1-6.

401. Regensburger, A. P.; Wagner, A. L.; Danko, V.; Jüngert, J.; Federle, A.; Klett, D.; Schuessler, S.; Buehler, A.; Neurath, M. F.; Roos, A., Multispectral optoacoustic tomography for non-invasive disease phenotyping in pediatric spinal muscular atrophy patients. *Photoacoustics* **2022,** *25*, 100315.

402. Manohar, S.; Gambhir, S., Clinical photoacoustic imaging. *Photoacoustics* **2020,** *19*.

403. Attia, A. B. E.; Balasundaram, G.; Moothanchery, M.; Dinish, U.; Bi, R.; Ntziachristos, V.; Olivo, M., A review of clinical photoacoustic imaging: Current and future trends. *Photoacoustics* **2019,** *16*, 100144.

404. Mantri, Y.; Tsujimoto, J.; Donovan, B.; Fernandes, C. C.; Garimella, P. S.; Penny, W. F.; Anderson, C. A.; Jokerst, J. V., Photoacoustic monitoring of angiogenesis predicts response to therapy in healing wounds. *Wound Repair and Regeneration* **2021**.

405. Himmelfarb, J.; Ikizler, T. A., Hemodialysis. *New England Journal of Medicine* **2010,** *363* (19), 1833-1845.

406. Charra, B., Fluid balance, dry weight, and blood pressure in dialysis. *Hemodialysis International* **2007,** *11* (1), 21-31.

407. Maggiore, Q.; Pizzarelli, F.; Santoro, A.; Panzetta, G.; Bonforte, G.; Hannedouche, T.; de Lara, M. A. A.; Tsouras, I.; Loureiro, A.; Ponce, P., The effects of control of thermal balance on vascular stability in hemodialysis patients: results of the European randomized clinical trial. *American journal of kidney diseases* **2002,** *40* (2), 280-290.

408. Stefánsson, B. V.; Brunelli, S. M.; Cabrera, C.; Rosenbaum, D.; Anum, E.; Ramakrishnan, K.; Jensen, D. E.; Stålhammar, N.-O., Intradialytic hypotension and risk of cardiovascular disease. *Clinical journal of the American Society of Nephrology* **2014,** *9* (12), 2124-2132.

409. Maggiore, Q. In *Isothermic dialysis for hypotension-prone patients*, Seminars in dialysis, Wiley Online Library: 2002; pp 187-190.

410. Secomb, T. W., Hemodynamics. *Comprehensive physiology* **2016,** *6* (2), 975.

411. Maneas, E.; Aughwane, R.; Huynh, N.; Xia, W.; Ansari, R.; Kuniyil Ajith Singh, M.; Hutchinson, J. C.; Sebire, N. J.; Arthurs, O. J.; Deprest, J., Photoacoustic imaging of the human placental vasculature. *Journal of biophotonics* **2020,** *13* (4), e201900167.

412. Saha, R. K.; Kolios, M. C., A simulation study on photoacoustic signals from red blood cells. *The Journal of the Acoustical Society of America* **2011,** *129* (5), 2935-2943.

413. Hysi, E.; Saha, R. K.; Kolios, M. C., On the use of photoacoustics to detect red blood cell aggregation. *Biomedical optics express* **2012,** *3* (9), 2326-2338.

414. Ozakin, E.; Yazlamaz, N. O.; Kaya, F. B.; Karakilic, E. M.; Bilgin, M., Perfusion index measurement in predicting hypovolemic shock in trauma patients. *The Journal of Emergency Medicine* **2020,** *59* (2), 238-245.

415. Bolignano, D.; Rastelli, S.; Agarwal, R.; Fliser, D.; Massy, Z.; Ortiz, A.; Wiecek, A.; Martinez-Castelao, A.; Covic, A.; Goldsmith, D., Pulmonary hypertension in CKD. *American Journal of Kidney Diseases* **2013,** *61* (4), 612-622.

416. Flythe, J. E.; Kimmel, S. E.; Brunelli, S. M., Rapid fluid removal during dialysis is associated with cardiovascular morbidity and mortality. *Kidney international* **2011,** *79* (2), 250-257.

417. Lavery, L. A.; Lavery, D. C.; Hunt, N. A.; La Fontaine, J.; Ndip, A.; Boulton, A. J., Amputations and foot-related hospitalisations disproportionately affect dialysis patients. *International wound journal* **2015,** *12* (5), 523-526.

418. Meloni, M.; Izzo, V.; Giurato, L.; Cervelli, V.; Gandini, R.; Uccioli, L., Impact of heart failure and dialysis in the prognosis of diabetic patients with ischemic foot ulcers. *Journal of clinical & translational endocrinology* **2018,** *11*, 31-35.

419. Evangelidis, N.; Sautenet, B.; Manera, K. E.; Howell, M.; Craig, J. C.; Viecelli, A. K.; O'Lone, E.; Scholes-Robertson, N.; Johnson, D. W.; Cho, Y., Perspectives on blood pressure by patients on haemo-and peritoneal dialysis. *Nephrology* **2021,** *26* (1), 62-69.

420. Gũnal, A. I.; Karaca, I.; Celiker, H.; Ilkay, E.; Duman, S., Paradoxical rise in blood pressure during ultrafiltration is caused by increased cardiac output. *Journal of nephrology* **2002,** *15* (1), 42-47.

421. Cirillo, M.; Laurenzi, M.; Trevisan, M.; Stamler, J., Hematocrit, blood pressure, and hypertension. The gubbio population study. *Hypertension* **1992,** *20* (3), 319-326.

422. Mantri, Y.; Tsujimoto, J.; Donovan, B.; Fernandes, C. C.; Garimella, P. S.; Penny, W. F.; Anderson, C. A.; Jokerst, J. V., Photoacoustic monitoring of angiogenesis predicts response to therapy in healing wounds. *medRxiv* **2021**.

423. Makhsous, M.; Priebe, M.; Bankard, J.; Rowles, R.; Zeigler, M.; Chen, D.; Lin, F., Measuring tissue perfusion during pressure relief maneuvers: insights into preventing pressure ulcers. *The journal of spinal cord medicine* **2007,** *30* (5), 497-507.

424. Choi, M.; Shapiro, A. J.; Zemp, R., Tissue perfusion rate estimation with compression-based photoacoustic-ultrasound imaging. *Journal of Biomedical Optics* **2018,** *23* (1), 016010.

425. Zhang, E.; Laufer, J.; Pedley, R.; Beard, P., In vivo high-resolution 3D photoacoustic imaging of superficial vascular anatomy. *Physics in Medicine & Biology* **2009,** *54* (4), 1035.

426. Goldman, R. J., Hyperbaric oxygen therapy for wound healing and limb salvage: a systematic review. *PM&R* **2009,** *1* (5), 471-489.

427. Gundogdu, Z., Relationship between BMI and blood pressure in girls and boys. *Public health nutrition* **2008,** *11* (10), 1085-1088.

428. Bakris, G. L., The importance of blood pressure control in the patient with diabetes. *The American journal of medicine* **2004,** *116* (5), 30-38.

429. Landahl, S.; Bengtsson, C.; Sigurdsson, J. A.; Svanborg, A.; Svärdsudd, K., Age-related changes in blood pressure. *Hypertension* **1986,** *8* (11), 1044-1049.

430. Mantri, Y.; Jokerst, J. V., Impact of skin tone on photoacoustic oximetry and tools to minimize bias. *Biomedical Optics Express* **2022,** *13* (2), 875-887.

431. Shroff, R. C.; McNair, R.; Figg, N.; Skepper, J. N.; Schurgers, L.; Gupta, A.; Hiorns, M.; Donald, A. E.; Deanfield, J.; Rees, L., Dialysis accelerates medial vascular calcification in part by triggering smooth muscle cell apoptosis. *Circulation* **2008,** *118* (17), 1748-1757.

432. Manwar, R.; Li, X.; Mahmoodkalayeh, S.; Asano, E.; Zhu, D.; Avanaki, K., Deep learning protocol for improved photoacoustic brain imaging. *Journal of biophotonics* **2020,** *13* (10), e202000212.

433. Sjoding, M. W.; Dickson, R. P.; Iwashyna, T. J.; Gay, S. E.; Valley, T. S., Racial bias in pulse oximetry measurement. *New England Journal of Medicine* **2020,** *383* (25), 2477-2478.

434. Bickler, P. E.; Feiner, J. R.; Rollins, M. D., Factors affecting the performance of 5 cerebral oximeters during hypoxia in healthy volunteers. *Anesthesia and analgesia* **2013,** *117* (4), 813-23.

435. Mendenhall, M. J.; Nunez, A. S.; Martin, R. K., Human skin detection in the visible and near infrared. *Applied optics* **2015,** *54* (35), 10559-70.

436. Szabo, P.; Wolf, M.; Bucher, H. U.; Fauchere, J. C.; Haensse, D.; Arlettaz, R., Detection of hyperbilirubinaemia in jaundiced full-term neonates by eye or by bilirubinometer? *Eur J Pediatr* **2004,** *163* (12), 722-7.

437. Shcherbina, A.; Mattsson, C. M.; Waggott, D.; Salisbury, H.; Christle, J. W.; Hastie, T.; Wheeler, M. T.; Ashley, E. A., Accuracy in Wrist-Worn, Sensor-Based Measurements of Heart Rate and Energy Expenditure in a Diverse Cohort. *J Pers Med* **2017,** *7* (2).

438. Colvonen, P. J.; DeYoung, P. N.; Bosompra, N.-O. A.; Owens, R. L., Limiting racial disparities and bias for wearable devices in health science research. Oxford University Press US: 2020.

439. Colvonen, P. J., Response To: Investigating sources of inaccuracy in wearable optical heart rate sensors. *NPJ Digital Medicine* **2021,** *4* (1), 1-2.

440. Li, X.; Dinish, U. S.; Aguirre, J.; Bi, R.; Dev, K.; Attia, A. B. E.; Nitkunanantharajah, S.; Lim, Q. H.; Schwarz, M.; Yew, Y. W.; Thng, S. T. G.; Ntziachristos, V.; Olivo, M., Optoacoustic mesoscopy analysis and quantitative estimation of specific imaging metrics in Fitzpatrick skin phototypes II to V. *J Biophotonics* **2019,** *12* (9), e201800442.

441. Kiani, J., Pulse Oximeters Are Not Racist. *Neonatology Today* **2021**, 143-144.

442. Brahimi-Horn, M. C.; Chiche, J.; Pouysségur, J., Hypoxia and cancer. *Journal of molecular medicine* **2007,** *85* (12), 1301-1307.

443. Bhandari, V.; Hoey, C.; Liu, L. Y.; Lalonde, E.; Ray, J.; Livingstone, J.; Lesurf, R.; Shiah, Y.-J.; Vujcic, T.; Huang, X., Molecular landmarks of tumor hypoxia across cancer types. *Nature genetics* **2019,** *51* (2), 308-318.

444. Graham, K.; Unger, E., Overcoming tumor hypoxia as a barrier to radiotherapy, chemotherapy and immunotherapy in cancer treatment. *International journal of nanomedicine* **2018,** *13*, 6049.

445. Kashani, K. B. In *Hypoxia in COVID-19: sign of severity or cause for poor outcomes*, Mayo Clinic Proceedings, Elsevier: 2020; pp 1094-1096.

446. Shenoy, N.; Luchtel, R.; Gulani, P., Considerations for target oxygen saturation in COVID-19 patients: are we under-shooting? *BMC medicine* **2020,** *18* (1), 1-6.

447. Howard, M. A.; Asmis, R.; Evans, K. K.; Mustoe, T. A., Oxygen and wound care: a review of current therapeutic modalities and future direction. *Wound Repair and Regeneration* **2013,** *21* (4), 503-511.

448. Hong, W. X.; Hu, M. S.; Esquivel, M.; Liang, G. Y.; Rennert, R. C.; McArdle, A.; Paik, K. J.; Duscher, D.; Gurtner, G. C.; Lorenz, H. P., The role of hypoxia-inducible factor in wound healing. *Advances in wound care* **2014,** *3* (5), 390-399.

449. MacCarthy-Morrogh, L.; Martin, P., The hallmarks of cancer are also the hallmarks of wound healing. *Science Signaling* **2020,** *13* (648).

450. Fu, Q.; Colgan, S. P.; Shelley, C. S., Hypoxia: the force that drives chronic kidney disease. *Clinical medicine & research* **2016,** *14* (1), 15-39.

451. Locatelli, F.; Fishbane, S.; Block, G. A.; Macdougall, I. C., Targeting hypoxia-inducible factors for the treatment of anemia in chronic kidney disease patients. *American journal of nephrology* **2017,** *45* (3), 187-199.

452. Yeo, E.-J., Hypoxia and aging. *Experimental & Molecular Medicine* **2019,** *51* (6), 1-15.

453. Burtscher, J.; Mallet, R. T.; Burtscher, M.; Millet, G. P., Hypoxia and brain aging: Neurodegeneration or neuroprotection? *Ageing research reviews* **2021,** *68*, 101343.

454. Sachdeva, S., Fitzpatrick skin typing: Applications in dermatology. *Indian journal of dermatology, venereology and leprology* **2009,** *75* (1), 93.

455. D'Orazio, J.; Jarrett, S.; Amaro-Ortiz, A.; Scott, T., UV radiation and the skin. *International journal of molecular sciences* **2013,** *14* (6), 12222-12248.

456. Jacques, S. L., Melanosome absorption coefficient. *Oregon Medical Laser Center* **1998,** *7*.

457. Prahl, S., Optical absorption of hemoglobin. *http://omlc. ogi. edu/spectra/hemoglobin* **1999**.

458. Omar, M.; Aguirre, J.; Ntziachristos, V., Optoacoustic mesoscopy for biomedicine. *Nature biomedical engineering* **2019,** *3* (5), 354-370.

459. Wang, L. V.; Wu, H.-i., *Biomedical optics: principles and imaging*. John Wiley & Sons: 2012.

460. Vienneau, E.; Vu, T.; Yao, J., Photoacoustic Imaging of Skin. *Imaging Technologies and Transdermal Delivery in Skin Disorders* **2019**, 411-442.

461. Manohar, S.; Razansky, D., Photoacoustics: a historical review. *Advances in optics and photonics* **2016,** *8* (4), 586-617.

462. Mantri, Y.; Tsujimoto, J.; Donovan, B.; Fernandes, C. C.; Garimella, P. S.; Penny, W. F.; Anderson, C. A.; Jokerst, J. V., Photoacoustic monitoring of angiogenesis predicts response to therapy in healing wounds. *medRxiv* **2021**, 2021.10.13.21264867.

463. Hindelang, B.; Aguirre, J.; Berezhnoi, A.; He, H.; Eyerich, K.; Ntziachristos, V.; Biedermann, T.; Darsow, U., Optoacoustic mesoscopy shows potential to increase accuracy of allergy patch testing. *Contact dermatitis* **2020,** *83* (3), 206-214.

464. Agrawal, S.; Kuniyil Ajith Singh, M.; Johnstonbaugh, K.; C Han, D.; R Pameijer, C.; Kothapalli, S.-R., Photoacoustic imaging of human vasculature using LED versus laser illumination: A comparison study on tissue phantoms and in vivo humans. *Sensors* **2021,** *21* (2), 424.

465. Dogan, B. E.; Menezes, G. L.; Butler, R. S.; Neuschler, E. I.; Aitchison, R.; Lavin, P. T.; Tucker, F. L.; Grobmyer, S. R.; Otto, P. M.; Stavros, A. T., Optoacoustic imaging and gray-scale US features of breast cancers: correlation with molecular subtypes. *Radiology* **2019,** *292* (3), 564-572.

466. Neuschler, E. I.; Butler, R.; Young, C. A.; Barke, L. D.; Bertrand, M. L.; Böhm-Vélez, M.; Destounis, S.; Donlan, P.; Grobmyer, S. R.; Katzen, J., A pivotal study of optoacoustic imaging to diagnose benign and malignant breast masses: a new evaluation tool for radiologists. *Radiology* **2018,** *287* (2), 398-412.

467. Menezes, G. L.; Pijnappel, R. M.; Meeuwis, C.; Bisschops, R.; Veltman, J.; Lavin, P. T.; Van De Vijver, M. J.; Mann, R. M., Downgrading of breast masses suspicious for cancer by using optoacoustic breast imaging. *Radiology* **2018,** *288* (2), 355-365.

468. O'driscoll, B.; Howard, L.; Davison, A., BTS guideline for emergency oxygen use in adult patients. *Thorax* **2008,** *63* (Suppl 6), vi1-vi68.

469. Gallagher, D.; Heymsfield, S. B.; Heo, M.; Jebb, S. A.; Murgatroyd, P. R.; Sakamoto, Y., Healthy percentage body fat ranges: an approach for developing guidelines based on body mass index. *The American journal of clinical nutrition* **2000,** *72* (3), 694-701.

470. Del Bino, S.; Bernerd, F., Variations in skin colour and the biological consequences of ultraviolet radiation exposure. *British Journal of Dermatology* **2013,** *169*, 33-40.

471. Vogt, W. C.; Jia, C.; Wear, K. A.; Garra, B. S.; Pfefer, T. J., Phantom-based image quality test methods for photoacoustic imaging systems. *Journal of biomedical optics* **2017,** *22* (9), 095002.

472. Alaluf, S.; Atkins, D.; Barrett, K.; Blount, M.; Carter, N.; Heath, A., Ethnic variation in melanin content and composition in photoexposed and photoprotected human skin. *Pigment Cell Res* **2002,** *15* (2), 112-8.

473. Dev, S. P.; Hillmer, M. D.; Ferri, M., Arterial puncture for blood gas analysis. *N Engl J Med* **2011,** *364* (5), e7.

474. Gehrung, M.; Bohndiek, S. E.; Brunker, J., Development of a blood oxygenation phantom for photoacoustic tomography combined with online pO 2 detection and flow spectrometry. *Journal of biomedical optics* **2019,** *24* (12), 121908.

475. Hurbain, I.; Romao, M.; Sextius, P.; Bourreau, E.; Marchal, C.; Bernerd, F.; Duval, C.; Raposo, G., Melanosome distribution in keratinocytes in different skin types: melanosome clusters are not degradative organelles. *Journal of Investigative Dermatology* **2018,** *138* (3), 647-656.

476. Thong, H. Y.; Jee, S. H.; Sun, C. C.; Boissy, R., The patterns of melanosome distribution in keratinocytes of human skin as one determining factor of skin colour. *British Journal of Dermatology* **2003,** *149* (3), 498-505.

477. Upputuri, P. K.; Pramanik, M., Photoacoustic imaging in the second near-infrared window: a review. *Journal of biomedical optics* **2019,** *24* (4), 040901.

478. Mohammadi, L.; Behnam, H.; Tavakkoli, J.; Avanaki, K., Skull acoustic aberration correction in photoacoustic microscopy using a vector space similarity model: a proof-of-concept simulation study. *Biomedical Optics Express* **2020,** *11* (10), 5542-5556.

479. Cai, C.; Wang, X.; Si, K.; Qian, J.; Luo, J.; Ma, C., Streak artifact suppression in photoacoustic computed tomography using adaptive back projection. *Biomedical optics express* **2019,** *10* (9), 4803-4814.

480. Turek, J. S.; Elad, M.; Yavneh, I., Clutter mitigation in echocardiography using sparse signal separation. *International journal of biomedical imaging* **2015,** *2015*.

481. Matrone, G.; Bell, M. A. L.; Ramalli, A., Spatial Coherence Beamforming with Multi-Line Transmission to Enhance the Contrast of Coherent Structures in Ultrasound Images Degraded by Acoustic Clutter. *IEEE Transactions on Ultrasonics, Ferroelectrics, and Frequency Control* **2021**.

482. Bulsink, R.; Kuniyil Ajith Singh, M.; Xavierselvan, M.; Mallidi, S.; Steenbergen, W.; Francis, K. J., Oxygen saturation imaging using LED-based photoacoustic system. *Sensors* **2021,** *21* (1), 283.

483. Schwab, H.-M.; Beckmann, M. F.; Schmitz, G. In *Photoacoustic clutter reduction using plane wave ultrasound and a linear scatter estimation approach*, 2015 IEEE International Ultrasonics Symposium (IUS), IEEE: 2015; pp 1-4.

484. Singh, M. K. A.; Steenbergen, W., Photoacoustic-guided focused ultrasound (PAFUSion) for identifying reflection artifacts in photoacoustic imaging. *Photoacoustics* **2015,** *3* (4), 123-131.

485. Alles, E. J.; Jaeger, M.; Bamber, J. C. In *Photoacoustic clutter reduction using short-lag spatial coherence weighted imaging*, 2014 IEEE International Ultrasonics Symposium, IEEE: 2014; pp 41-44.

486. Torp, K. D.; Modi, P.; Simon, L. V., Pulse oximetry. *StatPearls [Internet]* **2020**.

487. Coghill, E. M.; Johnson, T.; Morris, R. E.; Megson, I. L.; Leslie, S. J., Radial artery access site complications during cardiac procedures, clinical implications and potential solutions: the role of nitric oxide. *World journal of cardiology* **2020,** *12* (1), 26.

488. Feiner, J. R.; Severinghaus, J. W.; Bickler, P. E., Dark skin decreases the accuracy of pulse oximeters at low oxygen saturation: the effects of oximeter probe type and gender. *Anesthesia & Analgesia* **2007,** *105* (6), S18-S23.

489. Jensen, L. A.; Onyskiw, J. E.; Prasad, N., Meta-analysis of arterial oxygen saturation monitoring by pulse oximetry in adults. *Heart & lung* **1998,** *27* (6), 387-408.

490. Clarys, P.; Alewaeters, K.; Lambrecht, R.; Barel, A., Skin color measurements: comparison between three instruments: the Chromameter®, the DermaSpectrometer® and the Mexameter®. *Skin research and technology* **2000,** *6* (4), 230-238.